HYSTERETIC BEHAVIOUR OF STEEL- AND FIBRE-REINFORCED ELASTOMERIC ISOLATORS FITTED WITH SUPERELASTIC SHAPE MEMORY ALLOY WIRE

by

Farshad Hedayati Dezfuli

B.A.Sc. (Aerospace Engineering), Sharif University of Technology, Iran, 2007

M.A.Sc. (Aerostructures), Sharif University of Technology, Iran, 2009

A THESIS SUBMITTED IN PARTIAL FULFILLMENT OF

THE REQUIREMENTS FOR THE DEGREE OF

DOCTOR OF PHILOSOPHY

in

THE COLLEGE OF GRADUATE STUDIES

(Civil Engineering)

THE UNIVERSITY OF BRITISH COLUMBIA

(Okanagan)

April 2015

Abstract

Among different types of earthquake protective mechanisms, elastomeric base isolators, also called rubber bearings (RBs), are one of the most well-known systems that are widely used in buildings and bridges. They can regulate the seismic response of structures, increase the public safety, and reduce the cost of repair and rehabilitation by providing lateral flexibility and dissipating the earthquake's energy. RBs consist of elastomeric layers which are reinforced with steel shims or fibre-reinforced polymer composites. Seeking performance improvements, as well as cost and weight reduction led scientists to introduce different types of RBs. However, most RBs possess weaknesses such as limited shear strain capacity, un-recovered residual deformation, and instability due to large deformations. Using superelastic (ability to regain original shape upon unloading) shape memory alloy (SMA) in the form of wire, bar, or spring is a solution to partially overcome the aforementioned limitations. Its unique characteristics such as a flag-shaped hysteresis with zero residual deformation, superelastic effect (up to 13.5% recoverable strain) and a suitable fatigue property make it an ideal candidate for such applications. Objectives of this thesis are to propose a new generation SMA wire-based RBs (SMA-RB) and develop a novel constitutive model for such smart isolators in order to accurately capture their shear hysteretic behaviour. With the purpose of evaluating the performance of SMA-RBs in structural applications, the seismic fragility of a highway bridge isolated by SMA-RBs was assessed. First, a number of scaled carbon fibre-reinforced elastomeric isolators (C-FREIs) were manufactured and tested. Then, based on the experimental observations, numerical simulations were generated using finite element method (FEM). Results showed that incorporating SMA wires into natural and high-damping rubber bearings (NRB, HDRB) slightly improves the re-centring capability and energy dissipation capacity. However, equipping lead rubber bearing (LRB) with double cross SMA wires significantly reduces the residual deformation and noticeably enhances the energy damping property. It was also depicted that the developed hysteresis of SMA model can be characterized by three stiffnesses and two shear strain limits upon activation of SMA wires. Findings revealed that SMA wires can increase the reliability of elastomeric bearings and bridge system.

Preface

A version of Chapter 3 (sections 2 and 3) has been published. Hedayati Dezfuli, F., and Alam, M.S. 2012. Material modelling of high damping rubber in finite element method. *In proceedings of the 3rd International Structural Specialty Conference*, Edmonton, Alberta, Canada. June 6-9, 2012. I wrote the manuscript which was further edited by Dr. Alam.

A version of Chapter 3 (sections 3 to 5) has been published. Hedayati Dezfuli, F., and Alam, M.S. 2013. Multi-criteria optimization and seismic performance assessment of carbon FRP-based elastomeric isolator. *Engineering Structures*, 49: 525-540. I wrote the manuscript which was further edited by Dr. Alam.

A version of Chapter 4 (sections 4, 6, 8, and 9) has been published in two articles. Hedayati Dezfuli, F., and Alam, M.S. 2013. Sensitivity analysis of carbon fiber-reinforced elastomeric isolators based on experimental tests and finite element simulation. *Bulletin of Earthquake Engineering*, 12(2): 1025-1043; Hedayati Dezfuli, F., and Alam, M.S. 2014. Performance of carbon fiber-reinforced elastomeric isolators manufactured in a simplified process: experimental investigations. *Structural Control and Health Monitoring*. 21(11): 1347-1359. I conducted some parts of experimental tests in the Applied Dynamics laboratory at McMaster University. I wrote the manuscript which was further edited by Dr. Alam.

A version of Chapter 4 (section 7) has been published. Hedayati Dezfuli, F., and Alam, M.S. 2014. Finite element simulation of carbon fiber-reinforced elastomeric isolators manufactured through a cold-vulcanization process. In Proceedings of *9th International Conference on Short and Medium Span Bridges, SMSB,* Calgary, Alberta, Canada. July 15-18, 2014.

A version of Chapter 5 (section 2) has been published. The journal paper has been considered as the featured and the most downloaded article in Smart Materials and Structures journal and has been selected by the editors of the journal in the 'Highlights of 2013' collection on the basis of referee endorsement, novelty and scientific impact. Hedayati Dezfuli, F., and Alam, M.S. 2013. Shape memory alloy wire-based smart natural rubber bearing, *Smart Materials and Structures*, 22(4) 045013. I wrote the manuscript which was further edited by Dr. Alam.

A version of Chapter 5 (sections 3 and 5) has been published. Hedayati Dezfuli, F., and Alam, M.S. 2014. Performance-based assessment and design of FRP-based high damping rubber bearing incorporated with shape memory alloy wires. *Engineering Structures*, 61: 166-183. I wrote the manuscript which was further edited by Dr. Alam.

A version of Chapter 5 (sections 2 and 3) has been published. Hedayati Dezfuli, F., and Alam, M.S. 2013. Performance comparison between SMA-based natural rubber bearing and SMA-based high damping rubber bearing. *In Proceedings of 7th National Seismic Conference on Bridges & Highways*, Oakland, California, USA. May 20-22, 2013. I wrote the manuscript which was further edited by Dr. Alam.

A version of Chapter 5 (section 4) has been submitted to Journal of Bridge Engineering (ASCE). Hedayati Dezfuli, F., and Alam, M.S. 2015. Hedayati Dezfuli, F., and Alam, M.S. 2015. Smart lead rubber bearings equipped with ferrous shape memory alloy wires for seismically isolating highway bridges. Submitted to *Earthquake Engineering and Structural Dynamics,* Manuscript ID: EQE-15-0127. I wrote the manuscript which was further edited by Dr. Alam.

A version of Chapter 6 has been accepted for publication in Smart Materials and Structures journal. Hedayati Dezfuli, F., and Alam, M.S. 2015. Hysteresis model of shape memory alloy (SMA) wire-based laminated rubber bearing under compression and unidirectional shear loadings. *Smart Materials and Structures*, In Press. I wrote the manuscript which was further edited by Dr. Alam.

A version of Chapter 7 has been accepted in Structures Congress 2015 Conference. Hedayati Dezfuli, F., and Alam, M.S. 2015. Vulnerability assessment of multi-span continuous steel-girder bridges isolated by SMA wire-based natural rubber bearing (SMA-NRB). *Structures Congress 2015 Conference*, Portland, Oregon, USA. April 23-25, 2015. I wrote the manuscript which was further edited by Dr. Alam.

Publications arising from the work presented in this dissertation are listed as follows:

1- Hedayati Dezfuli, F., and Alam, M.S. 2015. Hysteresis model of shape memory alloy (SMA) wire-based laminated rubber bearing under compression and unidirectional shear loadings. *Smart Materials and Structures, In Press*.

2- Hedayati Dezfuli, F., and Alam, M.S. 2015. Vulnerability assessment of multi-span continuous steel-girder bridges isolated by SMA wire-based natural rubber bearing

(SMA-NRB), *Structures Congress 2015 Conference*, Portland, Oregon, USA (April 23-25, 2015).

3- Hedayati Dezfuli, F., and Alam, M.S. 2015. Smart lead rubber bearings equipped with ferrous shape memory alloy wires for seismically isolating highway bridges. Submitted to *Earthquake Engineering and Structural Dynamics,* Manuscript ID: EQE-15-0127.

4- Hedayati Dezfuli, F., and Alam, M.S. 2014. Performance-based assessment and design of FRP-based high damping rubber bearing incorporated with shape memory alloy wires. *Engineering Structures*, 61: 166-183.

5- Hedayati Dezfuli, F., and Alam, M.S. 2014. Performance of carbon fiber-reinforced elastomeric isolators manufactured in a simplified process: experimental investigations. *Structural Control and Health Monitoring*. 21(11): 1347–1359.

6- Hedayati Dezfuli, F., and Alam, M.S. 2014. Finite element simulation of carbon fiber-reinforced elastomeric isolators manufactured through a cold-vulcanization process. *In Proceedings of 9th International Conference on Short and Medium Span Bridges, SMSB,* Calgary, Alberta, Canada. July 15-18, 2014.

7- Hedayati Dezfuli, F., and Alam, M.S. 2013. Sensitivity analysis of carbon fiber-reinforced elastomeric isolators based on experimental tests and finite element simulation. *Bulletin of Earthquake Engineering*, 12(2): 1025-1043.

8- Hedayati Dezfuli, F., and Alam, M.S. 2013. Shape memory alloy wire-based smart natural rubber bearing," *Smart Materials and Structures*, 22(4): 045013.

9- Hedayati Dezfuli, F., and Alam, M.S. 2013. Multi-criteria optimization and seismic performance assessment of carbon FRP-based elastomeric isolator. *Engineering Structures*, 49: 525-540.

10- Hedayati Dezfuli, F., and Alam, M.S. 2013. Performance comparison between SMA-based natural rubber bearing and SMA-based high damping rubber bearing. *In Proceedings of 7th National Seismic Conference on Bridges & Highways*, Oakland, California, USA. May 20-22, 2013.

11- Hedayati Dezfuli, F., and Alam, M.S. 2012. Material modeling of high damping rubber in finite element method. *In Proceedings of the 3rd International Structural Specialty Conference*, Edmonton, Alberta, Canada. June 6-9 2012.

Table of Contents

List of Tables

List of Figures

List of Symbols and Abbreviations

A^f	Austenite finish temperature of SMA
A^s	Austenite start temperature of SMA
A_f	Plan area of reinforcement
d_y	Yield dispalcement
E_A	Elastic modulus of SMA at austenite phase
E_c	Compression modulus
E_f	Elastic modulus of reinforcement
E_M	Elastic modulus of SMA at martensite phase
F_{max}	Maximum shear force
F_{min}	Minimum shear force
F_y	Yield force
f	Cyclic frequency
G_r	Shear modulus of rubber
K_0	Initial stiffness
K_{Heff}	Effective horizontal stiffness
K_V	Vertical stiffness
L	Length of laminated pad
M^f	Martensite finish temperature of SMA
M^s	Martensite start temperature of SMA
n_e	Number of rubber layers
P	Vertical pressure
Q_d	Characteristic strength
r	Post-yield hardening ratio
r_{SMA}	Radius of cross section of SMA wire
S	Shape factor of rubber bearing
S_d	Median of demand
S_c	Median of capacity
t_e	Thickness of one rubber layer
t_r	Total thickness of rubber layers
t_f	Thickness of reinforcement
U_d	Energy dissipated per cycle
U_e	Energy restored in the rubber bearing
V_H	Horizontal velocity of lateral displacement
W	Width of laminated pad
β_c	Logarithmic standard deviation of capacity
$\beta_{D/IM}$	Logarithmic standard deviation of demand
β_{eq}	Equivalent viscous damping
ε_s	Superelastic strain in SMA
ε_{SMA}	Strain in SMA wires
γ	Shear strain
Δ_{max}	Maximum lateral displacement
Δ_{min}	Minimum lateral displacement
λ	Median of intensity measure
μ_d	Displacement ductility
ξ	Standard deviation of intensity measure
v	Poisson's ratio
ω	Angluar frequency

C-FREI	Carbon fibre-reinforced elastomeric isolator
CDF	Cumulative distribution function
CFR	Carbon fibre-reinforced
EDC	Energy dissipated per cycle
EDP	Engineering demand parameter
FEM	Finite element method
FEA	Finite element analysis
FPB	Friction pendulum bearing
FRP	Fibre-reinforced polymer
HDR	High damping rubber
HDRB	High damping rubber bearing
IM	Intensity measure
LDT	Laser displacement transducer
LRB	Lead rubber bearing
LS	Limit state
NRB	Natural rubber bearing
PGA	Peak ground acceleration
PGD	Peak ground displacement
PGV	Peak ground velocity
PSDM	Probabilistic Seismic demand model
SMA	Shape memory alloy
SPOT	String potentiometer
SREI	Steel-reinforced elastomeric isolator
SMA-RB	SMA wire-based rubber bearing
SMA-HDRB	SMA wire-based high damping rubber bearing
SMA-LRB	SMA wire-based lead rubber bearing
SMA-NRB	SMA wire-based natural rubber bearing

Acknowledgements

I would like to dedicate this doctoral dissertation to my parents, the most respectful, helpful, and compassionate in my whole life.

Chapter 1 Introduction and Thesis Organization

1.1 General

Earthquakes are one of the most unpredictable and difficult-to-control phenomena, which have catastrophic consequences to human civilization. In order to eliminate or reduce the disastrous effects of earthquakes, one effective way is to use protective systems in structures (e.g. buildings and bridges) such as base isolation mechanisms.

Base isolators play an important role in vibration attenuation and seismic response control of civil structures like buildings or bridges against earthquakes. They can significantly reduce seismic damages and prevent structures from collapse. Comprehensive research has been carried out on history and development of isolation systems (Kelly, 1986; Buckle and Mayes, 1990). In this system, a device with high vertical and bending stiffnesses but very low horizontal stiffness is mounted between the substructure and the superstructure. Rubber bearings are one of the most common base isolators with a cubic or cylindrical shape. Their application in ordinary low-rise buildings and highway bridges of developing countries is increasing considerably (Kelly, 2002).

In steel-reinforced elastomeric isolators (SREIs), steel shims can be replaced with fibre-reinforced polymer (FRP) composite plates in order to reduce their weight and make them easy to handle during transportation and placement (Kelly, 1999 and 2002). The production cost of fibre-reinforced elastomeric isolators (FREIs) is also reduced, as a potential saving, due to automated manufacturing process (Kelly, 1999; Tsai and Kelly, 2002). SREIs have axial and flexural rigidity while, FREIs are completely flexible under bending due to the presence of fibres (Kelly, 1999). Due to high strength-to-weight ratio of carbon fibre-reinforced polymer (CFRP) composite materials, carbon-FREIs are much lighter than SREIs with superior performance (Tsai and Kelly, 2002). Hence, they can be implemented into a wide range of applications such as bridges, buildings, and other civil infrastructures.

Shape memory alloys (SMAs) are one kind of smart and functional materials that can restore to their pre-determined and original shape after deformation via unloading or applying thermal load. They have two solid phases; martensite or unstable phase in which

material is at low temperature and austenite, parent, or high-temperature phase. In this regard, four characteristic temperatures are defined to determine the temperature ranges for starting and finishing the phase transformation between martensite and austenite. Superelastic and shape memory effects are two unique properties of SMAs. In superelastic effect, the generated strain due to mechanical loading is fully recovered after unloading while in shape memory effect, the mechanical deformation should be removed by applying thermal load and increasing its temperature. Thanks to the remarkable characteristics of SMAs such as high damping performance and energy dissipation capacity, significant stiffness hardening (variable stiffness), large ductility, long fatigue life and corrosion resistance capability, they are excellent candidates as damper or actuator (Graesser and Cozzarelli, 1991; Soong and Dargush, 1997). More details will be presented in Chapter 2, section 2.4.

SMA, as supplementary component, can improve the re-centring capability of elastomeric isolators and as a result, extend their service life (Choi et al., 2005; Andrawes and DesRoches, 2007; Ozbulut and Hurlebaus, 2010).

1.2   Objectives

The primary goal and the original contribution of this thesis to knowledge is to analytically develop a constitutive model for new smart steel- or fiber-reinforced elastomeric isolators which are equipped with superelastic SMA wires. The proposed model can be implemented in structural finite element softwares in order to accurately simulate the shear behaviour of such SMA-based rubber bearings (SMA-RBs) and capture their nonlinear hysteretic response. The objectives of this PhD research work are classified as follows:

1.2.1   Performance Evaluation of Carbon Fibre-Reinforced Elastomeric Isolators (C-FREIs)

The cold-vulcanization process, which is known as a fast and cost effective manufacturing process, has been used for producing fibre-reinforced elastomeric isolators (FREIs) in unbonded applications where the bearing is not fixed in its place. Here, the cold-vulcanization process is used to fabricate a number of scaled size carbon-FREIs for bonded applications for the first time. The effectiveness and performance of C-FREIs are explored by conducting different types of tests including

performance and sensitivity tests. Then, parametric (sensitivity) analyses are carried out at two levels; experimental and numerical. This objective is defined in order to attain an appropriate understanding of the behaviour of FREIs and correctly perceive their advantages and limitations.

1.2.2 Development of a Novel Shape Memory Alloy-based Rubber Bearing (SMA-RB)

With the goal of improving the energy dissipation capacity, the re-centring capability and as a result, the service life of existing elastomeric bearings, a novel seismic base isolator is developed using shape memory alloy (SMA) wires. In this passive earthquake protective system, SMA wires are wound around the rubber bearings with different configurations (e.g. straight, cross, and double cross).

1.2.3 Development of a New Hysteresis Model for SMA-RBs

By proposing a novel SMA wire-based elastomeric isolator, it is highly beneficial to properly simulate its hysteresis. Existing material models cannot accurately capture the response of such smart bearings. It becomes highly important when the seismic performance of a structure isolated by SMA-RBs is evaluated. Here, as a complementary part of the previous objective, a new hysteresis model is developed for SMA wire-based rubber bearings.

1.2.4 Seismic Fragility Assessment of a Highway Bridge Isolated by SMA-RBs

Seismic fragility assessment of a structure is a common tool to evaluate the failure probability of the structure under seismic events. In fact, the probability that a structural demand reaches or exceeds the capacity of a structure is estimated at different levels of damage (limit/damage states). In order to study the effect of SMA-RBs, as a new developed isolation system, on the seismic fragility of isolated structures, the vulnerability of a multi-span continuous steel-girder bridge isolated with SMA-RBs is assessed analytically, as the last objective of this thesis.

1.3 Outline of the Thesis

In Chapter 2 of this thesis, a literature review is performed on the base isolation concept and different types of elastomeric isolators including steel-reinforced elastomeric

isolators (SREIs), fibre-reinforced elastomeric isolators (FREIs), and smart SMA-based rubber bearings (SMA-RB).

Before going to the experimental phase, it is critical to have an appropriate understanding of the behaviour of elastomeric isolators. Chapter 3, as the first step, intends to facilitate this consideration through a design of experiment, sensitivity and regression analyses, and a multi-criteria optimization process. In this chapter, the effect of several factors such as the number and the shear modulus of rubber layers, as well as the thickness of reinforcement are investigated on the performance of carbon fibre-reinforced high damping rubber bearings (CFR-HDRBs) using finite element method (FEM). HDR has a complicated behaviour compared to other types of rubber such as natural low damping rubber. As a result, it is very challenging to simulate the response of HDR. However, by achieving a clear vision of the behaviour of such elastomer, it will be easier to use the attained knowledge and extend it to other types of rubbers. To accurately simulate the highly nonlinear behaviour of HDR, several material models are selected and compared together.

The achievements of the previous chapter help think systematically of possible scenarios to be defined in the experimental part of the thesis as presented in Chapter 4. A number of reduced scale carbon fibre-reinforced elastomeric isolators (C-FREIs) having different numbers and thicknesses of elastomeric and reinforced layers are manufactured and tested under different loading conditions. A parametric study is conducted based on the experimental results. However, because of the small size of samples, and limited number of factors and specimens, it is not appropriate to use the results at the design level. Therefore, it is necessary to perform a comprehensive study on the behaviour of full-size C-FREIs by considering an acceptable number of specimens. This goal is accomplished by modelling and analyzing C-FREIs using FEM. Similar procedure followed in material modelling of HDR (in Chapter 3) is used here to verify and validate the numerical results with experimental ones. Then a parametric study (sensitivity analysis) is conducted based on FEM.

After studying the behaviour of elastomeric isolators reinforced with carbon fibre fabrics, in Chapter 5, new shape memory alloy wire-based rubber bearings (SMA-RB) are proposed with different reinforcements; steel shims and carbon fibre-reinforced composites. The goal of introducing SMA-RBs is to overcome weaknesses (e.g. limited shear deformation capacity) of steel- and fibre-reinforced rubber bearings and improve their self-

centering and energy damping properties. The performance of such SMA-RBs is evaluated using FEM. Three different types of SMA-RBs are considered in this part; SMA-based natural rubber bearing (SMA-NRB), SMA-based high damping rubber bearing (SMA-HDRB), and SMA-based lead rubber bearing (SMA-LRB).

By proposing novel SMA wire-based elastomeric isolators, it is necessary to properly comprehend and analyze their mechanical response through hysteresis. Therefore, as a complementary part of the previous chapter, a new hysteresis model is developed in Chapter 6 for SMA-RBs in order to accurately capture their nonlinear behaviour. It should be noted that this model, as a link element, can be implemented in any structure under static or dynamic loadings in finite element environment.

In order to find out that such SMA-RBs are reliable to be used in structural applications, their effect, as new isolation systems, should be investigated on the seismic response of structures (e.g. buildings, bridges). Therefore, to check whether or not these new rubber bearings are efficient enough in seismic isolation, the fragility of a highway bridge isolated by SMA-RBs is assessed in Chapter 7.

Finally, in Chapter 8 of the thesis, a summary along with concluding remarks are presented and then, future works are discussed.

Figure 1.1 summarizes the goals of this PhD thesis and relates main chapters to each other by showing the topics which are covered in each section.

Chapter 3

Attaining an appropriate understanding of the behavior of elastomeric isolators

- Design of Experiment (DOE)
- Sensitivity and Regression Analyses
- Multi-Criteria Optimization

Chapter 4

Correctly perceiving advantages and limitations of modern fiber-reinforced rubber bearings

- Manufacturing and Testing Specimens
- Experimental Parametric Study
- Numerical Parametric Study

Chapter 5

Overcoming the limitations of elastomeric isolators by introducing a new SMA-based rubber bearing reinforced by steel shims or composites plates

- Numerical Investigation on SMA-NRB
- Numerical Investigation on SMA-HDRB
- Numerical Investigation on SMA-LRB

Chapter 6

Developing a constitutive model for the SMA-based rubber bearing

Chapter 7

Assessing the effect of SMA-based rubber bearings on the seismic fragility of a highway bridge

Primary Objectives

Figure 1.1. Summary of the goals and topics covered in the thesis

Chapter 2 Literature Review

2.1 General

In order to seismically protect a structure from the devastating effects of earthquake, different protective systems including active, hybrid, and passive vibration control systems have been developed. Passive systems have been extensively implemented in civil engineering applications due to their easier operation where there is no need for external power supplies (Ozbulut et al., 2007). Such systems are categorized into two types; rubber bearings and sliding bearings. Conventional elastomeric isolators or rubber bearings are laminated devices consisting of alternating layers of rubber and reinforcement. In sliding bearings, either flat or curved surfaces are in contact with each other in order to dissipate the energy through a frictional mechanism (Kunde and Jangid, 2003).

The operation of important structures such as hospitals, fire stations and emergency control centres during an earthquake is one of the most important parameters that should be considered in the construction or retrofitting. Consequently, uncoupling a structure (e.g. buildings or bridges) from devastating effects of earthquakes has been one of the major concerns for engineers for a long time. Although, many efforts have been made by introducing numerous devices based on seismic isolation of structures, they are mostly intricate and a limited number of them have been applied into buildings and bridges (Kelly, 1986; Buckle and Mayes, 1990). Kelly (1986) studied a wide range of publications from 1900 to 1984, which were related to seismic base isolators. He presented an extensive literature review about seismic isolation and various types of base isolators used in construction or rehabilitation of buildings. He conducted his study by focusing on characteristics and applications of base isolators.

Seismic isolation systems can prevent or minimize the structural damages of structures (e.g. buildings, bridges, and viaducts) to provide a continuous operation by regulating the seismic response of the structure (Ozkaya et al., 2011). As shown in Figure 2.1, these systems are placed between the substructure (e.g. foundation or pier) and the superstructure (e.g. columns or dock).
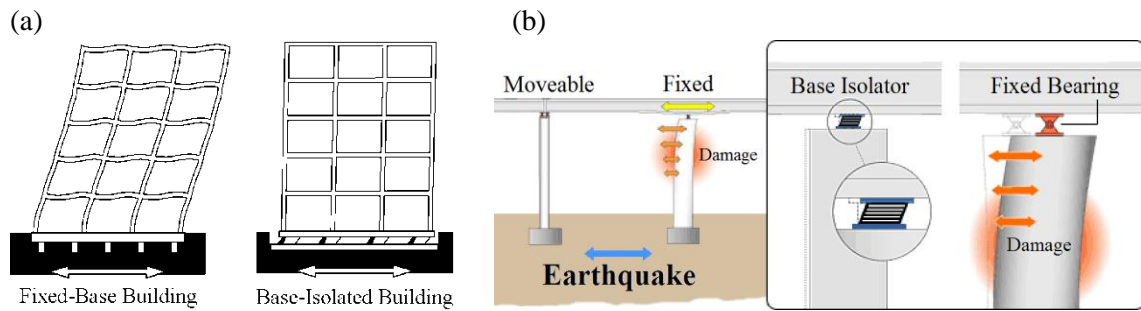
Figure 2.1. Applications of base isolation systems in (a) buildings and (b) bridges

Using base isolation systems in bridges can improve the seismic performance of the structure, increase the public safety, and reduce the cost of repair and rehabilitation (Ghobarah and Ali, 1988; Kikuchi and Aiken, 1997; Wilde et al., 2000; Chaudhary et al., 2000; Hwang et al., 2002; Zhang et al., 2009; Ozbulut and Hurlebaus, 2010 and 2011; Sarrazin et al., 2013; Siqueira et al., 2014). Base isolators can considerably decrease and dissipate the earthquake energy transmitted to the structure by providing a damping mechanism. Due to a low horizontal stiffness (high lateral flexibility), they can shift the fundamental horizontal frequency of an isolated structure away from the dominant frequency range of earthquake by increasing the base period of structure. The main goals of using base isolation techniques are to:

- Prevent the structural collapse in severe earthquakes
- Avoid or minimize the structural damage in moderate earthquakes
- Provide continuous operation in important buildings.

The efficiency of an elastomeric isolator is determined by evaluating its horizontal flexibility, vertical stiffness and damping capacity. Indeed, the shear behaviour of a rubber bearing under a combination of vertical pressure and cyclic horizontal loadings is a criterion to indicate its performance. It was shown that by reducing the horizontal stiffness of the rubber bearing, the period of the base-isolated structure increases (Toopchi-Nezhad, 2008a). In fact, when the horizontal stiffness decreases, the lateral flexibility increases and as a result, it takes a longer time for the structure to come back to its initial position in one cycle.

Elastomeric isolators, which are usually produced in a rectangular (see Figure 2.2) or circular shape, can be divided to conventional and modern devices depending on the type of the reinforcement (e.g. steel shim or fibre-reinforced composites).

8
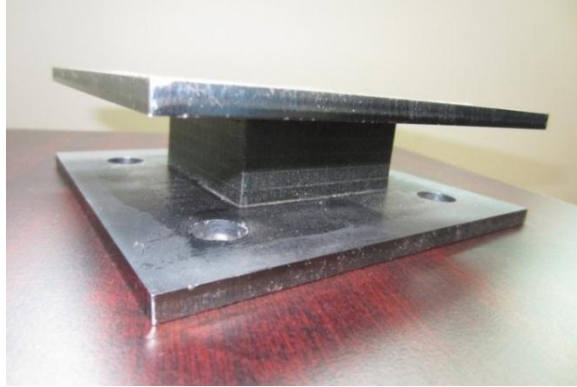
Figure 2.2. Elastomeric isolators in rectangular shapes

In elastomeric bearings, reinforcements provide adequate vertical rigidity to carry on the compressive loads due to the weight of the superstructure and also prevent the horizontal bulging of rubber layers. The elastomeric layers provide lateral flexibility as well as damping property.

2.2 Steel-Reinforced Elastomeric Isolators (SREI)

In conventional rubber bearings, also called steel-reinforced elastomeric isolators (SREIs), steel shims are bonded to rubber layers in order to provide a high compressive stiffness.

Depending on the material properties and auxiliary elements which are used in rubber bearings to improve their energy dissipation capacity, SREIs were developed and categorized into different types such as low-damping natural rubber bearing (NRB), lead-plug rubber bearings (LRB), high damping rubber bearings (HDRB) and ball rubber bearing (BRB). There are major concerns about these types of base isolators such as size, weight and cost. Consequently, they are applied to large bridges and high-rise buildings equipped with expensive and important appliances. NRB, HDRB, and LRB have been widely used in seismic response mitigation and control of structures subjected to ground motions (Warn and Whittaker, 2004; Andrawes and DesRoches, 2007; Bhuiyan et al., 2009; Alam et al., 2012; Bhuiyan and Alam, 2013).

2.2.1 Natural Rubber Bearing (NRB)

In low-damping natural rubber bearings (NRB), also called synthetic rubber bearings, natural rubber or neoprene is reinforced with steel shims through a hot-vulcanization process

under heat and pressure in a mold (Naeim and Kelly, 1999). Figure 2.3 shows a laminated rubber bearing. Steel shims are vulcanized to the rubber and surrounded by an elastomeric cover layer. Two fixing plates made of steel are attached to the top and bottom of the laminated pad. In order to mount the rubber bearing on the structure, steel supporting end plates are used.

Supporting End Plates

Rubber

Steel Shim

Fixing Plates
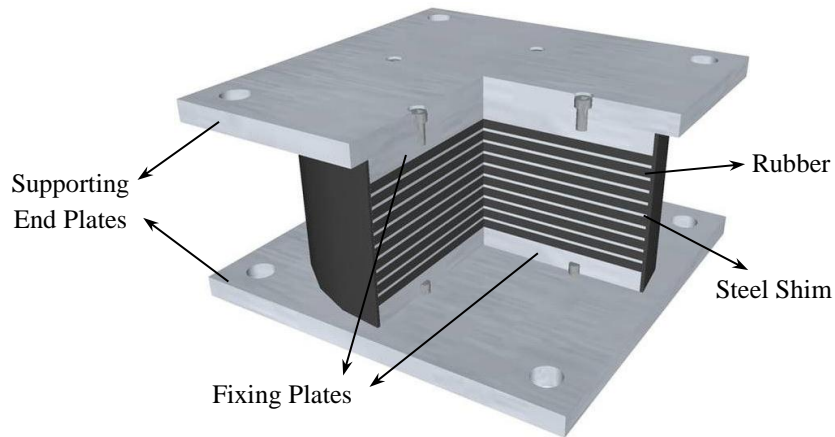
Figure 2.3. Laminated rubber bearing

These type of elastomeric isolators are extensively being used in buildings and bridges where supplementary components such as steel bars, viscous dampers, and frictional devices are implemented. NRBs possess critical damping ratios about 2-3% (Ozkaya et al., 2011). Natural low-damping rubber follows the behaviour of a hyperelastic material with low amount of energy damping capacity. This type of elastomer has a low sensitivity to the environmental conditions (e.g. temperature), loading rate, loading history (scragging), and aging. Scragging refers to a behaviour change (i.e. stiffness and damping reduction) during the initial cycles of motion, which is stabilized as the number of cycles increases. Simplicity in manufacturing of such bearings is considered as another advantage. NRB shows almost a linear behaviour up to shear strains above 100% and its hysteretic response encounters negligible changes (Naeim and Kelly, 1999). As a result, NRBs can be easily modelled. The main disadvantage of NRBs is their need to a complementary element such as lead core for providing extra amount of damping.

2.2.2   High Damping Rubber Bearing (HDRB)

High damping rubber bearings (HDRBs) consist of steel shims as reinforcement and high damping rubber (HDR) as elastomer for providing horizontal flexibility and damping capacity. HDRBs have 10-20% equivalent viscous damping (Marioni, 1998). Elastomer layers in the HDRB has much higher damping capacity compared to natural low damping rubbers (Ozkaya et al., 2011). The high damping property of the elastomeric isolator is due to adding specific materials like extra-fine carbon black, oils or resins and other proprietary fillers to the natural rubber (Naeim and Kelly, 1999). They also possess a high initial shear modulus compared to the NRBs (Skinner et al., 1993). By designing such base isolators, a rubber compound with sufficient damping property without auxiliary damping devices such as lead core was developed. HDRBs can undergo large shear strain levels (around 400%).

Because of the materials added to the natural rubber during vulcanization process, HDRs have specific characteristics such as energy absorption and hardening properties within a wide strain range from 1 to 400% (Yoshida et al., 2004). As a result, it is difficult to capture their mechanical properties like stress-strain relation and fatigue accurately. Many studies have been performed for modelling the behaviour of HDR materials and HDRBs based on the numerical and analytical approaches as well as experimental tests (Yoshida et al., 2004; Amin et al., 2006a; Bhuiyan et al., 2009). Results showed that although the hyperelastic material model can simulate the response of natural low damping rubber, this model cannot accurately capture the mechanical behaviour of HDR materials.

HDRBs possess a highly nonlinear and complex behaviour (e.g. scragging referred to a reduction in the stiffness and damping during the initial cycles of motion) at large deformations. Consequently, several considerations and assumptions should be taken into account to analytically model them. Many theoretical and experimental works have been performed to investigate the effects of different parameters on the dynamic performance of HDRBs under various conditions such as shear strain and amplitude (Amin et al., 2006a; Bhuiyan et al., 2009; Dall'Asta and Ragni, 2006; Tsai et al., 2003; Yoshida et al., 2004).

Tsai et al. (2003) proposed a model to capture the rate-dependent effects of HDRBs using analytical Wen's model (Wen, 1976). In order to validate the proposed mathematical model, different experimental tests were carried out and compared with results obtained from numerical finite element formulations. It was observed that, the lateral force-deflection

hysteresis loop calculated by the modified model is so close to that obtained by experimental tests under different shear strains. The model could also predict the nonlinear behaviour of HDRBs at various shear strains and frequencies by simulating the stiffening and velocity dependency.

Dall'Asta and Ragni (2006) proposed a viscoelastic material model to simulate the behaviour of rubber bearing under pure cyclic shear loads. Experimental results showed that the dynamic behaviour of HDRB includes a transient response followed by stable hysteresis loops as steady-state response. The lateral force-displacement hysteresis loop with "butterfly" shape is a function of strain-rate, strain amplitude and Mullins' effect. Mullin's effect in filled rubbers refers to a variation of the hysteretic (stress-strain) curve depending on the maximum load previously applied. This phenomenon is commonly applied to stress softening. Based on experimental achievements a constitutive analytical model without the limitations of previous models in capturing the nonlinearity behaviour was proposed using a rheological model (Dall'Asta and Ragni, 2006).

2.2.3 Lead Rubber Bearing (LRB)

Among different passive earthquake protective systems, lead rubber bearings (LRBs) with high energy dissipation capacity are extensively used in seismic isolation of structures (Turkington et al., 1989; Ozdemir et al., 2011; Bhuiyan and Alam, 2013). They consist of elastomeric layers bonded to steel shims, fixing and supporting steel plates at the top and the bottom, and a lead core located in the central part as shown in Figure 2.4. The main role of the lead core is to dissipate the earthquake's energy. Supporting steel plates restrain the whole elastomeric isolator and also confine the lead-plug in the middle of LRB.
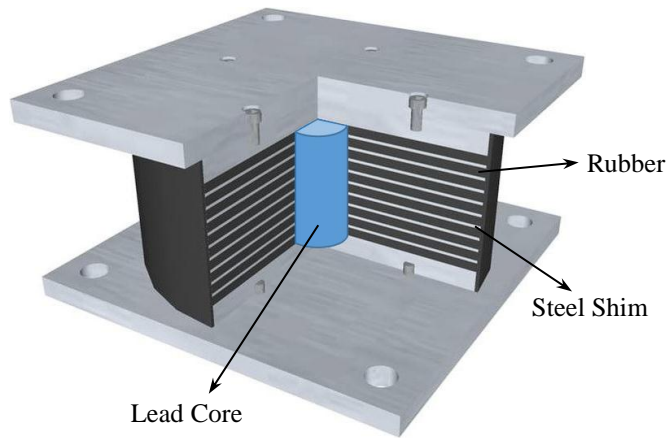
Figure 2.4. Lead-plug rubber bearing (LRB)

Several analytical studies have been done on the efficiency of lead-plug rubber bearings (Hwang and Chiou, 1996). Doudoumis et al. (2005) verified the accuracy of LRB models analyzed through finite element method (FEM). They considered two models to investigate the effect of lead cores constraint on the behaviour of rubber bearings under vertical and cyclic horizontal loadings. They recommended using such micromodels since lead core changes the internal stress and strain distribution (Doudoumis et al., 2005). Abe et al. (2004) experimentally studied the response of LRB, NRB and HDRB considering different loading types; small amplitude uniaxial load and large amplitude biaxial and triaxial loads. They showed that the vertical pressure has a significant effect on the restoring force of LRB. Experimental results revealed that under a combination of constant vertical pressure and lateral displacement in two directions (triaxial loading), the interaction effect of the loadings noticeably increases the effective lateral stiffness and the equivalent viscous damping in the cases of NRB and HDRB. However, the interaction of loading had a negligible effect on the stiffness and damping ratio of LRB. Therefore, they pointed out that the interaction effect cannot be ignored at the design level.

2.2.4 Ball Rubber Bearing (BRB)

A new type of steel-reinforced laminated bearing, called ball rubber bearing (BRB), has been designed and manufactured by implementing small steel balls in a central hole of NRB (Ozkaya et al., 2011). In this type, lead core is replaced with steel balls. BRBs can works as rubber and sliding bearings simultaneously due to the damping property of elastomeric layers and friction generated between steel balls (Ozkaya et al., 2011). Results

obtained from more than 200 different experiments through full-scale cyclic shear tests showed that the effective horizontal and vertical stiffnesses, and damping capacity of BRBs are higher than those of NRBs. The equivalent viscous damping of BRBs varies from 15 to 25%. It was also observed that almost 50% of the vertical pressure is resisted by its central core. It means that BRBs could have lower shape factor (i.e. ratio of loaded area to force-free area of one elastomeric layer) than NRBs. As a result, steel balls can carry larger portion of the vertical compressive load and thus, internal friction and energy dissipation is enhanced (Ozkaya et al., 2011). High weight and relatively high horizontal stiffness compared to other types of RBs (e.g. NRB, HDRB, and LRB) are two main disadvantages of such elastomeric bearings.

2.3   Fibre-Reinforced Elastomeric Isolators (FREI)

SREIs are the most common rubber bearings in use. However, they are large, heavy and expensive (Kelly, 2002). They are produced through a high cost process due to vulcanization bonding of steel shims and rubber layers in a mold. The main concern about these types of base isolators is their limited applications which are in large bridges and high-rise buildings having heights of greater than 23 m with expensive and important equipment because of their large size, high weight and cost (Kelly, 2002). Kelly suggested that both price and weight of SREIs can be decreased by replacing steel shims with fibre-reinforced composite plates (Kelly, 1999). Compared to a SREI which should be produced according to a designed size, fibre-reinforced elastomeric isolators (FREIs) can be produced in the form of long rectangular strips and then cut to the required size using a standard band-saw. Kelly also suggested to use micro-wave heating mechanism inside an autoclave instead of applying heat and pressure in a mold. This technique can be done through an automated process and as a result, significantly reduce the overall manufacturing cost in a mass production (Kelly, 1999). Rubber and fibre-reinforced layers can be bonded together using a cold-vulcanized bonding compound without any mold. As a result, labour expenses will decrease remarkably via an automated manufacturing process. Therefore, it is understood that the main goal of designing and producing FREIs is to reduce the cost and weight of elastomeric base isolators in order to extend their applications to ordinary and low-cost residential and public buildings

throughout the world especially in developing countries and high-risk seismic regions with severe earthquakes.

A big difference between the two types of reinforcement used in conventional and modern rubber bearings is the flexibility of the reinforcement. In contrast to the steel shims with a high flexural rigidity, fibre-reinforced sheets are completely flexible under bending (Kelly, 1999). This characteristic causes the FREI to show a rolling deformation under lateral shear force and as a result, it produces lower forces in the transverse direction compared to the SREI. Therefore, FREI can be laterally deformed with a higher flexibility. FRP composite materials have low density and high strength-to-weight ratio. The density of epoxy matrix composite reinforced with 70% carbon fibres is 1600 kg/m^3 while, mild steel has a density of 7850 kg/m^3. As a result, FREIs, with superior performance, are significantly lighter than SREIs (Moon et al., 2002). Reducing the weight of rubber bearings can significantly facilitate manufacturing, shipping, handling and installation processes. Consequently, a wide range of applications (e.g. public, residential, and low-rise buildings) have been found for such modern and light isolators (Toopchi-Nezhad et al., 2008b). Kelly (2002) studied the possibility of implementing FRP composite layers in rubber bearings by considering weight and cost. He clarified that FREI and SREI have comparable performances and it is possible to produce such isolators with suitable mechanical properties (Kelly, 1999 and 2002). Tsai and Kelly (2002) studied the effect of fibres on the flexibility of base isolators by presenting formulations for compressive and bending stiffnesses of rectangular FREIs based on analytical method (Tsai and Kelly, 2002). They assumed that the elastomer is incompressible and isolator is in the form of infinite strip pad. Results indicated that the lateral stiffness increases with increasing the shape factor and decreases by using more flexible reinforcement.

Carbon fibres exhibit excellent mechanical characteristics such as high elastic modulus (200-800 GPa), high tensile strength (2500-6000 MPa) and suitable fatigue life without creep or relaxation, so they are desirable candidates as reinforcement of FRP composite plates used in rubber bearings (Moon et al., 2002). Moon et al. (2002) fabricated FREIs consisting of different fibres (e.g. carbon, aramid, and glass) and compared them with SREIs. Experimental results revealed that FREIs are superior to SREIs in terms of vertical stiffness, effective horizontal stiffness, and equivalent viscous damping. They observed that,

compared to glass and aramid fibres, carbon fibres are more effective in increasing the vertical stiffness and the equivalent viscous damping. Moon et al. also manufactured circular carbon fibre- and steel-reinforced rubber bearings with a same size in order to evaluate and compare their performance. The diameter and the total height of both isolators are around 700 mm and 350 mm, respectively. They showed that the carbon FREI has a vertical stiffness of 3100 kN/mm which is three times higher than SREI. Moreover, the equivalent viscous damping of FREI (15.85%) was found to be 2.5 times greater than that of SREI (6.2%). Another finding was that FREI has an effective horizontal stiffness of 3.24 kN/mm which is lower than SREI with 3.43 kN/mm effective lateral stiffness. These characteristics depict that the carbon FREI is more efficient in terms of both stiffness and energy dissipation capacity. Dehghani Ashkezari et al. (2008) designed and manufactured different specimens of elastomeric bearings using layers of woven carbon fibres to study their mechanical characteristics and dynamic behaviour under compressive and shear loads. They found that carbon fibres can dissipate energy through frictional movements and provide additional damping to the system. It was also determined that the vertical pressure can considerably affect the damping coefficient of FREI, however, it has negligible influence on the shear response of FREIs (Dehghani Ashkezari et al., 2008). Another important finding was that, if cyclic lateral loading is repeated with amplitude less than the maximum load previously applied, horizontal flexibility and energy damping properties will decrease due to stress softening phenomenon.

Kang et al. (2003) probed the effect of lead-plug in fibre-reinforced seismic isolators based on experimental tests and analytical approaches. According to their findings, presence of lead-plug does not change the performance of rubber bearing significantly. Mordini and Strauss (2008) conducted experimental work on FREIs made of glass-fibre fabrics and HDR to provide required information in their numerical simulations and analytical model. The robustness and consistency of the proposed model was investigated by seismic response analysis of a liquid storage tank equipped with a FRP-reinforced HDRB. Rubber bearings with different geometries (e.g. number and thickness of rubber and reinforced layers), material models and loading and boundary conditions were tested to investigate their operational characteristics (e.g. effective horizontal and vertical stiffnesses) as well as internal stresses in glass fibres and elastomeric layers. They applied FREI in a full-scale

structure using simple nonlinear elements rather than complex FE model to significantly reduce the calculation time of seismic analysis. Results obtained from finite element analyses showed that the acceleration is decreased and the period is altered in the base-isolated structure (Mordini and Strauss, 2008).

Zhang et al. (2011) studied the mechanical properties of FREIs after manufacturing and testing a number of samples. Specimens were subjected to vertical pressure for calculating the effective vertical stiffness and compressive modulus. The effective horizontal and damping capacity were determined by applying cyclic horizontal displacements. The hysteretic curves for three FREIs with different thickness and number of elastomeric and reinforced layers subjected to vertical and cyclic shear loads illustrated that the operational characteristics of FREIs are comparable to those of traditional ones. FREIs have adequate efficiency in terms of the energy dissipation capacity (i.e. capacity of the device in damping the earthquake's energy) and the effective vertical stiffness. Therefore, implementing them in the seismic base isolation is an applicable idea.

Rubber bearings are either fixed in between the superstructure and the substructure using steel supporting plates (bonded application) or mounted without any connecting mechanism and supporting plates (unbonded application). With the purpose of studying the behaviour of unbonded C-FREI, Toopchi-Nezhad et al. (2008b) performed experimental tests and observed that a rollover deformation occurs in the laminated pad due to a very low flexural rigidity of the fibre-reinforced layers. As a consequence, the lateral flexibility of such unbonded C-FREI increases under cyclic shear displacements. In order to improve the low damping capacity and inadequate (very low) horizontal stiffness of such rubber bearings, they suggested that HDR or supplementary elements can be used. Focusing on the compressive behaviour of unbonded elastomeric bearings, Van Engelen et al. (2014) explored the effect of geometric modifications on the vertical stiffness and the compressive modulus of rectangular FREIs. They validated a 3-dimensional finite element (FE) model using experimental results and performed a parametric study. They observed that the vertical performance degrades with both interior and exterior modifications, but it is more sensitive to the exterior modification. The modifications were meant to improve the performance of the unbonded FREIs in the horizontal direction by reducing the effective lateral stiffness and increasing the energy dissipation capacity.

In addition to experimental work, several analytical studies have been done to describe the behaviour of fibre-reinforced bearing pads under bending, compression, and shear. Russo et al. (2013) proposed a geometric model to predict the deformation of fibre-reinforced pads (unbonded applications) under shear and compression. Using experimental tests conducted on a number of specimens, they considered different types of rubber (e.g. low and high damping neoprene); various reinforcements (e.g. bi-directional and quadri-directional carbon fibre fabrics); as well as aging and shape factor, and presented an expression for the lateral stiffness of the fibre-reinforced isolators.

The performance of FREIs made of carbon fibre fabrics and high-damping rubber was assessed through sensitivity analyses by Hedayati Dezfuli and Alam (2013a). They considered 27 C-FREIs and performed several finite element simulations validated by experimental results in order to propose the most efficient rubber bearing through a multi-objective optimization process. They developed regression models to predict the response of C-FREIs. The seismic response of a three-span continuous steel girder reinforced concrete pier supported bridge isolated by the optimized C-FREI was conducted through dynamic time history analyses. Hedayati Dezfuli and Alam (2013a) observed that the effective horizontal stiffness and the equivalent viscous damping are highly dependent on the shear modulus of the elastomeric layers. In addition, the number of rubber layers and the thickness of carbon fibre-reinforced sheets were found to have large effects on the vertical stiffness. Based on experimental tests and through a parametric study, Hedayati Dezfuli and Alam (2013b) examined the effect of mechanical and physical properties (e.g. shear modulus and thickness of elastomer) on the response of the scaled size C-FREIs in bonded applications. Findings revealed that the equivalent viscous damping and the effective horizontal stiffness are very sensitive to the shear modulus of the elastomer and the vertical stiffness is sensitive to the shape factor. In another experimental study, Hedayati Dezfuli and Alam (2014a) manufactured bonded carbon fibre-reinforced bearing pads in a cold vulcanization process in order to investigate the effectiveness of the process and the performance of the bonded C-FREIs. They observed that at 100% shear strain amplitude, a partial debonding occurs between exterior rubber layers and supporting plates due to the rollover deformation. This phenomenon did not lead to a malfunction in the bearing pads however; more comprehensive

work needs to be performed on full size specimens by conducting 3-dimensional excitation tests with extreme loading conditions.

2.4 Smart Rubber Bearings

2.4.1 Shape Memory Alloy (SMA)

Shape memory alloys (SMAs) are considered as smart and functional materials that can restore their pre-determined and original shape after deformation via unloading or by applying thermal load. They have two solid phases; martensite or unstable phase in which material is at low temperature, and austenite, parent or high-temperature phase. In this regard, four characteristic temperatures are defined to determine the temperature ranges for starting and finishing the phase transformation. The martensite start temperature, M^s, and the martensite finish temperature, M^f, respectively represent the starting and finishing phase transformation from austenite to martensite. Similarly, for starting and finishing phase transformation from martensite to austenite, the austenite start temperature, A^s, and the austenite finish temperature, A^f, are defined, respectively. Superelastic and shape memory effects are two unique characteristics of SMAs. In the superelastic effect (Figure 2.5a), the generated strain due to the mechanical loading is fully recovered after unloading while in shape memory effect (Figure 2.5b), the mechanical deformation should be removed by applying thermal load and increasing temperature of the alloy. The SMA materials will show the superelastic behaviour if they are in the austenite phase. In other words, when the temperature of SMA is above the austenite finish temperature, the strain generated in the SMA will be fully recovered if it is lower than the maximum superelastic strain.
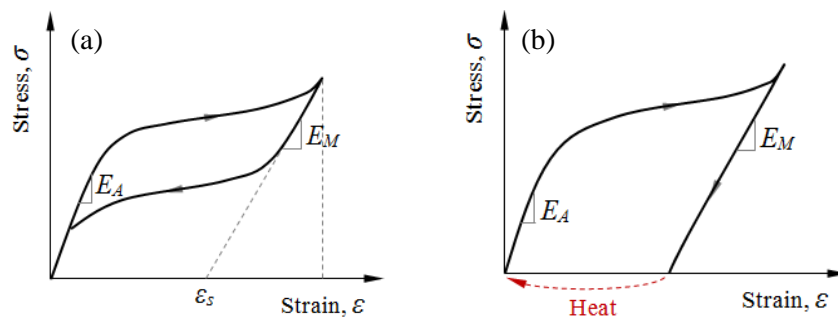
Figure 2.5. Stress-strain curve for SMAs; (a) superelastic effect, (b) shape memory effect

When the temperature of SMA is below the austenite finish temperature, the generated strain is not fully recovered upon unloading because a fraction or all of the alloy remains in the martensite phase depending on the temperature and the reverse phase transformation (martensite to austenite). In such a situation, increasing the temperature of SMA completes the transformation and the strain is fully recovered (Figure 2.5b).

SMAs have a larger hysteretic deformation and a higher elastic (superelastic) strain compared to conventional alloys and metallic materials (Lagoudas, 2008). The maximum superelastic strain, ε_s, in such materials can even reach up to 13.5% (Tanaka et al., 2010). SMAs are excellent candidates as dampers or actuators due to their remarkable characteristics such as high damping performance, large recoverable strain (up to 13%), significant stiffness hardening (variable stiffness), large ductility, long fatigue life, and corrosion resistance capability (Soong and Dargush, 1997; Alam et al., 2007).

There are different types of SMAs such as Nickel-Titanium, Cu-based shape memory alloys and ferrous shape memory alloys which have the potential for smart structural applications. Some mechanical properties like the elastic modulus (E_A), the austenite finish temperature (A_f) and the superelastic strain (ε_s) under the maximum applied strain (ε_{max}) for a number of SMAs are listed in Table 2.1.

Table 2.1. Mechanical characteristics of different shape memory alloys (SMAs)

Alloy	ε_{max} (%)	ε_s (%)	E_A (GPa)	A_f (°C)	Reference
Ni Ti$_{49.1}$	5.0	3.6	40.4	44.6	Strnadel et al. 1995
Ni Ti$_{49.5}$	5.7	4.6	45.3	53.0	Strnadel et al. 1995
Ni Ti$_{50}$	3.1	2.2	117.8	77.8	Strnadel et al. 1995
Ni Ti	8.2	6.8	30.0	42.9	Boyd and Lagoudas 1996
Ni Ti$_{45}$	6.8	6.0	62.5	-10.0	Alam et. Al. 2008
Ni Ti$_{44.1}$	6.5	5.5	39.7	0	Alam et. Al. 2008
Ti Ni$_{40}$ Cu$_{10}$	4.1	3.4	72.0	66.6	Strnadel et al. 1995
Ti Ni$_{41}$ Cu$_{10}$	4.1	3.1	91.5	50.0	Strnadel et al. 1995
Ti Ni$_{41.5}$ Cu$_{10}$	3.4	2.8	87.0	60.0	Strnadel et al. 1995
Ti Ni$_{25}$ Cu$_{25}$	10.0	2.5	14.3	73.0	Liu 2003
CuAlBe	3.0	2.4	32.0	-65.0	Zhang et al. 2009
FeMnAlNi	6.1	5.5	98.4	< -50°C	Omori et al. 2011
FeNiCoAlTaB	15.0	13.5	46.9	-62.0	Tanaka et al. 2010

The elastic modulus of the SMA represents the stiffness of the material in the austenite phase. The maximum strain, ε_{max}, is defined as a strain at which the deformation in the material can be fully recovered after unloading.

2.4.2   Shape Memory Alloy-based Rubber Bearings (SMA-RB)

Elastomeric bearings are extensively being used in several applications, however, they have some weaknesses such as limited shear strain capacity, unrecovered residual deformation, and instability due to a large deformation (Choi et al., 2005). Using SMA in the form of wire (Dolce et al., 2000; Choi et al., 2005; Ozbulut and Hurlebaus, 2010; Hedayati Dezfuli and Alam, 2013c and 2014b), bar (Wilde et al., 2000; DesRoches and Delemont, 2002), or spring (Attanasi and Auricchio, 2011) is a solution to partially overcome the limitations of conventional rubber bearings. SMAs can undergo an inelastic deformation due to stress-induced phase transformation occurred in microscopic scale. Compared to the other alloys and metallic materials, they have a larger hysteretic deformation without entering to the plastic region and consequently, their energy dissipation capacity is higher. Therefore, shape memory alloy, as a supplementary passive damper, can enhance the re-centring capability as well as the energy damping capacity. They can reduce forces and relative displacements transmitted from the substructure to the superstructure (Attanasi et al., 2008; Ozbulut and Hurlebaus, 2011).

Variable properties of SMAs (e.g. stiffness) make them suitable candidates to be used under various exciting forces with different magnitudes and frequencies. In small external loadings such as wind or small earthquakes, SMA-based rubber bearings can supply a stiff link between the substructure and superstructure to prevent the damage in the elements of the structure. In mid-size earthquakes, SMA-based elements enhance the damping capacity of the rubber bearing due to stress induced martensitic (SIM) transformation. In strong ground motions, in addition to providing additional hysteretic damping, they can confine the relative displacement of the superstructure as a controller owing to its stiffness hardening after finishing the phase transformation (Wilde et al., 2000). Wilde et al. (2000) combined a shape memory alloy device with a laminated rubber bearing in order to increase the energy dissipation capacity of the isolator and control the relative displacement of the elevated highway bridges isolated by such bearings. According to the results, they found that although the energy transmitted to the bridge through the proposed SMA-based isolator is large compared to that of a structure equipped with a LRB, the damage energy of the bridge is small.

Several researchers have proposed different types of superelastic SMA-based smart isolation devices in the past. Choi et al. (2005) performed numerical study considering NiTi SMA wire wrapped around an elastomeric bearing to improve its re-centring capability over the LRB. However, at very large shear deformation (200% shear strain), this device will malfunction since wires experience axial strain beyond the NiTi's superelastic strain range. Although Dolce et al. (2000) implemented SMA wires effectively in a base isolation device, the manufacturing of the device was quite complex. Another SMA-based isolation device, developed by Dolce et al. (2000), showed high sensitivity and considerable variation in forces with temperature, and inefficiency in energy dissipation capacity. Liu et al. (2008) used a diagonal arrangement of large diameter SMA strands around the rubber bearing. However, this arrangement did not improve the re-centring capability or the level of damping compared to the original rubber bearing. Attanasi and Aurichhio (2011) proposed an isolation device equipped with eight SMA coil springs, which is expensive due to its complex manufacturing process and the use of expensive large diameter SMA springs. Attanasi et al. (2008) investigated the possibility of using shape memory alloys in base isolation systems. They compared the behaviour of a proposed smart isolator with that of a traditional LRB and an equivalent linear elastic model. According to their results, the behaviour of the smart isolation device with flag-shaped hysteretic loops was similar to a system with elasto-plastic hysteresis. They concluded that it is possible to replace existing LRBs with SMA-based bearing systems considering the amount of energy dissipation capacity. They suggested that SMA-based restrainers can be applied to rubber bearings or friction pendulum systems in order to provide re-centring force and control the relative horizontal displacement and upward force transmitted to the superstructure.

DesRoches and Delemont (2002) showed that utilizing elastomeric bearings with SMA bars rather than conventional steel cable restrainers increases the efficiency of the isolation system. SMA-based bearing mechanisms have high re-centring capability as a consequence of the superelastic and shape memory effects in SMAs. Attanasi et al. (2008) investigated the possibility of using SMAs in base isolation systems. They compared the behaviour of a proposed smart isolator with that of LRBs and an equivalent linear elastic model. They showed that it is possible to replace SMA-based bearing systems with existing LRBs regarding the amount of energy dissipation capacity. They found that SMA-based

restrainers can be applied to rubber bearings in order to provide re-centring force and control the relative horizontal displacement and upward force transmitted to the superstructure. In addition to some limitations related to durability and aging, LRBs encounter a large amount of residual deformation because of the plastically deformed lead core under severe ground motions (Dolce et al., 2000). Choi et al. (2005) proposed a new type of seismic base isolator using shape memory alloy wires to overcome the disadvantages of LRBs. They applied an SMA-based rubber bearing to a three-span continuous steel bridge in order to evaluate the seismic performance of the proposed smart isolator and compare it with LRB. Results showed that LRB experienced a large unrecoverable deformation while, the proposed SMA-based elastomeric isolator could restrain the deck from large relative displacement without any permanent deformation under strong earthquake records. On the other hand, they found that the amount of the energy dissipated through the proposed smart rubber bearing is less than that of LRB. In this regard, they explained that by increasing the size of SMA wires or changing the heat treatment process, the energy dissipation capacity can be increased.

Suduo and Xiongyan (2007) introduced three types of SMA-based dampers and one base isolator using nickel-titanium SMA wires. They proposed theoretical models to estimate the behaviour of the devices with high amounts of damping capacity. In order to evaluate the performance of these smart mechanisms on the seismic response control of structures, they implemented SMA-MR damper and SMA-based rubber bearing into structures. According to the findings, SMA-MR damper could regulate the seismic responses of a canopy roof structure. Suduo and Xiongyan (2007) compared the performances of lattice shell structures using SMA-based (smart) elastomeric isolator and conventional rubber bearings with those of fixed supported structures. They found that not only the smart base isolators can efficiently mitigate the seismic response in terms of acceleration, displacement, and internal forces but also, they have superior performances relative to the existing rubber bearings. They concluded that these intelligent systems have many advantages such as stability, high energy dissipation capacity, good fatigue and corrosion resistance capabilities and as a result long service life.

Ozbulut and Hurlebaus (2011) probed the performance of a novel smart base isolator consisting of rubber bearing and an auxiliary device made of SMA wires on the seismic response of bridges against near-field earthquakes. Elastomeric bearing provides vertical

stiffness and horizontal flexibility while, the SMA-based device supplies additional energy dissipation capacity as well as re-centring capability. The SMA-based rubber bearing (SMA-RB) was implemented into a three-span continuous bridge and the whole system was numerically analyzed under several near-field ground motions matched to a design spectrum. For simulating the behaviour of nickel-titanium superelastic wires, a temperature- and rate-dependent model was used. They carried out several time-history analyses as well as a sensitivity analysis on the seismic response of the bridge by considering different factors such as the forward transformation strength and displacement, the pre-strain amount of SMA wires, the ambient temperature and the horizontal stiffness of the elastomeric isolator. It was found that by changing the deck displacement, the acceleration and the base shear change inversely at high values of forward transformation strength. Also, results demonstrated that the system is more sensitive to the negative changes of temperature than the positive ones. Ozbulut and Hurlebaus (2011) concluded that the influence of temperature on the isolation performance is very important and cannot be ignored. Another interesting finding was the improved efficiency of the system by using pre-strained SMA wires (1-1.5%).

Recent numerical studies on the performance of SMA-based elastomeric isolators show that using SMA in forms of wire and bars can effectively advance the efficiency of base isolators in terms of re-centring capability and energy dissipation capacity (Bhuiyan and Alam 2013; Hedayati Dezfuli and Alam, 2013c). Hedayati Dezfuli and Alam (2013c) performed numerical analyses on smart SMA wire-based NRBs considering different arrangements for the wires. They investigated the effect of several parameters (e.g. type of SMA, aspect ratio of the rubber bearing defined as the ratio of the height to the length, thickness of SMA wires, and pre-strain in wires) on the performance of the device. They found that for low-aspect-ratio NRBs (ratio of height to length = 0.38), it is more efficient to use pre-strained SMA wires in the straight configuration, while for high-aspect-ratio NRBs (0.38) using cross SMA wires with 2% pre-strain leads to a better performance. They concluded that the diameter of wires should be designed based on the requirements (i.e. lateral stiffness and equivalent viscous damping) in order to have SMA wires with the best performance as complementary dampers. HDRBs behave quite differently compared to NRBs, especially at high shear strain amplitudes. Hedayati Dezfuli and Alam (2013c) explored the effect of SMAs on the performance of NRBs and concluded that using SMA

24

wires can be beneficial to NRBs in terms of energy dissipation capacity and re-centring capability.

2.5 Summary

In order to reduce the seismic demand on civil infrastructures several techniques are commonly employed in seismic prone regions. Seismic isolation, which is one of the most popular techniques, is widely used to safeguard bridges from severe damages due to strong earthquake events. A historical appraisal on seismic isolation systems was provided in the literature. Various types of bridge isolators have been developed, tested and are in use all over the world as effective earthquake resisting systems, including lead-rubber bearing (LRB), high damping rubber bearing (HDRB), friction pendulum bearing (FPB), magneto-rheological damper, and steel plate damper. The most popular isolation devices are LRB and HDRB. They have been used in buildings and bridges for both new constructions and retrofit projects. The premise of using these devices is to have high flexibility, which shifts the natural period of the bridge structure to a value beyond the critical period range of the earthquake event. In addition, they are endowed with damping properties that prevent the bridge piers and decks from undergoing excessive displacement. However, because of high weight and cost of steel-reinforced elastomeric isolators (SREIs), they are mostly implemented in large and expensive structures (e.g. high-rise buildings, important structural centres, and bridges). With the goal of extending the application of such base isolators to residential and low-rise buildings in both developed and developing countries, FREIs were introduced. FREIs with much lower weight can be manufactured in the form of long laminated pads through cost-effective automated processes.

Nevertheless, most of these devices have known limitations related to ageing and durability (e.g., rubber-based dampers), maintenance (e.g., viscous fluid dampers), long-term reliability (e.g., friction dampers), temperature dependent mechanical performance (e.g., rubber-based dampers, viscoelastic dampers), and geometry restoration after a strong earthquake (for most dampers). In this regard, the use of superelastic shape memory alloy (SMA) can provide an effective solution to overcome several of these problems. Superelastic SMA is a unique material with the ability to undergo large deformation and potentially recover its inelastic deformation upon stress removal. Its flag-shaped hysteresis, large

recoverable strain and deformation capability, excellent endurance against fatigue, and corrosion resistance make superelastic SMA an ideal material for utilizing it in seismic protection devices.

Figure 2.6 presents a big picture of earthquake protective systems. By introducing smart SMA-based rubber bearings (SMA-RBs), as illustrated in the figure, it is highly important to establish an appropriate analytical model for such RBs in order to simulate their behaviour. As discussed in Chapter 1, section 1.2, this PhD thesis aims to address this topic which has not been covered in the literature.
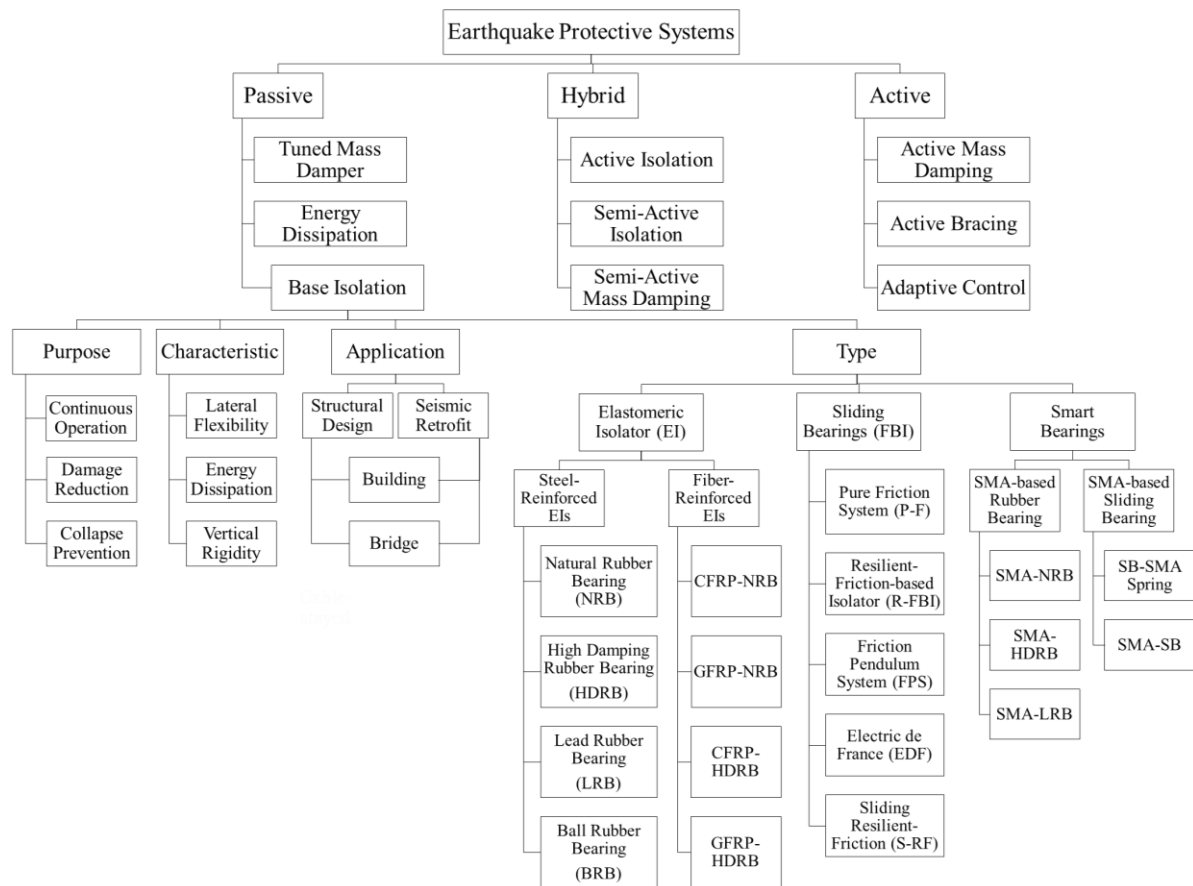
Figure 2.6. Earthquake protective systems

Chapter 3   Multi-Criteria Optimization of Rubber Bearings Reinforced with CFRP Composites

3.1   General

A material model was proposed for high damping rubber (HDR) in order to capture its highly nonlinear behaviour under shear and compressive loadings with different magnitudes and frequencies. In this regard, a comparison between six different nonlinear material models available in finite element software, ANSYS (ANSYS Mechanical APDL, Release 14.0) was carried out for modelling the HDR. The best-fitted and the most accurate material model was identified according to the behaviour of HDRB which has been evaluated through experimental study. The proposed model was validated by applying it to a steel-reinforced HDRB and comparing the lateral force-deflection hysteretic curve of the elastomeric isolator obtained from experimental tests and numerical simulations. In the next step, various carbon fibre-reinforced high damping rubber bearings (CFR-HDRBs) were simulated using FEM. The effects of different parameters such as number of rubber layers, thickness of fibre-reinforced polymer (FRP) composite plates and shear modulus of elastomer were investigated on the performance of CFR-HDRBs through a sensitivity analysis by proposing regression models for the response of the device. First, operational characteristics (effective horizontal and vertical stiffnesses, and equivalent viscous damping) of CFR-HDRBs were calculated. Then, depending on the importance level of each characteristic (criterion), a weight was assigned to each of them and the performance of the base isolator was optimized.

3.2   Material Modelling

Mechanical properties of HDRB are modelled in ANSYS (ANSYS Mechanical APDL, Release 14.0). Some of the nonlinear material models available in ANSYS are classified in Figure 3.1. According to this chart, there are different models for hyperelastic, viscoelastic, viscoplastic and inelastic rate-independent materials (ANSYS Documentation, Release 14.0). Each material can be applied to a component using several models which are indicated by grey boxes. Each model should be defined with a set of material constants. In

addition to the following models, hyper-viscoelastic material models which are a combination of the hyperelastic and viscoelastic models can be defined as well.
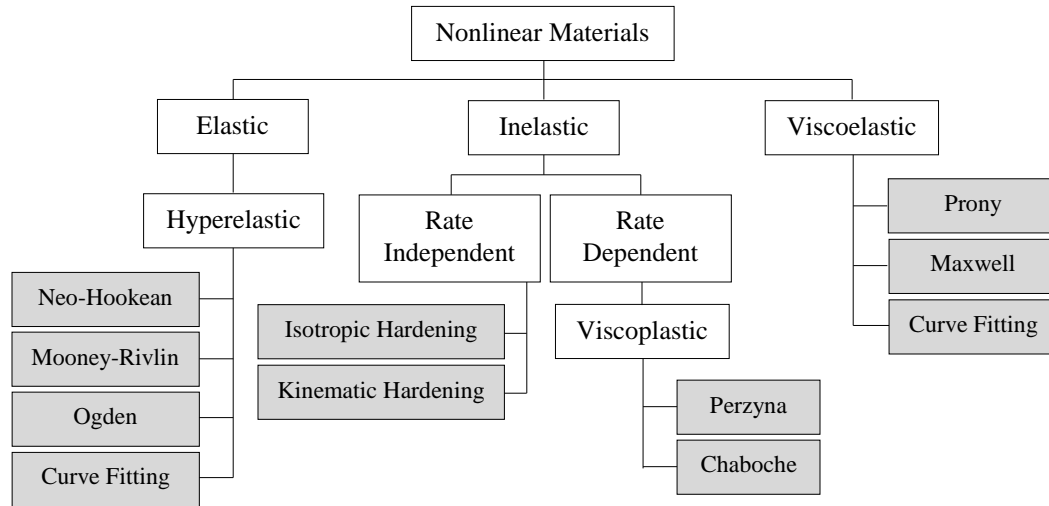
Figure 3.1. Nonlinear material models in ANSYS (ANSYS Documentation, Release 14.0)

3.2.1 Bilinear Model

A bilinear material is considered as a nonlinear, inelastic and strain-rate independent material. According to the Figure 3.2 which shows the stress-strain behaviour of a bilinear material, three different stiffnesses can be defined; the elastic stiffness, K_1, in the elastic region, the post-elastic stiffness, K_2, in the plastic region, and the effective stiffness which is ratio of the maximum force (F_{max}) to the maximum displacement (d_{max}). The terms d_y, F_y, and Q_d denote yield displacement, yield force, and characteristic strength, respectively.
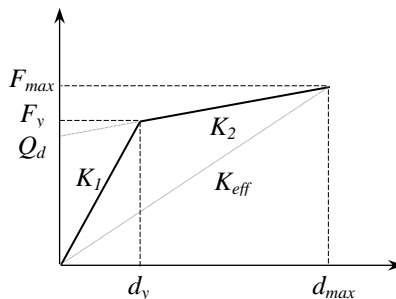
Figure 3.2. Force-displacement relation for bilinear material (adapted from (Ozkaya et al., 2011))

The Bauschinger effect which represents a decrease in the yield strength of the material by changing the direction of the strain can be included in this model (Bauschinger,

1881). Bilinear model can be used for applications with small strain levels but, it cannot accurately predict the response of the materials which undergoes a large amount of strain (ANSYS Documentation, Release 14.0). Since two equations of state can be easily defined with a limited number of material properties, a bilinear model can be easily applied to a material. Also, the finite element analyses (FEA) are done in a shorter time compared to the cases in which other material models are used.

In ANSYS, the bilinear model can be used with isotropic hardening plasticity or kinematic hardening plasticity. In the kinematic hardening plasticity, the Bauschinger effect is considered while in the isotropic one it is assumed that the yield strength does not change by altering the strain direction. For both options, the yield stress and the tangential modulus should be defined in addition to the elastic modulus and Poisson's ratio.

3.2.2 Hyperelastic Model

Hyperelasticity is usually assigned to the elastic, isotropic and nonlinear materials which are almost incompressible in volume and undergo large deformations. Elastomers such as rubber and some polymer materials can be categorized in this class. There are different models for simulating the behaviour of such materials in ANSYS such as Neo-Hookean, Mooney-Rivlin and Ogden models.

Neo-Hookean model with two material constants; the initial shear modulus (μ) and the incompressibility parameter (d), has the simplest form of strain energy potential which is defined as follows (Hoss and Marczak, 2010).

$$W = \frac{\mu}{2}(I_1 - 3)$$

(3.1)

where I_1 is the first strain invariant of the right Cauchy-Green deformation tensor.

Mooney-Rivlin model represents a strain energy function which contains compressible and incompressible parts. Due to taking the higher order parameters into account, this model can predict the behaviour of rubber materials more accurately compared to the Neo-Hookean model. The incompressible part is written as a polynomial of the strain invariants while compressible part is a function of bulk modulus. Since it is assumed that the hyperelastic materials are fully incompressible, the strain energy function, W, is simplified according to Equation (3.2) (Wadham-Gagnon et al., 2006; Hoss and Marczak, 2010)

$$W = \sum_{i+j=1}^{n} C_{ij}(I_1 - 3)^i (I_2 - 3)^j, \quad n = 1,2,3 \tag{3.2}$$

where C_{ij} is the material constant describing the deviatoric deformation of the material (ANSYS Documentation, Release 14.0), I_1 and I_2 are the first and second deviatoric strain invariants, respectively. i and j can vary from 0 to n. By increasing the value of n, the accuracy of the prediction is enhanced. 3-parameter, 5-parameter and 9-paramnter models correspond to values of n equal to 1, 2, and 3, respectively. As an example, the strain energy function for the 9-parameter Mooney-Rivlin model can be written as follows:

$$\begin{aligned} W = C_{10}(I_1 - 3) &+ C_{01}(I_2 - 3) + C_{20}(I_1 - 3)^2 + C_{11}(I_1 - 3)(I_2 - 3) + C_{02}(I_2 - 3)^2 \\ &+ C_{30}(I_1 - 3)^3 + C_{21}(I_1 - 3)^2(I_2 - 3) + C_{12}(I_1 - 3)(I_2 - 3)^2 \\ &+ C_{03}(I_2 - 3)^3 \end{aligned} \tag{3.3}$$

and

$$C_{10} + C_{01} = \frac{(1 - 2v)}{d} = \frac{\mu}{2} \tag{3.4}$$

where v, d, and μ are the Poisson's ratio, the material incompressibility parameter, and the initial shear modulus of the material, respectively.

The Ogden material model proposed by Ogden (1972) is capable of approximating large strain levels accurately. The strain can be increased up to 700% (ANSYS Documentation, Release 14.0). Five different combinations from 1 to 5 terms can be defined for the strain energy function. Although a higher parameter value can predict the behaviour of material more precisely, it may increase the numerical complexity in fitting the material constants. The strain energy function is written in terms of the principal stretches λ_1, λ_2 and λ_3 (Equation (3.5)).

$$W = \sum_{i=1}^{n} \frac{\mu_i}{\alpha_i} \left(\lambda_1^{\alpha_i} + \lambda_2^{\alpha_i} + \lambda_3^{\alpha_i} - 3 \right), \quad n = 1, 2, \dots, 5 \tag{3.5}$$

where μ_i and α_i are the material constants.

The material constants can be also calculated by the software when the curve fitting option is used rather than pre-defined models. In such a situation, different sets of results obtained from experimental tests should be provided as input. After specifying a material

model by which the behaviour of the material is simulated, the material constants are computed via solving the constitutive equations corresponding to the selected material model. In order to calculate the material constants of a hyperelastic model in ANSYS, uniaxial test, biaxial test, shear test, simple shear test and volumetric test should be carried out.

3.2.3 Viscoelastic Model

Viscoelastic materials are nonlinear, elastic and viscous. By applying a shear or tensile load, a viscous deformation is generated as a function of time. Prony and Maxwell models are two viscoelastic material models in ANSYS.

Prony model can be applied for estimating the shear and volumetric responses. For the shear response, variation of the shear modulus is calculated by changing the time while, for predicting the volumetric response, the bulk modulus decay is considered as a function of time. In Prony model, by defining a Prony series, the shear or bulk modulus is computed over the time. The Prony series for the shear modulus is given according to Equation (3.6) (Christensen, 1982; Mottahedi et al., 2010).

$$G(t) = G_\infty + \sum_{i=1}^{n} G_i e^{-\frac{t}{\tau_i}} \tag{3.6}$$

where τ_i and G_i are the relaxation time constant and the corresponding shear modulus at τ_i, respectively. Number of terms in the Prony series can be increased in order to enhance the accuracy of the prediction. On the other hand, the complexity of the response is increased and as a result, the processing time goes up considerably. A dimensionless material constants, α_i is defined as a ratio of the shear modulus at τ_i to the initial shear modulus, G_0. The initial shear modulus G_0 is:

$$G_0 = G_\infty + \sum_{i=1}^{n} G_i \tag{3.7}$$

By rewriting the Equation (3.6):

$$\alpha(t) = \frac{G(t)}{G_0} = 1 + \sum_{i=1}^{n} \alpha_i \left(e^{-\frac{t}{\tau_i}} - 1 \right) \tag{3.8}$$

where

31

$$\alpha_i = \frac{G_i}{G_0} \qquad (3.9)$$

After performing a relaxation shear test and determining the variation of shear modulus versus time, the material constants for the Prony series are specified.

In addition to the mentioned models, curve fitting option in which material constants are calculated by solving the constitutive equations and fitting curves to the mechanical properties of the material, also can be used in ANSYS. For instance, in order to model the shear and volumetric behaviours of a rubber using curve fitting option, respectively, the changes of the shear and bulk moduli versus time should be obtained through relaxation tests and these experimental results are used as the input data. The maximum number of terms for the Prony series used in the curve fitting option is 10.

3.2.4   Viscoplastic Model

A viscoplastic material is nonlinear, inelastic and strain-rate dependent. In such materials, the deformation is a function of the loading rate (Perzyna, 1966). When a permanent deformation happens in a viscoplastic material, it continues to undergo a creep flow through the time before removing the load. Such behaviour is not observed in the rate-independent plastic materials (Perzyna, 1966). Rate-dependency is very important in transient analyses where the applied load is a function of time.

In ANSYS, there are different models for viscoelastic materials such as Perzyna and Chaboche. It is recommended to combine these models with bilinear or multi-linear models with isotropic hardening plasticity. In the Perzyna model, two material constants are used; the strain-rate hardening parameter and the material viscosity parameter. The strain rate hardening effect is activated after plastic yielding by considering a yield surface. For simulating the monotonic hardening and the Bauschinger effect, the Chaboche model can be used (ANSYS Documentation, Release 14.0). Yield stress, two material constants for the first kinematic model and two material constants for the second kinematic model should be defined for this model.

3.2.5   Hyper-Viscoelastic Model

Hyper-viscoelastic models can be applied to materials which have both hyperelastic and viscoelastic properties. ANSYS software has a capability of modelling such materials by

combining hyperelastic and viscoelastic models. Bergstrom–Boyce, combined Ogden–Prony and combined Mooney-Rivlin–Prony are three models used in ANSYS. The hyper-viscoelastic model could capture the behaviour of the highly nonlinear materials such as HDR for the reason that, both hyperelastic behaviour and inelastic rate-dependent shear and volumetric responses of rubber subjected to a compressive loads and cyclic shear loads are considered (Bergstrom and Boyce, 1998).

The Bergstrom-Boyce material model can simulate the hysteretic behaviour of a strain-rate-dependent material (e.g. elastomers) with large elastic and inelastic strain levels (Bergstrom and Boyce 1998). The inelastic shear response of the material can be simulated through this model while just the elastic volumetric deformations can be captured. The Bergstrom-Boyce model describes a system with two parallel springs and one damper which is series with one of the springs (ANSYS Documentation, Release 14.0). The Prony viscoelastic model can be combined with the Ogden or Mooney-Rivlin hyperelastic material models as well.

3.2.6 Comparing Material Models

In order to specify an appropriate material model for HDR, a number of FEAs using different material models for HDR are carried out to check which model can be fitted more accurately with the actual response of the elastomer obtained from experimental tests. The complexity of the nonlinear behaviour of HDR and a large amount of elements used in the FEAs lead to a time-consuming simulation and the solution may diverge in some cases. Therefore, a HDR layer with thickness-to-length ratio of 0.05 as a simplified 2-D model is analyzed under a cyclic shear loading via ANSYS software. The bottom surface of the elastomer layer is completely fixed and the top surface is under a cyclic lateral displacement with frequency of 0.25 Hz and amplitude of $\gamma = 100\%$. Shear strain, γ, is the ratio of the elastomer thickness to the maximum lateral displacement of the top surface (Figure 3.3). The element used for the HDR is PLANE182.
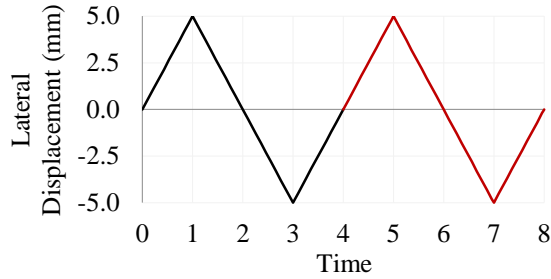
Figure 3.3. Cyclic horizontal displacement ($f = 0.25$ Hz, $\gamma = 100\%$)
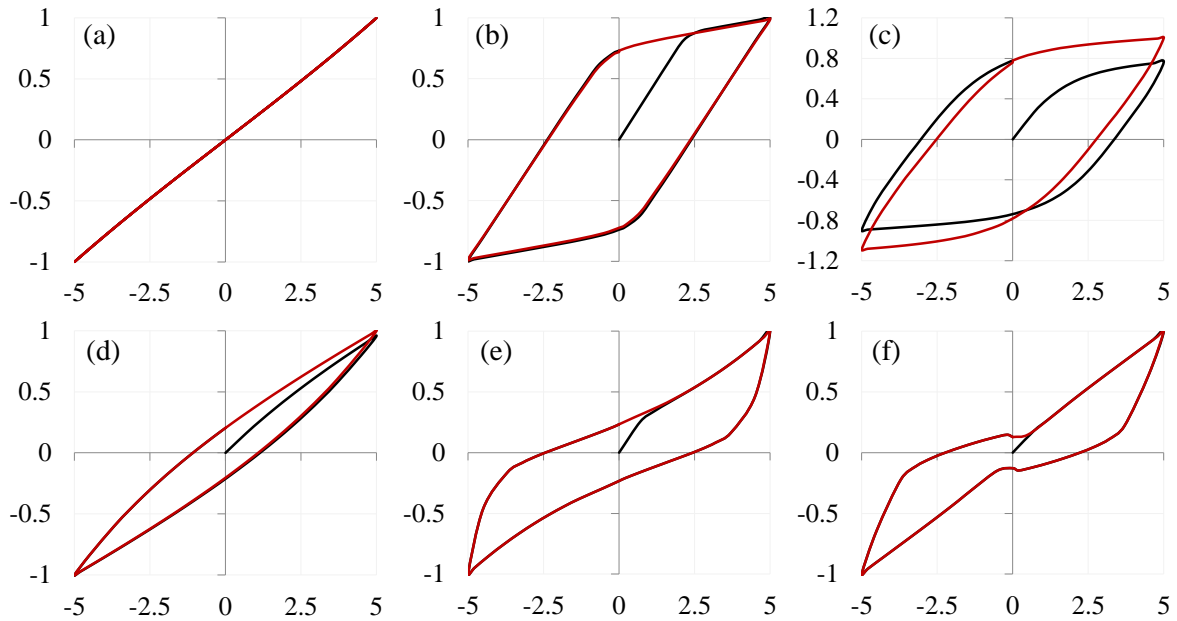
Figure 3.4. Normalized shear force versus lateral displacement for HDR layer simulated using different material models; (a) Hyperelastic (Mooney-Rivlin), (b) Bilinear with kinematic hardening, (c) Viscoplastic (Perzyna), (d) Hyper-viscoelastic (Ogden-Prony), (e) Hyper-viscoelastic (Mooney-Rivlin and Prony),(f) Hyper-viscoelastic (Bergstrom-Boyce)

Horizontal force-deflection hysteretic curve for each material model is plotted in Figure 3.4. By comparing the hysteretic response of the HDR layer modelled and analyzed with different material models, and according to the typical shear behaviour of this nonlinear material, the most applicable model can be specified. In Figure 3.4, the vertical axes are the normalized lateral force calculated by dividing each value of the load by the maximum value of the load. As a result, the responses can be compared together in an easier way.

The rubber layer modelled by 9-paramater Mooney-Rivlin model which is hyperelastic and rate-independent does not show any hysteresis effect in the force-deflection

34

response. For the bilinear model with kinematic hardening plasticity, the HDR layer undergoes a plastic deformation when the lateral deflection exceeds the yield displacement. Figure 3.4c, d, and e illustrate the hysteresis responses of hyper-viscoelastic rubber. The Bergstrom-Boyce model and the combined 3-parameter Ogden and 2-parameter Prony models could not capture the shear behaviour in the plastic region accurately while, the combined 9-parameter Mooney-Rivlin and 2-parameter Prony models can simulate the shear hysteretic response precisely. The HDR layer modelled with the viscoelastic Perzyna material model which is inelastic and rate-dependent shows a quasi-static hysteresis effect. Thus, the second loop of the force-deflection curve is different from the first one (Burtscher et al., 1998).

By comparing the load-deflection curve for each material model obtained from the FEAs with the typical hysteresis behaviour of a HDRB subjected to the pure cyclic lateral displacement with frequency of 1 Hz and strain ranges from 40% to 200% (Figure 3.5) (Dall'Asta and Ragni, 2006), it can be found that the hyper-viscoelastic models have a better estimation of the behaviour of HDR materials. The main reason is that both hyperelasticity and rate-dependency of the HDR under cyclic shear deformations are considered in the FE modelling. Among three suggested material models; Mooney Rivlin-Prony, Ogden-Prony and Bergstrom-Boyce, the first one can predict the hysteretic behaviour of HDR material under cyclic shear loadings more precisely. The Mooney-Rivlin option models hyperelasticity and the Prony model could describe the rate-dependency of HDR under pure shear loads.

Using curve fitting option in ANSYS, material constants of both Mooney-Rivlin and Prony models can be determined from experimental data obtained from ASTM or ISO standard tests. Here, data are gathered from the uniaxial tension-compression tests, the biaxial tension test, and the creep test conducted on HDR (Ibrahim, 2005). The uniaxial and biaxial tests are used for material characterization of hyperelastic model while, the material constants of viscoelastic model are determined through the creep test.
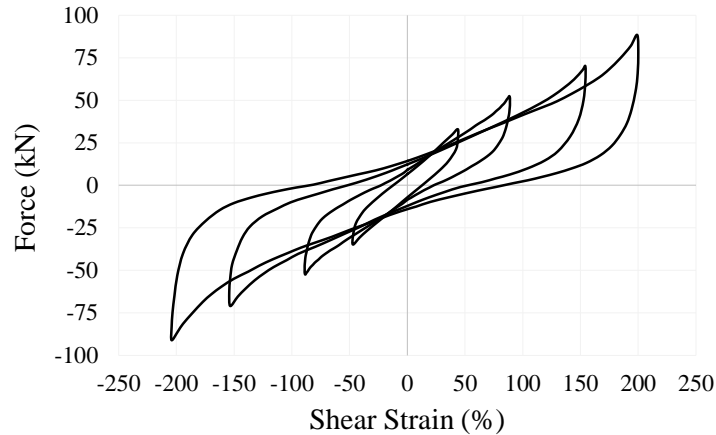
Figure 3.5. Stable hysteresis loops at different strain amplitudes
(adapted from (Dall'Asta and Ragni, 2006))

3.3 Numerical Validation and Verification

The proposed material model for HDR is used in a steel-reinforced HDRB which is numerically simulated in ANSYS. Lateral load-deflection hysteretic loop of the HDRB is determined through FEA and compared by experimental results obtained from Dall'Asta and Ragni (2006). The HDRB used in the experiments has two rubber layers, each of them with thickness of 5 mm, and one steel shim with thickness of 2 mm. Two supporting steel plates with 15 mm thickness restrain the device in the test setup. Figure 3.6 shows the dimensions of the HDRB.
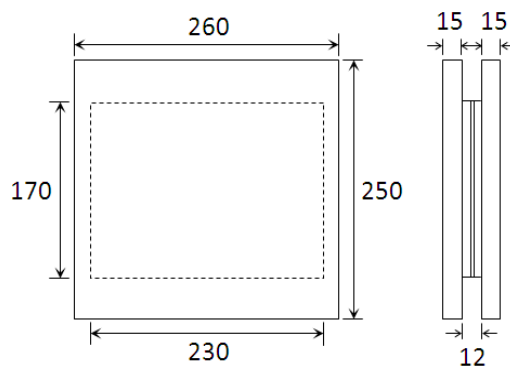
Figure 3.6. Top and side views of a HDRB (adapted from (Dall'Asta and Ragni, 2006))

To model the HDRB in ANSYS, solid element, SOLID185, with 8 nodes and three degrees of freedom at each node is selected for the steel and the rubber. The large-deflection effect is considered in FE analysis in order to simulate the large deformation of rubber layers

36

at large shear strain amplitudes. Figure 3.7 shows a HDRB with 8 rubber layers and 0.31 mm thick CFRP plates with a mapped mesh in ANSYS (ANSYS Mechanical APDL, Release 14). Blue, purple and red elements respectively illustrate steel, rubber, and CFRP materials. The lower surface of the bottom steel supporting plate is fixed in all degrees of freedom. In order to model the top steel plate to remain perfectly straight during loadings, all nodes on the upper surface of this plate are constrained to move together in the z (vertical) direction while they are free in the two other directions. The HDRB is analyzed under a given cyclic horizontal displacement with frequency of $f = 0.49$ Hz, and amplitude of $\gamma = 90\%$ with no vertical pressure since no vertical load has been applied in the experiment (Dall'Asta and Ragni, 2006). The hysteretic shear response of the device is evaluated through a full transient analysis during which the cyclic lateral displacement is linearly interpolated for each substep from the value of the previous load step.
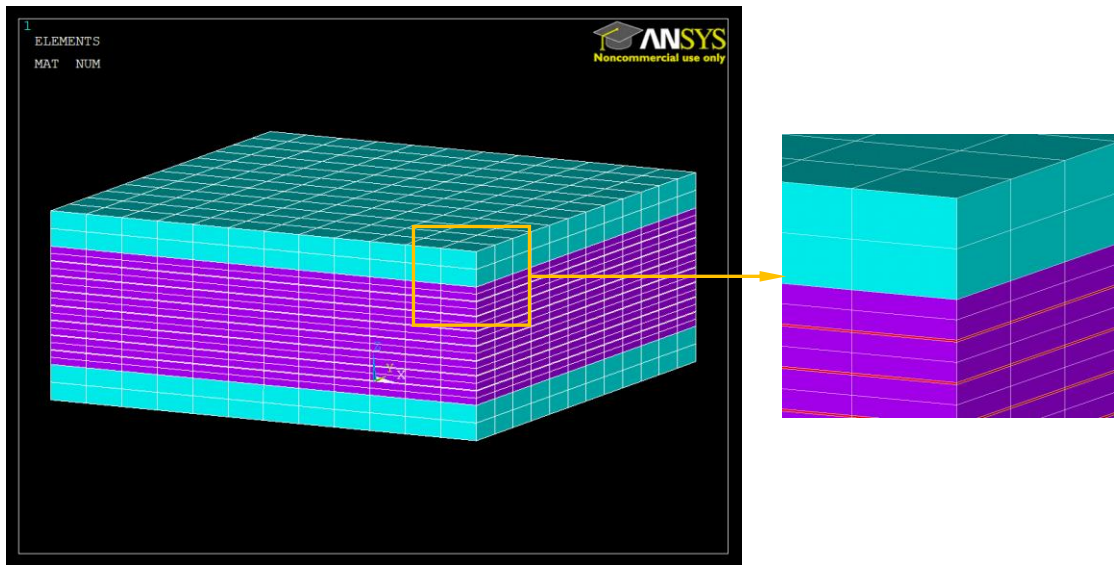
Figure 3.7. HDRB with mapped mesh in ANSYS (ANSYS Mechanical APDL, Release 14)

The material constants of hyper-viscoelastic model which is used for simulating the behaviour of high damping rubber are listed in Table 3.1.

Table 3.1. Hyper-viscoelastic material model constants

Mooney-Rivlin Model	Prony Model
$C_{10} = 2.147$	$\alpha_1 = 0.765$
$C_{01} = 0.193$	$\tau_1 = 0.041$
$C_{11} = -0.01$	$\alpha_2 = 0.061$
$C_{20} = 0.108$	$\tau_2 = 65.82$
$C_{02} = 0.047$	
$C_{30} = 0.003$	
$C_{21} = -0.013$	
$C_{12} = 0.0001$	
$C_{03} = 0.000$	

After modelling and analyzing the HDRB, the hysteresis curves are plotted and then, compared to the experimental results (see Figure 3.8). Figure 3.8 shows a good consistency between numerical and experimental results.
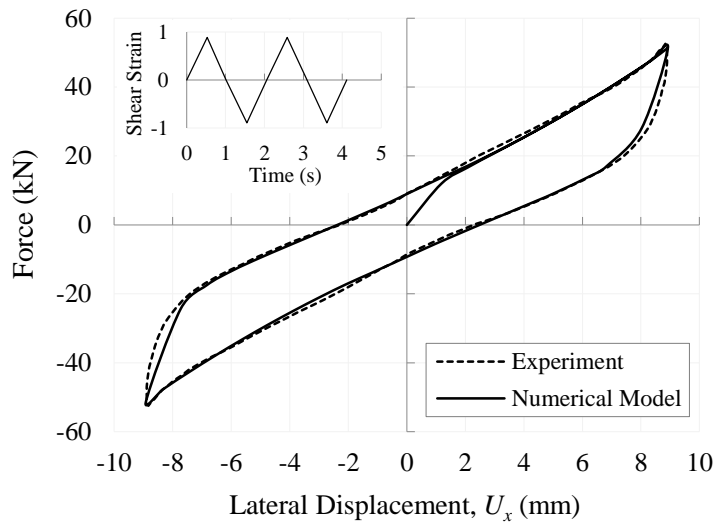
Figure 3.8. Lateral force-deflection hysteresis curve ($P = 0$ MPa, $f = 0.49$ Hz, $\gamma = 90\%$)
(Experimental results are adapted from (Dall'Asta and Ragni, 2006))

Verification refers to the correctness of result and validation indicates the accuracy of prediction. Therefore, in order to verify the hyper-viscoelastic material model proposed for HDRB, the hysteretic response of HDRB at different shear strain levels are estimated numerically and then compared to the experimental results. As can be observed in Figure 3.9, the FE model is capable of accurately simulating the hysteresis of HDRB.

38
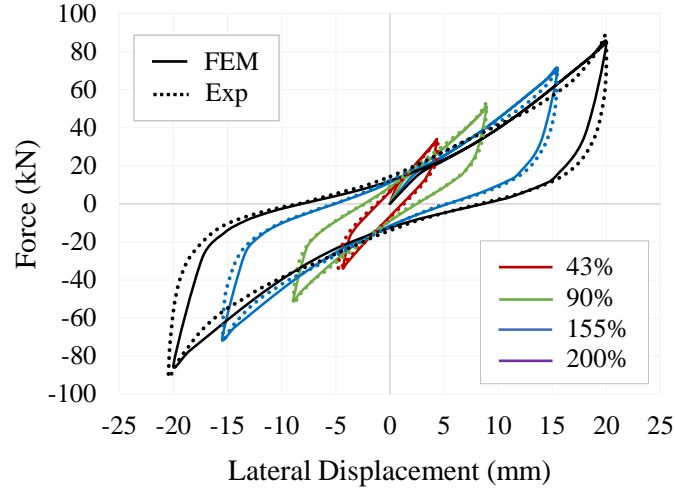
Figure 3.9. Lateral force-deflection hysteresis curves of HDRB at $\gamma = 43\%$, 90%, 155%, and 200% obtained through FEM and experiment (Dall'Asta and Ragni, 2006)

Based on the numerical results obtained from FE analyses, the effective horizontal stiffness of the HDRB is 7.76 kN/mm, 5.67 kN/mm, 4.56 kN/mm, and 4.23 kN/mm for 43%, 90%, 155%, and 200% shear strain amplitudes, respectively. The maximum difference between the numerical and experimental results in the horizontal stiffness is 5%, which happens at 200% shear strain. According to both experimental and numerical results, the maximum horizontal loads experienced at 43%, 90%, 155%, and 200% shear strains are 34 kN, 51 kN, 71 kN, and 85 kN, respectively.

3.4   Sensitivity Analysis

In order to evaluate the performance of CFR-HDRBs, three operational characteristics can be considered. These specifications which identify the vertical stiffness, the horizontal flexibility and the energy dissipation capacity of the seismic base isolators are vertical stiffness, effective horizontal stiffness, and equivalent viscous damping, respectively.

The effective horizontal stiffness, which is denoted by K_H, is calculated according to Equation (3.10) (Kelly, 1997):

$$K_H = \frac{F_{max} - F_{min}}{\Delta_{max} - \Delta_{min}}$$

(3.10)

where F_{max} and F_{min} are the maximum positive and negative shear forces, and Δ_{max} and Δ_{min} are the maximum positive and negative shear displacements, respectively.

To measure the equivalent viscous damping, β_{eq}, the energy dissipated in each cycle (*EDC*) which is the area inside the hysteresis loop of shear force-displacement curve should be computed (Naeim and Kelly, 1999).

$$\beta_{eq} = \frac{EDC}{2\pi \, K_H \, \Delta_{max}^2} \tag{3.11}$$

The vertical stiffness of a fibre-reinforced elastomeric isolator is given by Equation (3.12) (Tsai and Kelly, 2002):

$$K_V = \frac{E_c A_f}{t_r} \tag{3.12}$$

where A_f is the cross-sectional area of the reinforcement, t_r is the total thickness of rubber in the bearing and E_c is the instantaneous compression modulus of the FREI under a specific level of vertical load. The effective compressive modulus of a rectangular isolator with the plane size (length and width) of $2a$ by $2b$, is calculated using Equation (3.13) (Tsai and Kelly, 2002).

$$E_c = \frac{S^2 E_f t_f t_e}{a^2(1 - v^2)} \left(1 - \frac{\tanh \alpha a}{\alpha a}\right) C \tag{3.13}$$

$$C = \left\{1 + \frac{a}{b}[-0.59 + 0.026\alpha a + 0.074(\alpha a)^2 - 0.022(\alpha a)^3 + 0.0019(\alpha a)^4]\right\} \tag{3.14}$$

in which E_f and v are the elastic modulus and Poisson's ratio of the reinforcement, respectively. Here, t_f and t_e are the thickness of the equivalent sheet of reinforcement (total thickness of reinforcement layers) and the thickness of one rubber layer, respectively.

$$\alpha = \sqrt{\frac{12G_r(1 - v^2)}{E_f t_f t_e}} \tag{3.15}$$

where G_r is the shear modulus of the elastomer.

S is the shape factor and defined as the ratio of the bonded (loaded) area to the force-free area of one elastomeric layer. For a rectangular rubber bearing, this geometrical parameter is calculated from Equation (3.16).

$$S = \frac{L \times W}{2t_e(L + W)} \tag{3.16}$$

where L and W are length and width of each rubber layer, respectively.

The lateral force-deflection curve of each CFR-HDRBs is calculated. Then, the performance characteristics are obtained using Equations (3.10) to (3.12).

Mechanical properties of fibre-reinforced polymer (FRP) composite material made of carbon and epoxy are listed in Table 3.2.

Table 3.2. Material properties for CFRP composite material (Howie and Karbhari, 1994)

FRP Composite	Elastic Modulus (MPa)	Shear Modulus (MPa)	Poisson's Ratio	Tensile Strength (MPa)	Thickness (mm)
Carbon/Epoxy	$E_x = 73300$ $E_y = 4613.8$ $E_z = 4613.8$	$G_{xy} = 1761.0$ $G_{yz} = 1659.5$ $G_{zx} = 1761.0$	$v_{xy} = 0.310$ $v_{yz} = 0.390$ $v_{zx} = 0.019$	755	0.31

Different physical and mechanical properties such as the thickness and the number of rubber layers and FRP composite sheets as well as the shear modulus of elastomer can affect the response of the carbon fibre reinforced elastomeric isolator. In order to probe the effect of each parameter on the behaviour of device, different regression models will be proposed for each operational characteristic as different outputs of the system.

Total height of the laminated elastomeric isolator, H, is a function of different variables and is computed according to the Equation (3.17):

$$H = t_e n_e + t_f n_f + 2t_s \qquad (3.17)$$

in which, t_e, n_e, t_f and n_f are the thickness of one rubber layer, the number of rubber layers, and the thickness and number of FRP composite plates, respectively. T_s is the thickness of supporting steel plates mounted at the top and bottom of the device (Figure 3.10).
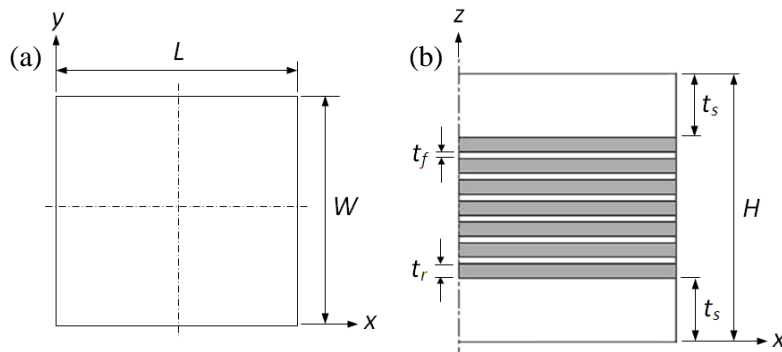
Figure 3.10. Fibre-reinforced elastomeric isolator; (a) plan view, (b) side view

Since the thickness of supporting plates is assumed to be constant in all cases and number of reinforced sheets is $n_r - 1$, the total height would be:

$$H = f(t_e, n_e, t_f) = t_e n_e + t_f(n_e - 1) + 2t_s \tag{3.18}$$

Here, the performance of different elastomeric base isolators with fixed length, width and height is compared to each other. Under this condition, for a constant height, thickness of rubber layers can be computed as follows:

$$t_e = f'(t_f, n_e) = \frac{H - 2t_s - t_f(n_e - 1)}{n_r} \tag{3.19}$$

According to Equation (3.19), thickness of elastomeric layers is a function of reinforcement thickness and number of rubber layers. Therefore, two physical characteristics (t_f and n_e) in addition to shear modulus as a mechanical property are considered in the sensitivity analysis. It should be mentioned that other parameters such as the temperature and the speed of loading also affect the performance of the elastomeric base isolator. The shear modulus of the elastomer is a function of the service temperature and the hardness. When the temperature rises, the shear modulus decreases for different values of hardness of rubber according to Figure 3.11. Here a constant temperature of 23°C is considered. The strain rate was considered in the process of validation of the HDR material model, however, it is not considered as a variable (factor) in the optimization process. Variation of temperature is also not considered. Taking these two factors into account in addition to three mentioned factors leads to a total number of 125 runs in a full factorial experiment with five factors and three levels for each. Hence, further study is required to in order to conduct a more comprehensive investigation with this amount of alternatives (rubber bearings).
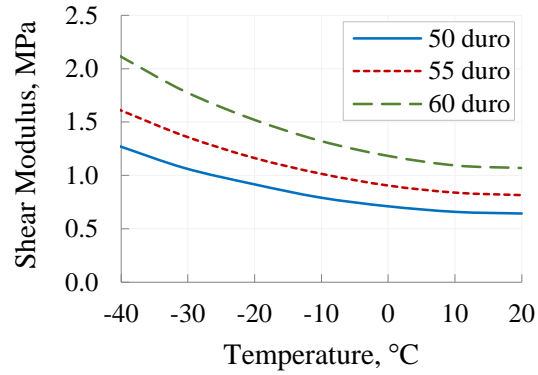
Figure 3.11. Shear modulus of rubber as a function of temperature
(adapted from (GoodCo Z-Tech, 2010))

For each factor, three levels as low, medium, and high values are determined. As a result, a full factorial experiment with three factors and three levels can be designed. By considering all combinations of three factors, each of them with three levels, a total number of 27 runs should be observed in this experiment. The factors and their levels are listed in Table 3.3.

Table 3.3. Parameters and their levels considered in the sensitivity analysis

Factor	Symbol	Level		
		1	2	3
n_r	A	8	9	10
t_f (mm)	B	0.31	0.62	0.93
G_r (MPa)	C	0.6	0.7	0.8

The 3^3 full factorial design will be arranged in Table 3.4. In this design, the number of rubber layers, thickness of reinforced plates and shear modulus of elastomer are denoted by n_r, t_f and G_r, respectively.

Table 3.4. A 3^3 full factorial design with 3 factors and 3 levels

Run	Factor		
	n_r	t_f	G_r
1	8	0.31	0.6
2	9	0.31	0.6
3	10	0.31	0.6
4	8	0.62	0.6
5	9	0.62	0.6
6	10	0.62	0.6
7	8	0.93	0.6
8	9	0.93	0.6
9	10	0.93	0.6
10	8	0.31	0.7
11	9	0.31	0.7
12	10	0.31	0.7
13	8	0.62	0.7
14	9	0.62	0.7
15	10	0.62	0.7
16	8	0.93	0.7
17	9	0.93	0.7
18	10	0.93	0.7
19	8	0.31	0.8
20	9	0.31	0.8
21	10	0.31	0.8
22	8	0.62	0.8
23	9	0.62	0.8
24	10	0.62	0.8
25	8	0.93	0.8
26	9	0.93	0.8
27	10	0.93	0.8

In order to obtain an accurate model for the response of the carbon-FREI, the main factor effects (A, B and C), the second order effects (A^2, B^2 and C^2) and the interaction effects (AB, AC, BC, and ABC) are considered in the calculations. The size of rubber bearings (length, width and height) and the thickness of supporting steel plates are listed in Table 3.5.

Table 3.5. Geometrical properties of CFR-HDRBs

Item	Symbol	Value	Unit
Length	L	200	mm
Width	W	200	mm
Height	H	80	mm
Thickness of supporting plate	t_s	20	mm

Figure 3.12 demonstrates the process of determining three outputs or responses (performance characteristics of the laminated elastomeric isolator) for the system by considering three factors as different inputs. Responses are calculated through a number of numerical simulations in ANSYS (ANSYS Mechanical APDL, Release 14).
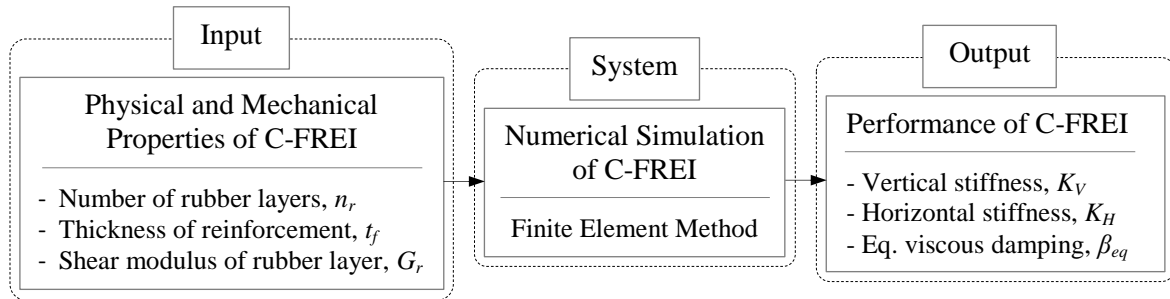
Figure 3.12. Input and output of the system for performance analysis

3.4.1 Performance of CFR-HDRB

By determining two physical properties and one mechanical property for CFR-HDRB as inputs of the system (Figure 3.12), 27 numerical simulations are performed using FEM. The output will be the system response in terms of vertical and horizontal stiffnesses, as well as equivalent viscous damping. For elastomeric bearings used in the bridges, the allowable pressure under permanent load is 4.5 MPa for the serviceability limit state (SLS) and 7.0 MPa for the ultimate limit state (ULS) (GoodCo Z-Tech, 2010). Here, each rubber bearing is subjected to a constant vertical pressure of 6 MPa and a cyclic lateral displacement with amplitude of $\gamma = 100\%$ and frequency of $f = 0.2$ Hz. The amplitude is ratio of maximum horizontal deflection to the total thickness of rubber layers. Since number and thickness of rubber layers change for each CFR-HDRB, the magnitude of lateral displacement, which is equal to the relative displacement of the supporting steel plates, varies in each run. In Table 3.6, the performance characteristics (outputs) are specified for each rubber bearing as an alternative.

Table 3.6. Responses of CFR-HDRBs in 3^3 full factorial design

CFR-HDRB	K_V (kN/mm)	K_H (kN/mm)	β (%)
1	114.1	0.410	15.03
2	147.3	0.414	14.95
3	185.5	0.417	14.88
4	132.3	0.434	14.60
5	174.5	0.441	14.56
6	224.6	0.447	14.52
7	153.5	0.458	14.45
8	207.3	0.468	14.42
9	273.5	0.479	14.40
10	132.7	0.471	15.18
11	171.2	0.475	15.10
12	215.6	0.478	15.04
13	154.2	0.497	14.77
14	203.3	0.504	14.73
15	261.6	0.511	14.70
16	178.9	0.523	14.63
17	241.6	0.535	14.60
18	318.8	0.547	14.58
19	151.1	0.530	15.28
20	195.0	0.534	15.20
21	245.6	0.538	15.14
22	175.9	0.558	14.88
23	232.0	0.566	14.85
24	298.5	0.574	14.81
25	204.3	0.587	14.75
26	275.9	0.600	14.72
27	363.9	0.614	14.70

Based on the 3^3 full factorial design as arranged in Table 3.4, the changes of three normalized outputs are compared together (Figure 3.13). For each performance characteristic, the normalized values in each column are obtained by dividing the output of each rubber bearing by the summation of 27 elastomeric bearings' outputs. These changes show that the vertical stiffness is much more sensitive to the number and shear modulus of rubber layer and the thickness of FRP composite plates compared to two other criteria. Moreover, the equivalent viscous damping fluctuates within a limited range while, the effective horizontal stiffness has an increasing trend.
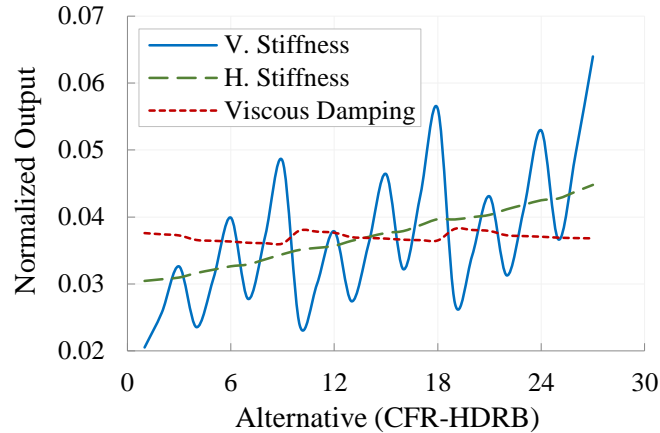
Figure 3.13. Normalized performance characteristics for different CFR-HDRBs

3.4.2 Regression Models

The importance level of a factor for estimating the response (stiffness or damping of rubber bearings) of the system can be evaluated based on the t-statistic value of that factor which is calculated by dividing the coefficient of the factor by its standard error. The coefficient and t-statistic value for each factor including main effects (A, B and C) and their second order and interaction effects (A^2, B^2, C^2, AB, AC, BC and ABC) are calculated using regression toolbox in Excel (Table 3.7).

Table 3.7. Coefficients of each factor in the regression models

Effect	K_V (kN/mm)		K_H (kN/mm)		β (%)	
	Coeff.	t-Stat	Coeff.	t-Stat	Coeff.	t-Stat
Intercept	396.9	4.2	0.005	0.2	14.77	36.1
n_r	-87.1	6.3	-0.003	0.1	-0.18	3.0
t_f	-41.0	0.4	0.018	0.7	-3.52	7.3
G_r	-66.1	1.0	0.352	22.7	2.53	8.5
n_r^2	4.9	7.9	0.0	0.8	0.004	1.4
t_f^2	35.7	5.5	0.008	5.5	1.27	45.3
G_r^2	-1.6	0.1	-0.018	5.0	-0.75	11.1
$n_r.t_f$	-0.9	0.1	0.005	0.2	0.10	1.8
$n_r.G_r$	18.2	3.1	-0.002	1.4	0.02	0.7
$t_f.G_r$	-212.6	2.7	-0.038	2.1	0.32	0.9
$n_r.t_f.G_r$	33.4	3.8	0.009	4.7	-0.02	0.4

For predicting the vertical stiffness, number of rubber layers is the dominant factor while, the shear modulus of elastomeric layers is the most effective factor for the effective horizontal stiffness. The equivalent viscous damping is influenced by all three main factors.

47

Higher order and interaction effects play an important role in estimating the horizontal and vertical stiffnesses of CFR-HDRBs. By comparing the predicted responses calculated from regression models with actual values obtained from numerical simulations and based on the t-statistic value for each coefficient, the simplified regression model for each response by considering the more significant factors are proposed as follows:

$$K_V = 396.9 - 87.1n_r - 41.0t_f - 66.1G_r + 4.9n_r^2 + 35.7t_f^2 + 18.2n_rG_r - 212.6t_fG_r \qquad (3.20)$$
$$+ 33.4n_rt_fG_r \quad (kN/mm)$$

$$K_H = 0.005 + 0.352G_r + 0.008t_f^2 - 0.018G_r^2 - 0.038t_fG_r + 0.009n_rt_fG_r \quad (kN/mm) \qquad (3.21)$$

$$\beta_{eq} = 14.77 - 0.18n_r - 3.52t_f + 2.53G_r + 1.27t_f^2 - 0.75G_r^2 + 0.10n_rt_f + 0.32t_fG_r \qquad (3.22)$$

where, n_r, t_f, and G_r are the number of rubber layers, thickness of FRP composite plates, and shear modulus of elastomeric layers, respectively.

In order to validate the proposed regression models and check their accuracy, eight new CFR-HDRBs with different values of n_r, t_f and G_r from the previously assumed values, are considered and the predicted responses are compared to values computed through FEM. Length, width, height and the thickness of supporting steel plates are kept constant. Specifications of 8 new elastomeric isolators are listed in Table 3.8.

Table 3.8. Physical properties of CFR-HDRBs

Factor	CFR-HDRBs							
	#1	#2	#3	#4	#5	#6	#7	#8
L (mm)	200	200	200	200	200	200	200	200
W (mm)	200	200	200	200	200	200	200	200
H (mm)	80	80	80	80	80	80	80	80
t_e (mm)	5.11	4.09	4.67	3.64	5.11	4.09	4.67	3.64
t_f (mm)	0.5	0.5	1	1	0.5	0.5	1	1
t_s (mm)	15	15	15	15	15	15	15	15
n_e	9	11	9	11	9	11	9	11
n_f	8	10	8	10	8	10	8	10

The relative error between the predicted responses (operational characteristics) calculated from the regression model and the results obtained from the FEAs are listed in Table 3.9.

48

Table 3.9. Performance characteristics of eight CFR-HDRBs obtained from FE analyses and

regression models

	Vertical stiffness (kN/mm)			Effective horizontal stiffness (kN/mm)			Equivalent viscous damping (%)		
	$K_{V\,FEM}$	$K_{V\,Reg.}$	Δ_{rel} (%)	$K_{H\,FEM}$	$K_{H\,Reg.}$	Δ_{rel} (%)	$\beta_{eq\,FEM}$	$\beta_{eq\,Reg.}$	Δ_{rel} (%)
1	203.8	203.1	-3.32	0.523	0.523	-1.30	14.88	14.91	2.72
2	325.2	328.7	-3.65	0.535	0.536	-1.58	14.80	14.82	4.04
3	269.4	271.2	-4.87	0.575	0.575	0.88	14.64	14.67	2.04
4	465.8	446.0	1.44	0.604	0.603	1.07	14.60	14.66	2.94
5	270.3	270.8	-4.01	0.679	0.671	-0.98	15.15	14.99	4.27
6	431.2	431.3	-2.59	0.694	0.687	-1.46	15.08	14.91	5.60
7	358.4	360.9	-4.64	0.745	0.735	0.88	14.94	14.80	3.21
8	619.5	587.2	2.67	0.782	0.770	0.86	14.90	14.78	4.11

Figure 3.14 to Figure 3.16 present the FE results along with regression models proposed for each characteristic.
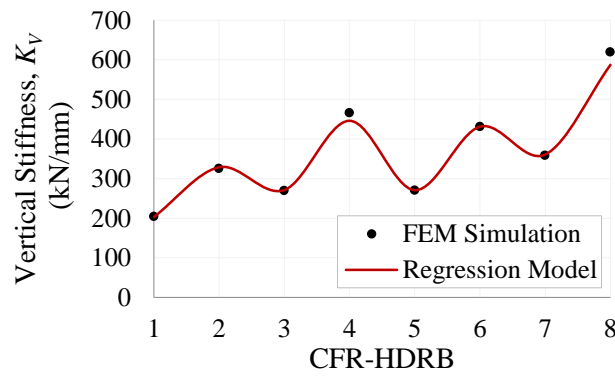
Figure 3.14. Vertical stiffness calculated through FE analysis and regression model
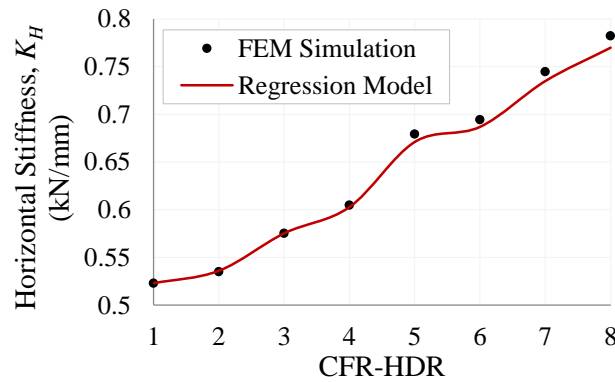
for 8 CFR-HDRBs

Figure 3.15. Effective horizontal stiffness calculated through FE analysis and regression model
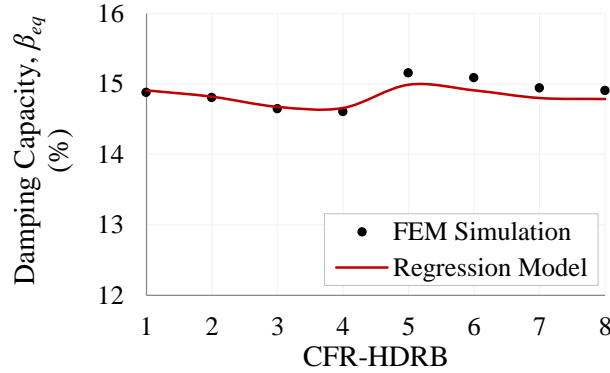
for 8 CFR-HDRBs

Figure 3.16. Equivalent viscous damping calculated through FE analysis and regression model for 8 CFR-HDRBs

Low relative errors for all criteria show that the proposed simplified regression models could accurately predict the response of the system. Since in the simplified regression models unimportant factors are eliminated, the maximum error for the vertical stiffness, the effective horizontal stiffness, and the equivalent viscous damping increase to 4.9%, 1.6% and 5.6%, respectively.

3.4.3   Effect of Number of Rubber Layers

The effect of number of elastomeric layers (n_e) on the performance of CFR-HDRBs is investigated in this part. Figure 3.17 depicts the changes of each output by increasing the number of rubber layers from 8 to 10 for three different cases in which two other factors (thickness of reinforcement and shear modulus of rubber layers) are fixed at their low, intermediate and high levels, respectively.
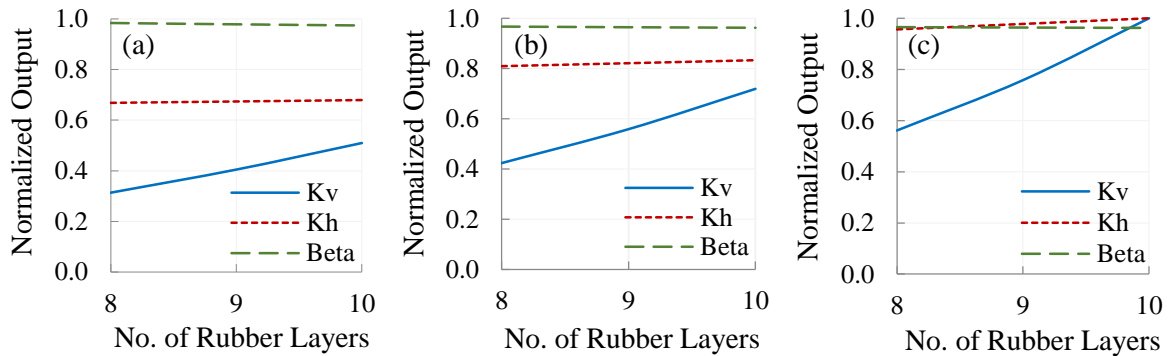
Figure 3.17. Effect of number of rubber layers on the CFR-HDRB's behaviour;

(a) $t_f = 0.31$ mm, $G_r = 0.6$ MPa, (b) $t_f = 0.62$ mm, $G_r = 0.7$ MPa, (c) $t_f = 0.93$ mm, $G_r = 0.8$ MPa

50

For all three cases, by increasing the number of rubber layers, the vertical stiffness increases considerably while the effective horizontal stiffness rises slightly and the equivalent viscous damping almost remains constant. For the first case, when the thickness of reinforcement (t_f) and the shear modulus of rubber layers (G_r) are 0.31 mm and 0.6 MPa, respectively, if the number of rubber layers increases from 8 to 10, the vertical stiffness and the effective horizontal stiffness increase about 62% and 2%, respectively. For the second case, these changes are 70% for the vertical stiffness and 3% for the horizontal stiffness. In the last case in which t_f and G_r are at their high levels, the changes of K_V and K_H are 78% and 5%, respectively.

3.4.4 Effect of Thickness of FRP Reinforcement

The second physical property which affects the efficiency of the CFR-HDRB with unidirectional carbon fibres is the thickness of FRP composite plates. Figure 3.18 shows the changes of each output by increasing the thickness of reinforced sheets from 0.31 mm to 0.93 mm for three different cases in which n_e and G_r are fixed at their low, intermediate and high levels. For all three cases, by increasing the thickness of reinforced plates, the vertical and horizontal stiffnesses increase while the equivalent viscous damping decreases marginally.
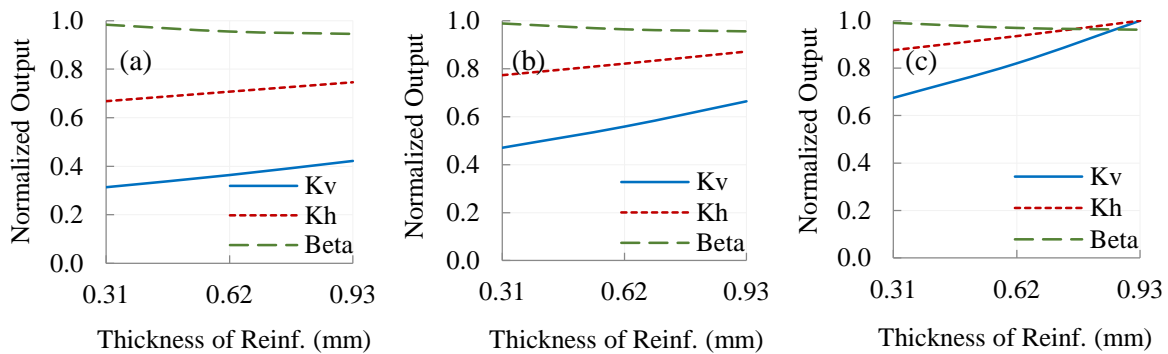
Figure 3.18. Effect of thickness of fibre-reinforced plates on the CFR-HDRB's behaviour; (a) $n_e = 8$, $G_r = 0.6$ MPa, (b) $n_e = 9$, $G_r = 0.7$ MPa, (c) $n_e = 10$, $G_r = 0.8$ MPa

In the first case, when 8 rubber layers with shear modulus of 0.6 MPa are used, by increasing t_f from 0.31 mm to 0.93 mm, the vertical stiffness, the effective horizontal stiffness and the equivalent viscous damping changes about +35%, +12% and -4%, respectively. For the second case, these variations are +41% for the vertical stiffness, +13% for the horizontal stiffness and -3% for the damping capacity. In the last case in which n_r and

51

G_r are at their high levels, the changes of K_V, K_H and β_{eq} are +48%, +14% and -3%, respectively.

3.4.5 Effect of shear modulus of rubber layers

Shear modulus of elastomer changes the behaviour of a base isolator. Figure 3.19 exhibits the changes in the performance characteristics by increasing the shear modulus of rubber layers (G_r) from 0.6 MPa to 0.8 MPa for three different cases in which n_e and t_f are fixed at their low, intermediate and high levels.
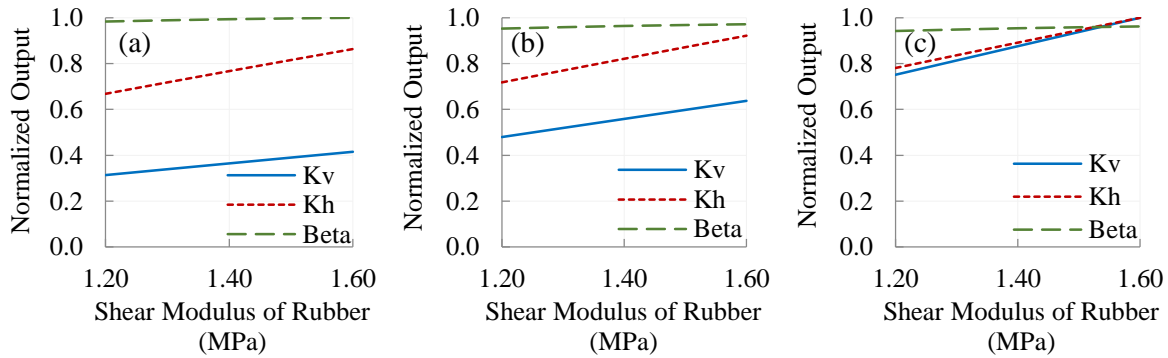
Figure 3.19. Effect of shear modulus of elastomer on the CFR-HDRB's behaviour;
(a) $n_e = 8$, $t_f = 0.31$ mm, (b) $n_e = 9$, $t_f = 0.62$ mm, (c) $n_e = 10$, $t_f = 0.93$ mm

All three outputs; the vertical and horizontal stiffnesses, and damping capacity, ascend by increasing the shear modulus of elastomer. The rate of changes in β_{eq} is lower than that of K_V and K_H.

For the first case, when 8 rubber layers and 0.31 mm thick FRP composite sheets are used, by increasing G_r from 0.6 to 0.8 MPa, the vertical stiffness, the effective horizontal stiffness and the equivalent viscous damping increased by 32%, 29% and 2%, respectively. In the case of CFR-HDRB with 9 elastomer layers and 0.62 mm thick reinforced sheets, the changes include; 33%, 28% and 2% increase in vertical stiffness, horizontal stiffness and equivalent viscous damping, respectively. When n_e and t_f are at their high levels, the variations of K_V, K_H, and β_{eq} are almost same as the second case.

3.5 Multi-Criteria Optimization

3.5.1 Theory

In each multi-criteria decision making (MCDM) problem there are a number of alternatives (A_i) and criteria (C_j). According to the main goal which is defined by the decision maker or physics of the problem, each criterion should be maximized, minimized or calibrated (when a target is defined) and the best case or the optimized alternative is specified when all of the criteria are in their best conditions.

There are different weighting and scoring methods by which the ranking of alternatives in a MCDM problem is determined. Weights can be assigned to each attribute by the decision maker (direct assignment method) or can be calculated according to the statistical data in the problem through Entropy method (Hwang and Yoon, 1981). The score of each alternative is computed by taking all criteria into account using different scoring methods such as weighted sum method (WSM) or TOPSIS which are two well-known techniques (Yoon and Hwang, 1995). The alternative with the highest score is selected as the best one and is placed in the first rank when the goal of MCDM is maximizing all criteria. On the other hand, the worst alternative has the lowest score.

The first step in the multi-criteria decision making is to transform data in order to have a problem with "the higher, the better" condition or "the lower, the better" condition for all attributes. For example, if one criterion (C_j) is needed to be minimized while the others should be maximized, by reversing C_j, the goal would be maximizing all criteria. Also, the unit and scale of one attribute may be different from those of other ones. So, in the next step, each criterion should be normalized. There are many methods for normalization. Here, each criterion is divided by the summation of that criterion for all alternatives.

In the direct assignment method which is used here, the weight of each attribute is determined according to the qualitative evaluations tabulated in Table 3.10.

Table 3.10. Assignment of values for a 10-point scale

Attribute evaluation	Value
Extremely Unimportant	0
Very Unimportant	1
Unimportant	3
Average	5
Important	7
Very Important	9
Extremely Important	10

The normalized weight for each criterion is calculated by dividing the evaluation value of each one by the summation of values. If the normalized criterion j for alternative i is denoted by $\hat{C}_{ij}$ and the normalized weight for criterion j is indicated by $\hat{W}_j$, the score of alternative i (S_i) using WSM method is calculated by Equation (3.23):

$$S_i = \sum_{j=1}^{n} \hat{W}_j \hat{C}_j \tag{3.23}$$

where n is the number of total criteria considered in the MCDM problem.

The lower and upper limits of each operational characteristic are determined based on the type of base isolator (NRB, HDRB etc.) and also the application in which the rubber bearing is used (buildings or bridges). Here, HDRBs reinforced with carbon fibre fabrics are implemented in a three-span continuous steel bridge. The equivalent viscous damping of HDRBs is 10-16% (Marioni, 1998). The lower and upper bounds of the effective horizontal and vertical stiffnesses are identified according to the elastomeric bearings datasheet of GoodCo Z-Tech Company, which is the largest manufacturer of the elastomeric and sliding bearings for bridges in Canada (GoodCo Z-Tech, 2010). The minimum and the maximum effective horizontal stiffness of laminated bearing (Series EL) with a minimum available plan size of 300 mm by 200 mm and a height of 80 mm is 0.82 kN/mm and 1.22 kN/mm, respectively. Since dimensions of CFR-HDRBs are 200 mm × 200 mm × 80 mm, the upper and lower limits of the horizontal stiffness should be recalculated. According to the analytical formula of $K_H = G_r A/t_e$ (Kelly, 1997), if the width of the rubber bearing decreases from 300 mm to 200 mm, the minimum and the maximum effective lateral stiffness respectively reduces to 0.547 kN/mm and 0.813 kN/mm. Similarly, using Equation (3.12), the vertical stiffness decreases to 109.5 kN/mm.

The performance characteristics are selected as attributes for each rubber bearing which is considered as an alternative. As a result, a multi-criteria decision making problem has been defined with 27 alternatives and three criteria. Since the elastomeric isolators should have sufficient vertical stiffness under a wide range of compressive loads, the vertical stiffness (K_V) should be maximized. Also, they should be more flexible in the horizontal direction so, the horizontal stiffness (K_H) should be minimized. The higher damping capacity means the higher amount of energy dissipation. Accordingly, the damping capacity (β_{eq}) should be maximized. Since the second criterion (the effective horizontal stiffness) should be minimized while two others should be maximized, the effective horizontal stiffness for all 27 alternatives is reversed in order to transform the MCDM problem to "the higher, the better" condition for all attributes. Consequently, the ranking of CFR-HDRBs are easily determined based on the highest and lowest scores.

According to the WSM method, the score of each alternative (rubber bearing) is found as follows:

$$S_i = \widehat{W}_1 \, \widehat{K}_{V_i} + \widehat{W}_2 \, \widehat{K}'_{H_i} + \widehat{W}_3 \, \hat{\beta}_{eq_i} \tag{3.24}$$

where, $\hat{K}_{V_i}$, $\hat{K}'_{H_i}$, and $\hat{\beta}_{eq_i}$ are normalized vertical stiffness, normalized inversed horizontal stiffness, and normalized equivalent viscous damping, respectively. $\hat{W}_1$, $\hat{W}_2$, and $\hat{W}_3$ are the normalized weights corresponded to the first, second and third criteria, respectively. The optimized CFR-HDRB which is the most efficient rubber bearing in terms of vertical stiffness, lateral flexibility and energy dissipation capacity should have the highest score among 27 alternatives with different performance specifications.

Figure 3.20 shows the procedure of optimizing the performance of CFR-HDRBs through a multi-criteria decision making process.
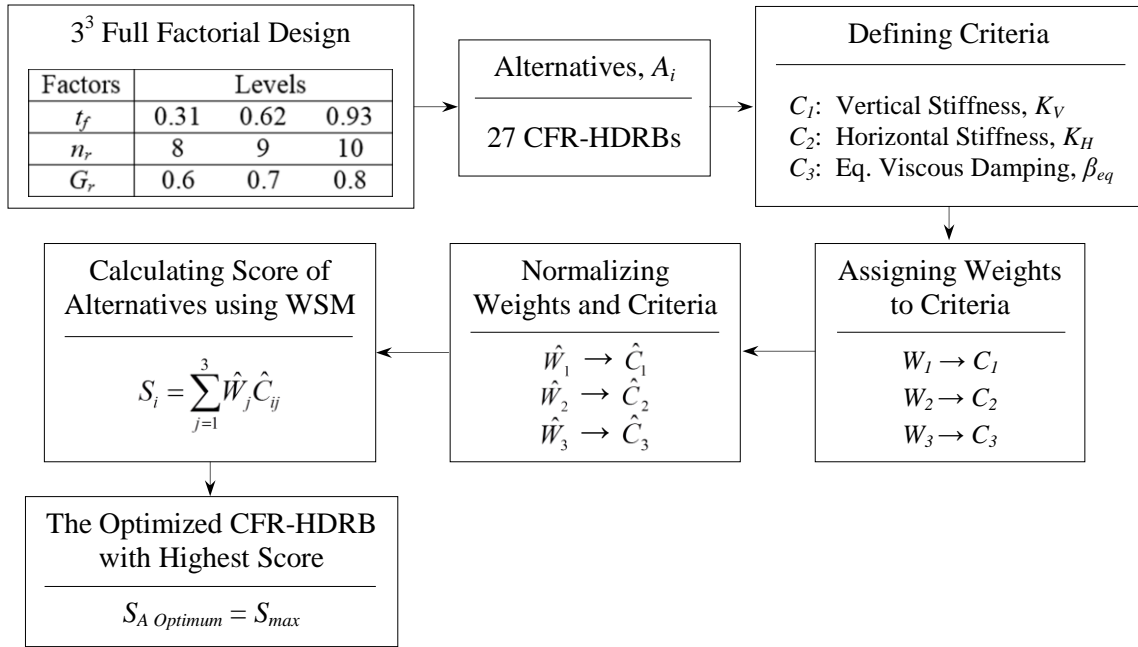
Figure 3.20. Flow chart of multi-objective optimization

3.5.2 Optimization of CFR-HDRB

After inversing the effective horizontal stiffness (K'_H) and normalizing all criteria for each CFR-HDRB, using weighted sum method (Equation (3.25)), the score of each alternative (rubber bearing), S_i, is calculated based on the normalized weights of each criteria in Table 3.11. It should be noted that the equivalent viscous damping and the horizontal stiffness are considered as extremely important and very important criteria, respectively, and the evaluation value of vertical stiffness is assumed to be 4 (according to Table 3.10). The weights listed in Table 3.11 are normalized using the summation of evaluation values.

Table 3.11. Assigned normalized weights to criteria

Criterion	Weight
Vertical Stiffness	0.18
Horizontal Stiffness	0.39
Damping Capacity	0.43

$$S_i = 0.18 \, \widehat{K}_{V_i} + 0.39 \, \widehat{K}'_{H_i} + 0.43 \, \hat{\beta}_{eq_i} \qquad (3.25)$$

By sorting the alternatives from highest to lowest scores, the best rubber bearing which is placed in the 1st rank is determined. In Table 3.12, five best CFR-HDRBs are listed.

Table 3.12. Properties of 1st to 5th ranked CFR-HDRBs

| Rank | Specifications | | | | Stiffness | | Damping |
	ID	n_r	t_f (mm)	G_r (MPa)	K_V (kN/mm)	K_H (kN/mm)	β (%)
1st	A3	10	0.31	0.6	185.5	0.417	14.88
2nd	A9	10	0.93	0.6	273.5	0.479	14.40
3rd	A27	10	0.93	0.8	363.9	0.614	14.70
4th	A18	10	0.93	0.7	318.8	0.547	14.58
5th	A6	10	0.62	0.6	224.6	0.447	14.52

According to this ranking, the optimized CFR-HDRB, as the most efficient rubber bearing, has 10 rubber layers with shear modulus of 0.6 MPa and nine FRP composite plates with thickness of 0.31 mm. Since the total height of all base isolators is 80 mm, the thickness of each rubber layer would be 4.72 mm for the optimized CFR-HDRB. For the five best cases, the elastomeric isolator has the maximum number of rubber layers ($n_r = 10$).

On the other hand, the worst alternative with the lowest score is an elastomeric bearing with characteristics listed in Table 3.13.

Table 3.13. Properties of the worst CFR-HDRB

| Rank | Specifications | | | | Stiffness | | Damping |
	ID	n_r	t_f (mm)	G_r (MPa)	K_V (kN/mm)	K_H (kN/mm)	β (%)
27th	A22	8	0.62	0.8	175.9	0.558	14.88

Based on the applied load which is a combination of 6 MPa vertical pressure and cyclic lateral displacement with frequency of 0.2 Hz and shear strain of $\gamma = 100\%$, the lateral force-displacement hysteretic loops for the optimized CFR-HDRB and the 2nd best rubber bearing are plotted in Figure 3.21.
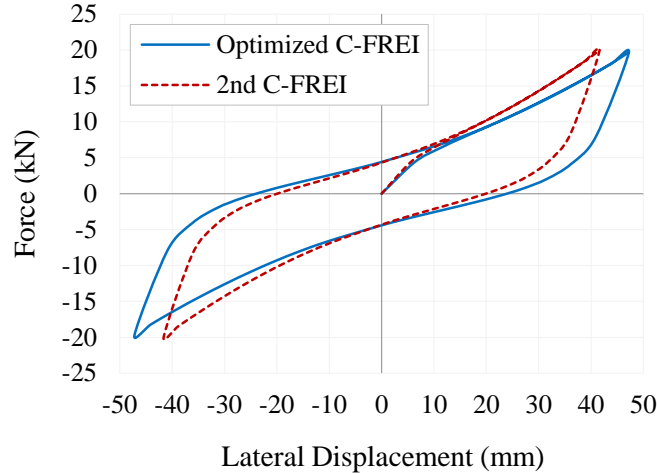
Figure 3.21. Lateral force-deflection hysteresis curve for the 1st and 2nd best CFR-HDRBs ($f = 0.2$ Hz, $\gamma = 1.0$)

3.6   Summary

Elastomeric base isolators are able to minimize structural damage in moderate seismic events and prevent structural collapse in extreme conditions such as severe earthquakes. They considerably decrease and dissipate the earthquake energy transmitted to the structure by providing a damping mechanism between the substructure and the superstructure due to their very low horizontal to vertical stiffness ratio. HDRB is one type of conventional elastomeric isolators in which thin layers of high damping rubber (HDR) are bonded to steel shims. In this chapter, a material model was proposed for HDR in order to capture its highly nonlinear behaviour under compressive and cyclic shear loadings. Among different kinds of material models including bilinear, hyperelastic, viscoelastic and viscoplastic ones; hyper-viscoelastic model was the best-fitted and the most accurate one to predict the hyperelasticity and strain-rate-dependent behaviour of HDRB subjected to the cyclic lateral displacement.

The efficiency of carbon fibre-reinforced high damping rubber bearing (CFR-HDRB) was numerically optimized through a multi-criteria optimization process. After validating and verifying the hyper-viscoelastic material model with experimental results, the effect of different parameters on the performance of FREIs was investigated through a sensitivity analysis. In this regard, regression models were established for predicting the behaviour of rubber bearings. The performance of CFR-HDRB was optimized by assigning different

weights to the operational specifications, which are the effective horizontal and vertical stiffnesses, and the equivalent viscous damping. Results showed that the effective horizontal stiffness and viscous damping are highly dependent on the shear modulus of the elastomer layers. Also, the number of rubber layers and thickness of FRP composite plates had large effects on the vertical stiffness.

Chapter 4   Performance of Fibre-Reinforced Elastomeric Isolators: Experimental and Numerical Investigations

4.1   General

In Chapter 3, with the purpose of acquiring an insight into the cause-and-effect relations between the input and output of the system (C-FREI), numerical investigations (regression and sensitivity analyses) were performed using design of experiments (DOE) method through which the effect of three factors was assessed on the output (performance) of the C-FREI. In this chapter, experimental investigations were conducted on C-FREIs as a complementary part of the previous chapter.

This chapter aimed to introduce a simple and fast manufacturing process developed for fabricating carbon fibre-reinforced elastomeric isolators (C-FREIs) in bonded applications. Moreover, the performance of such fibre-reinforced isolators was evaluated through experimental and numerical investigations. In order to show the efficiency of C-FREIs under different loading conditions, operational specifications of C-FREIs in the vertical and horizontal directions were determined through experimental tests. In this regard, nine 1/4 scale C-FREIs were produced and then the performance characteristics including vertical and horizontal stiffnesses, as well as energy dissipation capacity and equivalent viscous damping were assessed through experimental investigations. Bonded C-FREIs were fixed to the substructure and superstructure using steel supporting plates. Long strip laminated pads consisting of rubber layers and carbon fibre fabrics were fabricated without using a mold and cut to small sizes. This technique reduces the time of the manufacturing process and makes it simple. The performance characteristics were determined by conducting vertical pressure and horizontal cyclic displacement tests. Furthermore, future investigations were suggested regarding the performance variation of C-FREIs through a sensitivity analysis.

The performance sensitivity of C-FREIs was experimentally assessed. The main motivation was the lack of adequate information on the response sensitivity of bonded FREIs which were manufactured in the proposed process. The effect of different parameters, including the number of rubber layers, the thickness of carbon fibre fabric, the vertical pressure, and the rate of lateral cyclic displacements, was investigated on the operational

characteristics of the C-FREIs. The sensitivity analyses were performed by conducting pressure and rate sensitivity tests. In the analyses, the shear hysteretic responses of C-FREIs were evaluated in order to calculate the effective horizontal stiffness and the equivalent viscous damping.

In the next step, a detailed parametric study on the effect of various parameters affecting the performance of full size C-FREIs was conducted numerically. First, full-scale C-FREIs were modelled using finite element method (FEM) in ANSYS (ANSYS Mechanical APDL, Release 14.0). Then, C-FREIs were validated and verified through the performed experimental tests. In a comprehensive study, a wide range of C-FREIs were considered by changing the plan size of elastomeric layers (length and width) as well as the height of the laminated pad. The vertical and effective horizontal stiffnesses as well as the equivalent viscous damping were determined for various combinations. In order to assess the sensitivity of the response of C-FREIs in the vertical and horizontal directions, the effect of three factors; the number and the thickness of rubber layers, and the thickness of carbon fibre reinforced layers were investigated on the behaviour of rubber bearings. Since, three levels as low, medium, and high, were defined for each factor, nine cases were evaluated for C-FREIs with the same plan size, and a total number of 36 specimens were considered for four different sets of plan size.

4.2 Manufacturing Process

Nine 1/4 scale C-FREIs are manufactured using the commercial high quality neoprene with a hardness of 55 Shore A and a minimum tensile strength of 17 MPa specified by the CHBDC CAN/CSA S6-06 (CHBDC, 2006), bi-directional carbon fibre fabrics (orientations 0/90°) with a tensile strength of 4413 MPa (ACP Composites, 2012), and steel supporting end plates. All specimens have an identical width and length of 70 mm by 70 mm but with different numbers and thicknesses of elastomeric and reinforcement layers. The shape factor (i.e. ratio of loaded (plan) area to load free (side) area of a rubber layer) is 11.7, 5.8, and 3.9 for base isolators with elastomeric layers' thickness of 1.5 mm, 3 mm, and 4.5 mm, respectively.
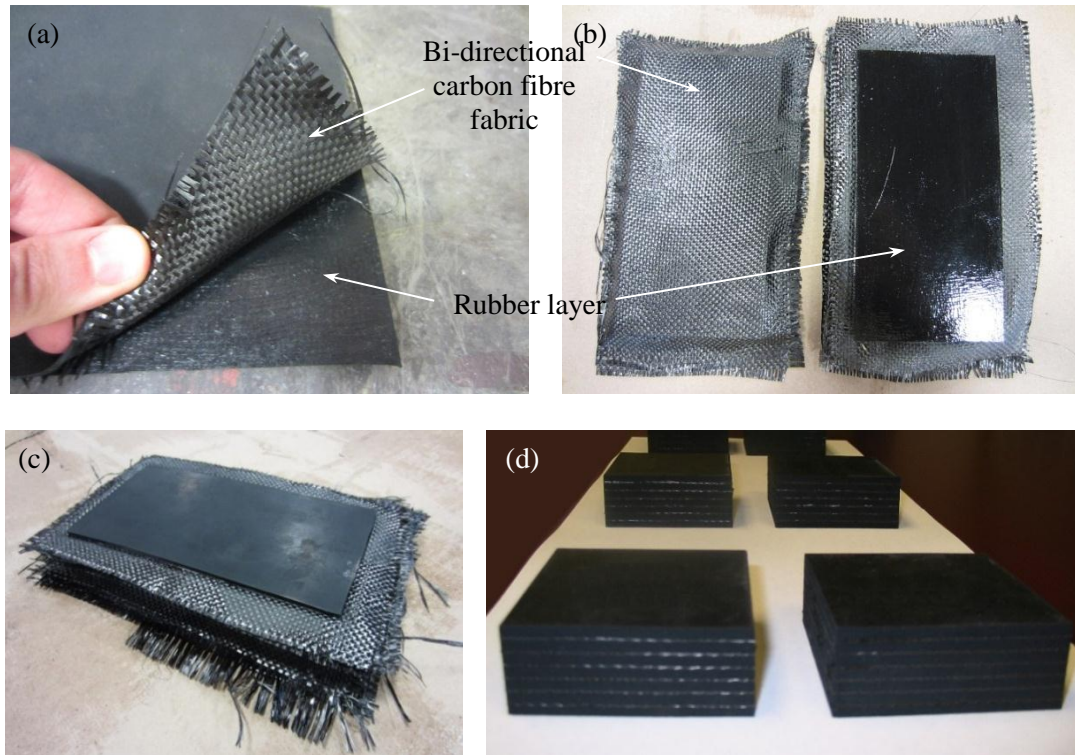
Figure 4.1. Manufacturing process of C-FREIs; (a) bi-directional carbon fibre fabric between two rubber layers, (b) attaching fibre fabrics to rubber layers by adding glue (rubber cement), (c) cured laminated pad, (d) laminated pad cut with water-jet technology

Elastomeric layers are bonded to bi-directional (orientations 0/90°) carbon fibre fabrics using rubber cement. Rubber cement is a cold bonding compound made of elastic polymers (typically latex). It is used to attach elastomeric layers to bi-directional carbon fibre fabrics (see Figure 4.1). After fabricating a laminated pad consisting of alternating layers of elastomer and reinforcement, in the curing process, laminated pads are subjected to a uniform pressure of 4 MPa for 24 hours at the room temperature without using a mold. According to the rubber cement manufacturer's instruction, 70% to 80% of the bond strength is developed during 24 hours at room temperature and the rest is developed over the next 14 days. Then, the laminated pads in the form of long strips are cut to the required size (70 mm by 70 mm) using the water-jet (see Figure 4.1d) in order to create very smooth side surfaces and prevent delamination between layers during the cutting process. Finally, in order to improve the bonding between layers and prevent premature delamination that might occur during shipping, installation, or testing, side faces are coated with two layers of adhesive (rubber cement). The same bonding compound is used to attach steel supporting plates to the C-

FREI. Nine C-FREIs with different numbers and thicknesses of rubber and carbon fibre-reinforced layers are depicted in Figure 4.2. Table 4.1 demonstrates the geometrical properties of the manufactured rubber bearings.
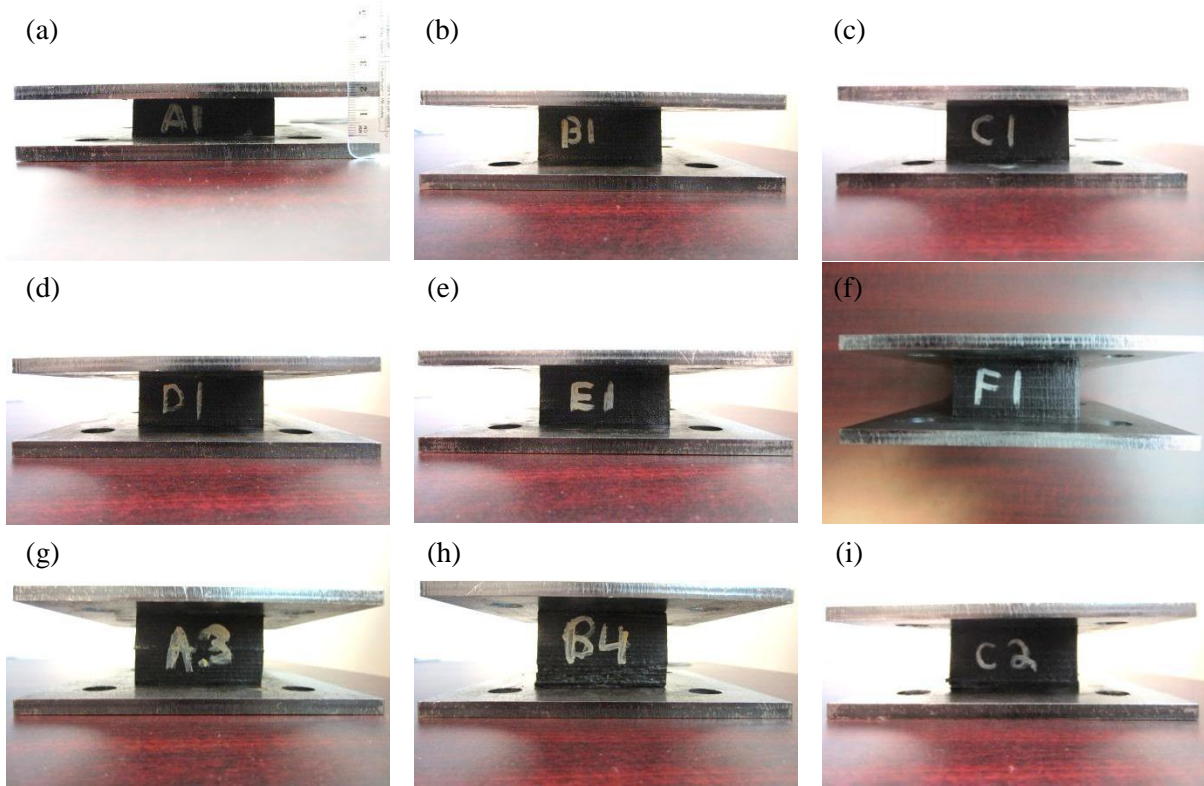
Figure 4.2. C-FREIs manufactured with different properties;

(a) A1; (b) B1; (c) C1; (d) D1; (e) E1; (f) F1; (g) A3; (h) B4; (i) C2

Table 4.1. Physical and geometrical properties of C-FREIs

C-FREI	Plan size of steel plates (mm × mm)	Plan size of reinforcement (mm × mm)	H (mm)	t_s (mm)	t_e (mm)	t_f (mm)	n_e	n_f	S
A1	150 × 150	70 × 70	31.8	6.35	1.5	0.25	8	7	11.7
B1	150 × 150	70 × 70	41.9	6.35	1.5	0.25	12	11	11.7
C1	150 × 150	70 × 70	43.4	6.35	3.0	0.25	8	7	5.8
D1	150 × 150	70 × 70	40.5	6.35	3.0	0.50	7	6	5.8
E1	150 × 150	70 × 70	41.8	6.35	3.0	0.75	7	6	5.8
F1	150 × 150	70 × 70	45.5	6.35	4.5	0.25	6	5	3.9
A3	150 × 150	70 × 70	50.6	6.35	1.5	0.25	16	15	11.7
B4	150 × 150	70 × 70	54.5	6.35	1.5	0.25	17	16	11.7
C2	150 × 150	70 × 70	45.9	6.35	3.0	0.25	9	8	5.8

H: total height of C-FREI; t_s: thickness of steel supporting plates; t_e: thickness of elastomeric layers; t_f: thickness of carbon fibre fabrics; n_e: number of elastomeric layers; n_f: number of fibre-reinforced layers; S: shape factor.

4.3 Test Setup

The test setup is equipped with vertical and horizontal hydraulic jacks. Force and displacement in the horizontal and vertical directions are measured in each test. Three load cells, each of them with a capacity of 10,000 lb (44.5 kN), measure the load applied through the vertical hydraulic jack. The computer receives the electrical signal generated by the load cells and estimates the corresponding force. The same mechanism is implemented for evaluating the lateral force applied through the horizontal hydraulic jack using one load cell. Four laser displacement transducers (LDT) mounted at four sides of the C-FREI are used to measure an average value for vertical displacement (see Figure 4.3). The horizontal displacement is determined by a string potentiometer (SPOT), a transducer for measuring the linear position of rubber bearings.
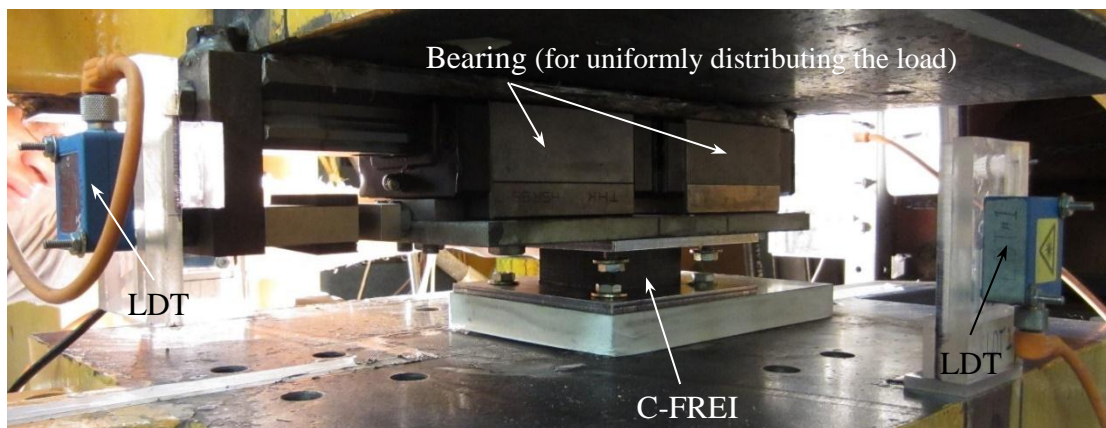
Figure 4.3. C-FREI fixed in the test setup

Different parts of test setup are identified in Figure 4.3 and Figure 4.4. Eight bolts are used to connect the steel supporting plates to the test setup and fix the C-FREI in its place. In all tests, the vertical pressure is applied through the upper supporting plate which does not move in the horizontal direction. The cyclic lateral displacements are applied to rubber bearings through the lower supporting plate which has no movement in the vertical direction.

Figure 4.4. Test setup and related equipment

4.4 Experimental Tests

In order to explore the functionality of C-FREIs, performance tests are conducted in the vertical and horizontal directions.

4.4.1 Failure Tests

Before defining the loading scenarios in cases of vertical pressure and lateral cyclic displacements, failure tests are conducted in order to determine the capacity of the manufactured C-FREIs in both vertical and horizontal directions. In this regard, two specimens are chosen to be tested under extreme loading conditions.

In order to evaluate the vertical stiffness capacity of C-FREIs, specimen F1 as the worst case is selected since rubber layers with maximum considered thickness (4.5 mm) are used. C-FREI-F1 is subjected to a maximum of 6.1 MPa vertical pressure. Figure 4.5 shows three stages of the tests in which the base isolator is subjected to 0 MPa, 3 MPa, and 6.1 MPa. At 3 MPa vertical load, rubber layers bulges but no failure was observed. However, when the pressure increased to 6.1 MPa, elastomeric layers encountered an extra bulging because fibre-reinforced layers could not prevent them from extra deformation (see Figure 4.5c). After removing the load, local delamination between CFR and rubber layers and also complete detachments between rubber layers and steel supporting plates were observed.
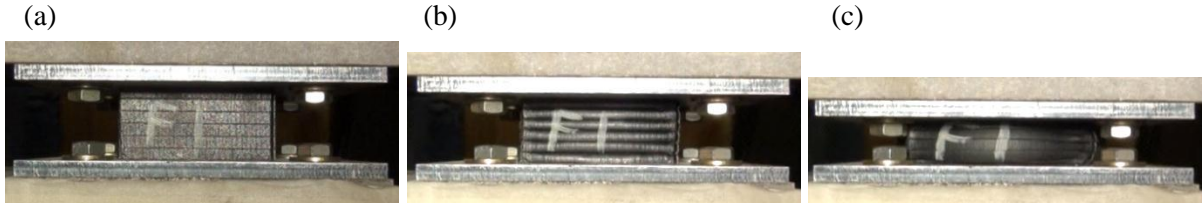
Figure 4.5. C-FREI-F1 under vertical pressures of (a) 0 MPa, (b) 3 MPa, and (c) 6.1 MPa

To determine the capacity of C-FREIs in the horizontal direction, C-FREI-C1 is subjected to a lateral displacement equals to 200% of the total thickness of rubber layers ($t_r = 24$ mm) while a constant 1.5 MPa vertical pressure is applied to the base isolator. Figure 4.6 demonstrates different stages at which the shear strain, defined as the ratio of lateral displacement to total thickness of elastomeric layers, increases from 100% to 200% and then is removed. It is observed that at all shear strain levels (from 100% to 200%), first and last rubber layers are locally detached from the steel plates as a result of rollover deformation happened in the laminated pad. In addition, at 200% shear strain (see Figure 4.6c), delamination occurred between rubber layers and fibre-reinforced sheets. Consequently, it can be observed that when the lateral displacement reaches zero (Figure 4.6d), a permanent deformation happened in the rubber bearing due to a complete debonding between CFR and rubber layers.
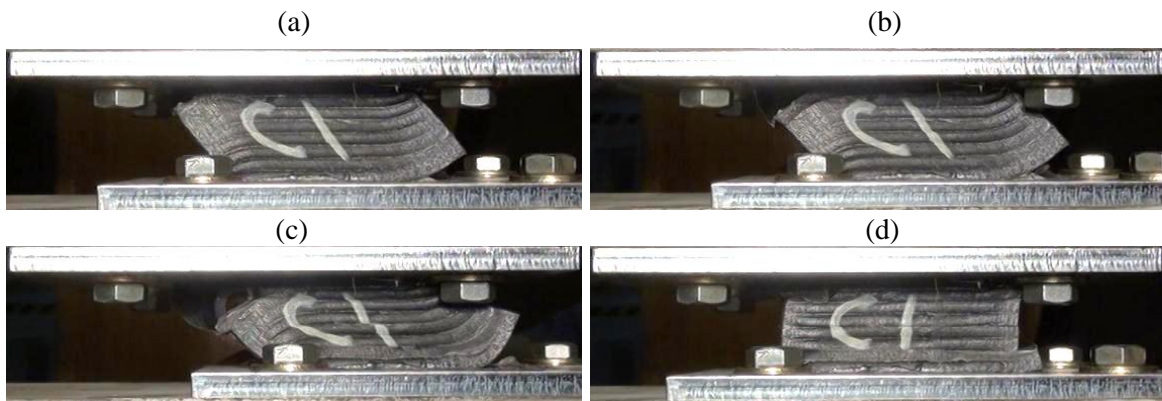
Figure 4.6. C-FREI-C1 under a combination of 3 MPa vertical pressure and lateral displacements of (a) 100% t_r, (b) 125% t_r, (c) 200% t_r, and (d) 0%

Based on the results obtained from the failure tests, it was decided to limit the maximum vertical pressure and the shear strain amplitude to 3 MPa and 100%, respectively, in order to complete all tests scenarios without any global failure. It should be noted that

66

since specimens C-FREIs C1 and F1 encountered unrecoverable damage during failure tests, they cannot be used in experimental tests. Moreover, specimen C-FREI-C2 was damaged during the shipping process and as a result, it was not used.

4.4.2 Vertical Compression Test

4.4.2.1 Test Procedure

The objectives of the vertical compression test are to evaluate the vertical stiffness and the vertical deflection of rubber bearing. This test is performed under load control since the vertical force is controlled during the tests. For each C-FREI, three tests with different values of design vertical pressure, P_D, including 0.75, 1.50, and 3.00 MPa (3.7, 7.4, and 14.7 kN) were conducted. C-FREI is loaded monotonically up to the design pressure. Then, three fully reversed cycles with a variation of 20% of the design pressure is applied with a frequency of $f_V = 0.2$ Hz. Finally, C-FREI is monotonically unloaded. Figure 4.7 shows the behaviour of pressure changes versus time for three considered design pressures.
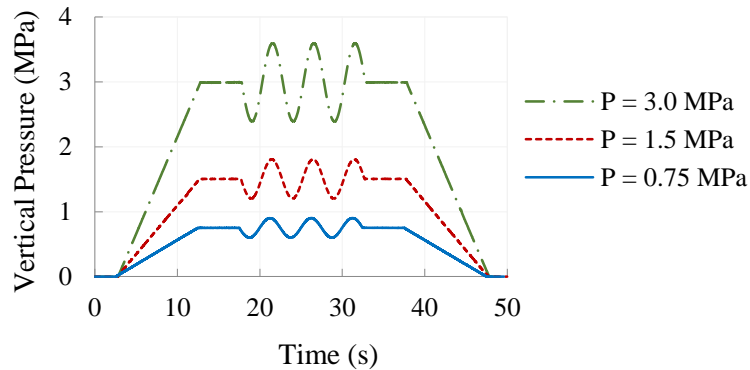
Figure 4.7. Variation of vertical pressure over time for three design pressures

After conducting the vertical tests, the operational characteristics including the vertical stiffness, K_V, the compressive modulus, E_c, and the maximum vertical deflection at the design pressure, Δ_V are determined. According to Equation (4.1), the compressive modulus can be calculated from the vertical stiffness obtained from the tests (Naeim and Kelly, 1999).

$$E_c = \frac{K_V t_r}{A_f} \tag{4.1}$$

where t_r is the total thickness of rubber layers and A_f is the cross-sectional area of the fibre-reinforced layer which is bonded to the elastomer.

4.4.2.2 Vertical Characteristics

In order to determine the vertical stiffness as well as the maximum vertical deflection, changes of vertical force are plotted versus vertical deflection for each C-FREI. Figure 4.8 depicts the corresponding results for three different pressure levels (0.75 MPa, 1.5 MPa, and 3.0 MPa). The slope of the dashed lines is the tangent vertical stiffness of C-FREI at the corresponding design pressure. Table 4.2 represents the vertical operational characteristics.
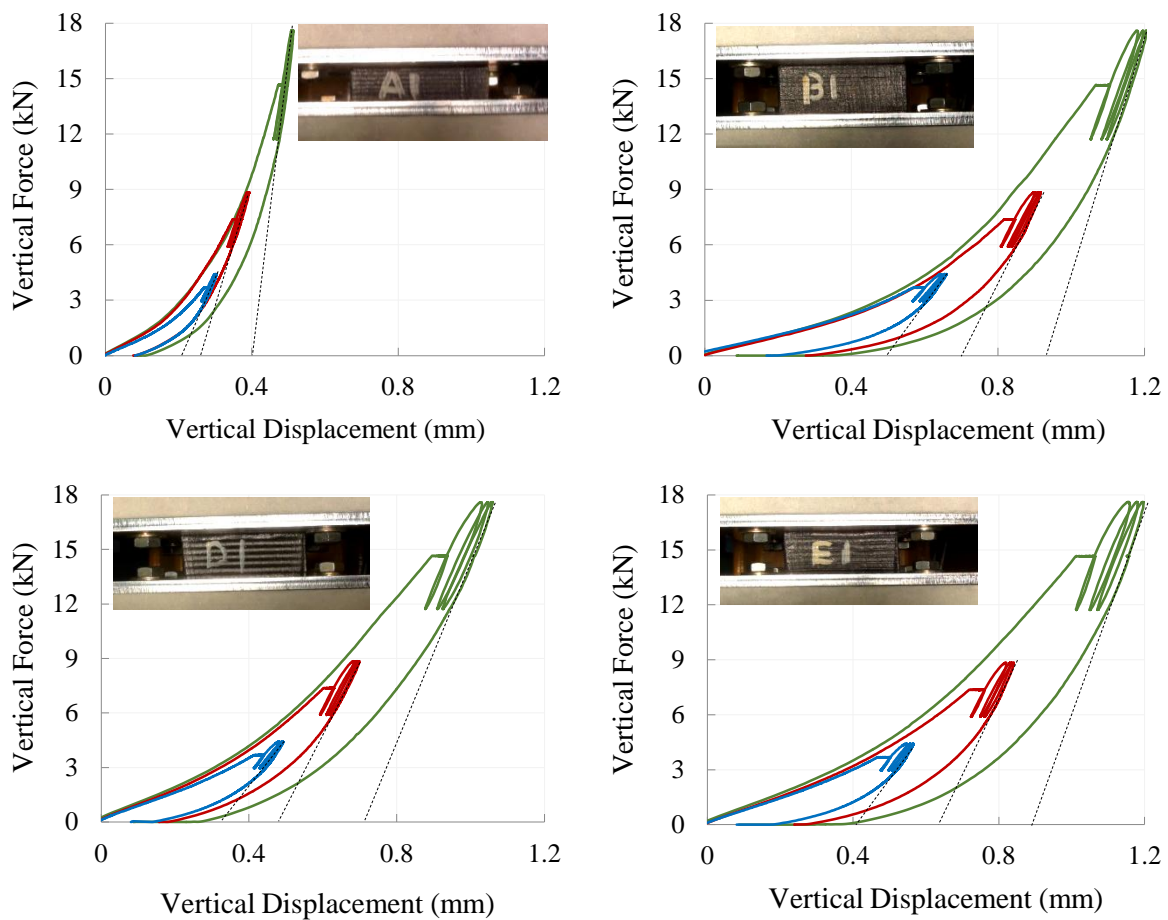
Figure 4.8. Vertical force-deflection curves under 0.75 MPa, 1.5 MPa, and 3.0 MPa pressures; (a) C-FREI-A1; (b) C-FREI-B1; (c) C-FREI-D1; (d) C-FREI-E1

Results show that for all C-FREIs, the vertical stiffness increases with increasing the design pressure. This fact is due to, first, the stiffening of rubber layers and second, the

presence of bi-directional carbon fibres. Elastomeric layers bulge under vertical pressure and as a result lateral in-plane forces are applied to the fibre-reinforced layers in both directions. When the vertical pressure increases, the transverse shear forces between rubber and reinforcement layers cause fibres to be stretched more tightly. Therefore, the vertical stiffness of fibre-reinforced layers enhances due to the stress stiffening. The nonlinear response of C-FREIs in monotonic loading and unloading parts is mainly because of the nonlinear behaviour of elastomer under compression. When the pressure reaches the target value, P_D, before starting the cyclic variations, a creep happens in the C-FREI. In fact, the vertical deflection continues to increase under a constant vertical load (i.e. the design pressure). Rubber bearings undergo a plastic deformation in the vertical direction as the pressure is released in the unloading phase. This behaviour can be seen in Figure 4.8.

Table 4.2. Performance characteristics of C-FREIs in the vertical direction

C-FREI	t_r (mm)	F_V (kN)	P_D (MPa)	K_V (kN/mm)	E_C (MPa)	Δ_V (mm)
A1	12	3.7	0.75	52.9	129.4	0.28
		7.4	1.5	61.7	151.0	0.37
		14.7	3.0	147.0	360.0	0.50
B1	18	3.7	0.75	24.7	90.6	0.63
		7.4	1.5	38.9	143.1	0.89
		14.7	3.0	56.5	207.7	1.17
D1	21	3.7	0.75	28.5	122.0	0.47
		7.4	1.5	41.1	176.2	0.67
		14.7	3.0	47.4	203.2	1.01
E1	21	3.7	0.75	28.5	122.0	0.55
		7.4	1.5	38.9	166.9	0.81
		14.7	3.0	54.4	233.3	1.15

The maximum amount of the vertical stiffness, at 3.0 MPa vertical pressure, is 147 kN/mm for A1 which has the minimum total thickness of rubber layers (12 mm) among four rubber bearings (see Table 4.2). When the total thickness of rubber layer increases, the flexibility of C-FREI in the vertical direction increases and accordingly, the vertical stiffness decreases. Although C-FREIs D1 and E1 have the same total thickness of rubber layers, the effective vertical stiffness of E1 is higher than that of D1 since E1 is made of thicker carbon fibre-reinforced sheets ($t_f = 0.75$ mm). Therefore, increasing the thickness of reinforcement layers causes an increase in the vertical stiffness of C-FREIs against the vertical compressive loads. Variation of compressive modulus can be described similarly. E1 has higher total

thickness of elastomeric layers and compressive modulus compared to B1. This fact can be interpreted by considering Equation (4.1). Both C-FREIs have identical cross-sectional areas while, E1 has a greater t_r, which causes E_V to increase. The vertical deflection goes up with increasing both the vertical load and the thickness of rubber layers. The maximum displacement reaches around 1.2 mm for B1 and E1 under a vertical pressure of 3.0 MPa.

4.4.3 Lateral Cyclic Test

4.4.3.1 Test Procedure

Cyclic test is performed under vertical load control and horizontal displacement control by applying a vertical pressure and lateral cyclic displacements simultaneously. The horizontal stiffness and the equivalent viscous damping are two performance specifications of rubber bearing evaluated through this test. The horizontal stiffness determines the flexibility of base isolator in the lateral direction. The equivalent viscous damping represents the capability of the device in dissipating the earthquake's energy transmitted to the elastomeric isolator.

While the C-FREI is under a constant vertical pressure of 3.0 MPa, the cyclic horizontal displacements are applied. At each amplitude of horizontal deflection including 25% t_r, 50% t_r, and 100% t_r, three fully reversed sinusoidal cycles are applied at constant horizontal rate of $V_H = 20$ mm/s. Variation of vertical pressure and cyclic horizontal displacement versus time are demonstrated in Figure 4.9a and Figure **4.9**b, respectively.
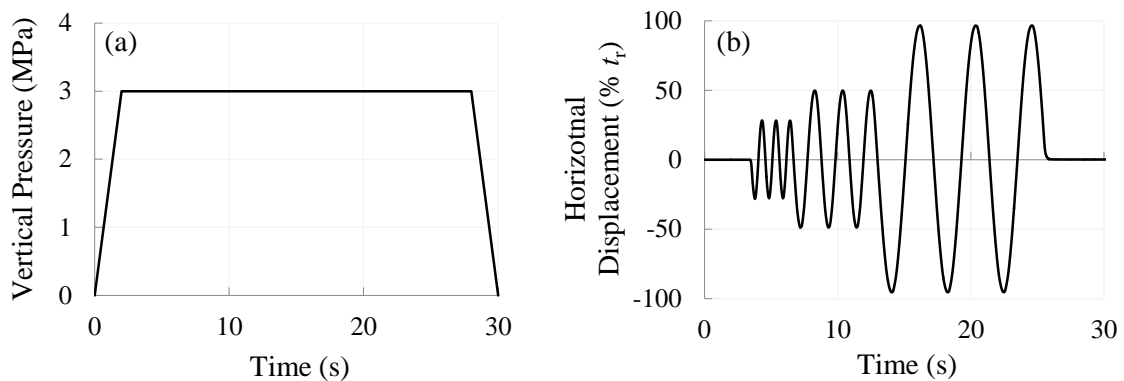
Figure 4.9. Input load in the cyclic tests; (a) vertical pressure, (b) cyclic displacements at shear strains of 25%, 50%, and 100%

Knowing that the effective horizontal stiffness of C-FREIs, $K_{H\ eff}$, is a function of shear strain and is calculated from Equation (3.10), the effective shear modulus, G_{eff}, at each shear strain amplitude (γ), is computed according to Equations (4.2) (Kelly, 1997).

$$G_{eff}(\gamma) = \frac{K_{H_{eff}}(\gamma)t_r}{A} \tag{4.2}$$

A is the cross-sectional area of the elastomeric layer which is in contact with the fibre-reinforced layer. The equivalent viscous damping of rubber bearing, β, is defined as a ratio of the dissipated energy to the elastic energy restored in the C-FREI (Naeim and Kelly, 1999).

$$\beta = \frac{1}{4\pi}\frac{U_d}{U_e} \tag{4.3}$$

in which U_d is the energy dissipated per cycle and equals to the area inside the lateral force-deflection hysteresis curve in each cycle and U_e is the energy restored in the rubber bearing measured according to Equation (4.4).

$$U_e = \frac{1}{2}K_{H_{eff}}\Delta_{avg}^2 \tag{4.4}$$

where $\Delta_{avg} = (\Delta_{max} + |\Delta_{min}|)/2$.

In order to show the whole cyclic test for each specimen, four stages are selected as shown in Figure 4.10. At the first stage, the rubber bearing is subjected to a constant vertical pressure. Then, the maximum lateral displacement during the cyclic sinusoidal deflections is depicted at stages two, three, and four by increasing the shear strain amplitude from 25% t_r to 100% t_r while the vertical pressure remains constant.
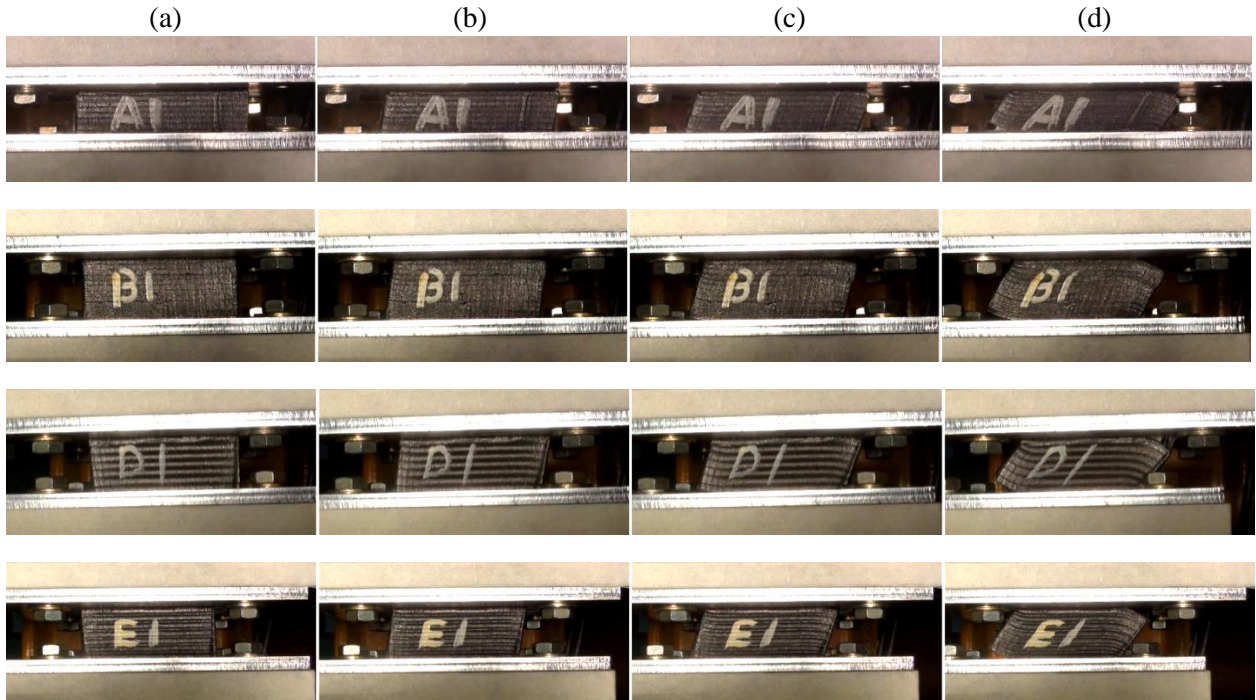
Figure 4.10. C-FREIs under cyclic tests at different shear strains; (a) applying constant pressure, (b) shear strain of 25%, (c) shear strain of 50%, (d) shear strain of 100%

4.4.3.2 Horizontal Characteristics

The operational characteristics of C-FREIs are obtained from the lateral force-deflection hysteresis curves plotted at different amplitudes. Figure 4.11 shows the hysteretic shear behaviours of four C-FREIs. Table 4.3 represents the effective horizontal stiffness, the effective shear modulus, the dissipated energy, and the equivalent viscous damping of C-FREIs at three shear strains. The energy dissipated by C-FREIs is tabulated for one cycle at each shear strain amplitude, U_d.
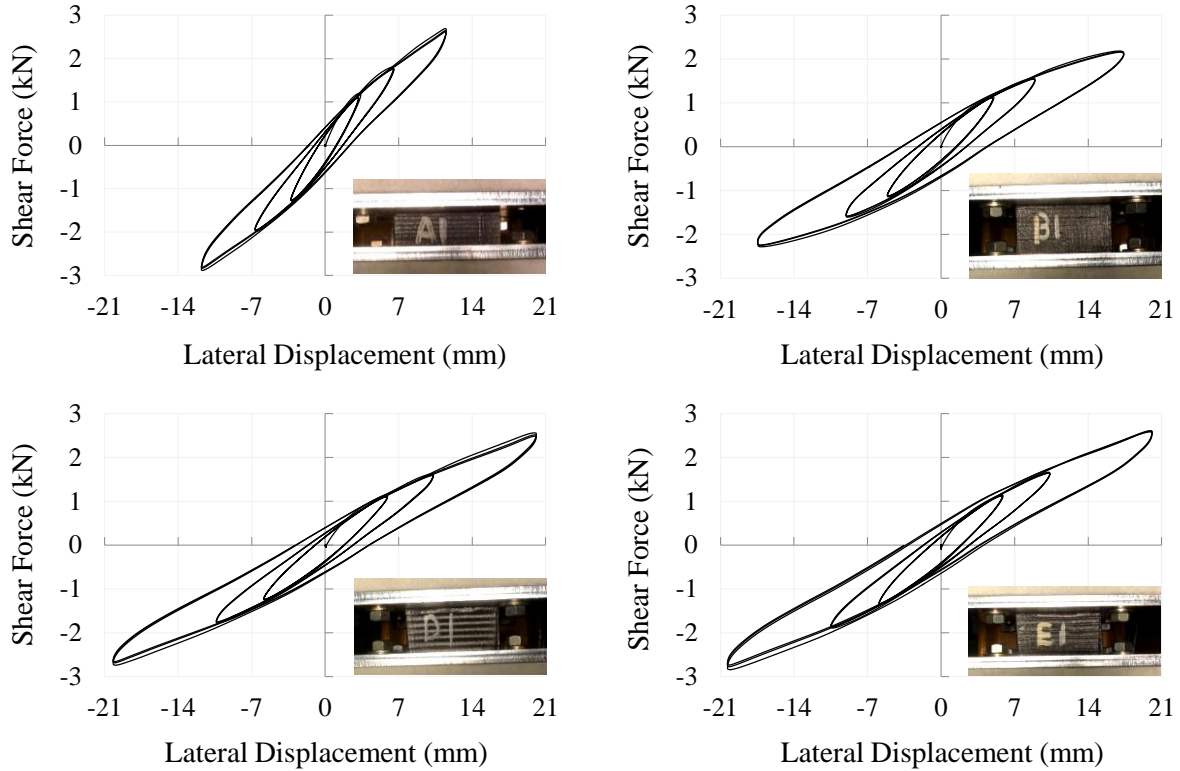
Figure 4.11. Shear hysteretic response of C-FREIs at 25%t_r, 50%t_r, and 100%t_r

Table 4.3. Horizontal operational characteristics of C-FREIs at three shear strain amplitudes

C-FREI	γ (%)	K_H (kN/mm)	G_{eff} (MPa)	U_d (J)	U_e (J)	β (%)
	25	0.375	0.918	3.1	2.1	11.8
A1	50	0.287	0.702	8.2	6.3	10.4
	100	0.239	0.586	18.3	16.3	9.0
	25	0.226	0.829	4.8	2.9	13.1
B1	50	0.177	0.649	11.3	7.1	12.6
	100	0.128	0.471	31.1	19.5	12.7
	25	0.203	0.869	4.9	3.5	11.1
D1	50	0.165	0.706	11.5	8.8	10.3
	100	0.132	0.564	30.9	26.7	9.2
	25	0.212	0.911	5.4	3.7	11.6
E1	50	0.170	0.731	12.3	9.3	10.6
	100	0.135	0.578	33.1	27.6	9.6

4.4.3.2.1 Effective Horizontal Stiffness

By increasing the amplitude of lateral displacement, a nonlinear behaviour is observed in the hysteresis curves (Figure 4.11). The effective horizontal stiffness has a decreasing rate when the shear strain increases. This is mainly due to a nonlinear softening

behaviour in elastomer as a result of the rollover deformation which is demonstrated in Figure 4.12 for C-FREI-E1, as an example. At high shear strains ($\gamma = 100\%$), the top and bottom rubber layers are detached from the steel plates. Unlike the steel shims used in the conventional elastomeric isolators, fibre-reinforced layers almost have no flexural rigidity and as a result, they can be deformed under large lateral displacements. This deflection which can be seen in Figure 4.12, for all C-FREIs, applies a peel-off force due to the tensile stress at the top and bottom rubber layers near the edges generated from coupling moment at large shear strains. Under such a condition, the stress between the elastomeric layer and the supporting steel plate exceeds the bonding strength of the glue used for attaching the rubber and steel and consequently, detachment starts to increase from the edges. Results show that the local delamination due to the rollover deformation mainly affects the effective horizontal stiffness of the base isolators.
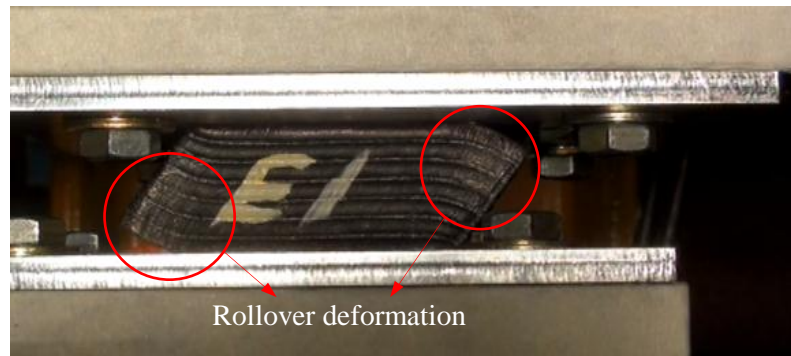
Figure 4.12. Deformation of C-FREI-E1 under the maximum applied shear strain amplitude (100%) and a vertical pressure of 3 MPa

The reduction in the effective horizontal stiffness with increasing the shear amplitude is mostly due to the decrease in the shear modulus of elastomer and the rollover deformation. Figure 4.13 shows the reduction in the effective shear modulus of natural rubber as a function of shear strain.
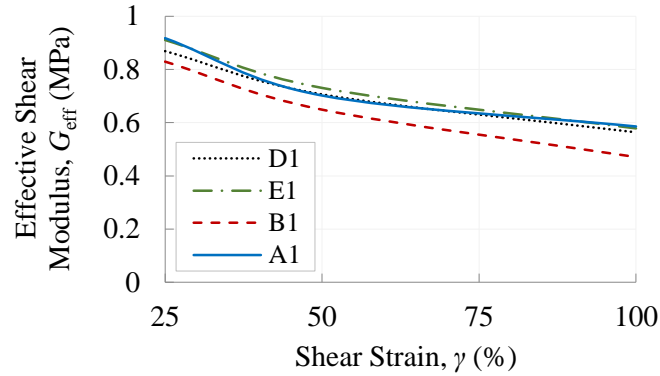
Figure 4.13. Effective shear modulus decay versus shear strain for four C-FREIs

Rubber bearings D1 and E1 have the lowest effective horizontal stiffness since they have the maximum amount of total thickness of rubber layers (t_r) among four C-FREIs. It shows that increasing the thickness of elastomers increases the lateral flexibility of the device. Increasing the lateral flexibility of the elastomeric isolator leads to an increase in the fundamental periods of the isolation system and accordingly improves its performance in regulating the behaviour of the structure by shifting its natural period. On the other hand, the lateral flexibility of the base isolator should be greater than a minimum value determined through a design process; otherwise, the device undergoes a permanent residual deformation and cannot work efficiently under cyclic loads. In such a situation, by determining the lower and upper limits of the horizontal stiffness in the design procedure, the lateral flexibility (inverse of the horizontal stiffness) can be maximized by increasing the total thickness of rubber layers.

4.4.3.2.2 Energy Dissipation Capacity and Damping Ratio

Although the dissipated energy in all C-FREIs increases with increasing the amplitude of the lateral displacement, the damping ratio, β, decreases. This fact can be clarified according to the definition of the equivalent viscous damping which is proportional to the ratio of the dissipated energy to the restored energy (Equation (4.3)). Since the increase rate of the energy restored in the C-FREIs is greater than that of the dissipated energy, the damping ratio decreases as listed in Table 4.3. Pinched hysteresis loops are another reason of decreasing the damping ratio when the lateral displacement increases. Pinching refers to a behaviour in which hysteresis loops get thinner in the middle due to a sudden reduction in the stiffness caused by the delamination. This behaviour can be clearly observed in the hysteresis

curves in Figure 4.11. When the lateral displacement increases to 100% of t_r ($\gamma = 100\%$), the central part of the loops get thinner compared to the loops with a shear strain of 25%.

Increasing the thickness of rubber layer increases the energies which are dissipated and restored by the base isolators. If the amount of energies for D1 and E1, having same t_r, are compared to each other, it will be understood that E1 has a higher capability in dissipating and restoring energy at all shear strain levels. The reason is that, E1 has a higher thickness of fibre-reinforced layer (0.75 mm) compared to D1 (0.5 mm). It can be interpreted that, carbon fibre-reinforced layers with almost no flexural rigidity are the second source of energy absorption and dissipation due to their frictional damping as a result of interfacial slip between carbon fibres (Kelly, 2002).

Here, an important finding is that the damping ratios of C-FREIs are larger than the damping of the natural rubber itself. This is due to the type of the reinforcement and the interaction between the reinforced plates and rubber layers. In fact, the additional amount of equivalent viscous damping is attributed to the carbon fibre-reinforced polymer composite layers. The bi-directional carbon fibre fabrics are bonded to the elastomeric layers using the rubber cement (glue) which is considered as the matrix for the CFRP layers. After curing, the fibre-reinforced layer still has a specific amount of flexibility under shear forces. Therefore, in addition to the frictional damping due to the slip between fibres, the matrix (the cured glue) absorbs and dissipates a certain amount of energy and as a result, the reinforced layers can increase the damping ratio of the elastomeric isolator compared to a case in which rigid steel shims are used.

4.5 Experimental Parametric Study

In this section, two operational characteristics of C-FREIs in the lateral direction, (the effective horizontal stiffness and the equivalent viscous damping), are evaluated through sensitivity analyses. The vertical pressure, the lateral cyclic rate, the number of rubber layers, and the thickness of fibre-reinforced layers are factors considered in the parametric study.

4.5.1 Vertical Pressure

4.5.1.1 Pressure Sensitivity Test Procedure

The objective of the pressure sensitivity tests is to evaluate the effect of vertical pressure on the effective horizontal stiffness and the equivalent viscous damping of the base isolator. The horizontal stiffness is a measure of lateral flexibility and the equivalent viscous damping represents the capability of the device in dissipating the earthquake's energy. In order to explore the effect of pressure on the efficiency of the device, different cyclic tests are performed by changing the vertical compressive load (1 MPa, 2 MPa, and 3 MPa) while other parameters are kept constant. Cyclic tests are performed under vertical load control and horizontal displacement control by applying vertical pressure and lateral cyclic displacements, simultaneously.

In each test, while the C-FREI is subjected to a constant vertical pressure, P, the cyclic horizontal displacements are applied. At each amplitude of horizontal deflection including 25% t_r, 50% t_r, and 100% t_r (t_r is the total thickness of rubber layers), three fully reversed sinusoidal cycles are applied at constant horizontal rate of $V_H = 20$ mm/s. Variations of vertical pressure and cyclic horizontal displacements versus time are demonstrated in Figure 4.14a and b, respectively. It should be mentioned that at shear strain levels higher than 100%, unrecoverable deformations occured.Consequently, the shear strain amplitude limited to 100% in all tests.
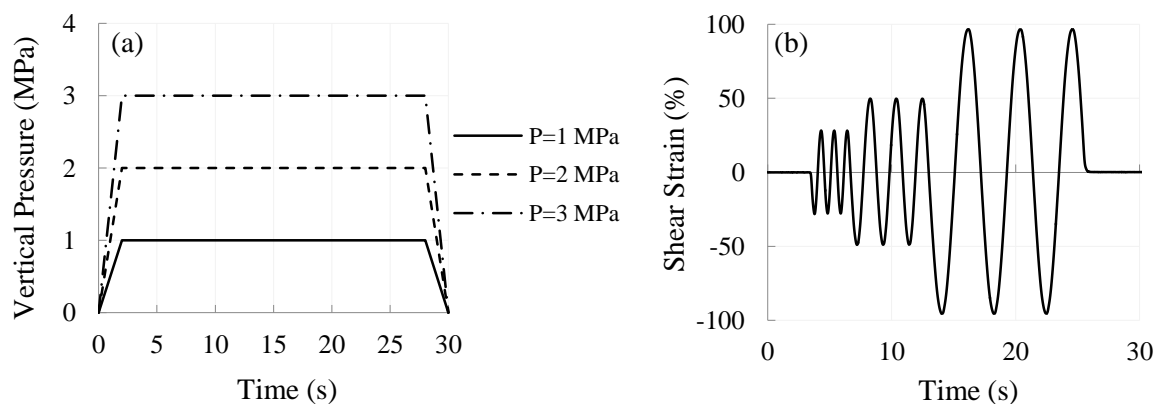
Figure 4.14. Input loads in the cyclic tests; (a) variation of vertical pressure over time, (b) variation of shear strain over time (25%, 50%, and 100%)

For each C-FREI, three lateral force-deflection hysteresis curves are presented for three vertical pressures. Figure 4.15 shows the shear behaviour of the rubber bearings at different shear strains and pressure levels.
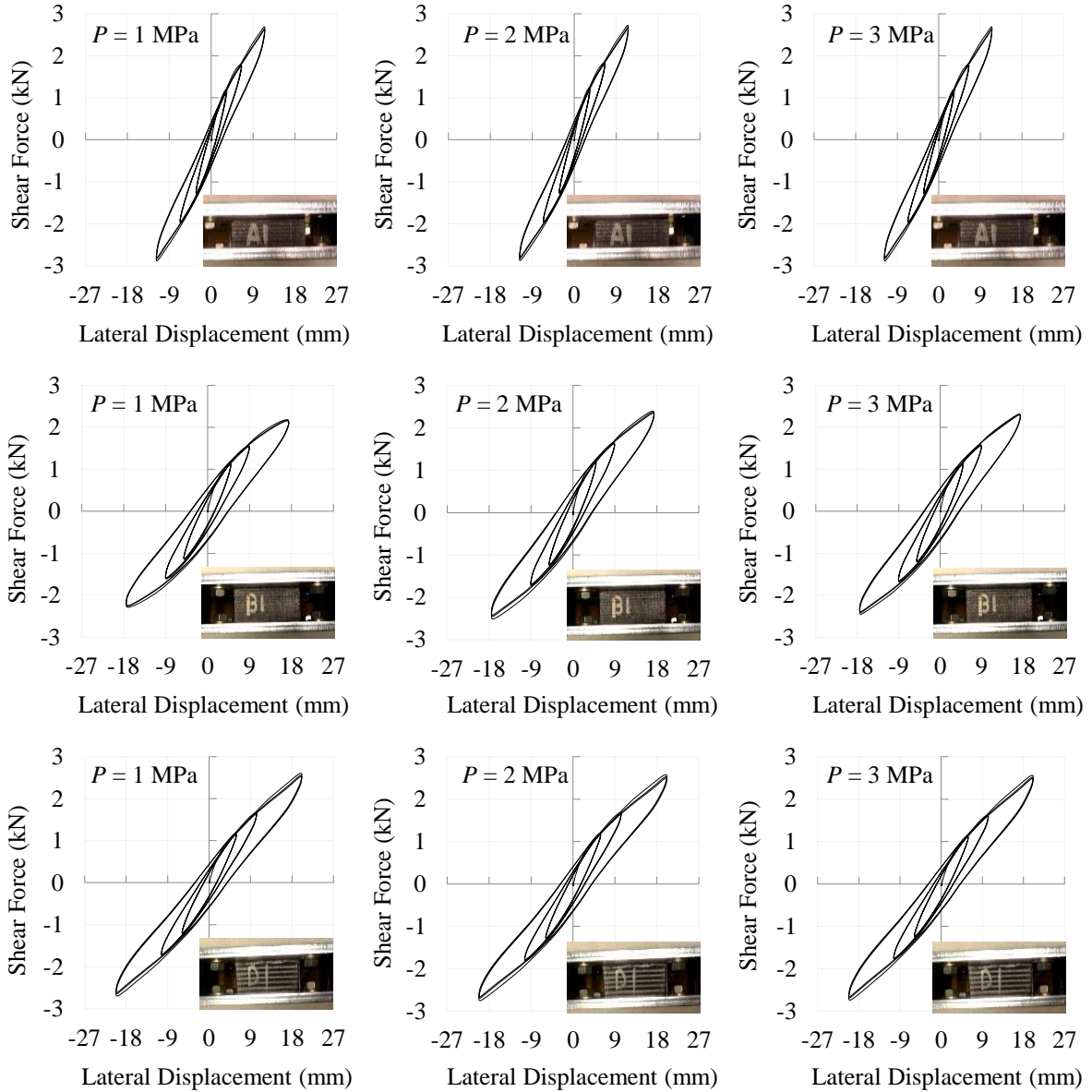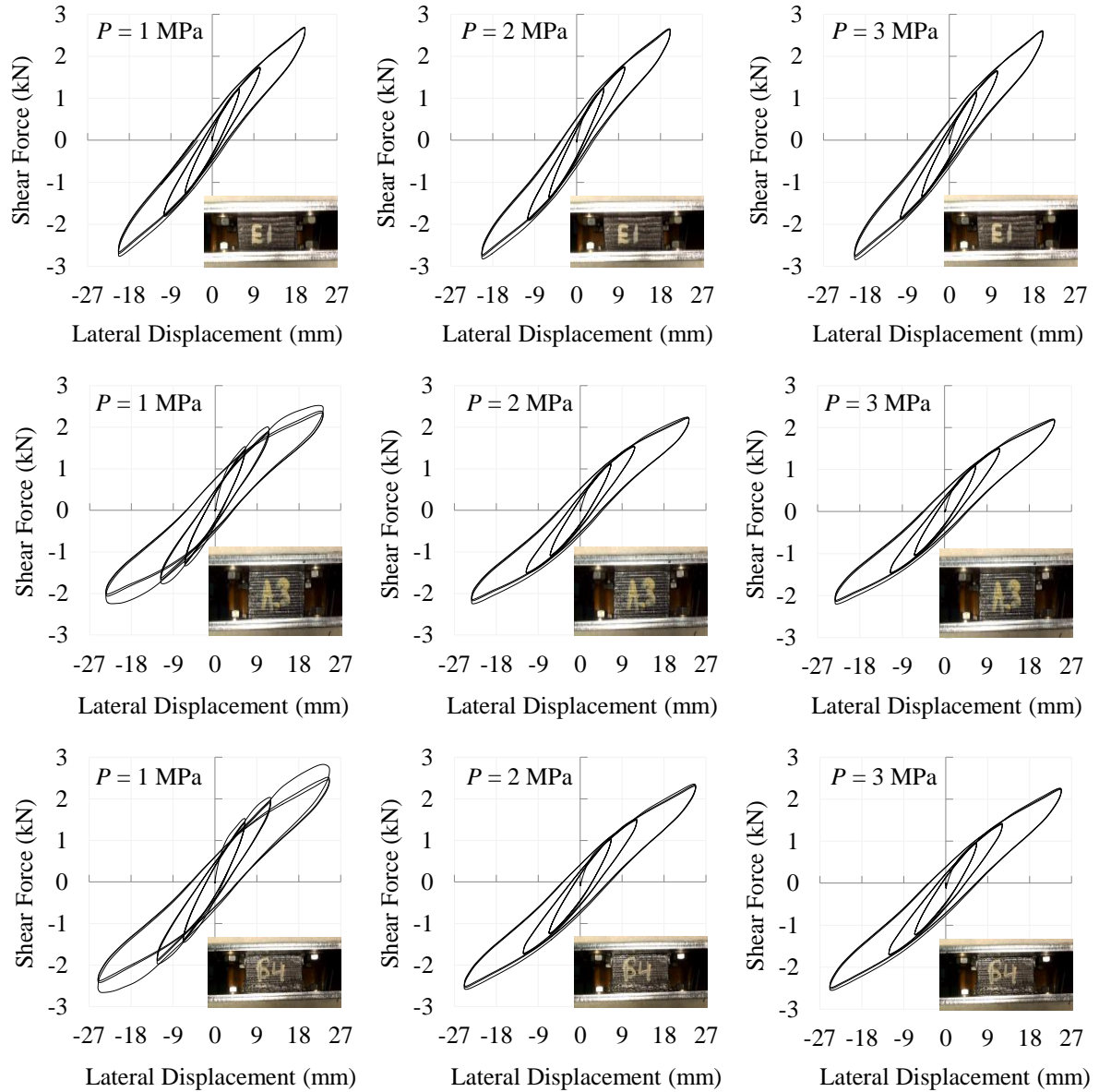
Figure 4.15. Lateral force-displacement hysteresis curves of manufactured C-FREIs under different vertical pressures ($P = 1$ MPa, 2 MPa, and 3 MPa) and shear strains ($\gamma = 25\%$, 50%, and 100%)

By comparing the hysteretic responses, it can be observed that C-FREI-A1, with the lowest thickness of rubber layers, has the maximum amount of effective horizontal stiffness. This behaviour shows that the elastomeric layers mainly contribute to the lateral flexibility of the device. On the other hand, the area inside the hysteresis loops, which represents the energy dissipated by the device, increases for C-FREIs with a higher total thickness of rubber layers (t_r) such as A3 and B4.

When C-FREIs A3 and B4 are subjected to a vertical pressure of 1 MPa, the first cycle of the lateral loading at 50% and 100% shear strain levels is different from the second and third cycles. This fact is due to scragging and also the delamination which occurs in the exterior layers of the laminated pad after the first cycle. It should be noted that no scragging was observed for other C-FREIs. As a result, the slope of the lateral force-deflection curve decreases. Since the total number of elastomeric layers in A3 and B4 is higher than that of four other C-FREIs (see Table 4.1), the possibility of debonding of either the rubber layer from the steel supporting plate or the rubber layer from the reinforcement noticeably increases. Such a behaviour is not observed when the pressure increases to 2 MPa and 3 MPa because the vertical load postpones the delamination (debonding).

The effective horizontal stiffness and the equivalent viscous damping are measured using Equations (3.10) and (4.3), respectively. The average of the three hysteresis loops, at each displacement, was calculated and the results are listed in Table 4.4.

Table 4.4. Effective horizontal stiffness and equivalent viscous damping of C-FREIs at different shear strain amplitudes and vertical pressures

C-FREI	P (MPa) / γ (%)	K_H (kN/mm)			β (%)		
		1	2	3	1	2	3
A1	25	0.375	0.380	0.375	11.7	11.9	11.7
	50	0.287	0.289	0.287	10.3	10.4	10.3
	100	0.239	0.240	0.239	9.1	9.2	9.1
B1	25	0.226	0.244	0.233	13.0	13.0	13.2
	50	0.177	0.188	0.181	12.6	12.3	12.5
	100	0.128	0.141	0.137	12.7	11.9	11.6
D1	25	0.203	0.211	0.203	11.1	11.0	11.1
	50	0.165	0.169	0.165	10.3	10.2	10.3
	100	0.132	0.132	0.132	9.3	9.3	8.9
E1	25	0.212	0.223	0.212	11.6	11.4	11.6
	50	0.170	0.176	0.170	10.5	10.3	10.5
	100	0.135	0.136	0.135	9.7	9.7	9.8
A3	25	0.209	0.171	0.165	12.5	12.6	12.6
	50	0.153	0.132	0.128	11.2	11.6	11.7
	100	0.095	0.096	0.094	13.2	11.2	11.2
B4	25	0.213	0.173	0.166	12.8	12.9	13.1
	50	0.158	0.133	0.129	11.4	11.8	12.0
	100	0.099	0.099	0.097	12.3	10.7	10.9

4.5.1.2 Effective Horizontal Stiffness

In this part, the effect of vertical pressure on the lateral flexibility of C-FREIs is investigated while rubber bearings are subjected to cyclic lateral displacements. At each shear strain (25%, 50%, and 100%), the effective horizontal stiffness of each C-FREI is calculated under three vertical pressures (1 MPa, 2 MPa, and 3 MPa).

Figure 4.16 shows that the vertical pressure has a negligible influence on the lateral flexibility of the C-FREIs regardless of the shear strain amplitude. At low lateral displacements ($\gamma = 25\%$), minor changes are observed in the horizontal stiffness with increasing the pressure. However, at 100% shear strain, the fluctuation of the effective horizontal stiffness almost vanishes. This characteristic demonstrates that the manufactured C-FREIs are almost insensitive to the vertical pressure. This insensitivity is due to material properties of elastomer (neoprene) used in the C-FREIs. Compared to the HDR, which has a highly nonlinear behaviour depending on the loading and environmental conditions, the neoprene used in this study has a low sensitivity to the vertical pressure. Hence, almost the same responses are observed for C-FREIs when the vertical pressure changes.
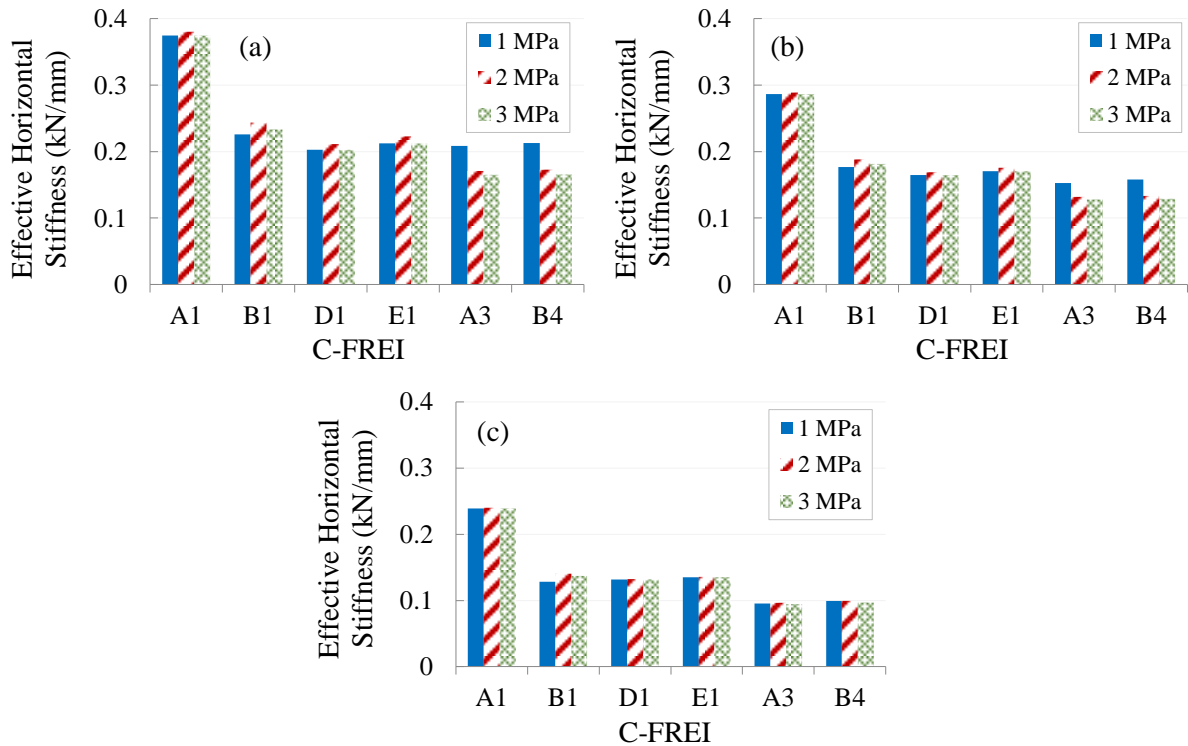
Figure 4.16. Effective horizontal stiffness of C-FREIs under different vertical pressures (1 MPa, 2 MPa, and 3 MPa) and shear strains of (a) 25%, (b) 50%, and (c) 100%

At 25% and 50% shear strains, the effective horizontal stiffnesses of A3 and B4 are reduced when the vertical pressure increases from 1 MPa to 2 MPa. The reason is that these two C-FREIs have higher lateral flexibility under low vertical pressure (1 MPa) due to their higher thickness of rubber layers compared to other bearings.

4.5.1.3 Equivalent Viscous Damping

The second considered specification is the equivalent viscous damping of rubber bearing. Here, results are presented in three bar charts; each plot corresponds to one shear strain amplitude where the vertical pressure increases from 1 MPa to 3 MPa (Figure 4.17).
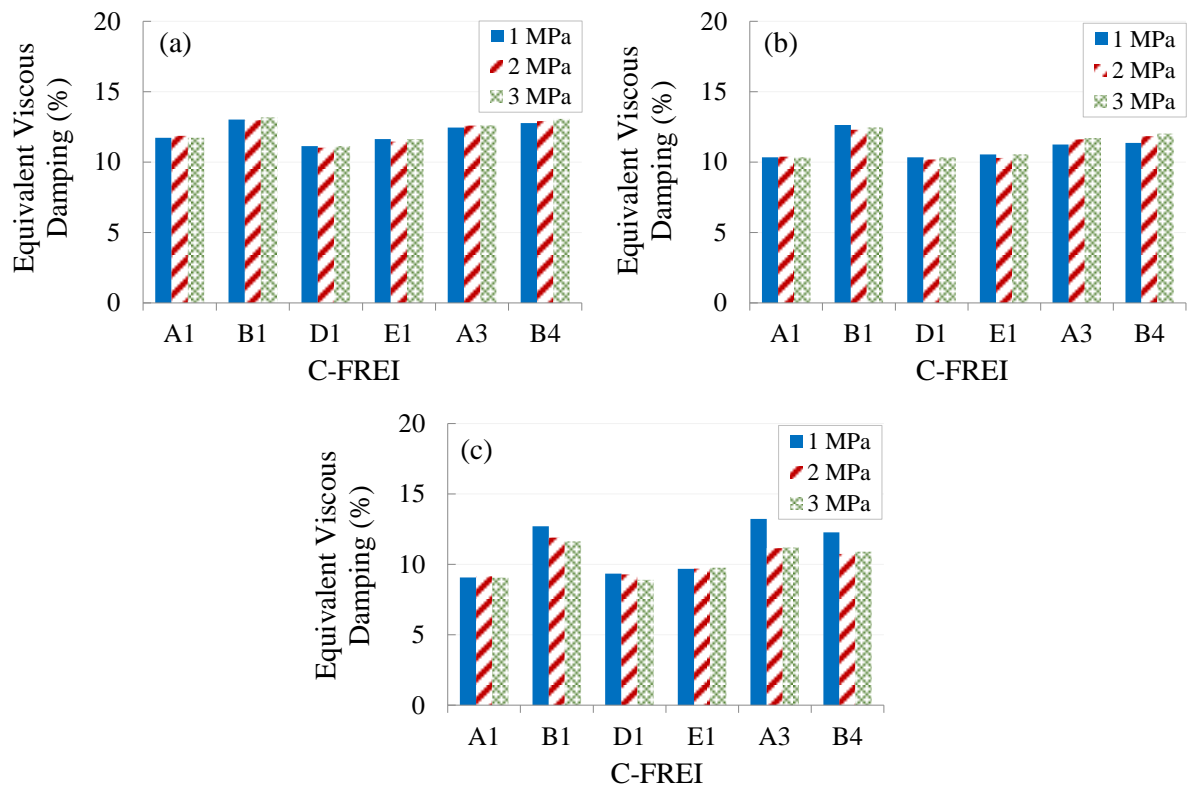
Figure 4.17. Equivalent viscous damping of C-FREIs under different vertical pressures (1 MPa, 2 MPa, and 3 MPa) and shear strains of (a) 25%, (b) 50%, and (c) 100%

By increasing the pressure, the equivalent viscous damping changes between 9.1% and 13.2% (see Table 4.4). With respect to the magnitude of the damping coefficients, the variation of this parameter is negligible. When the vertical pressure changes, at low shear strain levels (25% and 50%), the equivalent viscous damping remains almost constant (see Figure 4.17a and b). However, at 100% shear strain, the damping coefficient of B1, A3, and

B4 encounter a slight reduction when the vertical pressure increases from 1 MPa to 2 MPa. The reason is that these three C-FREIs have a higher capability in dissipating the energy under low vertical loads (1 MPa) due to their higher number of rubber layers compared to other bearings. As a result of using the commercial high quality neoprene, known as the primary source of energy dissipation, C-FREIs have a higher damping capacity compared to low-damping (unfilled) rubber bearings. However, compared to HDRBs, the C-FREIs have a lower capacity.

4.5.2   Lateral Cyclic Rate

Different earthquakes with different magnitudes and frequency contents hit the base-isolated structures. In such a situation, investigating the effect of lateral cyclic rate or frequency on the performance of the elastomeric bearings will be of great interest.

4.5.2.1   Rate Sensitivity Test Procedure

In the rate sensitivity test, the influence of the lateral cyclic rate on the performance of the C-FREIs is investigated. Cyclic tests are conducted by changing the rate of the cyclic horizontal displacements (20 mm/s, 30 mm/s, and 75 mm/s) while the pressure and the lateral displacement amplitude are kept constant. The procedure of performing the tests is the same as the horizontal cyclic tests. While the C-FREI is under a constant vertical pressure of 1.5 MPa, the cyclic horizontal displacements are applied. At a lateral amplitude of 50% t_r, three fully reversed sinusoidal cycles are applied. Variation of cyclic horizontal displacements versus time is depicted in Figure 4.18 for three different rates.
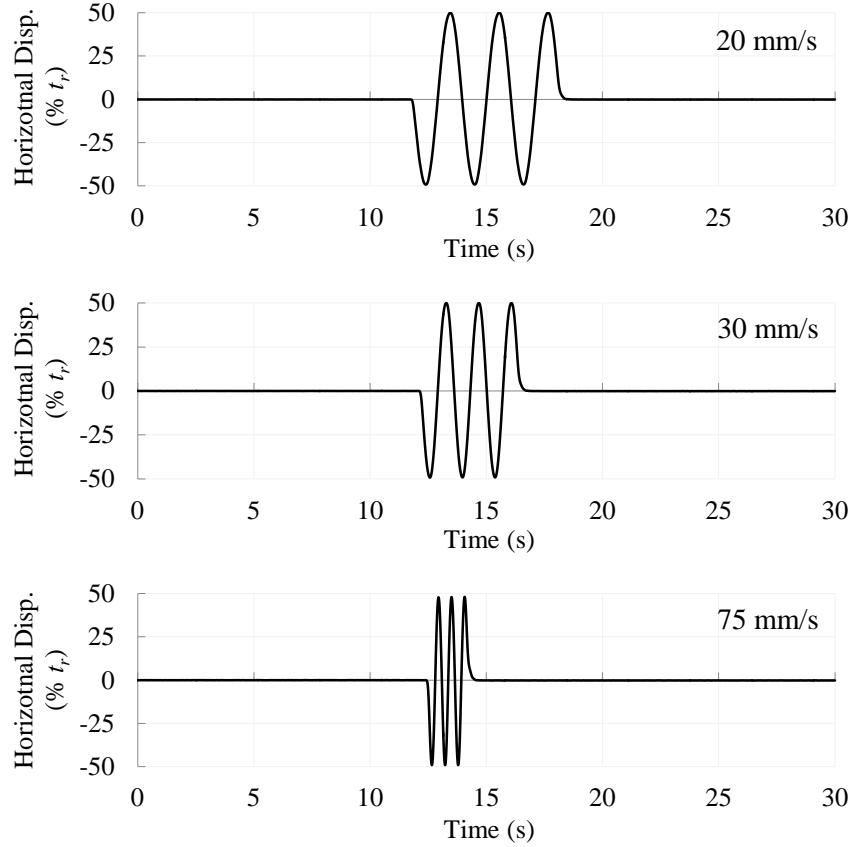
Figure 4.18. Lateral cyclic displacement (50% t_r) for three different cyclic rates

In a sinosoidal harmonic motion, the amplitude of the linear velocity, V, is related to the amplitude of the displacement using the angular frequency, ω, according to Equation (4.5). Since ω can be expressed in terms of cyclic frequency, f, ($\omega = 2\pi f$), and the amplitude of cyclic lateral displacement, A, is equal to the shear strain, γ, multiplied by the total thickness of rubber layers, t_r, ($A = \gamma t_r$), the lateral cyclic frequency, f_H, at 100% shear strain, can be calculated from the horizontal rate, V_H, as follows.

$$V = \omega A \tag{4.5}$$

$$f_H = \frac{V_H}{2\pi t_r} \tag{4.6}$$

Based on the test procedure defined for the rate sensitivity experiment, the hysteretic shear response at 50% shear strain are illustrated for six elastomeric isolators (Figure 4.19). For each C-FREI, three hysteresis curves are plotted in one figure in order to compare the behaviours of the laminated rubber bearing by changing the cyclic rate, V_H.
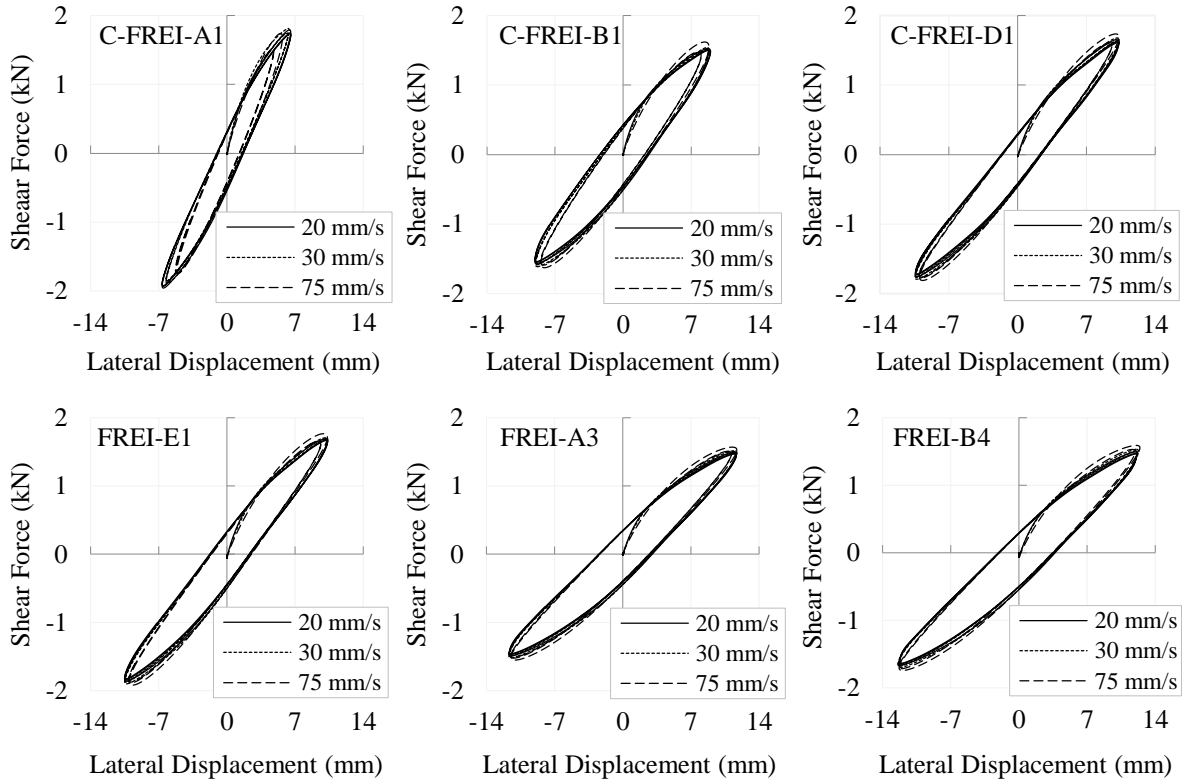
Figure 4.19. Lateral force-displacement hysteresis curves at different lateral rates

(20 mm/s, 30 mm/s, and 75 mm/s) and 50% shear strain

The effective horizontal stiffness and the equivalent viscous damping are calculated at different lateral cyclic rates, V_H, as listed in Table 4.5. It should be noted that the horizontal frequency, f_H, is computed according to Equation (4.6). By considering a constant shear strain (e.g. 100%) and a constant lateral cyclic rate, the horizontal frequency changes for different elastomeric bearings because C-FREIs have different total thicknesses of rubber layer (t_r).

Table 4.5. Effective horizontal stiffness and equivalent viscous damping of C-FREIs at different lateral cyclic rates (20 mm/s, 30 mm/s, and 75 mm/s)

C-FREI	V_H (mm/s)	f_H (Hz)	K_H (kN/mm)	β (%)
A1	20	0.27	0.284	10.5
	30	0.40	0.293	10.5
	75	1.00	0.317	9.9
B1	20	0.18	0.171	14.1
	30	0.27	0.176	13.5
	75	0.66	0.187	12.2
D1	20	0.15	0.165	10.3
	30	0.23	0.167	10.1
	75	0.57	0.174	9.6
E1	20	0.15	0.171	10.6
	30	0.23	0.173	10.5
	75	0.57	0.181	10.1
A3	20	0.13	0.128	12.2
	30	0.20	0.130	11.9
	75	0.50	0.134	11.5
B4	20	0.12	0.129	12.1
	30	0.19	0.131	11.8
	75	0.47	0.135	11.4

4.5.2.2 Effective Horizontal Stiffness

In order to determine whether or not the loading rate (V_H) affects the horizontal stiffness of C-FREIs, lateral cyclic displacements with three different rates including 20 mm/s, 30 mm/s, and 75 mm/s are applied to the rubber bearings. The following bar chart compares this parameter at different rates (Figure 4.20).
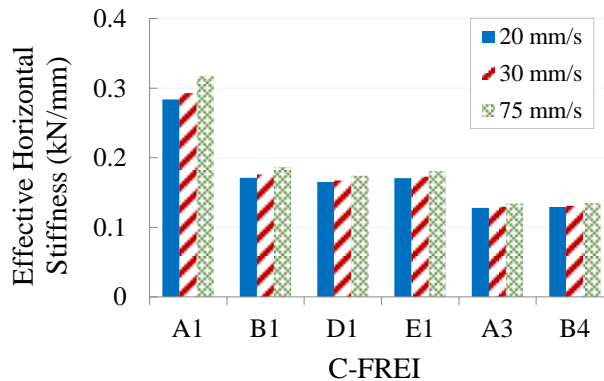
Figure 4.20. Effective horizontal stiffness of C-FREIs under different lateral cyclic rates (20 mm/s, 30 mm/s, and 75 mm/s) at 50% shear strain

For all C-FREIs, increasing the rate leads to an increase in the effective horizontal stiffness. However, the amount of change is negligible when the lateral rate is low (20 mm/s and 30 mm/s). By increasing the cyclic rate to 75 mm/s, a greater increase is observed in the lateral stiffness. In order to clarify this behaviour, it can be mentioned that, when the rate of the lateral cyclic loading increases, the elastomeric layers are stiffened and as a result, the rubber bearings show a lower flexibility in the horizontal direction.

4.5.2.3 Equivalent Viscous Damping

In contrast to the effective horizontal stiffness, the equivalent viscous damping decreases by increasing the lateral cyclic rate. This fact can be observed in Figure 4.21 that depicts the variation of the damping coefficient for each C-FREI by changing the loading rate. The flexibility of rubber layers is reduced at high lateral loading rates and as a result, the energy restored in the C-FREIs increases according to Equation (4.4). On the other hand, the capability of the device in dissipating the earthquake's energy degrades because the rubber layers are stiffened by increasing the lateral loading rate. Therefore, the equivalent viscous damping, which is proportional to the ratio of the dissipated energy to the restored energy (see Equation (4.3)), decreases by increasing the horizontal loading rate.
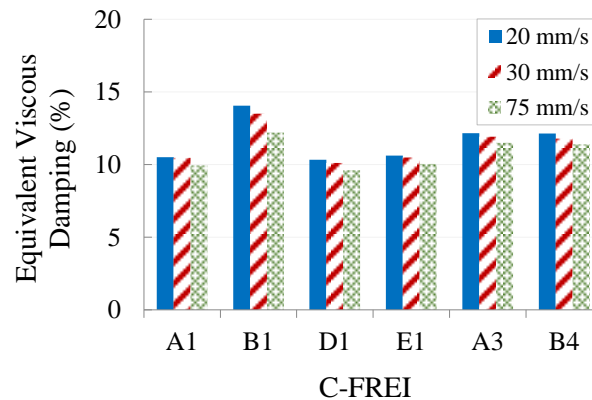
Figure 4.21. Equivalent viscous damping of C-FREIs under different lateral cyclic rates (20 mm/s, 30 mm/s, and 75 mm/s) at 50% shear strain

4.5.3 Number of Rubber Layers

In order to study the effect of the number of rubber layers, n_e, on the response of C-FREIs, this parameter changes while the thicknesses of elastomeric and fibre-reinforced layers remain constant. Consequently, C-FREIs A1, B1, and A3, with n_e equals to 8, 12, and

16, respectively, are selected among nine specimens (Table 4.1). Figure 4.22 illustrates the effect of the number of rubber layers on the effective horizontal stiffness and the equivalent viscous damping of C-FREIs. As expected, when the number of elastomeric layers increases, the lateral flexibility of the rubber bearings increases and the horizontal stiffness decreases. Figure 13a shows similar behaviours for three shear strain levels.
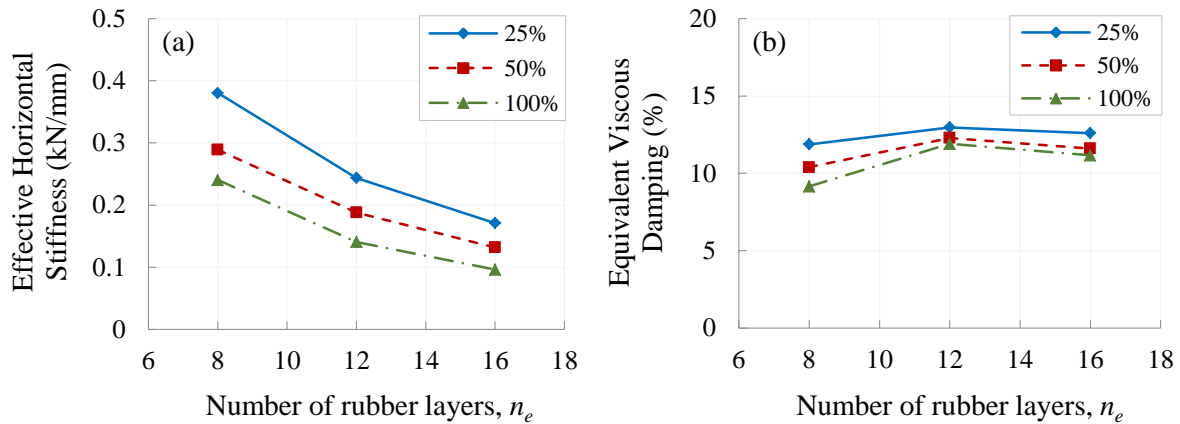
Figure 4.22. Effect of number of rubber layers on the performance of bearings
at different shear strain amplitudes (25%, 50%, and 100%);
(a) effective horizontal stiffness, (b) equivalent viscous damping.

By increasing the number of rubber layers, the performance of the C-FREIs improves in terms of the damping capacity (Figure 4.22b). This behaviour can be clearly observed when n_e changes from 8 to 12. However, by increasing ne from 12 to 16, the equivalent viscous damping is slightly reduced. The reason is that when n_e increases from 12 to 16, both the restored elastic energy and the dissipated energy are increased, but the restored energy changes more than the dissipated energy. Therefore, the ratio of the restored energy to the dissipated energy, which denotes the equivalent viscous damping, decreases.

4.5.4 Thickness of Fibre-reinforced Layers

Among geometrical properties considered in this study, only the thicknesses of reinforcement (t_f) of C-FREIs C1, D1, and E1 are different (see Table 4.1). However, specimen C-FREI-C1 experience unrecoverable damages during the failure tests. For that reason, C-FREIs D1 and E1 are selected in order to perform a sensitivity analysis on the thickness of the carbon fibre fabrics. In D1 and E1, two and three layers of bi-directional

carbon fibre fabrics are used, respectively. Since a single fibre fabric has a thickness of 0.25 mm, the thickness of reinforcements in D1 and E1 is 0.50 mm and 0.75 mm, respectively.

The effective horizontal stiffness of C-FREI-E1 is higher than that of the D1. This difference disappears by increasing the lateral deflection (see Figure 4.23a). Increasing the thickness of the reinforced layers decreases the lateral flexibility. The reason is that fibre-reinforced layers become stiffer when their thickness increases.
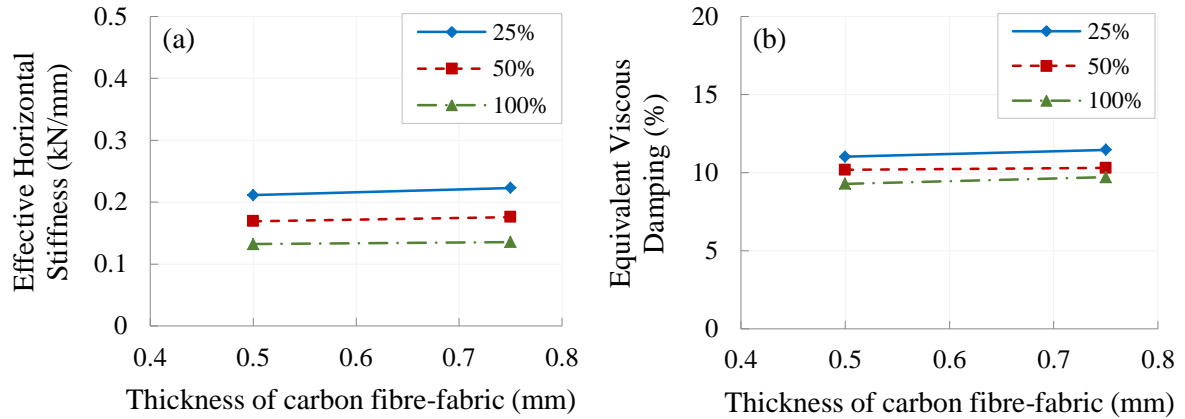
Figure 4.23. Effect of fibre-reinforced layers on the performance of bearings at different shear strain amplitudes (25%, 50%, and 100%); (a) effective horizontal stiffness, (b) equivalent viscous damping

Slight changes are observed in the equivalent viscous damping when the thickness of reinforcement increases. The minor increase in the damping coefficient is due to using a greater amount of adhesive for three layers of fibre fabrics ($t_f = 0.75$ mm) compared to two layers ($t_f = 0.50$ mm) (Figure 4.23b). In the case of $t_f = 0.75$ mm, three coats of adhesive are applied to three fibre fabric layers (one coat for each layer). The combination of bi-directional carbon fibre fabric and the adhesive, as the matrix, provides a flexible reinforcement. As a result, fibre-reinforced layers can slightly contribute to the energy dissipation and be considered as a minor source of energy dissipation.

In order to accurately investigate the condition of C-FREIs after conducting the shear and the compression tests, the elastomeric pad of C-FREI-B1 is detached from the supporting plates and then cut as shown in Figure 4.24. The laminated pad is checked for any internal delamination between rubber and fibre-reinforced layers. The specimen is cut using the water-jet in order to minimize or even eliminate any damage (e.g. debonding) that might

occur during the cutting phase. As indicated in Figure 4.24, an internal delamination is observed between the exterior rubber layer and the first reinforcement at the top. The reason is that the interfacial stress in the layers, close to the top and bottom of the pad, exceeds the bonding strength of the adhesive and detachment occurs. Another point is that no delamination between internal layers shows the acceptable performance of the fibre-reinforced pads under shear and compression.
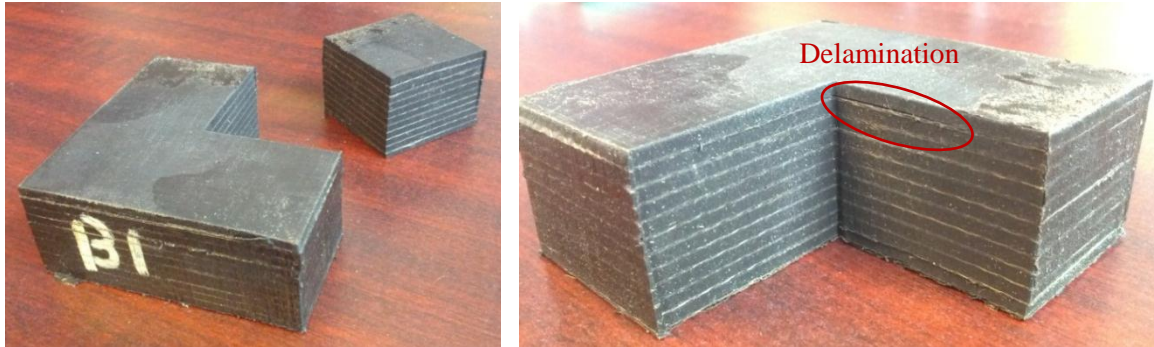
Figure 4.24. Carbon fibre-reinforced elastomeric pad (B1) after being tested

In order to check whether the manufactured C-FREIs possess advantages over steel-reinforced elastomeric isolators (SREIs), their performances (e.g. stiffness and damping ratio) are compared. Since the SREI was not fabricated through this study, the comparison is made between the manufactured C-FREIs and a SREI manufactured by Dehghani Ashkezari et al. (2008). It should be noted that the loading conditions (e.g. vertical pressure and shear strain magnitude) are the same for both cases. Based on the experimental results in this study, at 3 MPa vertical pressure and 100% shear strain magnitude, the equivalent viscous damping of the manufactured C-FREIs ranges between 8.9% and 13.2%, and the effective lateral stiffness varies from 0.094 kN/mm to 0.240 kN/mm. Under a 3 MPa vertical pressure, the maximum vertical stiffness of C-FREIs is 147 kN/mm (Hedayati Dezfuli and Alam, 2014a). For the SREI, the equivalent viscous damping, and the effective horizontal and vertical stiffnesses are 8.0%, 0.381 kN/mm, and 153 kN/mm, respectively. Results show that the C-FREIs have higher damping ratio and lateral flexibility, and a vertical stiffness which is comparable to that of the SREI. In terms of weight, the laminated pad of a SREI is 2.6 times heavier than that of a C-FREI.

4.6 Possibility of Using C-FREIs in Bonded Applications

The most well-known local failures in FREIs are delamination between reinforced and elastomeric layers and debonding between rubber layer and steel supporting plate. These modes of failure usually occur due to a very low flexural rigidity of reinforcement. If the bonding strength of adhesive used for attaching rubber layers to reinforcement and steel plates is lower than the interfacial stress generated between layers, it can be another reason of failure. For the C-FREIs manufactured through the cold-vulcanization process no delamination or debonding was observed during and after vertical tests when the compressive load increased from 0.75 MPa to 3 MPa. In order to increase the capacity of base isolators in carrying the vertical pressure, their vertical stiffness should be enhanced by either increasing the number or the thickness of fibre-reinforced layers through a design process.

In the cyclic displacement tests, a partial debonding between rubber layers and supporting plates were observed at shear strains greater than 50%. However, this local failure did not lead to a malfunction up to 100% shear strain and after performing tests, the rubber bearings did not undergo a global failure. It should be mentioned that since neither delamination nor debonding is acceptable, the manufacturing process should be modified in a way that no failure (partial or global) occurs. If the bonded C-FREIs are properly designed and manufactured through the proposed process, they can be used rather than steel-reinforced NRBs or HDRBs in buildings and bridges. In addition, this method of manufacturing can be extended to LRBs which are implemented in bridges, viaducts and buildings.

4.7 Numerical Validation and Verification

A limited number of specimens were manufactured in scaled size. Therefore, in order to perform a comprehensive study on the behaviour of full size C-FREIs, a numerical method, FEM, is used. In this regard, one of the manufactured C-FREIs (CFREI-E1) is chosen to be modelled and analyzed using FEM in ANSYS and then, the FE modelling is validated with experimental results in order to assess the correctness of numerical simulations. In the next step, the accuracy of FE model in predicting the behaviour of C-FREIs is evaluated. After verifying the FEM (Hedayati Dezfuli and Alam, 2014c), real-size C-FREIs are modelled and analyzed in ANSYS.

4.7.1 Finite Element Modelling

The first step in numerical simulations using FEM is to determine the type of elements by considering the number of nodes and degrees of freedom at each node. Defining the material properties is the most challenging part of the process since the behaviour of materials used in the device should be correctly captured in order to have an accurate simulation. In fact, the accuracy of FE results is highly dependent on the material properties of each component. In the next step, the model is created and then discretized into finite number of elements by meshing. Finally, boundary conditions (BCs) and loading conditions are applied to the model and the whole system is solved and analyzed.

Modelling, solving and analyzing the C-FREIs are performed in ANSYS (ANSYS Mechanical APDL, Release 14.0). Element SOLID185 with eight nodes and three degrees of freedom at each node is selected for both steel shims and rubber layers. Carbon fibre-reinforced (CFR) layers are modelled as shells, 4-noded rectangular element, SHELL181, with six degrees of freedom at each node is chosen. This element has a capability to be used in layered composite shells and capture the in-plane bending. SHELL181 is suitable for thin to moderately-thick shell structures used in nonlinear applications with large strain and/or rotation (ANSYS Documentation, Release 14.0). Among different types of nonlinear material models available in ANSYS, Ogden-Prony as a hyper-viscoelastic model is used to simulate the nonlinear behaviour of natural rubber under combined vertical pressure and cyclic lateral displacements. The material constants of the model used for rubber are listed in Table 4.6. Amin et al. (2006a and b) also conducted a research on the modelling of the response of natural and high damping rubbers based on experimental and numerical results. Steel shims are modelled as an isotropic material with the Young's modulus of 210 GPa and a Poisson's ratio of 0.3. The large-deflection effect is considered in full transient analyses in order to simulate the large deformation of rubber layers at large shear strain amplitudes. A perfect bonding is assumed between rubber and CFR layers.

Table 4.6. Material constants of Ogden-Prony model

Ogden		Prony	
μ_1	0.056	α_1	0.375
α_1	2.564	τ_1	0.062
μ_2	4041.7	α_2	0.061
α_2	0.00095	τ_2	65.82

Figure 4.25 demonstrates the top, side and 3D views of C-FREI-E1. The FE model with a mapped mesh in ANSYS is plotted in Figure 4.26. Mapped mesh is an organized type of meshing in which the size and the number of elements can be controlled. Purple and blue elements, respectively, illustrate the elastomeric layers and supporting steel plates. Since CFR layers are modelled as shell (area), their elements cannot be seen in the figure.
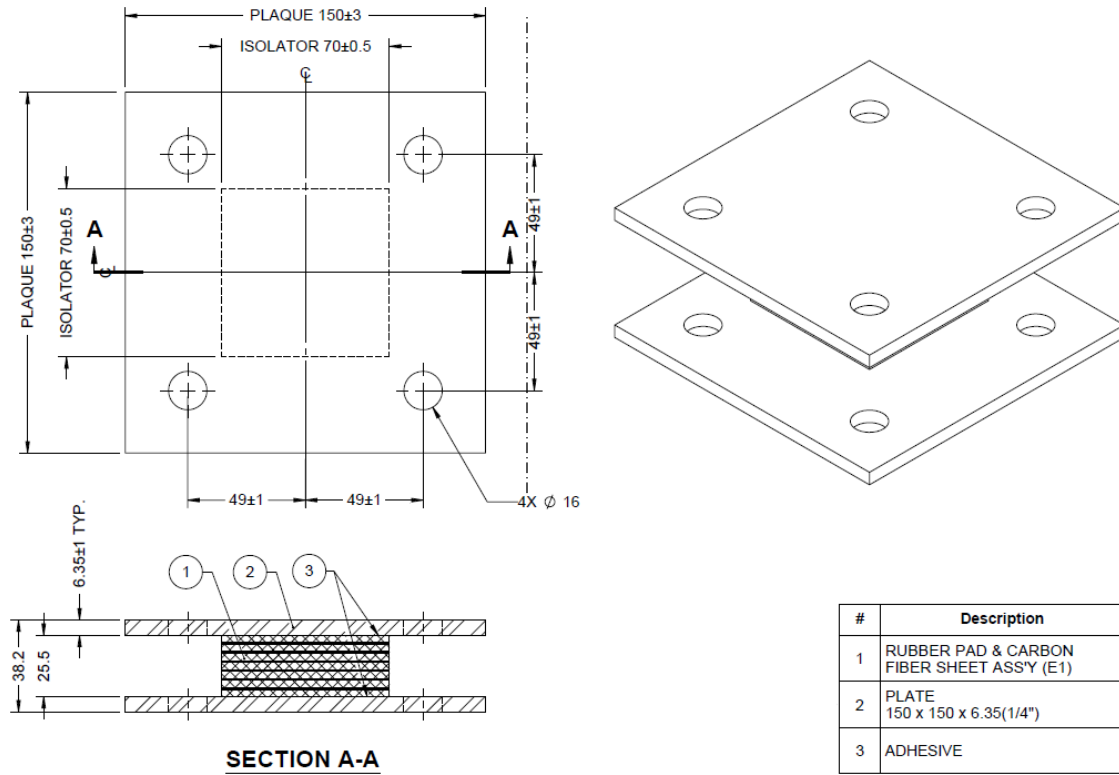
Figure 4.25. Carbon fibre-reinforced elastomeric isolator, C-FREI-E1
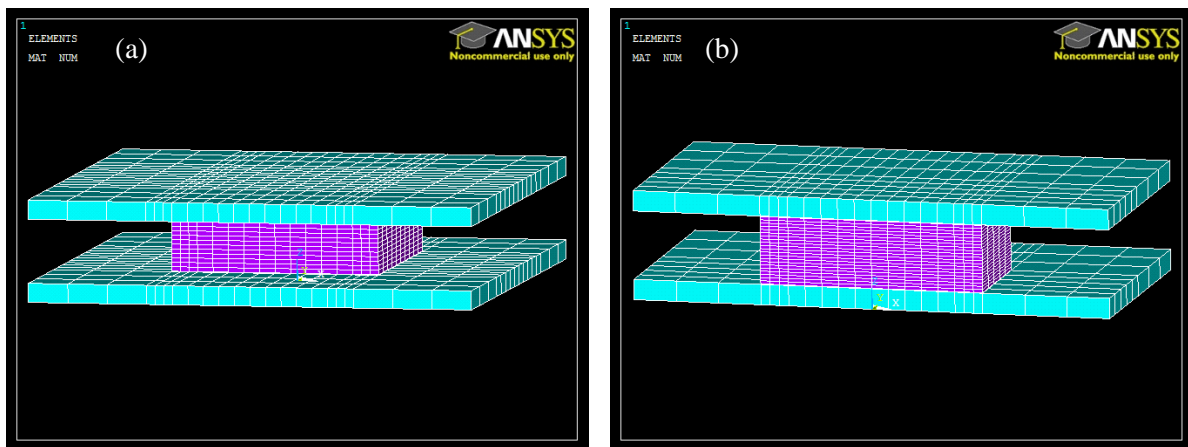
Figure 4.26. C-FREI-E1 with a mapped mesh in ANSYS (ANSYS Mechanical APDL, Release 14.0); (a) full model, (b) half model

93

Since C-FREIs have a plane of symmetry according to the geometry, BCs and loading conditions, half of the rubber bearing is modelled by applying a symmetry BC, on the xz plane at $y = 0$, in order to significantly reduce the processing time of FE analyses (Figure 4.26b).

4.7.2 Delamination

Based on the experimental tests, at 100% shear strain amplitude, a detachment occurs between the rubber layers (the first and the last) and the steel plates when the lateral displacement exceeds 50% of the maximum deflection. This delamination is due to (1) very small flexural rigidity in carbon fibre-reinforced layers, and (2) insufficient bonding strength in the glue used for attaching the laminated core to the steel plates. Unlike steel shims used in the SREIs, the CFR layers in the manufactured C-FREIs almost have no flexural rigidity and as a result, they can be deformed (rollover deformation) under large lateral displacements. Consequently, the first and the last rubber layers are subjected to a peel-off force near the edges. When the bearing is subjected to lateral displacement, tensile stresses are developed near the edges of the laminated pad due to the moment. Under such a condition, the stress between the elastomeric layer and the steel plate exceeds the bonding strength of the glue and detachment starts from the edges. This local delamination due to the rollover deformation mainly affects the lateral flexibility of the base isolators (Toopchi-Nezhad et al. 2008b).

In order to model the debonding behaviour in FE numerical simulation, two different approaches could be applied. In the first one, a layer of glue is modelled between rubber layer and steel plate at the top and bottom of the laminated core. The material properties of the glue, which behaves as a hyperelastic material, degrade over time (time steps) and as a result, the bonding strength of glue decreases. When the base isolator reaches a certain amount of lateral deflection, the glue cannot tolerate the peeling force introduced by the tension and the shear force generated between rubber layer and steel plate. Consequently, the rubber layer is detached from the steel supporting plate. The glue is modelled using a two-parameter Mooney-Rivlin material model with an initial shear modulus of 0.87 MPa and a constant Poisson's ratio of 0.499 (close to 0.5) representing the behaviour of a nearly incompressible material. The material constants of the glue are listed in Table 4.7 at different time steps. In the second method, instead of modelling the glue as a continuous material

94

(solid element) between the rubber layer and the steel plate, glue is modelled as beam elements. In this case, when the lateral displacement reaches a certain value, a number of beam elements are destroyed in the delamination region due to a high amount of shear force generated between the rubber layer and the steel plate. This technique is applied by using birth and death concepts in ANSYS. In fact, element birth and death options reactivate and deactivate selected elements, respectively. The number of killed elements increases when the horizontal deflection reaches its maximum value. As a result, there will be no element (material) to resist against the shear force and accordingly, debonding is started. Since modelling the glue with degradable material properties is closer to the reality and provides more accurate results, the first approach was selected in FE simulations.

Table 4.7. Hyperelastic material constants of the glue

Time Step	C_{10}	C_{01}
1	0.180	0.253
2	0.130	0.165
3	0.090	0.125
4	0.070	0.105
5	0.060	0.095
6	0.054	0.089
7	0.050	0.085
8	0.048	0.083
9	0.046	0.083
10	0.045	0.080
11	0.044	0.079

Figure 4.27 shows the C-FREI-E1 before and after detachment. When the lateral deflection reaches 100% of the total thickness of rubber layers ($\gamma = 100\%$), the glue between rubber layer and steel plate undergoes a very large deformation because of the increased amount of peel-off force.
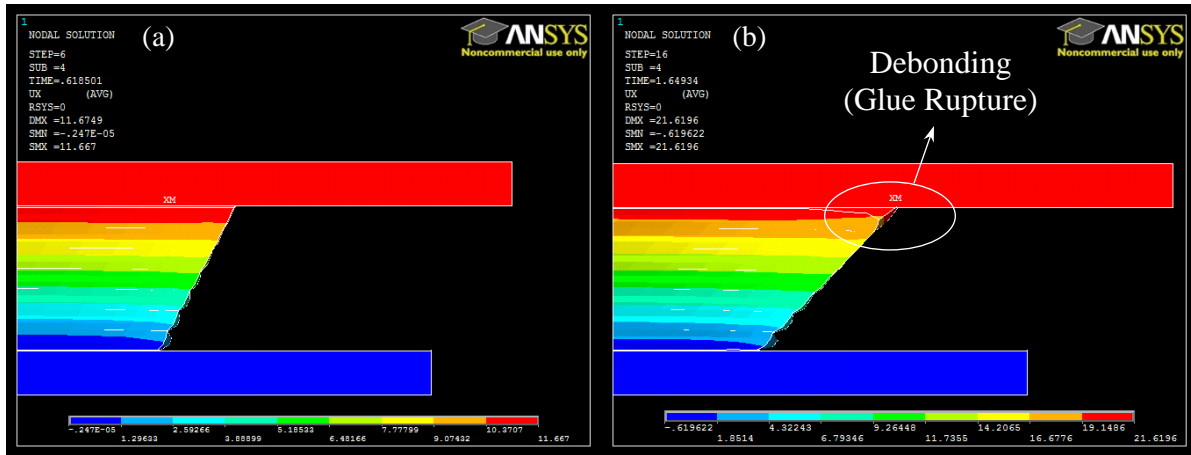
Figure 4.27. C-FREI-E1 before and after delamination; (a) $\gamma = 50\%$, (b) $\gamma = 100\%$

4.7.3 Comparison

While the C-FREI-E1 is under a constant vertical pressure of 3.0 MPa, the cyclic horizontal displacements are applied. At each amplitude of horizontal deflection including 25% t_r, 50% t_r, and 100% t_r, three fully reversed sinusoidal cycles are applied at constant horizontal rate of $V_H = 20$ mm/s. Variation of vertical pressure and cyclic horizontal displacement versus time are demonstrated in Figure 4.9, respectively.

Figure 4.28 depicts the FE half model of C-FREI-E1 and the manufactured specimen under 3 MPa vertical pressure. In the FE simulation, the lower supporting plate is fixed in all directions and the vertical load is applied to the upper steel plate. The lateral bulging of elastomeric layers due to the vertical compressive load is clearly observed in both cases.
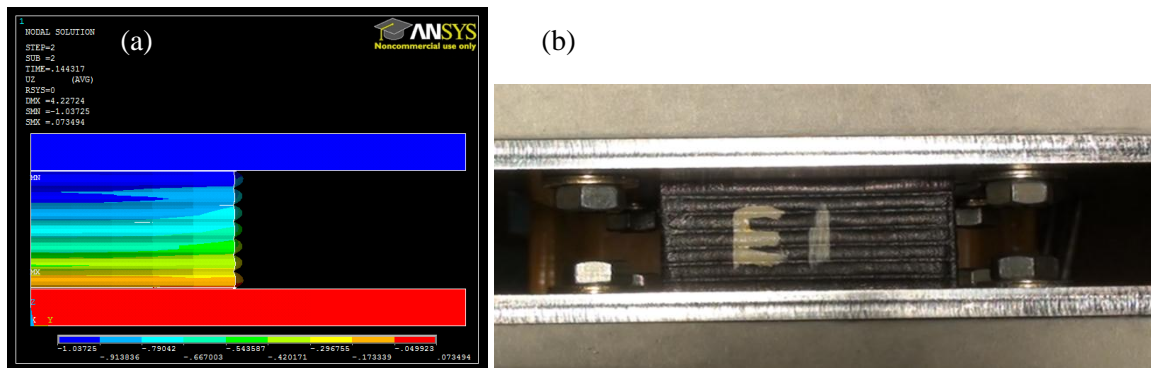
Figure 4.28. C-FREI-E1 under 3 MPa vertical pressure; (a) FE half model, (b) manufactured sample

In order to compare the results obtained from the FEM with those of the experimental tests, shear force-deflection hysteresis curves of C-FREI-E1 evaluated from both

96

experimental tests and numerical simulations are plotted at different shear strain levels (25%, 50%, and 100%) in Figure 4.29.
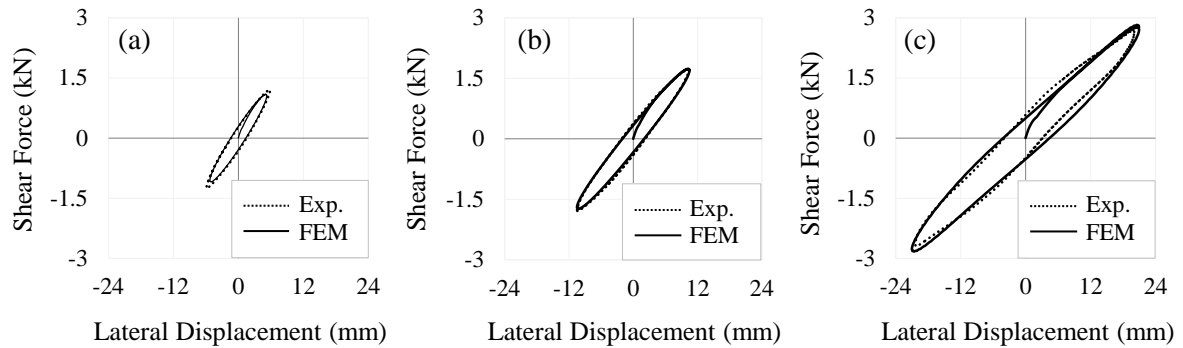
Figure 4.29. Shear hysteretic response of C-FREI-E1 under 3 MPa vertical pressure at
(a) $\gamma = 25\%$, (b) $\gamma = 50\%$, and (c) $\gamma = 100\%$ obtained from experimental and FE numerical results

Based on the experimental results, the maximum force at 25%, 50%, and 100% shear strains are 1.17 kN, 1.74 kN, and 2.69 kN, respectively. The peak shear forces obtained from the FE simulations at same shear strain amplitudes (25%, 50%, and 100%) are 1.10 kN, 1.74 kN, and 2.82 kN, respectively. The maximum relative difference, Δ_{max}, defined as a ratio of difference between experimental and numerical results to the experimental result (in percentage), is found to be 6% which happens at $\gamma = 25\%$. When the energy dissipation capacity per cycle defined as the area inside the force-displacement hysteresis curve is measured though experiment and FEM, the maximum relative difference is 11.5%. Table 4.8 shows the peak shear force, F_{max}, the energy dissipation capacity per cycle, EDC, and their corresponding relative differences at each shear strain amplitude obtained from the experimental tests and FEM. It should be mentioned that at 25% shear strain, the maximum lateral displacement exceeds 5.25 mm which is 25% of the total thickness of rubber layers ($t_r = 21$ mm). This happened because of the limitations and initial calibrations in the test setup.

Table 4.8. Results obtained from experimental tests and FE numerical simulations

γ (%)	F_{max} (kN)			EDC (N.m)		
	FEM	Exp.	Δ^* (%)	FEM	Exp.	Δ^* (%)
25	1.09	1.24	11.6	4.8	5.4	11.5
50	1.74	1.74	0.4	11.4	12.3	7.5
100	2.82	2.69	4.8	35.8	33.1	8.0

Δ: ratio of difference between experimental and numerical results to the
experimental result in percentage

A good agreement between experimental and numerical results shows the accuracy of the FE model. In order to validate the FE results further, the shear hysteretic behaviour of C-FREI-D1 obtained from the numerical simulations is compared to that of C-FREI-D1 determined from the experimental tests at 50% shear strain. Figure 4.30 depicts the FEM results along with the experimental results, which provides the validity of the model for extending it to other models.
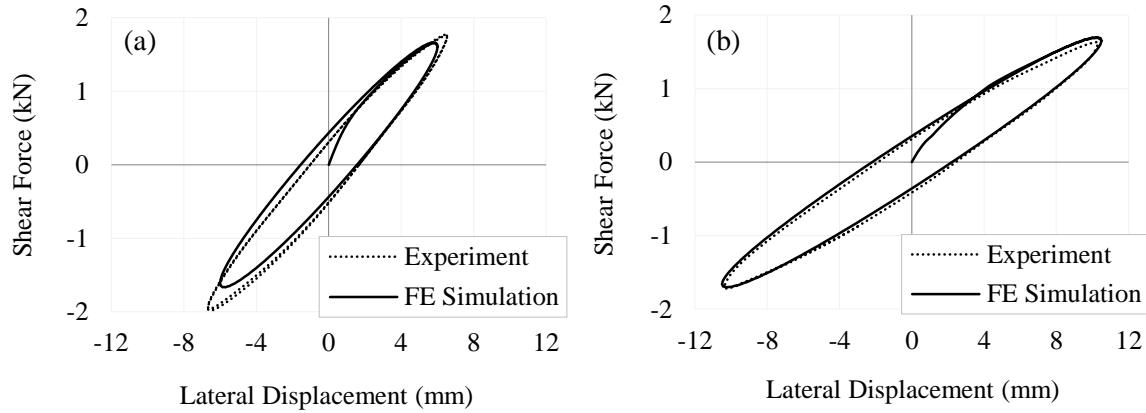
Figure 4.30. Shear hysteretic response of (a) C-FREI-A1 and (b) C-FREI-D1

at $\gamma = 50\%$ and $P = 3$ MPa

It should be noted that the maximum displacement values in the lateral force-deflection curve of C-FREI-A1 obtained from the experimental test exceed the 50% shear strain (6 mm) because of the limitations in the test setup. Therefore, the difference between experimental and numerical results increases for this rubber bearing. It is worthy to mention that the shear strain amplitude in FEM can be matched to that in the experimental tests in order to make a direct comparison.

4.8 Performance of Full Scale C-FREIs

Due to limited capacity of the actuator and reaction frame, it was not possible to perform full scale testing of the C-FREIs. This section, therefore, will determine the performance of full scale C-FREIs produced through the proposed manufacturing process in finite element environment. In this regard, full-size elastomeric isolators are modelled and analyzed using FEM in ANSYS based on the half model of C-FREI-E1 used for experimental results verification.

C-FREIs with different sizes (length, width, and height), number and thickness of rubber layers, and thickness of carbon fibre-reinforced sheets are considered and their specifications are calculated from shear force-deflection hysteretic loops and vertical force-displacement curves obtained from numerical simulations. Table 4.9 presents the geometrical properties of C-FREIs.

Table 4.9. Geometrical properties of C-FREIs with different sizes

Rubber Bearing	$L \times W$ (mm × mm)	H (mm)	n_e	t_e (mm)	t_f (mm)	S
C-FREI-23NE6	200×300	31	6	4.5	0.75	13.3
C-FREI-23NE9		47	9	4.5	0.75	13.3
C-FREI-23NE12		62	12	4.5	0.75	13.3
C-FREI-23NE15		78	15	4.5	0.75	13.3
C-FREI-34NE6	300×400	31	6	4.5	0.75	19.0
C-FREI-34NE9		47	9	4.5	0.75	19.0
C-FREI-34NE12		62	12	4.5	0.75	19.0
C-FREI-34NE15		78	15	4.5	0.75	19.0
C-FREI-45NE6	400×500	31	6	4.5	0.75	24.7
C-FREI-45NE9		47	9	4.5	0.75	24.7
C-FREI-45NE12		62	12	4.5	0.75	24.7
C-FREI-45NE15		78	15	4.5	0.75	24.7
C-FREI-56NE6	500×600	31	6	4.5	0.75	30.3
C-FREI-56NE9		47	9	4.5	0.75	30.3
C-FREI-56NE12		62	12	4.5	0.75	30.3
C-FREI-56NE15		78	15	4.5	0.75	30.3

The full-scale dimensions of C-FREIs and the performance characteristics of elastomeric isolators in the vertical and horizontal directions are presented in Table 4.10. The name of each rubber bearing contains three parts. The first letter (C) refers to the material of fibres used in the reinforced layers and the second part is the abbreviation of fibre-reinforced elastomeric isolator. The first two digits in the last part are for length and width of the laminated pad, respectively; NE represents the number of rubber layers since at each plan size, the height changes as the number of rubber layers alters; and the last number refers to the number of rubber layers.

Table 4.10. Performance specifications of C-FREIs in the horizontal and vertical directions for different lengths, widths and heights of laminated core

Rubber Bearing	Dimensions			Horizontal Specifications			Vertical Specifications	
	$L \times W$	H	Δ_{max}	K_H	β		K_V	E_c
	(mm $\times$ mm)	(mm)	(mm)	(kN/mm)	(%)		(kN/mm)	(MPa)
C-FREI-23NE6		31	13.5	1.74	18.2		329.7	0.148
C-FREI-23NE9	200×300	47	20.3	1.05	14.5		220.7	0.149
C-FREI-23NE12		62	27.0	0.73	12.3		166.0	0.149
C-FREI-23NE15		78	33.8	0.55	11.0		133.0	0.150
C-FREI-34NE6		31	13.5	3.60	16.9		1592.9	0.358
C-FREI-34NE9	300×400	47	20.3	2.23	12.9		1069.8	0.361
C-FREI-34NE12		62	27.0	1.61	10.4		805.4	0.362
C-FREI-34NE15		78	33.8	1.25	8.7		645.7	0.363
C-FREI-45NE6		31	13.5	6.06	16.6		4858.3	0.656
C-FREI-45NE9	400×500	47	20.3	3.77	12.5		3278.7	0.664
C-FREI-45NE12		62	27.0	2.75	9.9		2474.2	0.668
C-FREI-45NE15		78	33.8	2.16	8.2		1986.8	0.671
C-FREI-56NE6		31	13.5	9.12	16.5		11250.0	1.013
C-FREI-56NE9	500×600	47	20.3	5.69	12.4		7627.1	1.030
C-FREI-56NE12		62	27.0	4.15	9.7		5769.2	1.038
C-FREI-56NE15		78	33.8	3.27	8.0		4639.2	1.044

In Table 4.10, the vertical stiffness, K_V, and the compressive modulus, E_c, are measured from vertical tests simulated at 6 MPa vertical pressure and a vertical frequency of 0.2 Hz. The effective horizontal stiffness, K_H, as well as the equivalent viscous damping are calculated from cyclic tests at a shear strain amplitude of 50%, a vertical pressure of 6 MPa, and a lateral rate of 50 mm/s. The maximum horizontal displacement (Δ_{max}) at which the cyclic tests are performed is also provided.

By increasing the number of elastomeric layers from 6 to 15, the equivalent viscous damping reduces from 18.2% to 11.0% for C-FREIs with the smallest plan size (200 mm by 300 mm) and from 16.5% to 8.0% for C-FREIs with the largest plan size (500 mm by 600 mm). The reason is that the increase rate of the elastic energy restored by the elastomeric isolator is more than that of the energy dissipated per cycle and as a result the equivalent viscous damping decreases (see Equation (4.3)). When the number of rubber layers increases from 6 to 15, the effective horizontal stiffness reduces from 1.74 kN/mm to 0.55 kN/mm and the vertical stiffness decreases from 329.7 kN/mm to 133.0 kN/mm for C-FREI with the smallest plan size. For C-FREIs with 500 mm by 600 mm plan size, increasing the number of elastomeric layers from 6 to 15 causes the effective lateral stiffness and the vertical stiffness

to be decreased from 9.12 kN/mm to 3.27 kN/mm and from 11250.0 kN/mm to 4639.2 kN/mm, respectively.

4.9   Numerical Parametric Study

In this section, the effects of different factors are investigated on the performance of C-FREIs through sensitivity analyses. Here, three factors including the number of elastomeric layers (n_e), the thickness of rubber layers (t_e), and the thickness of CFR sheets (t_f) are chosen. The sensitivity of the effective horizontal stiffness, the equivalent viscous damping, and the vertical stiffness of manufactured C-FREIs is assessed. By considering three levels for each factor, nine C-FREIs are defined for each plan size. Effect of each factor is studied separately according to the following sections.

4.9.1   Number of Elastomeric Layers

Low, medium, and high levels are considered as six, nine, and twelve, respectively for the number of rubber layers. Table 4.11 depicts the operational specifications of C-FREIs considered by changing n_e. Thicknesses of rubber layer and carbon fibre-reinforced sheet are 4.5 mm and 0.75 mm, respectively, for all base isolators. If the number of elastomeric layers increases from 6 to 12, the effective horizontal stiffness, the equivalent viscous damping, and the vertical stiffness will reduce 138%, 99%, and 69%, respectively.

Table 4.11. Stiffnesses and damping coefficient of C-FREIs with different numbers of rubber layers

Rubber Bearing	$L \times W$ (mm × mm)	H (mm)	n_e	K_V (kN/mm)	K_H (kN/mm)	β (%)
C-FREI-23NE6		31	6.0	329.7	1.74	18.2
C-FREI-23NE9	200 × 300	47	9.0	220.7	1.05	14.5
C-FREI-23NE12		62	12.0	166.0	0.73	12.3
C-FREI-34NE6		31	6.0	1592.9	3.60	16.9
C-FREI-34NE9	300 × 400	47	9.0	1069.8	2.23	12.9
C-FREI-34NE12		62	12.0	805.4	1.61	10.4
C-FREI-45NE6		31	6.0	4858.3	6.06	16.6
C-FREI-45NE9	400 × 500	47	9.0	3278.7	3.77	12.5
C-FREI-45NE12		62	12.0	2474.2	2.75	9.9
C-FREI-56NE6		31	6.0	11250.0	9.12	16.5
C-FREI-56NE9	500 × 600	47	9.0	7627.1	5.69	12.4
C-FREI-56NE12		62	12.0	5769.2	4.15	9.7

Figure 4.31 shows the effect of number of rubber layers on the operational characteristics of C-FREIs for different lengths and widths of elastomers. By increasing this parameter, the vertical stiffness decreases since the strength of the device degrades against the vertical loads. When the total thickness of rubber layers (which are mainly responsible for providing the lateral isolation) goes up, the lateral flexibility increases and accordingly, the effective horizontal stiffness reduces. However, increasing ne causes the lateral displacement of rubber bearing to be increased and as a result, the elastic energy restored in the C-FREI remarkably enhances since it is proportional to the square of lateral displacement, Δ_{avg}, (see Equation (4.4)). The energy dissipated by the device also increases when a higher amount of elastomer is used. However, the restored energy increases with a higher rate compared to the energy dissipated per cycle. Hence, the equivalent viscous damping decreases according to Equation (4.3).
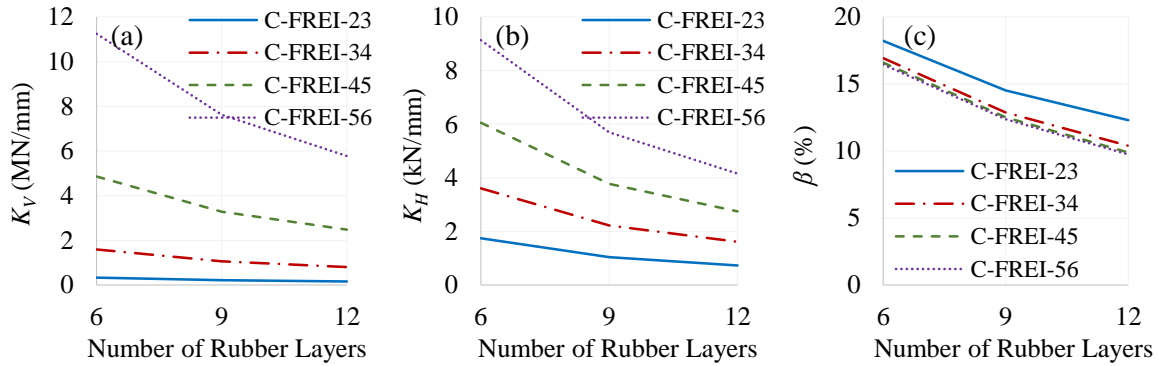
Figure 4.31. The effect of number of rubber layers on; (a) vertical stiffness, (b) effective horizontal stiffness, (c) equivalent viscous damping

In order to determine how much each performance specification (response) is sensitive to the variation of number of rubber layers, Table 4.12 is constructed. Since the unit and the magnitude of order of responses are not the same, first, performance characteristics are normalized by dividing each specification by the maximum value. Then, the rate of change, R, of each specification is measured at each plan size using Equation (4.7).

$$R_V = \left|\frac{\Delta \widehat{K}_V}{\Delta n_e}\right|, \quad R_H = \left|\frac{\Delta \widehat{K}_H}{\Delta n_e}\right|, \quad R_\beta = \left|\frac{\Delta \hat{\beta}}{\Delta n_e}\right| \tag{4.7}$$

where $\hat{K}_V$, $\hat{K}_H$, and $\hat{\beta}$ are normalized vertical stiffness, normalized effective horizontal stiffness, and normalized equivalent viscous damping, respectively. Δn_e refers to the changes in the number of rubber layers between each two base isolators.

Table 4.12. Normalized operational characteristics and their change rates

for different numbers of rubber layers

No.	Rubber Bearing	$\hat{K}_V$ (kN/mm)	$\hat{K}_H$ (kN/mm)	$\hat{\beta}$ (%)	Two way comparison	R_V	R_H	R_β
1	C-FREI-23NE6	1	1	1	1 – 2	0.11	0.13	0.07
2	C-FREI-23NE9	0.67	0.60	0.80	2 – 3	0.06	0.06	0.04
3	C-FREI-23NE12	0.50	0.42	0.68	1 – 3	0.08	0.10	0.05
4	C-FREI-34NE6	1	1	1	4 – 5	0.11	0.13	0.08
5	C-FREI-34NE9	0.67	0.62	0.76	5 – 6	0.06	0.06	0.05
6	C-FREI-34NE12	0.51	0.45	0.61	4 – 6	0.08	0.09	0.06
7	C-FREI-45NE6	1	1	1	7 – 8	0.11	0.13	0.08
8	C-FREI-45NE9	0.67	0.62	0.75	8 – 9	0.06	0.06	0.05
9	C-FREI-45NE12	0.51	0.45	0.60	7 – 9	0.08	0.09	0.07
10	C-FREI-56NE6	1	1	1	10 – 11	0.11	0.13	0.08
11	C-FREI-56NE9	0.68	0.62	0.75	11 – 12	0.06	0.06	0.05
12	C-FREI-56NE12	0.51	0.46	0.59	10 – 12	0.08	0.09	0.07

It should be mentioned that R is calculated between each two C-FREIs as shown in the three last columns of Table 4.12. For example, R_V in the second row is obtained by comparing the vertical stiffnesses of C-FREI-23NE6 and C-FREI-23NE9. At each plan size, every two base isolators (from three considered C-FREIs) should be compared together in order to check whether increasing n_e from 6 to 9 and 9 to 12 has a higher effect or increasing n_e from 6 to 12 is more significant. In the "Two way comparison" column, every three cases (rows) having the same plan sizes are compared to each other. For example, in the two way comparison of 2 – 3, C-FREI-23NE9 is compared with C-FREI-23NE12.

The operational characteristic which exhibits the maximum rate of variation has the most sensitivity to the factor n_e. Based on the results presented in Table 4.12, the effective horizontal stiffness is the most sensitive response and the equivalent viscous damping is the least sensitive response regardless of the length and width of rubber sheets.

4.9.2 Thickness of Elastomeric Layers

While the number of rubber layers ($n_e = 9$) and the thickness of CFR sheets ($t_f = 0.75$ mm) are kept constant, the thickness of elastomer was increased from 3.0 mm to 6.0 mm

with an increment of 1.5 mm. Stiffnesses and equivalent viscous damping of C-FREIs for different plan sizes and heights of C-FREIs are listed in Table 4.13.

Table 4.13. Stiffnesses and damping coefficient of C-FREIs
with different thicknesses of rubber layers

Rubber Bearing	$L \times W$ (mm × mm)	H (mm)	t_e	K_V (kN/mm)	K_H (kN/mm)	β (%)
C-FREI-23TE3		33	3.0	730.2	1.79	17.2
C-FREI-23TE4	200 × 300	47	4.5	220.7	1.05	14.5
C-FREI-23TE6		60	6.0	98.7	0.67	14.3
C-FREI-34TE3		33	3.0	3529.4	3.63	16.6
C-FREI-34TE4	300 × 400	47	4.5	1069.8	2.23	12.9
C-FREI-34TE6		60	6.0	452.3	1.57	10.8
C-FREI-45TE3		33	3.0	10256.4	6.09	16.4
C-FREI-45TE4	400 × 500	47	4.5	3278.7	3.77	12.5
C-FREI-45TE6		60	6.0	1400.2	2.72	10.1
C-FREI-56TE3		33	3.0	23076.9	9.15	16.4
C-FREI-56TE4	500 × 600	47	4.5	7627.1	5.69	12.4
C-FREI-56TE6		60	6.0	3327.2	4.13	9.9

The variations of operational specifications by changing the thickness of elastomeric layers are observed in Figure 4.32. Similar to the first factor (number of rubber layers), the vertical and the effective horizontal stiffnesses, as well as the equivalent viscous damping decrease when rubber sheets with higher thicknesses are used. The reason is that a higher total thickness of elastomer leads to a device with a higher lateral flexibility and a lower vertical rigidity. The results also show that using thicker rubber layers does not improve the energy dissipation capability of a base isolator. When the thickness of rubber sheets double to 6, in the extreme conditions, the effective lateral stiffness, the equivalent viscous damping and the vertical stiffness decrease 167%, 66%, and 640%, respectively.
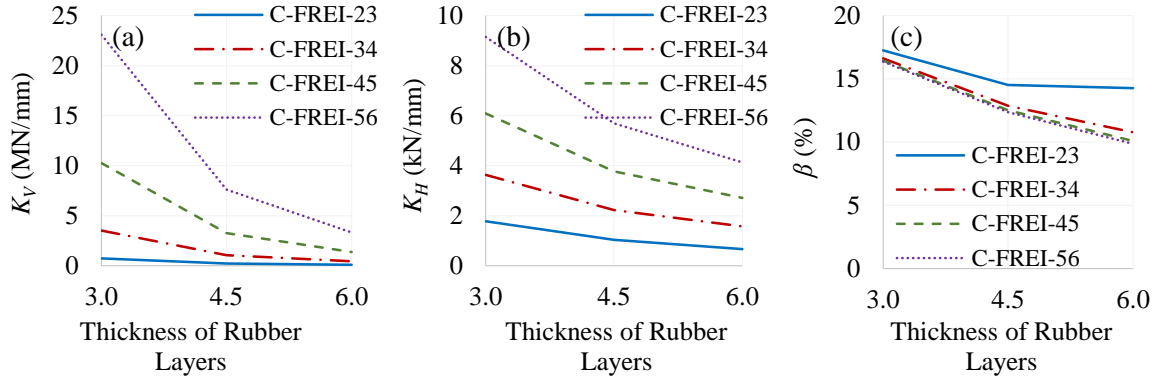
Figure 4.32. The effect of thickness of rubber layers on; (a) vertical stiffness, (b) effective horizontal stiffness, (c) equivalent viscous damping

Rate of change of performance characteristics calculated by changing the thickness of rubber layers are listed in Table 4.14. By comparing the change rates at each plan size, it is observed that the vertical stiffness is more sensitive to the thickness of rubber layers. However, for C-FREIs with the largest plan size (500 mm by 600 mm), both the vertical and horizontal stiffnesses experience similar amount of changes when the thickness of elastomer increases.

Table 4.14. Normalized operational characteristics and their change rates
for different thicknesses of rubber layers

No.	Rubber Bearing	$\hat{K}_V$ (kN/mm)	$\hat{K}_H$ (kN/mm)	$\hat{\beta}$ (%)	Two way comparison	R_V	R_H	R_β
1	C-FREI-23TE3	1	1	1	1 – 2	0.47	0.28	0.11
2	C-FREI-23TE4	0.30	0.59	0.84	2 – 3	0.11	0.14	0.01
3	C-FREI-23TE6	0.14	0.37	0.83	1 – 3	0.29	0.21	0.06
4	C-FREI-34TE3	1	1	1	4 – 5	0.46	0.26	0.15
5	C-FREI-34TE4	0.30	0.61	0.78	5 – 6	0.12	0.12	0.09
6	C-FREI-34TE6	0.13	0.43	0.65	4 – 6	0.29	0.19	0.12
7	C-FREI-45TE3	1	1	1	7 – 8	0.22	0.25	0.16
8	C-FREI-45TE4	0.67	0.62	0.76	8 – 9	0.26	0.12	0.10
9	C-FREI-45TE6	0.29	0.45	0.61	7 – 9	0.24	0.18	0.13
10	C-FREI-56TE3	1	1	1	10 – 11	0.21	0.25	0.17
11	C-FREI-56TE4	0.68	0.62	0.75	11 – 12	0.25	0.11	0.10
12	C-FREI-56TE6	0.30	0.45	0.60	10 – 12	0.23	0.18	0.13

Equation (4.8) represents the variation rates of three specifications.

$$R_V = \left|\frac{\Delta \hat{K}_V}{\Delta t_e}\right|, \quad R_H = \left|\frac{\Delta \hat{K}_H}{\Delta t_e}\right|, \quad R_\beta = \left|\frac{\Delta \hat{\beta}}{\Delta t_e}\right|$$ (4.8)

4.9.3 Thickness of Fibre-Reinforced Sheets

In order to investigate the effect of thickness of fibre-reinforced layers on the performance of C-FREIs, CFR sheets with thicknesses of 0.50 mm, 0.75 mm, and 1.25 mm are selected. Two other factors (n_e and t_e) are kept constant at 6 and 4.5 mm, respectively. Table 4.15 shows the vertical and horizontal stiffnesses, as well as the equivalent viscous damping for twelve considered C-FREIs.

Table 4.15. Stiffnesses and damping coefficient of C-FREIs
with different thicknesses of fibre-reinforced layers.

Rubber Bearing	$L \times W$ (mm × mm)	H (mm)	t_f	K_V (kN/mm)	K_H (kN/mm)	β (%)
C-FREI-23TF5		30	0.50	327.3	1.73	18.3
C-FREI-23TF7	200 × 300	31	0.75	329.7	1.74	18.2
C-FREI-23TF12		33	1.25	331.2	1.75	18.1
C-FREI-34TF5		30	0.50	1568.6	3.59	17.0
C-FREI-34TF7	300 × 400	31	0.75	1592.9	3.60	16.9
C-FREI-34TF12		33	1.25	1610.7	3.61	16.9
C-FREI-45TF5		30	0.50	4724.4	6.05	16.6
C-FREI-45TF7	400 × 500	31	0.75	4858.3	6.06	16.6
C-FREI-45TF12		33	1.25	4979.3	6.07	16.6
C-FREI-56TF5		30	0.50	10843.4	9.11	16.5
C-FREI-56TF7	500 × 600	31	0.75	11250.0	9.12	16.5
C-FREI-56TF12		33	1.25	11688.3	9.13	16.5

Figure 4.33 demonstrates the effect of thickness of CFR layers on the stiffnesses and damping coefficient of C-FREIs with different plan sizes. An increasing trend is observed for the vertical stiffness and the effective horizontal stiffness when the thickness of CFR sheets goes up from 0.5 mm to 1.25 mm. however, the changes are very small compared to the cases in which two other factors (n_e and t_e) vary. The equivalent viscous damping encounters negligible alteration while increasing the thickness of reinforcement. It can be understood that CFR sheets have almost no contribution to the energy dissipating. By changing the carbon fibre-reinforced layers' thickness from 0.5 mm to 1.25 mm, the vertical stiffness and the effective horizontal stiffness increase 7.2% and 0.9%, respectively and the equivalent viscous damping diminishes 0.9%.
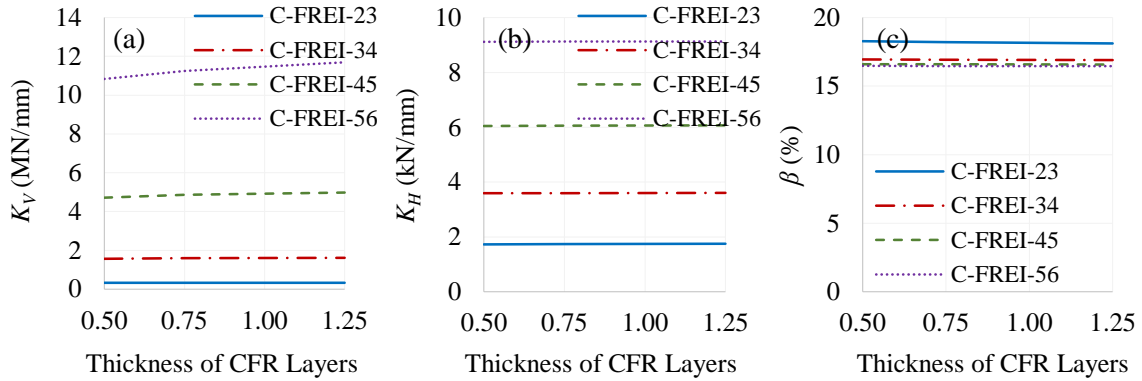
Figure 4.33. The effect of thickness of carbon fibrereinforced layers on; (a) vertical stiffness, (b) effective horizontal stiffness, (c) equivalent viscous damping

When the change rates of the operational specifications are compared for different plan sizes (see Table 4.16), it can be observed that the vertical stiffness has the maximum variation when CFR sheet with higher thicknesses are used in the rubber bearing. This fact shows that the fibre-reinforced layers are mainly responsible for providing vertical stiffness. Although the effect of CFR sheets on the performance of C-FREIs is small compared to the rubber layers, increasing the thickness of fibre-reinforced layers can increase the vertical stiffness up to 7.2% when the thickness increases from 0.5 mm to 1.25 mm.

Table 4.16. Normalized operational characteristics and their change rates
for different thicknesses of carbon fibre-reinforced layers

No.	Rubber Bearing	$\hat{K}_V$ (kN/mm)	$\hat{K}_H$ (kN/mm)	$\hat{\beta}$ (%)	Two way Comparison	R_V	R_H	R_β
1	C-FREI-23TF5	0.988	0.991	1	1 – 2	0.029	0.017	0.015
2	C-FREI-23TF7	0.995	0.995	0.996	2 – 3	0.009	0.010	0.011
3	C-FREI-23TF12	1	1	0.991	1 – 3	0.016	0.012	0.012
4	C-FREI-34TF5	0.974	0.994	1	4 – 5	0.060	0.010	0.007
5	C-FREI-34TF7	0.989	0.997	0.998	5 – 6	0.022	0.006	0.005
6	C-FREI-34TF12	1	1	0.996	4 – 6	0.035	0.007	0.005
7	C-FREI-45TF5	0.949	0.996	1	7 – 8	0.108	0.003	0.002
8	C-FREI-45TF7	0.976	0.997	0.999	8 – 9	0.049	0.006	0.003
9	C-FREI-45TF12	1	1	0.998	7 – 9	0.068	0.005	0.003
10	C-FREI-56TF5	0.928	0.998	1	10 – 11	0.139	0.007	0.003
11	C-FREI-56TF7	0.963	0.999	0.999	11 – 12	0.075	0.001	0.001
12	C-FREI-56TF12	1	1	0.999	10 – 12	0.096	0.003	0.002

Change rates of the operational characteristics can be calculated using Equation (4.9) when the thickness of CFR layers varies.

$$R_V = \left|\frac{\Delta \widehat{K}_V}{\Delta t_f}\right|, \quad R_H = \left|\frac{\Delta \widehat{K}_H}{\Delta t_f}\right|, \quad R_\beta = \left|\frac{\Delta \hat{\beta}}{\Delta t_f}\right| \tag{4.9}$$

4.10 Summary

FREIs are relatively new elastomeric bearings in which fibre-reinforced polymer (FRP) composite plates are used as reinforcements rather than steel shims. Producing FREIs in the form of long laminated pads without using a mold and cutting them to the required size significantly reduces the complexity, time and overall cost of the manufacturing process. In addition, FREIs are much lighter than SREIs. Due to the lack of adequate information on the performance of bonded FREI, which are manufactured using the proposed cold-vulcanization process, the goal of this chapter was to assess the efficiency and performance sensitivity of bonded carbon-FREIs (C-FREIs) based on experimental and numerical investigations.

Nine 1/4 scale C-FREIs were fabricated using a simple and fast manufacturing process, which has a potential to be applied in developing countries. Experimental results showed that under cyclic displacements, although a partial delamination occurs between rubber layer and steel supporting plate due to the rollover deformation at shear strains greater than 50%, the rubber bearings perform properly up to 100% shear strain. The vertical stiffness increases with increasing the fibre-reinforced layers' thickness and with decreasing the elastomers' thickness. The flexibility in the horizontal direction increases by increasing the total thickness of rubber layers while, the energy dissipation capacity enhances with increasing the thickness of both fibre-reinforced and elastomeric layers. The effect of several factors including the vertical pressure, the lateral cyclic rate, the number of rubber layers and the thickness of carbon fibre-reinforced layers were explored on the behaviour of rubber bearings. Results revealed that the effect of vertical pressure on the response of base isolators is negligible. However, decreasing the cyclic loading rate increases the lateral flexibility and the damping capacity. Another finding was that, carbon fibre-reinforced layers can be considered as a minor source of energy dissipation. A numerical parametric study was performed by exploring the effect of number and thickness of rubber layers, as well as

thickness of carbon fibre reinforced sheets on the performance of C-FREIs. The results showed that by increasing the number and thickness of rubber layers, the efficiency of C-FREIs degrades in terms of vertical stiffness and damping capacity, however, the performance improved in terms of lateral flexibility. Another important observation was that the increasing thickness of fibre-reinforced layers can increase the vertical rigidity of the base isolator. The vertical stiffness had the most sensitivity to the thickness of elastomeric layers and the thickness of CFR sheets. On the other hand, the effective lateral stiffness was mostly affected by increasing the number of rubber layers.

Chapter 5   Smart Elastomeric Isolators Equipped with Shape Memory Alloy Wires

5.1   General

Based on the results obtained in Chapter 4, it was found that fiber-reinforced rubber bearings have limited shear deformation capacity and can undergo local failures (e.g. partial delamination) under shear strain levels equal to and greater than 100%. In order to provide a solution for the aforementioned limitations, in this chapter, shape memory alloy (SMA), as a supplementary component, was implemented in elastomeric bearings.

A diagonal (cross) configuration of SMA wires was proposed for NRBs and its performance was compared to the straight arrangement suggested by Choi et al. (2005). First, the most efficient SMA was determined for smart elastomeric isolators based on the superelastic strain range and compatibility with environmental conditions (temperature). In order to simulate the nonlinear behaviour of the elastomer, a hyper-viscoelastic material model was used and validated by experimental results. After evaluating the hysteretic shear response of SMA-based natural rubber bearings (SMA-NRB) through finite element method (FEM), the effective horizontal stiffness, the residual deformation, the energy dissipation capacity, and the equivalent viscous damping of SMA-NRB were calculated according to analytical equations. The effect of aspect ratio of rubber bearing (i.e. ratio of the height to the length), arrangement and thickness of wires, and pre-strain in SMA wires were investigated on the performance of base isolators.

Similar cross configuration of SMA wire was used for carbon fibre-reinforced high damping rubber bearings (CFR-HDRB) by considering two types of SMA (NiTi- and ferrous-based). Then, the most efficient SMA in terms of the superelastic strain range and compatibility with environmental thermal conditions was identified through a performance assessment. The effective horizontal stiffness and the residual deformation of the proposed smart base isolators were calculated from the lateral force-deflection hysteresis curves through numerical simulations. After validating the FE results obtained from the numerical simulations, the hysteretic shear response of SMA-based CFR-HDRB was evaluated. The effect of different factors, including the aspect ratio of rubber bearing, the SMA types, and the arrangement and thickness of wires was investigated on the performance of the device.

In order to study the effect of SMA on the LRB, SMA wires were wrapped around the LRB with a symmetric double cross configuration. The finite element (FE) model of LRB was validated with experimental tests and then extended to SMA-LRB. Hysteretic shear response of SMA wire-based LRB was determined through FEM in ANSYS (ANSYS Mechanical APDL, Release 14.0) at different shear strain levels and with different radii of SMA wire.

Finally, in order to appropriately determine the pre-strain and the radius of cross section of SMA wires, a performance-based design approach was developed along with a design example for SMA wire-based rubber bearings.

5.2 SMA-based Natural Rubber Bearings (SMA-NRB)

SMA-based smart base isolators have many advantages such as stability, re-centring capability, high energy dissipation capacity and long service life. They not only will mitigate the seismic response of structures in terms of acceleration, displacement and internal forces but also, they will have superior performance in terms of fatigue property and energy dissipation capacity compared to existing rubber bearings (Suduo and Xiongyan, 2007).

In this section, SMA wires are used as a supplementary element to improve the performance of steel-reinforced NRBs in terms of energy dissipation capacity and residual deformation, which occurs at large shear strain amplitudes. Regarding the maximum superelastic strain in SMA wires, two different configurations are considered for wires. The effect of several factors such as the aspect ratio of rubber bearing, the thickness of wires, and the pre-strain in SMA wires in addition to the arrangement of wires is investigated on the performance of the smart base isolator. Geometrical properties of two NRBs with different numbers of elastomeric layers are listed in Table 5.1.

Table 5.1. Geometrical properties of NRBs

Specimen	Horizontal dimensions of isolator (mm × mm)	Horizontal dimensions of steel shims (mm × mm)	t_E (mm)	t_r (mm)	t_s (mm)	n_r	n_s	R	S
NRB-1	240 × 240	200 × 200	15	4.5	1.0	8	7	0.22	0.075
NRB-2	240 × 240	200 × 200	15	4.5	1.0	14	13	0.38	0.075

t_E: thickness of supporting steel plates; t_r: thickness of rubber layers; t_s: thickness of steel shims; n_r: number of rubber layers; n_s: number of steel shims; R: aspect ratio of the rubber bearing, i.e. the ratio of the height to the length; S: shape factor, i.e. the ratio of loaded area to force-free area of one rubber layer

111

The thickness of elastomer layers and steel shims are 4.5 mm and 1 mm, respectively, for both cases. While, the number of rubber layers, n_r, is increased from 8 to 14. The aspect ratio of rubber bearing is defined as a ratio of the effective height to the length.

$$R = \frac{H_{eff}}{L} \qquad (5.1)$$

where the effective height is the total thickness of rubber layers and steel shims.

$$H_{eff} = t_r n_r + t_s n_s \qquad (5.2)$$

The schematic view of NRB-1 and NRB-2 consisting of 8 and 14 rubber layers, respectively, is plotted in Figure 5.1.
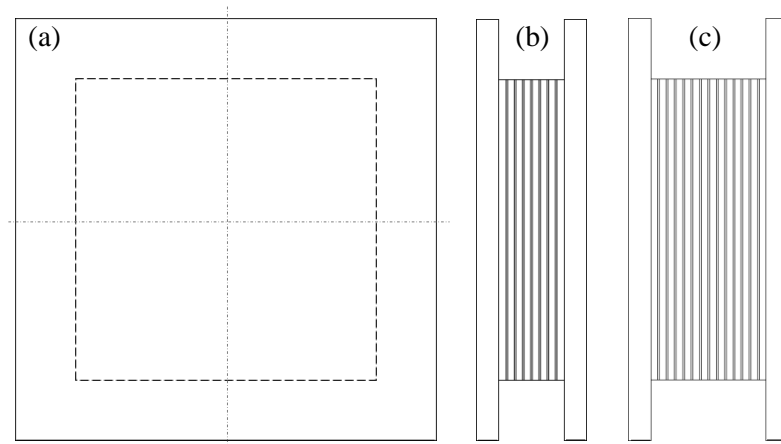
Figure 5.1. Schematic view of the elastomeric isolator; (a) Plan view of NRB-1 and NRB-2, (b) Side view of NRB-1, (c) Side view of NTB-2

5.2.1 SMA-NRB equipped with Straight Wires

In the SMA-NRB with straight wire (SMA-NRB-S), two continuous SMA wires with a radius of 2.5 mm are wounded in two opposite sides of the rubber bearing as shown in Figure 5.2a. This type of arrangement of SMA wires was previously proposed by Choi et al. (2005). Each wire passes through four steel hooks which are mounted at each corner. In such configuration, since one continuous wire is used instead of four wires fixed at each corner of the supporting plates, the induced strain along the SMA wire due to the cyclic lateral displacement of rubber bearing noticeably decreases.
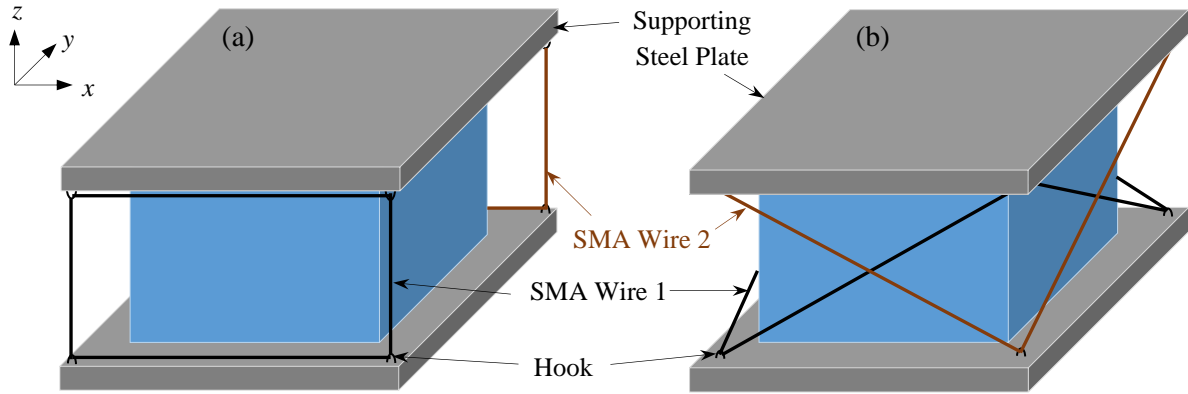
Figure 5.2. Smart rubber bearing; (a) straight SMA wires, (b) cross SMA wires

The total length of SMA wires, L_{SMA}, which is required for the straight configuration, is presented in Table 5.2 for each aspect ratio.

Table 5.2. Required length for SMA wires in the straight configuration (Figure 5.2a)

Specimen	R	L_{SMA} (mm)
SMA-NRB-S1	0.22	1092
SMA-NRB-S2	0.38	1224

The strain in SMA wires (ε_{SMA}) is a function of the shear strain amplitude, γ, and the aspect ratio, R. When the shear strain is increased from 25% to 200%, the strain noticeably goes up in the SMA wires. E_{SMA} also increases with the increase in aspect ratio of the base isolator.

5.2.2 SMA-NRB equipped with Cross Wires

In the SMA-NRB with cross wires (SMA-NRB-C), two SMA wires with a radius of 2.5 mm are wounded around the rubber bearing diagonally as shown in Figure 5.2b. A steel hook is mounted at each corner on the lower and upper surfaces of the top and bottom supporting plates, respectively. The SMA wires pass through these hooks (see Figure 5.2b). Compared to the straight configuration, the main reason of using wires in such an arrangement is to effectively reduce the maximum strain in the wires due to large shear strain amplitudes of rubber bearing.

The total length of wires needed for this arrangement is presented in Table 5.3. Although a larger length of SMA wire is required for this configuration compared to the

113

straight arrangement, the generated strain in cross wires due to the lateral deflection of rubber bearing is much lower than that of straight wires. The strain in cross and straight SMA wires will be calculated in the section of efficiency of SMAs (next section) for different shear strain amplitudes and two aspect ratios.

Table 5.3. Required length for SMA wires in the cross configuration (Figure 5.2b)

Specimen	R	L_{SMA} (mm)
SMA-NRB-C1	0.22	1871.9
SMA-NRB-C2	0.38	1937.9

Figure 5.3 depicts the variation of strain in straight and cross SMA wires by increasing the shear strain amplitude. Strain in the SMA wires is geometrically calculated by increasing the shear strain and by considering the dimensions of the base isolator and the configuration of wires. Figure 5.3 illustrates that at each shear strain amplitude the strain in the SMA wires is higher when the smart elastomeric isolator has a larger aspect ratio. It can be also observed that when the shear strain amplitude is lower than 150%, the strain induced in SMA wires will not exceed 15% for both SMA-NRBs. However, at 200% shear strain amplitude, the SMA wires in SMA-NRB-S1 ($R = 0.22$) and SMA-NRB-S2 ($R = 0.38$) experience about 15% and 23% strain, respectively (Figure 5.3a).
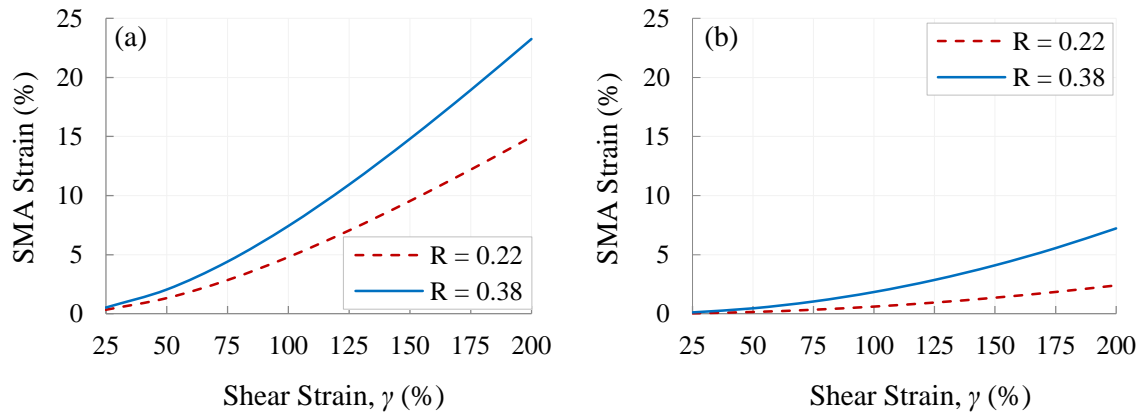
Figure 5.3. Variation of strain in SMA wire as a function of shear strain amplitude and aspect ratio for (a) straight configuration and (b) cross configuration

In the cross configuration (Figure 5.3b), there is a significant reduction in the SMA wire strain compared to that of the straight configuration. In this case, the SMA strain is lower than 8% for both aspect ratios. The maximum strain generated in cross SMA wires is

114

7.2% which occurs in the SMA-NRB-C2 with an aspect ratio of 0.38 at 200% shear strain. It shows that when the aspect ratio of the elastomeric isolator is increased, unlike the straight configuration, the cross SMA wires in smart NRBs can operate in a superelastic range under large shear strain amplitudes.

5.2.3 Efficiency of SMAs

For each aspect ratio, the SMA strain (ε_{SMA}) in wires with 2.5 mm radius is calculated at eight different levels of shear strain amplitudes, form 25% to 200%, in the case of cross and straight configurations (Table 5.4). Since most of SMAs have a superelastic strain below 6% (see Table 5.5), SMA wires with the straight configuration cannot operate in a superelastic range at large shear strain amplitudes, especially when the height of the rubber bearing is increased. Whereas, the cross SMA wires can operate within its superelastic range at large lateral cyclic displacements. This fact demonstrates the effectiveness of the cross configuration over the straight one. In the straight configuration, when the shear strain is higher than 150% (see Figure 5.3a), using any type of SMA listed in Table 5.5 is inefficient for $R = 0.38$ since the strain in wires exceeds the superelastic strain range. However, a comparison is performed between the straight and the cross configurations, with $R = 0.38$ at 200% shear strain, in order to investigate the behaviour of SMA wires and consequently the hysteretic shear response of rubber baring when the wires are subjected to strains above the superelastic strain range. It should be mentioned that a different alloy, which is not considered in this thesis, with different properties (e.g. yield stress and superelastic strain range) may lead to different results when it is implemented in the straight configuration. Therefore, further investigations can be conducted in the future works.

Table 5.4. Strain in SMA wires for two configurations and two aspect ratios

at different shear strain amplitudes

Wire γ (%)	$\varepsilon_{\mathrm{SMA}}$ (%)			
	$R = 0.22$		$R = 0.38$	
	Straight	Cross	Straight	Cross
25	0.3	0.04	0.5	0.1
50	1.3	0.2	2.1	0.5
75	2.9	0.3	4.4	1.0
100	4.8	0.6	7.4	1.8
125	7.1	1.0	10.9	2.9
150	9.5	1.4	14.8	4.1
175	12.2	1.9	18.9	5.6
200	15.0	2.4	23.3	7.2

Table 5.5. Mechanical characteristics of different shape memory alloys (SMAs)

Alloy	$\varepsilon_{\max}$ (%)	ε_{s} (%)	E_{A} (GPa)	A_{f} (°C)	Reference
$Ni\,Ti_{49.1}$	5.0	3.6	40.4	44.6	Strnadel et al. 1995
$Ni\,Ti_{49.5}$	5.7	4.6	45.3	53.0	Strnadel et al. 1995
$Ni\,Ti_{50}$	3.1	2.2	117.8	77.8	Strnadel et al. 1995
$Ni\,Ti$	8.2	6.8	30.0	42.9	Boyd and Lagoudas 1996
$Ni\,Ti_{45}$	6.8	6.0	62.5	-10.0	Alam et. Al. 2008
$Ni\,Ti_{44.1}$	6.5	5.5	39.7	0	Alam et. Al. 2008
$Ti\,Ni_{40}\,Cu_{10}$	4.1	3.4	72.0	66.6	Strnadel et al. 1995
$Ti\,Ni_{41}\,Cu_{10}$	4.1	3.1	91.5	50.0	Strnadel et al. 1995
$Ti\,Ni_{41.5}\,Cu_{10}$	3.4	2.8	87.0	60.0	Strnadel et al. 1995
$Ti\,Ni_{25}\,Cu_{25}$	10.0	2.5	14.3	73.0	Liu 2003
CuAlBe	3.0	2.4	32.0	-65.0	Zhang et al. 2009
FeMnAlNi	6.1	5.5	98.4	$<$ -50°C	Omori et al. 2011
FeNiCoAlTaB	15.0	13.5	46.9	-62.0	Tanaka et al. 2010

Table 5.6 presents the effectiveness of various types of SMA wires in cross configuration applied to the rubber bearing for a range of aspect ratios. It shows that all six types of SMA can operate in the elastic range when the aspect ratio is smaller than 0.24. The TiNi$_{40}$Cu$_{10}$ will remain within its superelastic range for all shear strain amplitudes when the aspect ratio is equal to or smaller than 0.27. For SMA-NRBs with 0.38 aspect ratio, strain in TiNi$_{40}$Cu$_{10}$ and CuAlBe exceed the superelastic limit at shear strain amplitudes equal to and higher than 150%. If FeMnAlNi wires are used, the lateral displacement of the rubber bearing can go up to 175% of the height without causing plastic deformation in the SMA wires. However, when the elastomeric base isolator with an aspect ratio of 0.38 is subjected

to 200% shear strain, only NiTi, NiTi$_{45}$, and FeNiCoAlTaB (FeNCATB) can operate in their superelastic range. It means that these three types of SMA can be considered as good candidates to be used in cross configuration.

Table 5.6. Superelastic range of SMAs for different aspect ratios and shear strain amplitudes in cross configuration

γ (%) \ R	TiNi$_{40}$Cu$_{10}$		CuAlBe		FeMnAlNi		NiTi	NiTi$_{45}$	FeNCATB
	≤0.27	0.38	≤0.24	0.38	≤0.33	0.38	≤0.38	≤0.38	≤0.38
≤ 125	✓	✓	✓	✓	✓	✓	✓	✓	✓
150	✓	✗	✓	✗	✓	✓	✓	✓	✓
175	✓	✗	✓	✗	✓	✓	✓	✓	✓
200	✓	✗	✓	✗	✓	✗	✓	✓	✓

Different environmental conditions such as temperature and humidity can affect the performance of elastomeric base isolators. The operational temperature range varies according to the location in which a rubber bearing operates. Since, the superelastic effect of SMA wires occurs at temperatures above the austenite finish temperature, in order to have a smart elastomeric bearing with superelastic SMA wires, the austenite finish temperature of the SMA wires should be lower than the ambient temperature. In such circumstances, since the minimum ambient temperature in countries with cold climatic conditions often gets below 0°C and in some places reaches -40°C, the austenite finish temperature of the SMA wire should be lower than this minimum temperature. Therefore, NiTi$_{45}$, CuAlBe, FeMnAlNi, and FeNCATB with A_f lower than zero (see Table 5.5) can be implemented in elastomeric base isolators.

When both the superelastic strain and the austenite finish temperature are considered as two important criteria for choosing the most efficient SMA, FeNCATB with 13.5% superelastic strain and -62°C austenite finish temperature will be the best candidate to be used in SMA-NRBs. Hence, FeNCATB SMA wires are implemented in smart NRBs.

5.2.4 Finite Element Modelling

5.2.4.1 Material Model

Modelling, meshing and analyzing the NRB is performed in ANSYS (ANSYS Mechanical APDL, Release 14.0). In this regard, among different types of nonlinear material

models available in ANSYS, Mooney Rivlin – Prony (hyper-viscoelastic) model is used to simulate the nonlinear behaviour of natural rubber under combined vertical pressure and cyclic lateral displacements. In FE analyses, the shear modulus of rubber is 0.50 MPa and the Poisson's ratio is assumed to be 0.4998. The material constants of the hyper-viscoelastic model are listed in Table 5.7. Steel shims are modelled as an isotropic material with the Young's modulus of 210 GPa and a Poisson's ratio of 0.3. Element SOLID185 with 8 nodes and three degrees of freedom at each node is selected for both steel shims and rubber layers. The large-deflection effect is considered in full transient analyses in order to simulate the large deformation of rubber layers at large shear strain amplitudes. In order to validate the material models used for rubber layers and steel shims, the lateral force-deflection hysteresis curves of a NRB assessed using FEM are compared with the experimental results.

Table 5.7. Material constants of hyper-viscoelastic model

Mooney-Rivlin Model		Prony Model	
C_{10}	0.502	α_1	0.565
C_{01}	0.307	τ_1	0.130
C_{11}	-0.018	α_2	0.061
		τ_2	65.82

Figure 5.4 demonstrates a schematic view of an NRB consisting of 16 elastomer layers with a thickness of 2.73 mm and 15 steel shims with a thickness of 1 mm. Two supporting steel plates with 9.8 mm thickness are mounted at the top and the bottom. The NRB is covered by a layer of rubber with a thickness of 5 mm. Figure 5.5 shows the NRB with a mapped mesh in ANSYS. Elements with purple and blue colours respectively illustrate the elastomeric cover layer and supporting steel plates. The hysteretic shear behaviour of NRB is evaluated under 6 MPa vertical pressure, three different shear strain amplitudes (100%, 150%, and 184%), and a horizontal frequency of 0.2 Hz through full transient analyses.
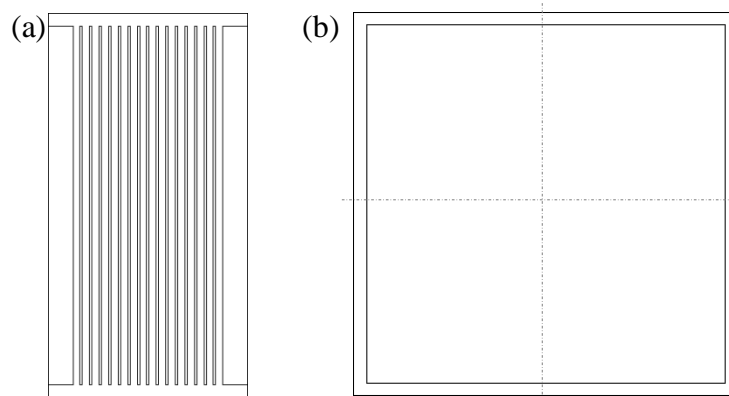
Figure 5.4. Steel-reinforced NRB; (a) side view, (b) plan view
(adapted from (Dehghani Ashkezari et al., 2008))
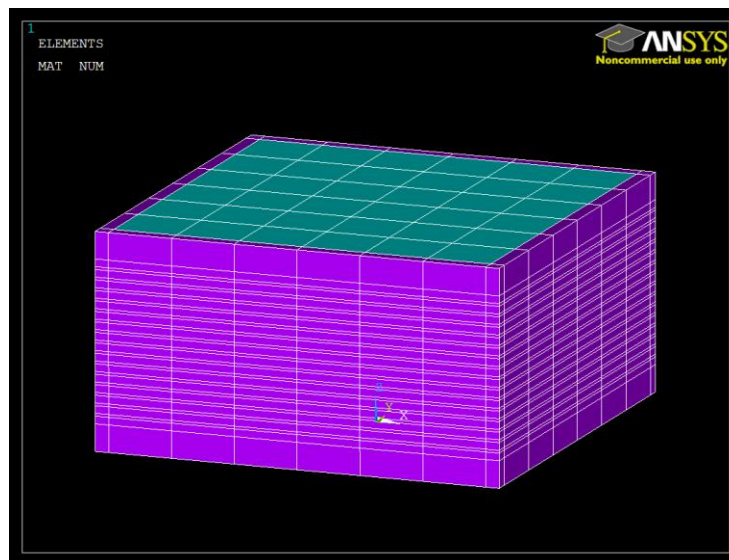
Figure 5.5. NRB with a mapped mesh in ANSYS (ANSYS Mechanical APDL, Release 14.0)

According to the hysteresis curves plotted in Figure 5.6, a good consistency is observed between the results obtained from FE simulations and experimental tests conducted by Dehghani Ashkezari et al. (2008). Based on the numerical results, the effective horizontal stiffness of the NRB is 0.38, 0.34, and 0.33 kN/mm for 100%, 150%, and 184% shear strain amplitudes, respectively. The maximum difference between the numerical and experimental results in the horizontal stiffness is 4% which occurs at 150% shear strain. Also, the maximum horizontal loads corresponding to 100%, 150%, and 184% shear strains are 16.7, 22.3, and 26.4kN, respectively which closely match with the experimental results.

119
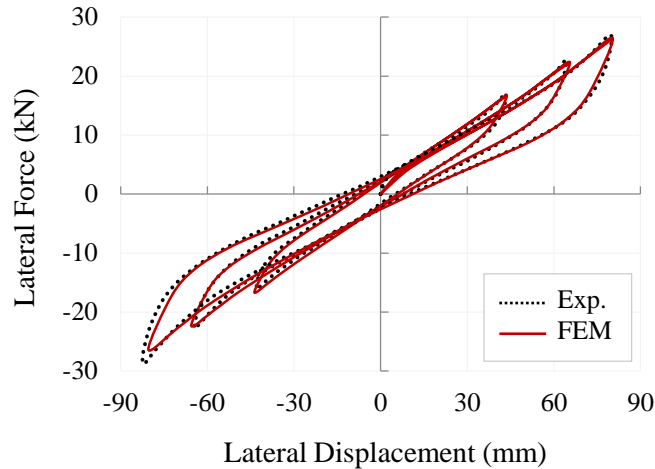
Figure 5.6. Lateral force-deflection curves of steel-reinforced NRB
(experimental results are adapted from (Dehghani Ashkezari et al., 2008))

5.2.4.2 Modelling of SMA wires

In generating the FE model of the SMA-NRB, a method of superposition is implemented in order to simplify the system by decoupling the rubber bearing and SMA wires. Here, a smooth contact is assumed between the steel hook and the SMA wire. Instead of modelling steel hooks, and the contact between the hooks and continuous SMA wires, exerted forces to the elastomeric isolator due to SMA wires are considered. These assumptions considerably reduce the complexity of the FE simulation. Otherwise, running nonlinear full transient analysis for determining the hysteretic shear behaviour of base isolators with different aspect ratios and wire configurations might not converge, especially at high shear strain amplitudes. In reality, a frictional force is generated between the wire and the hook in the contact area. In such a situation, the relative displacement between the wire and the hook will be limited or even fixed in the worst case. In a future work, more realistic comparisons can be performed by considering two types of contact including smooth (current case) and friction (real case). This further study can indicate how much the smooth contact assumption is close to the real case.

In order to simplify the FE model, before analyzing the system, first, the strain generated in SMA wires at each pre-defined time step is calculated according to the geometry of the device and the arrangement of wires. In the next step, the axial stress in SMA wires can be determined form the stress-strain relationship of shape memory alloy based on the Auricchio's superelasticity model (Auricchio, 2001). Since Auricchio's model is utilized for

120

SMAs in ANSYS, the superelastic behaviour of SMA wire is simulated using this model and by considering the properties of SMA obtained from experimental results (Tanaka et al., 2010). Here, we assume that the stress-strain hysteresis of FeNCATB SMA wire does not change by increasing the number of loading cycles. However, further experimental study is required in order to accurately simulate the dynamic behaviour of SMA wires and take into account the strain time history. Using the axial stress in SMA wires and the direction of wires at each time step, the force vectors exerted from the SMA wire to the hook are computed. The idealized stress-strain curve of FeNCATB (Tanaka et al., 2010) at room temperature is plotted in Figure 5.7. In such a situation, instead of modelling the SMA wires, the steel hooks, and the contact between them, the equivalent forces are applied to the rubber bearing at each time step while running the nonlinear transient analysis. In fact, the rubber bearing and the SMA wires are decoupled as two separate systems in FE simulations. Then, by measuring the force generated in SMA wires as a function of time, the effect of one system (SMA wires) is estimated on the other one (elastomeric isolator). Decoupled systems for the smart rubber bearing with cross SMA wires are depicted in Figure 5.8.
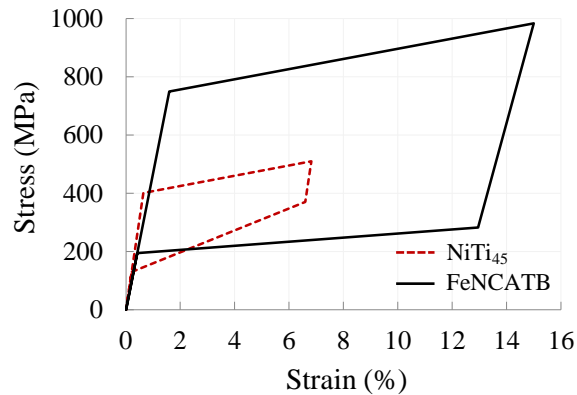
Figure 5.7. Idealized stress-strain curve of $NiTi_{45}$ and FeNCATB SMAs at room temperature
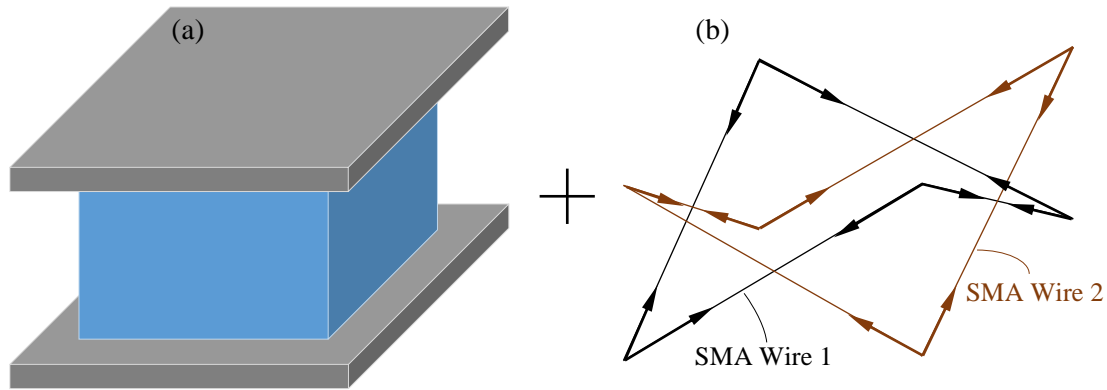
Figure 5.8. Decoupled systems; (a) Elastomeric isolator, (b) SMA wires with internal forces

Since SMAs have thermo-mechanical behaviour, both thermal and mechanical loadings affect the response of SMAs. Here, it is assumed that the environmental temperature does not change during cyclic loading. As a result, the coupling between the thermal and the mechanical loads can be neglected during an earthquake. However, the yield stress and consequently the hysteretic behaviour of an SMA wire operating at 30°C will be different from the response of the SMA wire which works at temperatures below 0°C. Therefore, the temperature at which the base isolator is operating plays an important role in the behaviour and performance of the device. The operational temperature (temperatures of the environment and SMA wires) is assumed to remain constant at 20°C. It should be mentioned that in order to investigate the effect of this parameter on the overall performance of the smart rubber bearing, further research needs to be conducted.

5.2.5 Results and Discussions

By computing the hysteretic behaviour of SMA-NRBs subjected to a frequency of 0.2 Hz, and 6 MPa vertical pressure, the effect of the shear strain amplitude, the aspect ratio of rubber bearing, the configuration and thickness of wires, and the pre-strain in SMA wires have been assessed on the performance of the base isolator. In each case, four operational characteristics of the base isolator including the horizontal stiffness (K_H), the residual deformation (RD) (i.e. a lateral displacement at which the shear force becomes zero when the rubber bearing is coming back to its initial position), the energy dissipation (energy dissipated per cycle, EDC), and the equivalent viscous damping (β) are calculated in order to compare the performances of NRBs with those of SMA-NRBs. The effective horizontal

stiffness and the equivalent viscous damping are obtained according to Equations (3.10) and (4.3), respectively.

Since in each configuration of wires (cross and straight), two aspect ratios (0.22 and 0.38) are considered for smart elastomeric isolators, in total, four cases are investigated (Table 5.8). The hysteretic shear response of each SMA-NRB is compared with that of a NRB with the same geometrical and mechanical properties under three different shear strain amplitudes: 100%, 150%, and 200%. As discussed in sections 5.2.2 and 5.2.3, although implementing SMA wires in the straight configuration is ineffective for NRB with $R = 0.38$ at shear strains higher than 150%, a comparison is performed between the straight and the cross configurations, with $R = 0.38$ and $\gamma = 200\%$, in order to investigate the behaviour of SMA wires and the hysteretic shear response of SMA-NRB-S2.

Table 5.8. Four cases of SMA-based NRBs considered in the FE simulations

Case	Wire	R	Specimen
1	Cross	0.22	SMA-NRB-C1
2	Cross	0.38	SMA-NRB-C2
3	Straight	0.22	SMA-NRB-S1
4	Straight	0.38	SMA-NRB-S2

5.2.5.1   Low Aspect Ratio SMA-NRB

Figure 5.9 shows the lateral hysteretic behaviour of NRB-1, SMA-NRB-C1 and SMA-NRB-S1. When SMA wires are used in the straight configuration, the response of the base isolator noticeably changes, whereas in the cross configuration these changes are negligible at 100% shear strain amplitude. Under a specific horizontal deflection, the strain generated in SMA wires with straight arrangement is much higher than that with the cross configuration. As a result, the axial stress in the straight wires is considerably increased and a larger force will be applied to the elastomeric isolator from the SMA wires with straight arrangement. This behaviour leads to significant changes in the lateral stiffness and the maximum horizontal force of SMA-NRB-S1 with straight wires.
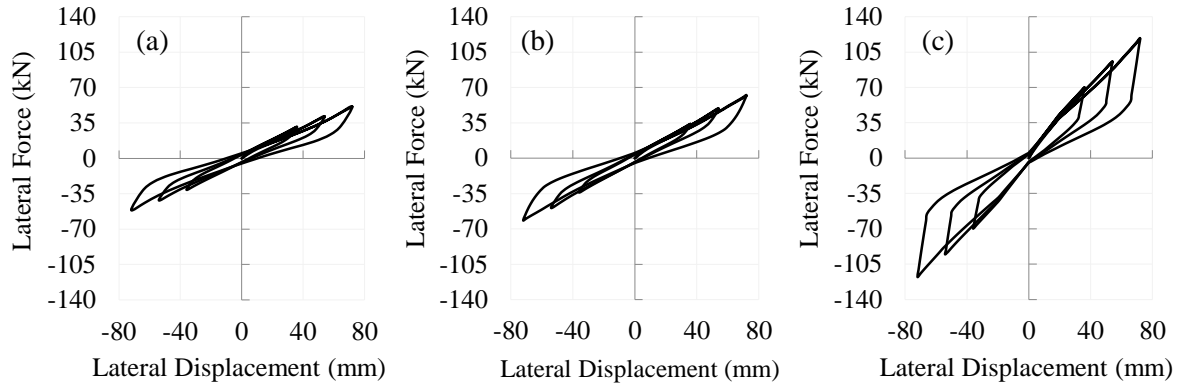
Figure 5.9. Lateral force-deflection curve of (a) NRB-1, (b) SMA-NRB-C1, and (c) SMA-NRB-S1; at $\gamma = 100\%$, 150%, and 200%

Operational characteristics of the natural and the smart rubber bearings are listed in Table 5.9. Changes in the performance of SMA-NRBs are also investigated by measuring the difference between each characteristic of the SMA-NRBs and that of the NRB. Each characteristic is calculated at three different shear strain amplitudes (100%, 150%, and 200%). At 100% shear strain, the effective horizontal stiffness of the NRB-1 with an aspect ratio of 0.22 is 0.86 kN/mm. When straight SMA wires are used, the horizontal stiffness increases to 1.95 kN/mm which is 125% higher than that of the NRB-1. On the other hand, SMA wires in the cross configuration (SMA-NRB-C1) increase the effective lateral stiffness to 9% at shear strain of 100%. A similar trend is observed for other shear strain amplitudes. However, the increase in the effective horizontal stiffness of SMA-NRB-S1 follows a regular pattern. At 100%, 150%, and 200% shear strains, the horizontal stiffness is increased by 125%, 131%, and 132%, respectively, compared to that of NRB-1. When the shear strain amplitude increases from 100% to 200%, the stiffness of SMA wires goes up due to the forward phase transformation. As a result, the stress generated in the wires noticeably increases and consequently, the rate of increase of the lateral stiffness of SMA-NRB-S1 rises from 125% to 131%. In terms of lateral flexibility, the SMA-NRB-C1 exhibited superior performance compared to SMA-NRB-S1.

Table 5.9. Operational characteristics of NRB and SMA-NRBs

for different wire configurations and aspect ratios

	γ (%)	NRB-1	SMA-NRB-S1 $(\Delta_{NRB})^*$	SMA-NRB-C1 (Δ_{NRB})	NRB-2	SMA-NRB-S2 (Δ_{NRB})	SMA-NRB-C2 (Δ_{NRB})
Horizontal Stiffness (kN/mm)	100	0.86	1.95 (125%)	0.94 (9%)	0.49	1.13 (129%)	0.71 (44%)
	150	0.77	1.77 (131%)	0.91 (18%)	0.44	1.08 (147%)	0.63 (44%)
	200	0.71	1.65 (132%)	0.87 (22%)	0.40	1.13 (183%)	0.58 (45%)
Residual Deform. (mm)	100	4.8	3.2 (-33%)	4.4 (-9%)	8.5	5.7 (-33%)	7.3 (-14%)
	150	6.3	3.9 (-38%)	5.2 (-18%)	11.1	6.7 (-40%)	9.2 (-17%)
	200	10.2	5.4 (-47%)	8.7 (-15%)	18.1	16.1 (-11%)	13.7 (-24%)
Dissipated Energy (kJ)	100	0.5	1.3 (167%)	0.5 (0%)	0.9	2.3 (174%)	1.2 (43%)
	150	0.9	2.8 (203%)	0.9 (0%)	1.6	5.1 (220%)	2.7 (67%)
	200	1.7	5.0 (186%)	2.1 (24%)	3.0	11.1 (268%)	4.8 (59%)
Viscous Damping (%)	100	7.0	8.3 (18%)	6.4 (-8%)	7.0	8.4 (19%)	6.9 (-1%)
	150	6.5	8.5 (31%)	5.5 (-16%)	6.5	8.4 (30%)	7.5 (16%)
	200	7.5	9.2 (23%)	7.6 (1%)	7.6	9.8 (30%)	8.3 (10%)

*Difference between operational characteristics of SMA-NRBs and those of the NRB

SMA wires can reduce the residual deformation of the NRBs due to their re-centring capability. The SMA-NRB-C1 reduces the residual deformation of the NRB by 9%, 18%, and 15% at 100%, 150%, and 200% shear strain amplitudes, respectively. While, the SMA-NRB-S1 decreases the residual deformation by 33%, 38%, and 47% at 100%, 150%, and 200% shear strain amplitudes, respectively. It shows that the straight configuration of wires is more efficient than the cross wires in reducing the plastic deformation of the rubber bearing after releasing the horizontal shear force. Due to the lower effective length of SMA wires in the straight configuration compared to that of cross wires, straight wires are subjected to a higher strain and as a result, the axial stress induced in these wires is higher. In terms of reducing the residual deformation, the SMA-NRB-S1 is more efficient compared to the SMA-NRB-C1.

Another important characteristic of the NRB which is affected by SMA wires is the energy dissipation capacity. This specification is increased when SMA wires are used either in the form of straight or cross. In fact, the flag-shape hysteresis curve of a SMA wire under loading and unloading enlarges the shear hysteresis of the NRB and as a result, the area inside the lateral force-deflection curve which represents the dissipated energy by the elastomeric isolator is enhanced. The SMA-NRB-S1 increases the energy dissipated per

cycle more than 160% at all shear strain amplitudes. In contrast, the SMA-NRB-C1 does not change this parameter at shear strains of 100% and 150% while at 200% shear strain amplitude, the dissipated energy encounters a 24% increase. Changes in the equivalent viscous damping are different from the energy dissipation capacity. For the straight configuration, the maximum increase in the damping capacity occurs at 150% shear strain which is 31% more than that of the NRB. At $\gamma = 200\%$, due to the large amount of the restored energy, the increase in the equivalent viscous damping is lower. In the SMA-NRB-C1, since at 100% and 150% shear strains, the energy dissipated per cycle does not change and the effective horizontal stiffness increases, the equivalent viscous damping decreases.

5.2.5.2 High Aspect Ratio SMA-NRB

When the aspect ratio of NRB is increased by increasing the number of elastomeric layers, the elongation in SMA wires is enhanced for both straight and cross configurations. According to Table 5.4, for an aspect ratio of 0.38, the strain induced in straight and cross SMA wires reaches 23.3% and 7.2%, respectively, at 200% shear strain amplitude. It means that by increasing the amplitude of cyclic lateral displacement, the straight SMA wires will not remain in the superelastic range and as a result, they encounter a plastic deformation. In other words, when SMA-NRB goes back to its initial position (zero lateral displacement) after a half cycle, a residual strain is generated in the SMA wires. Based on the idealized stress-strain curve of FeNCATB subjected to strains more than 15% (Tanaka et al., 2010), changes of the stress in SMA wires can be estimated as a function of stress. When a maximum strain of 23% is applied to FeNCATB wires due to a cyclic loading, nearly 6.5% strain remains in the wires after a half cycle. This fact causes SMA-NRB-S2 to work ineffectively under large shear strains (e.g. more than 200%). Figure 5.10 represents the hysteretic behaviour of NRB-2, SMA-NRB-C2, and SMA-NRB-S2, respectively. At 200% shear strain, when the SMA-NRB-S2 (Figure 5.10c) goes back to its initial position from the maximum and minimum lateral displacements, it undergoes sudden changes in the lateral force in about 60 mm and -75 mm displacements, respectively. The reason is that the axial stress in the SMA wires reaches zero before finishing each half cycle due to a plastic deformation which is occurred in the wires. As a result, the force exerted from SMA wires to the rubber bearing is removed and consequently, the SMA-NRB-S2 follows the behaviour of

NRB-2 (see Figure 5.10a). The maximum shear force in SMA-NRB-S2 significantly increases by increasing the shear strain. It is because of a huge force transferred from the elongated SMA wires having much higher strain compared to wires in SMA-NRB-C2.
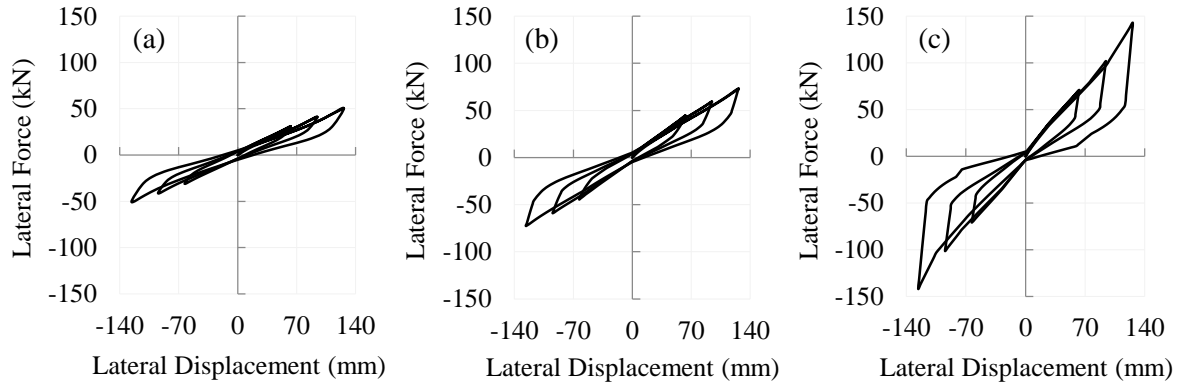
Figure 5.10. Lateral force-deflection curve of (a) NRB-2, (b) SMA-NRB-C2, and (c) SMA-NRB-S2; at $\gamma = 100\%$, 150%, and 200%

Figure 5.11 to Figure 5.14 show the performance characteristics of NRBs and SMA-NRBs in the form of bar charts. By comparing the overall trend of changes in the effective horizontal stiffness, it can be observed that the NRBs and SMA-NRBs with higher aspect ratios are more flexible in the lateral direction. Similar to elastomeric isolators with 0.22 aspect ratios, when straight SMA wires are used in a NRB with an aspect ratio of 0.38 (SMA-NRB-S2), the increase in the horizontal stiffness is higher than a case in which cross SMA wires are implemented (SMA-NRB-C2). It indicates that the straight configuration is not an effective option for NRBs with high aspect ratios since they significantly stiffen the base isolator.
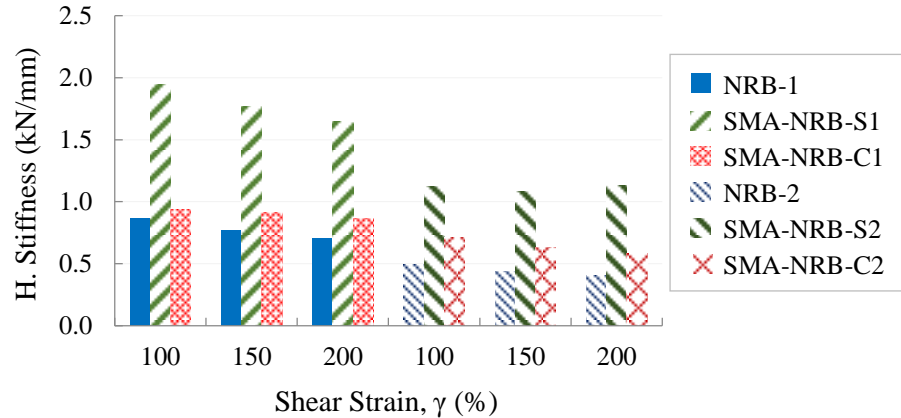
Figure 5.11. Effective horizontal stiffness of NRBs and SMA-NRBs with straight and cross configurations of wires; $\gamma = 100\%$, 150%, and 200%

The residual deformation of NRB-2 decreases about 33% and 40% for 100% and 150% shear strain amplitudes, respectively, when straight SMA wires are used (see Table 5.9). The reduction in the residual deformation of SMA-NRB-C2 at 100%, 150%, and 200% shear strains are 14%, 17% and 24%. As it is observed in Figure 5.12, SMA-NRB-S2 has superior performance in terms of residual deformation reduction. However at large shear strain amplitudes (200% and more), SMA wires encounter a plastic deformation in the straight configuration. Since the flag-shape hysteresis curve of FeNCATB wires noticeably shrinks by increasing the number of cyclic displacements, generating residual deformation in wires causes the SMA-NRB-S2 to have an inferior performance compared to SMA-NRB-C2.
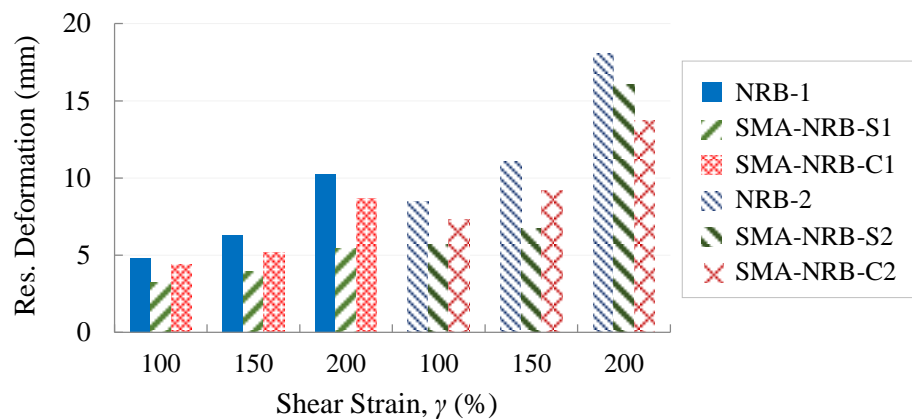
Figure 5.12. Residual deformation of NRBs and SMA-NRBs with straight and cross configurations of wires; $\gamma = 100\%$, 150%, and 200%

128

According to Figure 5.13 and results listed in Table 5.9, straight SMA wires in SMA-NRB-S2 can noticeably increase the energy dissipation capacity of NRB-2 up to 268% at shear strain amplitude of 200%. The energy dissipated per cycle in the SMA-NRB-C2 is 1.2kJ, 2.7kJ, and 4.8kJ for 100%, 150% and 200% shear strains, respectively. The maximum enhancement in the energy dissipation capacity of SMA-NRB-C2 is 67%. When the equivalent viscous damping of SMA-NRB-S2 and SMA-NRB-C2 are compared together (Figure 5.14), it is observed that the straight wires are more efficient since SMA-NRB-S1 and SMA-NRB-S2 have higher damping capacity due to a greater strain and consequently a larger hysteresis curve in FeNCATB SMA wires. However, at 200% shear strain, SMA wires in the straight configuration are deformed plastically and exert a large amount force to the rubber bearing. As a result, SMA-NRB-C1 and SMA-NRB-C2 can be considered as better alternatives at high shear strains.
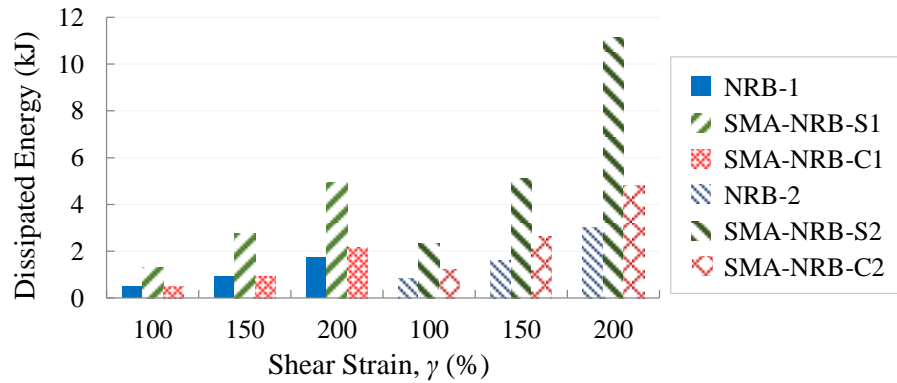
Figure 5.13. Dissipated energy of NRBs and SMA-NRBs with straight and cross configurations of wires; γ = 100%, 150%, and 200%
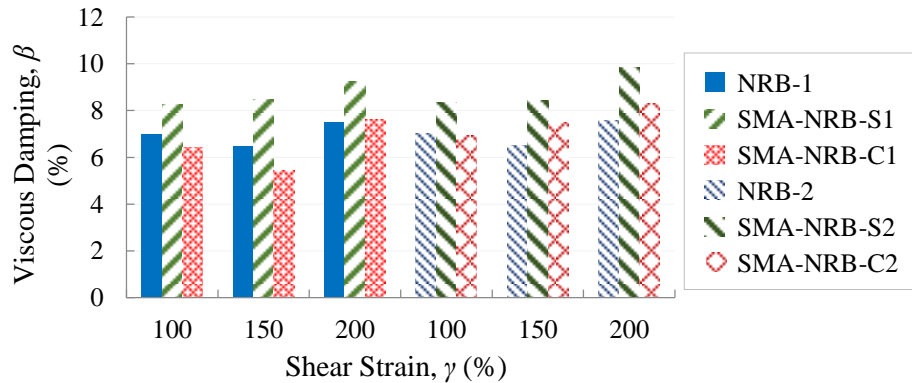
Figure 5.14. Equivalent viscous damping of NRBs and SMA-NRBs with straight and cross configurations of wires; γ = 100%, 150%, and 200%

5.2.5.3 Thickness of SMA Wires

The thickness of SMA wire can affect the hysteretic behaviour of the SMA-NRB. When the radius of the wire's cross section increases, the force exerted from wires to the base isolator is significantly enhanced. Among four considered cases (Table 5.8), the SMA-NRB-C2 in which cross SMA wires are implemented in a NRB with an aspect ratio of 0.38 is selected as a case study. Wires with three different radii; 1.25 mm, 2.5 mm and 4 mm are mounted on this rubber bearing. In order to investigate the effect of SMA wires' thickness on the performance of the NRB, hysteretic behaviours of smart base isolators are evaluated and the effective horizontal stiffness and the energy dissipation capacity are compared to those of the NRB.

The hysteretic shear behaviours of SMA-NRB-C2 with different wire's radii (1.25 mm, 2.5 mm, and 4 mm) are plotted in Figure 5.15. As can be seen, when a thicker SMA wire is used, the maximum shear force in smart elastomeric isolators is increased since the force generated in SMA wires increases with their thickness. It shows that the hysteretic shear response of SMA-NRB-C2 is highly dependent on the thickness of SMA wires which are installed with the cross configuration. Four characteristics including the effective horizontal stiffness, the residual deformation, the energy dissipation capacity, and the equivalent viscous damping are listed in Table 5.10. The lateral stiffness increases almost equally when the shear strain amplitude changes from 100% to 200%. However, by enhancing the radius of wire's cross section from 1.25 mm to 4 mm, the effective horizontal stiffness, at 200% shear strain, increases from 12% to 112%.
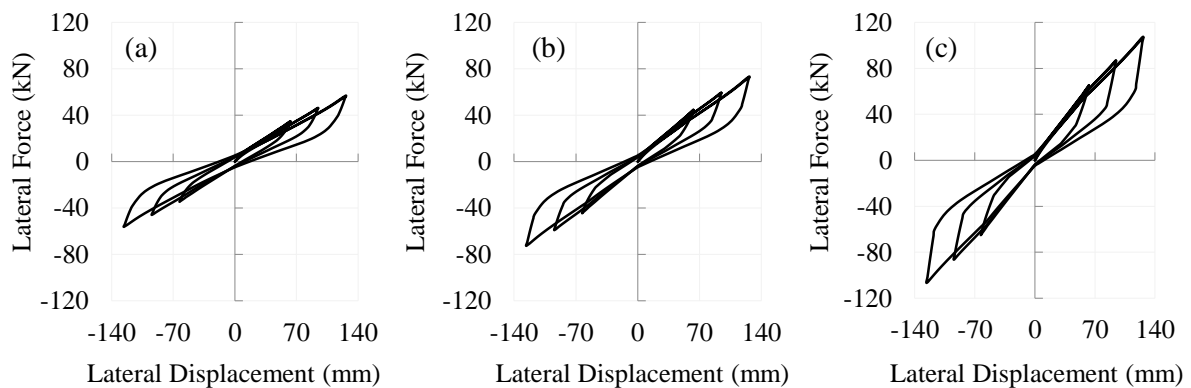
Figure 5.15. Lateral force-deflection curve of SMA-NRB-C2 for different thicknesses of SMA wires; (a) $r_{SMA} = 1.25$ mm, (b) $r_{SMA} = 2.5$ mm, and (c) $r_{SMA} = 4$ mm; $\gamma = 100\%$, 150%, and 200%

Table 5.10. Operational characteristics of SMA-NRB-C2 with different wire radii compared to NRB-2

	γ (%)	NRB-2	SMA-NRB-C2 $r_{SMA} = 1.25$mm (Δ_{NRB})*	$r_{SMA} = 2.5$mm (Δ_{NRB})*	$r_{SMA} = 4.0$mm (Δ_{NRB})*
Horizontal Stiffness (kN/mm)	100	0.49	0.55 (12%)	0.71 (44%)	1.04 (111%)
	150	0.44	0.49 (12%)	0.63 (44%)	0.92 (111%)
	200	0.40	0.45 (12%)	0.58 (45%)	0.85 (112%)
Residual Deform. (mm)	100	8.5	8.2 (-3%)	7.3 (-14%)	6.0 (-29%)
	150	11.1	10.6 (-4%)	9.2 (-17%)	7.1 (-36%)
	200	18.1	16.5 (-9%)	13.7 (-24%)	10.1 (-44%)
Dissipated Energy (kJ)	100	0.9	1.0 (13%)	1.2 (43%)	1.8 (105%)
	150	1.6	1.9 (22%)	2.7 (67%)	4.1 (160%)
	200	3.0	3.6 (18%)	4.8 (59%)	7.4 (144%)
Viscous Damping (%)	100	7.0	7.0 (0%)	6.9 (-1%)	6.8 (-3%)
	150	6.5	7.1 (9%)	7.5 (16%)	8.0 (23%)
	200	7.6	7.9 (5%)	8.3 (10%)	8.7 (15%)

*Difference between operational characteristics of SMA-NRB-C2s and those of the NRB-2

As it is expected, SMA wires with 4 mm radius of cross section, decreases the residual deformation of NRB-2 more than that of wires with lower thickness. At 200% shear strain, the residual deformation reduces by 9%, 24%, and 44% for SMA-NRBs with 1.25 mm, 2 mm, and 4 mm wire's radii, respectively.

Although the maximum energy dissipation capacity for SMA-NRB-C2 with different thickness of wires is achieved at 200% shear strain amplitudes, the maximum changes in the dissipated energy occur at 150% shear strain amplitude when it is compared to NRB-2. For example in the case of SMA-NRB-C2 with 1.25 mm wires (Figure 5.15a), the dissipated energy at 150% shear strain is 1.9 kJ which is 22% of the dissipated energy in NRB-2 while, SMA-NRB-C2 can dissipates the energy by 3.6 kJ at 200% shear strain which is 18% of the NRB-2. It shows that the rate of increasing the energy dissipation capacity is not constant when the shear strain amplitude increases. The trend of changes in the equivalent viscous damping for shear strains of 150% and 200% is similar to the dissipated energy. For SMA-NRB-C2 with 2.5 mm and 4 mm SMA wires subjected to 100% shear strain amplitude (Figure 5.15b and c), although both the dissipated and the restored energies in SMA-NRB-C2 increase, changes in the equivalent viscous damping is negative compared to that of the

NRB-2. The reason is that the rate of changes of the restored energy is more than that of the dissipated energy due to a significant increase in the horizontal stiffness and subsequently, the ratio of the restored energy to the dissipated energy for SMA-NRB-C2 is lower than that of the NRB-2. When the lateral cyclic displacement increases to 150% of the total thickness of rubber layers in SMA-NRB-C2 with 2.5 mm and 4 mm wires, the energy dissipation capacity enhances by 67% and 160%, respectively, and the equivalent viscous damping increases by 16% and 23%, respectively.

According to Figure 5.16 which demonstrates the changes trend in four operational characteristics of SMA-NRBs, increasing the thickness of SMA wires causes a reduction in the lateral flexibility and the residual deformation, and an increase in the energy dissipation capacity. The equivalent viscous damping is enhanced by increasing the thickness at shear strain amplitudes greater than 150%. Therefore, using SMA wires with a higher thickness improves the performance of the NRB-2 in terms of residual deformation, energy dissipation capacity, and equivalent viscous damping. Since the lateral flexibility significantly decreases by increasing the thickness of wires, the radius of SMA wires' cross section should be designed for a required lateral stiffness.
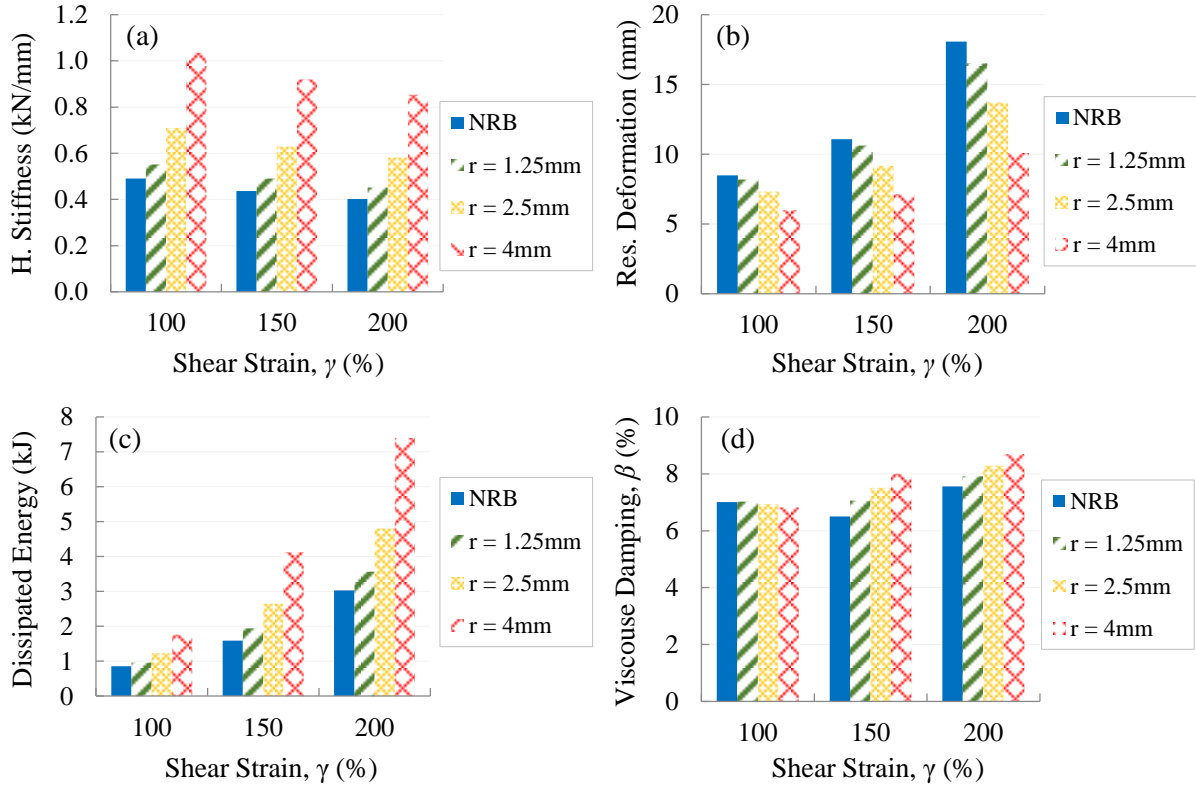
Figure 5.16. Operational characteristics of NRB-2 and SMA-NRB-C2 with different wires' thickness; (a) Effective horizontal stiffness, (b) Residual deformation, (c) Dissipated energy per cycle, (d) Equivalent viscous damping

5.2.5.4 Pre-strain in SMA wires

The yield strength of the ferrous SMA, FeNCATB, which represents the starting stress in the forward phase transformation from austenite to martensite, is aroud 750 MPa (Figure 5.7). The rate of increasing the stress from 0 to 750 MPa which denotes the initial elastic stiffness in the austenite phase is about 47 GPa. The large amount of yield stress, corresponds to 1.6% strain, induces a large normal force in SMA wires and consequently, a large lateral force is exerted to the NRB in the opposite direction of the cyclic horizontal displacement. In such a situation, the lateral flexibility is noticeably reduced and as a result, the effective horizontal stiffness is significantly increased compared to a NRB. In order to efficiently use the SMA wire as a damper in the rubber bearing, the initial elastic part of ferrous shape memory alloy should be removed by pre-straining the SMA wire (Choi et al., 2005). In the pre-strained SMA wire, the forward phase transformation occurs at a lower strain and as a result, the yield stress considerably decreases. Subsequently, when the SMA

133

wire is elongated and subjected to a tension due to the cyclic displacement of the rubber bearing, a smaller force will be transferred to the superstructure. By applying a pre-strain (e.g. 2%) to the SMA wire, the stress-strain curve shifts according to Figure 5.17a.
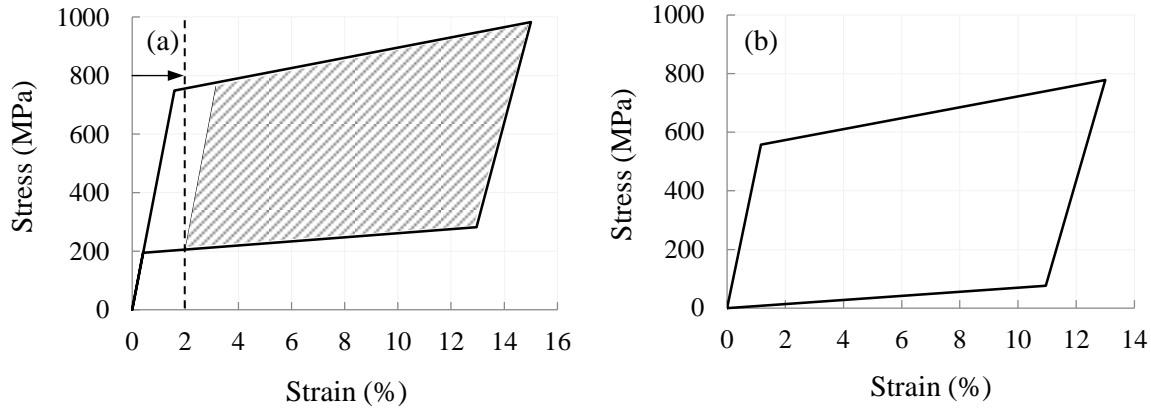
Figure 5.17. Stress-strain curve of ferrous SMA (FeNCATB);
(a) regular (non-pre-strained) wire, (b) 2% pre-strained wire

Figure 5.17b describes the stress-strain curve of the SMA wire with a 2% pre-strain. In pre-strained wires, the strain at the completion of forward phase transformation (8%) and the maximum strain in the fully martensite phase (13%) correspond to stresses of 620 MPa and 780 MPa, respectively, which are much lower than those of the regular (non-pre-strained) SMA wire (820 MPa and 980 MPa, respectively). Thus, pre-strained SMA wires have a lower effect on the lateral stiffening of the NRB which can be considered as a desirable effect.

In order to investigate the effect of pre-straining on the performance of NRBs, SMA wires with different amount of pre-strain are used in SMA-NRB-C2. Figure 5.18 depicts the hysteresis shear behaviour of SMA-NRB-C2s with 0%, 2%, and 4% pre-strained wires. All elastomeric isolators are subjected to three shear strain amplitudes (100%, 150%, and 200%) with horizontal frequency of 0.2 Hz and 6 MPa vertical pressure. As can be seen in Figure 5.18, the maximum shear force in SMA-NRB-C2 is reduced when pre-strained wires are used. The reason is that the stress generated in the SMA wires decreases when they are installed with a pre-strain due to a shift in the stress-strain curve. Consequently, a lower amount of force is exerted to the base isolator from pre-strained SMA wires.
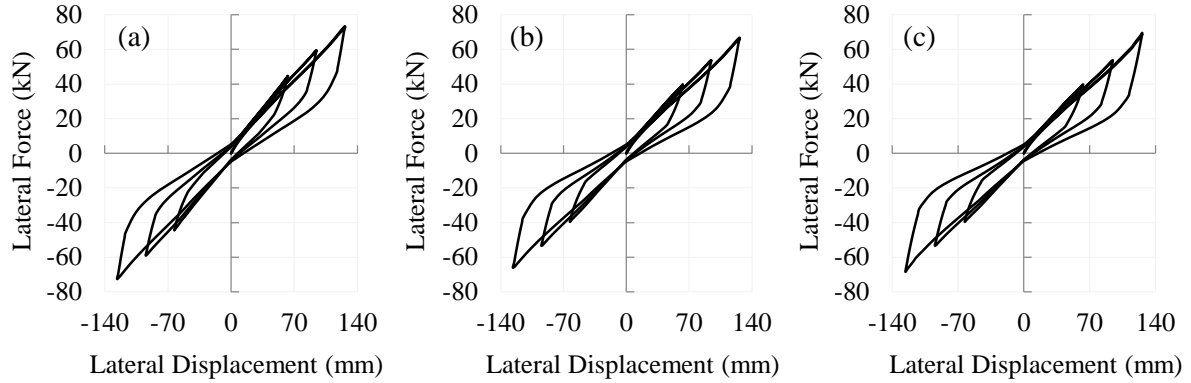
Figure 5.18. Lateral force-deflection curve of SMA-NRB-C2 for different amounts of pre-strain in SMA wires; (a) $\varepsilon_0 = 0\%$, (b) $\varepsilon_0 = 2\%$, and (c) $\varepsilon_0 = 4\%$; $\gamma = 100\%$, 150%, and 200%

When 2% pre-strained SMA wires are used, the effective horizontal stiffness of the rubber bearing decreases compared to the SMA-NRB-C2 with 0% pre-strain. According to Table 5.11, by comparing the horizontal stiffnesses at 200% shear strain amplitude, it is observed that 45% increase for SMA-NRB-C2 with $\varepsilon_0 = 0$ reduces to 32% increase for SMA-NRB-C2 with $\varepsilon_0 = 2\%$. However, increasing the amount of pre-strain from 2% to 4% has negligible effect on the lateral flexibility of the SMA-NRB-C2. 2% pre-strained SMA wires can considerably reduce the large yield stress though, when the amount of pre-strain increases to 4%, the hysteresis curve of SMA slightly changes compared to 2% pre-strain. In fact, when the pre-strain is greater than the strain corresponding to the forward phase transformation (1.6%), if it increases, the yield and the maximum stresses will not noticeably change. Therefore, the alteration of operational characteristics in SMA-NRB-C2 with 4% pre-strained wires will be negligible. Since the maximum axial stress generated in 4% pre-strained SMA wires is more than that in 2% pre-strained wires at 200% shear strain, the increase in the lateral stiffness of the SMA-NRB-C2 with $\varepsilon_0 = 4\%$ at this shear strain is more (see Table 5.11).

Table 5.11. Operational characteristics of NRB-2 and SMA-NRB-C2

for different amounts of pre-strain

| | γ (%) | NRB-2 | SMA-NRB-C2 | | |
			$\varepsilon_0 = 0\%$ $(\Delta_{NRB})^*$	$\varepsilon_0 = 2\%$ $(\Delta_{NRB})^*$	$\varepsilon_0 = 4\%$ $(\Delta_{NRB})^*$
Horizontal Stiffness (kN/mm)	100	0.49	0.71 (44%)	0.63 (28%)	0.63 (28%)
	150	0.44	0.63 (44%)	0.57 (30%)	0.57 (30%)
	200	0.40	0.58 (45%)	0.53 (32%)	0.55 (37%)
Residual Deform. (mm)	100	8.5	7.3 (-14%)	8.2 (-4%)	8.3 (-2%)
	150	11.1	9.2 (-17%)	10.1 (-9%)	10.3 (-7%)
	200	18.1	13.7 (-24%)	15.4 (-15%)	15.3 (-16%)
Dissipated Energy (kJ)	100	0.9	1.23 (43%)	1.26 (47%)	1.27 (48%)
	150	1.6	2.65 (67%)	2.60 (64%)	2.63 (65%)
	200	3.0	4.81 (59%)	5.26 (74%)	4.85 (60%)
Viscous Damping (%)	100	7.0	6.9 (-1%)	8.0 (15%)	8.1 (16%)
	150	6.5	7.5 (16%)	8.2 (26%)	8.3 (27%)
	200	7.6	8.3 (10%)	10.0 (32%)	8.8 (17%)

[*]Difference between operational characteristics of SMA-NRB-C2s and those of the NRB-2

Although pre-straining SMA wires can increases the lateral flexibility as an advantage, it has negative effect on the reduction of the residual deformation of the SMA-NRB-C2 due to a decrease in the maximum stress induced in wires. For 100%, 150%, and 200% shear strain amplitudes, SMA-NRB-C2 with 0% pre-strain decreases the residual deformation of NRB-2 by 14%, 17%, and 24%, respectively, while, the SMA-NRB-C2 with 2% pre-strain decreases this specification by 4%, 9%, and 15%, respectively.

Figure 5.19a, b, c, and d show changes in the horizontal stiffness, the residual deformation, the energy dissipation capacity and the equivalent viscous damping of the NRB-2 and SMA-NRB-C2s by changing the pre-strain level, respectively. It can be observed that at shear strain amplitudes equal and smaller than 150%, the performance of smart NRBs with different pre-strains are almost the same in terms of the dissipated energy. However, SMA-NRB-C2s with pre-strained wires are more efficient in terms of the equivalent viscous damping since their restored elastic energy is lower than that of the SMA-NRB-C2 with 0% pre-strain. Moreover, at 200% shear strain, SMA-NRB-C2 with $\varepsilon_0 = 2\%$ has a higher energy dissipation capacity and equivalent viscous damping. Since the maximum shear force in the 4% pre-strained SMA-NRB-C2 is larger than that in the 2% pre-strained SMA-NRB-C2 at

200% shear strain, the lateral stiffness is increased. As a result, the equivalent viscous damping of the 4% pre-strained SMA-NRB-C2 decreases according to Equation (4.3). When the performance of SMA-NRB-C2s with different pre-strains are compared together, it is observed that the 2% pre-strained SMA-NRB-C2 is more efficient than the other smart NRBs in terms of the lateral flexibility, the energy dissipation capacity and the equivalent viscous damping.
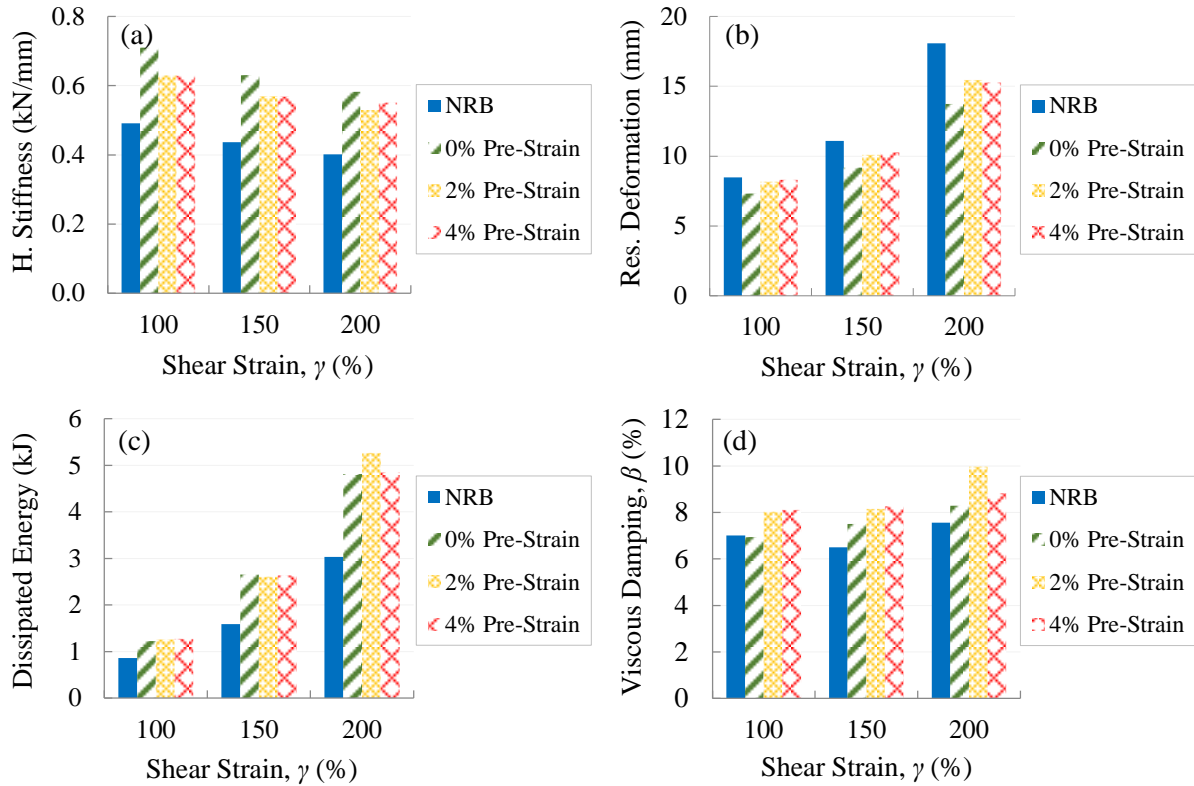
Figure 5.19. Operational characteristics of NRB-2 and SMA-NRB-C2s with different amounts of pre-strain in SMA wires; (a) effective horizontal stiffness, (b) residual deformation, (c) dissipated energy per cycle, (d) equivalent viscous damping

5.3 SMA-based High Damping Rubber Bearing (SMA-HDRB)

Similar to wire configurations proposed for SMA-NRB, two arrangements of wires (straight and cross) are applied to HDRB reinforced with CFRP composite. The effect of different factors, such as the type of SMA and the aspect ratio of bearing are studied on the performance of SMA-HDRBs. In this regard, seven CFR-HDRB are considered with different aspect ratios I. Their geometrical properties are listed in Table 5.12.

Table 5.12. Geometrical properties of CFR-HDRBs

CFR-HDRB	#1	#2	#3	#4	#5	#6	#7
L (mm)	250	250	250	250	250	250	250
W (mm)	250	250	250	250	250	250	250
H (mm)	60	70	80	90	100	110	120
t_s (mm)	15	15	15	15	15	15	15
t_e (mm)	4.74	4.73	4.72	4.72	4.71	4.71	4.71
t_f (mm)	0.31	0.31	0.31	0.31	0.31	0.31	0.31
n_e	6	8	10	12	14	16	18
n_f	5	7	9	11	13	15	17
R	0.12	0.16	0.20	0.24	0.28	0.32	0.36

The thickness of the elastomer layer, t_e, is kept constant (4.7 mm in all cases), while the number of HDR layers, n_e, is increased from 6 to 18.

5.3.1   SMA-HDRB Equipped with Straight Wires

As shown in Figure 5.2a, in the straight configuration, two continuous SMA wires are wound in two opposite sides of the rubber bearing. In the straight configuration, the total length of the SMA wires (L_{SMA}) required at each aspect ratio is presented in Table 5.13.

Table 5.13. Required length of SMA wire for seven CFR-HDRBs

in the straight and cross configurations

CFR-HDRB	#1	#2	#3	#4	#5	#6	#7
R	0.12	0.16	0.20	0.24	0.28	0.32	0.36
L_{SMA} (mm) (straight)	1240	1280	1320	1360	1400	1440	1480
L_{SMA} (mm) (cross)	2252.8	2262.7	2275.4	2290.9	2308.9	2329.6	2352.9

The strain in the SMA wires (ε_{SMA}) is a function of the shear strain amplitude, γ, and the aspect ratio, R. When the shear strain increases from 50% to 200%, the strain generated in SMA wires increases. The SMA strain also goes up by enhancing the aspect ratio of the base isolator. Figure 5.20a shows the variation of SMA wire strain by increasing the shear strain amplitude and the aspect ratio of the rubber bearing. At 200% shear strain amplitude, the SMA wires in all of the base isolators experience a strain greater than 10%. It can be also observed that the strain induced in SMA wires will not exceed 10% when the base isolator is subjected to shear strains lower than 100%. However, at larger shear strains, the SMA wire in the base isolator with high aspect ratio can experience as high as 27% strain.
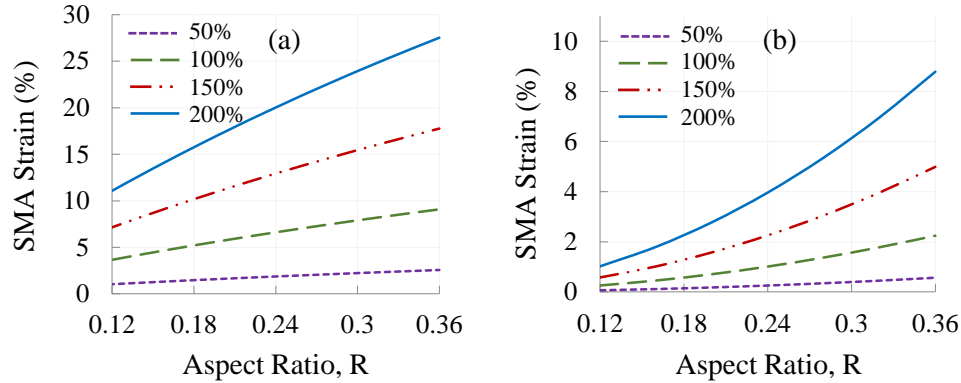
Figure 5.20. Variation of strain in SMA wire as a function of shear strain amplitude and aspect ratio for (a) straight configuration and (b) cross configuration

5.3.2 SMA-HDRB equipped with Cross Wires

In the cross configuration proposed in section 5.2.2, two continuous SMA wires are wrapped around the rubber bearing diagonally (see Figure 5.2b).

The total length of wires needed for this arrangement is presented in Table 5.13. Although a larger length of SMA wire is required for this configuration relative to the straight one, the generated strain in wires due to the lateral deflection of rubber bearing is much lower.

Figure 5.20 shows that in the case of cross configuration there is a significant reduction in the SMA wire strain compared to the straight configuration. At 200% shear strain amplitude with an aspect ratio of 0.36, the maximum strain induced in the SMA wires does not exceed 9%. It shows that unlike straight configuration in which SMAs can operate in a limited range of γ and R, different types of SMA can be used in the cross arrangement. Figure 5.20b illustrates that at each shear strain level, the strain in the SMA wires reaches its maximum value when the smart elastomeric isolator has the maximum considered aspect ratio.

5.3.3 Efficiency of Wires

In order to investigate the efficiencies of different types of SMAs (see Table 5.5) in the cross and straight configurations, two aspect ratios, 0.12 and 0.36, and four shear strain amplitudes, 50%, 100%, 150%, and 200%, are considered. According to Table 5.14, when the aspect ratio is 0.12, the maximum strain in the SMA wire, ε_{SMA}, at 200% shear strain is

1% for the cross configuration and 11.1% for the straight configuration. At same shear strain level, when the aspect ratio increases to 0.36, the SMA strain in the cross and straight configurations reaches 8.8% and 27.5%, respectively. Since most of the SMAs have superelastic strain lower than 6% (Table 5.5), SMA wires with the straight configuration cannot operate in a superelastic range at large shear strain amplitudes, especially in high-aspect-ratio elastomeric isolators. Whereas, the cross SMA wires can operate within an elastic range at large lateral cyclic displacements (150% and 200% shear strains). This fact demonstrates the effectiveness of the cross configuration over the straight one.

Table 5.14. Strain in SMA wires of SMA-HDRBs with different wire configurations and aspect ratios

Symbol	Wire Configuration	R	γ (%) 50	100	150	200
			ε_{SMA} (%)			
SMA-HDRB-C1	Cross	0.12	0.1	0.3	0.6	1.0
SMA-HDRB-S1	Straight		1.0	3.7	7.2	11.1
SMA-HDRB-C2	Cross	0.36	0.6	2.2	5.0	8.8
SMA-HDRB-S2	Straight		2.6	9.1	17.8	27.5

Table 5.15 presents the effectiveness of various types of SMA wires in cross configuration applied to the rubber bearing with two different aspect ratios. For a rubber bearing with a 0.12 aspect ratio, the maximum induced strain in wires with cross configuration is about 1% (see Table 5.14). However, in the case of straight arrangement, the strain in SMA wires exceeds the superelastic strain for most of the SMAs at shear strains higher than 150%. Another point is that, if a smart elastomeric base isolator with an aspect ratio of 0.36 is subjected to 200% shear strain, only FeNCATB (with about 13.5% superelastic strain range) can be utilized.

Table 5.15. Operational range of SMAs for different shear strains and aspect ratios

in cross configuration

γ (%) \ R	Ni Ti $\leq$0.24	0.36	Ni Ti$_{45}$ $\leq$0.24	0.36	Ti Ni$_{40}$Cu$_{10}$ $\leq$0.24	0.36	Cu Al Be $\leq$0.24	0.36	Fe Mn Al Ni $\leq$0.24	0.36	FeNCATB $\leq$0.24	0.36
$\leq$ 100	✓	✓	✓	✓	✓	✓	✓	✓	✓	✓	✓	✓
125	✓	✓	✓	✓	✓	✓	✓	✗	✓	✓	✓	✓
150	✓	✓	✓	✓	✓	✗	✓	✗	✓	✓	✓	✓
175	✓	✓	✓	✗	✓	✗	✗	✗	✓	✗	✓	✓
200	✓	✗	✓	✗	✓	✗	✗	✗	✓	✗	✓	✓

Based on the fact that the superelastic effect of SMA wires occurs at temperatures above the austenite finish temperature, the austenite finish temperature of the SMA wires should be lower than the ambient temperature. Since the minimum ambient temperature in countries with cold climatic conditions may go below -20°C, the austenite finish temperature of the SMA wire should be lower than this temperature. Therefore, NiTi$_{45}$ and FeNCATB, with respective A_f values of -10°C and -62°C, are chosen for SMA-HDRBs.

5.3.4   Finite Element Modelling

FE modelling is performed by considering appropriate element types, material properties, geometry, mesh, and boundary conditions (load and displacement). Element SOLID185 with eight nodes and three degrees of freedom (translation in x, y, and z directions) at each node is selected for both reinforcement and elastomeric layers. Hyperelasticity, stress stiffening, large deflection, and large strain can be modelled using this element. In order to simulate the large deformation of rubber layers at large shear strain amplitudes, the large-deflection effect is considered in full transient analyses. Steel shim used in HDRB is modelled as an isotropic material with a Young's modulus of 210 GPa and a Poisson's ratio of 0.3. Material properties of carbon fibre-reinforced sheets (carbon/epoxy), which behave as an orthotropic material, are the same as CFRP composite used in Chapter 3 (see Table 3.2). Mooney-Rivlin hyperelastic model is combined with Prony viscoelastic model in order to simulate the behaviour of HDR. As described in Chapter 3, section 3.2.6, material constants of both Mooney-Rivlin and Prony models are determined from experimental data gathered from the uniaxial tension-compression tests, the biaxial tension test, and the creep test conducted on HDR (Ibrahim, 2005). The material constants of hyper-viscoelastic model are listed in Table 5.16 for a 9-parameter Mooney-Rivlin model and a 2-parameter Prony model.

Table 5.16. Hyper-viscoelastic material model constants

Mooney-Rivlin Model		Prony Model
$C_{10} = 1.192$	$C_{12} = 0.000$	$\alpha_1 = 0.765$
$C_{01} = 0.547$	$C_{21} = -0.013$	$\tau_1 = 0.124$
$C_{11} = -0.038$	$C_{03} = 0.000$	$\alpha_2 = 0.061$
$C_{02} = 0.047$	$C_{30} = 0.002$	$\tau_2 = 65.82$
$C_{20} = 0.108$		

It should be noted that the FE model of HDR, which has been validated and verified in Chapter 3, section 3.3, is used here.

In generating the FE model of SMA-HDRB, same as SMA-NRB, a method of superposition is implemented in order to simplify the system by decoupling the rubber bearing and SMA wires. Here, a smooth contact with no friction is assumed between the steel hook and the SMA wire. The frictional force generated between the wire and the hook in the contact area can be minimized by using steel hooks with a very smooth surface and minimizing the contact area between wire and hook. Figure 5.21 shows a schematic of such a contact surface. Lubricating the contact surface can also reduce the friction generated due to back and forth movements of SMA wire inside the hook.
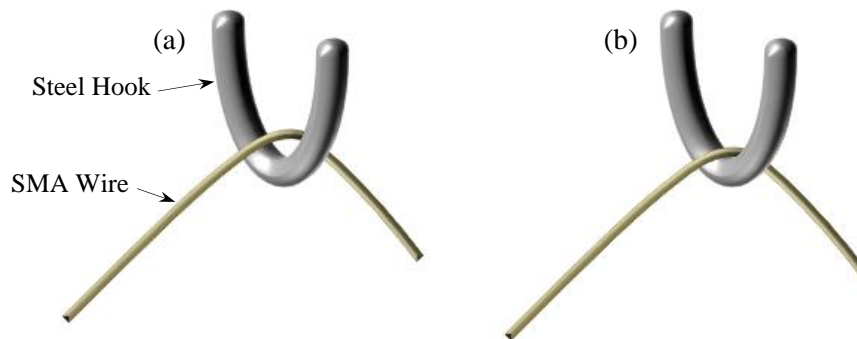
Figure 5.21. Schematic of steel hook and SMA wires in contact; (a) loose, (b) tight

Instead of modelling steel hooks and the contact between the hooks and continuous SMA wires, exerted forces to the elastomeric isolator due to SMA wires are considered. This assumption considerably reduces the complexity of the FE simulation. Otherwise, nonlinear full transient analyses for determining the hysteretic shear behaviour of base isolators with different aspect ratios and wire configurations might not converge, especially at high shear strain levels. In order to simplify the FE model, before analyzing the system, the strain generated in SMA wires at each pre-defined time step is calculated according to the geometry of the device and the arrangement of wires. Rubber bearings have deformations along three axes: x, y, and z. Here, it is assumed that the effects of torsion, rotation about all axes, delamination due to the shear deformation in laminated pad, and vibration in the vertical direction are ignored. Based on these simplifications, the formula of SMA strain in two cases is provided; (1) strain induced by displacements in x, y, and z directions and (2) strain induced by a displacement in the x direction. In the latter case, the effect of vertical

142

displacement, ΔZ, due a constant compressive load is assumed to be negligible on the SMA strain since the vertical deflection is very small compared to the lateral displacements in the *xy* plane.
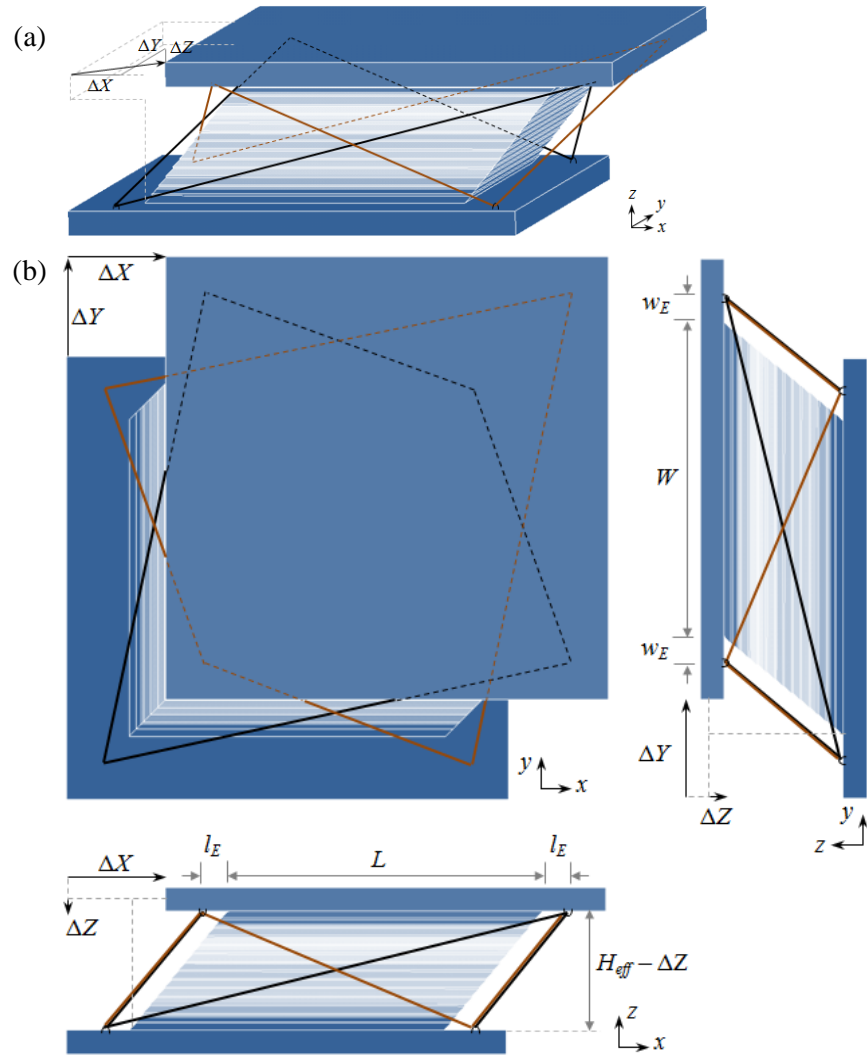
Figure 5.22. SMA-HDRB with a cross arrangement of wires subjected to displacements in *x*, *y*, and *z* directions; (a) 3D view, (b) orthographic views (top, front, and side views)

Figure 5.22 shows the rubber bearing equipped with cross SMA wires and subjected to a combination of vertical displacement in the *z* direction and lateral displacement in the *xy* plane. According to this figure, the strain in the wire is calculated using Equation (5.3). In this equation, the initial length, L_0, remains constant (Equation (5.4)) while, length *L* changes over the time since it is a function of displacements, ΔX, and ΔY (Equation (5.5)). It should

be noted that ΔZ has a constant value due to a constant vertical pressure applied on the isolator.

$$\varepsilon_{SMA} = \frac{L_{SMA} - L_{0\,SMA}}{L_{0\,SMA}} \tag{5.3}$$

$$L_{0\,SMA} = 2\left(\sqrt{(L + 2l_e)^2 + H_{eff}^2} + \sqrt{(W + 2w_e)^2 + H_{eff}^2}\right) \tag{5.4}$$

$$L_{SMA} = \sqrt{(L + 2l_e + \Delta X)^2 + \Delta Y^2 + \left(H_{eff} - \Delta Z\right)^2} \tag{5.5}$$
$$+ \sqrt{(L + 2l_e - \Delta X)^2 + \Delta Y^2 + \left(H_{eff} - \Delta Z\right)^2}$$
$$+ \sqrt{\Delta X^2 + (W + 2w_e + \Delta Y)^2 + \left(H_{eff} - \Delta Z\right)^2}$$
$$+ \sqrt{\Delta X^2 + (W + 2w_e - \Delta Y)^2 + \left(H_{eff} - \Delta Z\right)^2}$$

If the displacement is in one direction (x), considering aforementioned assumptions, Equation (5.5) will be simplified to Equation (5.6).

$$L_{SMA} = \sqrt{(L + 2l_e + \Delta X)^2 + H_{eff}{}^2} + \sqrt{(L + 2l_e - \Delta X)^2 + H_{eff}{}^2} \tag{5.6}$$
$$+ 2\sqrt{\Delta X^2 + (W + 2w_e)^2 + H_{eff}{}^2}$$

It should be noted that, for decoupling the effect of SMA wires from the rubber bearing in a general case, the effect of displacement in 3D on SMA strains can be calculated in order to find out the force in wires and add to the response of rubber bearing. It is assumed that isolators are subjected to a cyclic lateral displacement only in the x direction.

The axial stress in SMA wires can be determined from the strain based on the constitutive model of SMA (Auricchio, 2001). The idealized stress-strain curve for FeNCATB and NiTi$_{45}$ are plotted in Figure 5.7. Then, using the value of the axial stress and the direction of wires at each time step, the force vectors (with x, y, and z components) exerted from the SMA wire to the hooks are computed. Since the SMA wires with cross arrangement (wrapped around the elastomeric bearing) has a 3-D form, at each corner where the SMA wire is in contact with the steel hook, the generated force along the wires has components in all three directions of x, y, and z. In the decoupled system, all of these components are taken into account for FE simulations.

5.3.5   Results and Discussions

Based on the nonlinear material model of HDR, which has been verified with the experimental tests (Dall'Asta and Ragni, 2006), finite element analyses (FEAs) have been performed to simulate the behaviour of the SMA-HDRB using ANSYS (ANSYS Mechanical APDL, Release 14.0). By calculating the hysteretic response of SMA-HDRBs subjected to a frequency of 0.2 Hz and 6 MPa vertical pressure, the influence of the shear strain amplitude, the aspect ratio of rubber bearing, the types of SMA, the wire arrangement, the thickness of SMA wires, and the pre-strain in SMA wires on the performance of base isolators have been assessed.

5.3.5.1   Fe- and NiTi-based SMA wires

FeNCATB and $NiTi_{45}$ wires having cross configurations are used in SMA-HDRBs with aspect ratios of 0.12 (SMA-HDRB-C1). Both types of SMA wires have the same cross sectional areas (19.6 mm^2). Figure 5.23 shows lateral force-deflection curves of SMA-HDRB-C1s consisting of different types of SMA at different shear strain amplitudes. According to Table 5.14, at 200% shear strain, the strain in SMA wires reaches 1.0%. As shown in Figure 5.7, the strain at which the forward phase transformation is started in FeNCATB and $NiTi_{45}$ wires is 1.6% and 0.6%, respectively. Consequently, when the SMA-HDRB-C1 equipped with $NiTi_{45}$ is subjected to 200% shear strain, wires enter the phase transformation region (see Figure 5.7). The maximum shear force in smart rubber bearings at $\gamma = 200\%$ is 141 kN and 147 kN when FeNCATB and $NiTI_{45}$ wires are used, respectively. The reason is that $NiTi_{45}$ has a higher elastic stiffness (in austenite phase) compared to FeNCATB and as a result, a higher axial stress is generated in $NiTi_{45}$ wire for same amount of strain in wires. However, the performances of SMA-HDRB-C1s are very similar when ferrous and NiTi-based SMA wires are implemented. This fact can be understood by comparing the effective horizontal stiffnesses and residual deformations of SMA-HDRB-C1s according to Table 5.17. This consistency in results is due to a low amount of strain in wires (1%), which is much smaller than the superelastic strain for both types of SMA wires. In other words, if the wire strain increases by increasing the aspect ratio of rubber bearing or changing the wire configuration, the behaviours of SMA-HDRBs will vary.

145
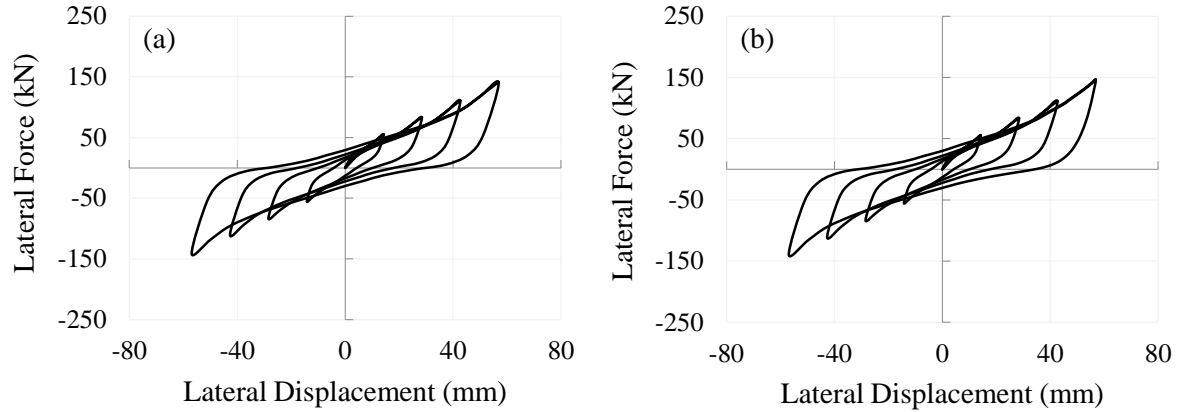
Figure 5.23. Hysteresis curves of SMA-HDRB-C1; (a) FeNCATB SMA, (b) NiTi$_{45}$ SMA

($\gamma = 50\%, 100\%, 150\%, 200\%$)

Table 5.17. Effective horizontal stiffness and residual deformation of SMA-HDRB-C1s

with FeNCATB and NiTi$_{45}$ wires

| γ (%) | FeNCATB | | | | NiTi$_{45}$ | | | |
	K_H (kN/mm)	Δ_{KH} (%)	R.D. (mm)	Δ_{RD} (%)	K_H (kN/mm)	Δ_{KH} (%)	R.D. (mm)	Δ_{RD} (%)
50	3.89	0	4.3	-11	3.89	0	4	-10.9
100	2.93	0	10.3	-12	2.94	0	10	-11.5
150	2.60	0	18.1	-14	2.61	0	18	-13.4
200	2.49	0	29.5	-16	2.58	0	34	-14.6

Note: Δ is the relative difference between performance characteristics of SMA-HDRBs and CFR-HDRB

5.3.5.2 Low Aspect Ratio SMA-HDRB

Figure 5.24 shows the lateral force-deflection curves of the CFR-HDRB with two aspect ratios of 0.12 and 0.36 at four different shear strain amplitudes. Figure 5.25 depicts the hysteresis loops of low-aspect-ratio SMA-HDRBs ($R = 0.12$), which are equipped with ferrous SMA wires in the cross configuration (SMA-HDRB-C1) and the straight configuration (SMA-HDRB-S1). Wires in both arrangements have the same cross sectional areas (19.6 mm^2).
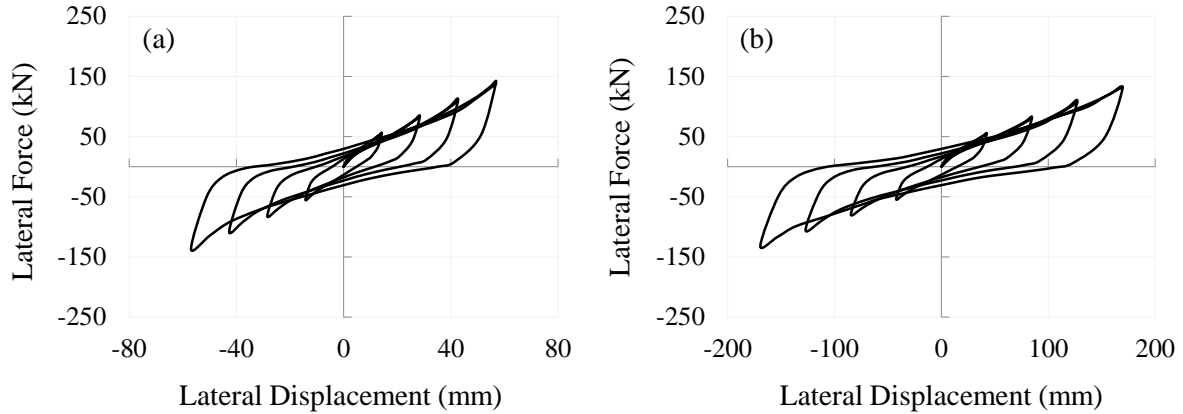
Figure 5.24. Hysteresis curves of CFR-HDRB; (a) $R = 0.12$, (b) $R = 0.36$

($\gamma = 50\%, 100\%, 150\%, 200\%$)
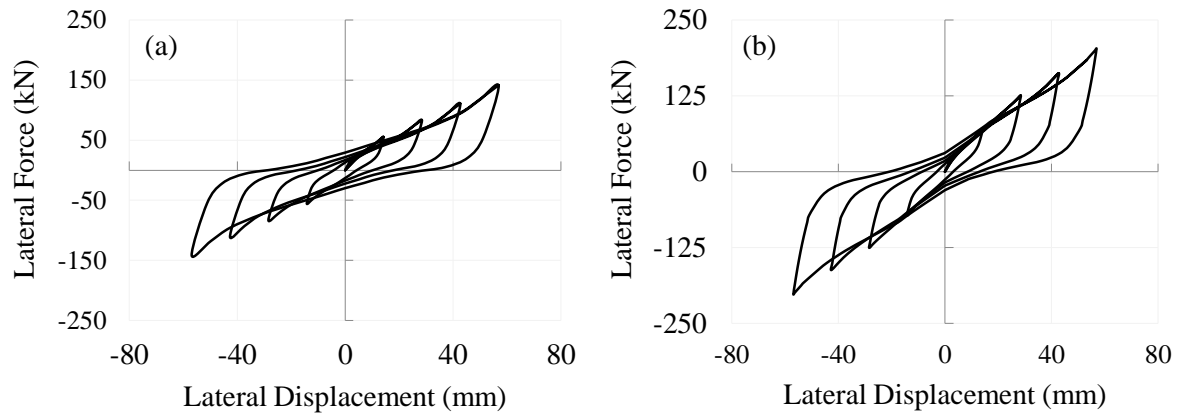
Figure 5.25. Hysteresis curves of (a) SMA-HDRB-C1, (b) SMA-HDRB-S1

($\gamma = 50\%, 100\%, 150\%, 200\%$)

By comparing the hysteretic behaviours of CFR-HDRB (Figure 5.24a) and SMA-HDRB-C1 and SMA-HDRB-S1 (Figure 5.25), it is observed that the effective horizontal stiffness and the residual deformation change due to the use of SMA wires. When the stress along the SMA wires increases, a forward phase transformation from austenite to martensite occurs in the wires. As a result, the horizontal component of the force exerted to the rubber bearing noticeably goes up in the opposite direction of the lateral cyclic displacements. This increase in the lateral force causes horizontal stiffening and re-centring in the whole system. Therefore, the effective horizontal stiffness increases and the residual deformation decreases.

The strain induced in the SMA wires in the straight configuration increases with a very high rate from 1.0% at 50% shear strain to 11.1% at 200% shear strain (Table 5.14). As a result, the stress along the SMA wires increases rapidly. In such a situation, using

147

FeNCATB wires instead of NiTi$_{45}$ wires is advantageous since FeNCATB has a higher superelastic strain range (13.5%).

Table 5.18 and Table 5.19 demonstrate the changes in the effective horizontal stiffness and the residual deformation, respectively, by changing the arrangement of wires for the aspect ratio of 0.12. In the cross configuration (SMA-HDRB-C1), slight changes in the stiffness and the residual deformation are observed compared to performance characteristics of the CFR-HDRB. On the other hand, when SMA wires are installed in the straight configuration (SMA-HDRB-S1), the horizontal stiffness increases and the residual deformation considerably decreases. This is because of a large amount of stress generated in SMA wires due to the higher elongation compared to the wires with cross arrangement.

Table 5.18. Effective horizontal stiffness of CFR-HDRB and SMA-HDRBs ($R = 0.12$)

γ (%)	CFR-HDRB K_H (kN/mm)	SMA-HDRB-C1 K_H (kN/mm)	Δ_{KH} (%)	SMA-HDRB-S1 K_H (kN/mm)	Δ_{KH} (%)
50	3.93	3.89	0	5.03	28
100	2.95	2.93	0	4.41	50
150	2.61	2.60	0	3.80	46
200	2.48	2.49	0	3.56	43

Note: Δ is the relative difference between effective horizontal stiffnesses of SMA-HDRBs and CFR-HDRB

Table 5.19. Residual deformation of CFR-HDRB and SMA-HDRBs ($R = 0.12$)

γ (%)	CFR-HDRB $R.D.$ (mm)	SMA-HDRB-C1 $R.D.$ (mm)	Δ_{RD} (%)	SMA-HDRB-S1 $R.D.$ (mm)	Δ_{RD} (%)
50	4.8	4.3	-11	3.1	-36
100	11.6	10.3	-11	8.5	-27
150	21.1	18.1	-14	13.0	-38
200	35.2	29.5	-16	18.3	-48

Note: Δ is the relative difference between residual deformations of SMA-HDRBs and CFR-HDRB

As can be seen in Figure 5.25, Table 5.18, and Table 5.19, at 200% shear strain, although the phase transformation in the FeNCATB wires is not completed, a high amount of yield stress, defined as the starting stress for the forward phase transformation, causes a significant growth of 43% in the effective horizontal stiffness and a high reduction of 48% in

the residual deformation. It is also observed that, for rubber bearings with low aspect ratio (0.12), the performance of SMA-HDRB-S1 is superior to that of the SMA-HDRB-C1.

5.3.5.3 High Aspect Ratio SMA-HDRB

Figure 5.26b depicts the lateral force-deflection curves of SMA-HDRBs with an aspect ratio of 0.36 and two wires arrangements. Similar to the previous cases, SMA wires used in the cross and the straight configurations have equal cross sectional area (19.6 mm^2). In the cross configuration (SMA-HDRB-C2), for shear strain amplitudes up to 150%, the maximum strain induced in the SMA wires is 5% which is lower than the superelastic strain range of FeNCATB. In the SMA-HDRB-S2, when the aspect ratio is 0.36, the strain in the SMA wire increases from 2.6% to 27.5% with increasing the shear strain from 50% to 200%. At 150% and 200% shear strain levels, the strain generated in the straight FeNCATB wires is higher than the superelastic strain (13.5%). As a result, FeNCATB SMA wires undergo a plastic deformation. Since the plastic deformation substantially degrade the performance of SMA wires subjected to cyclic loadings, the lateral force-deflection curves of SMA-HDRB-S2 are plotted for the first cycle at 150% and 200% shear strains.
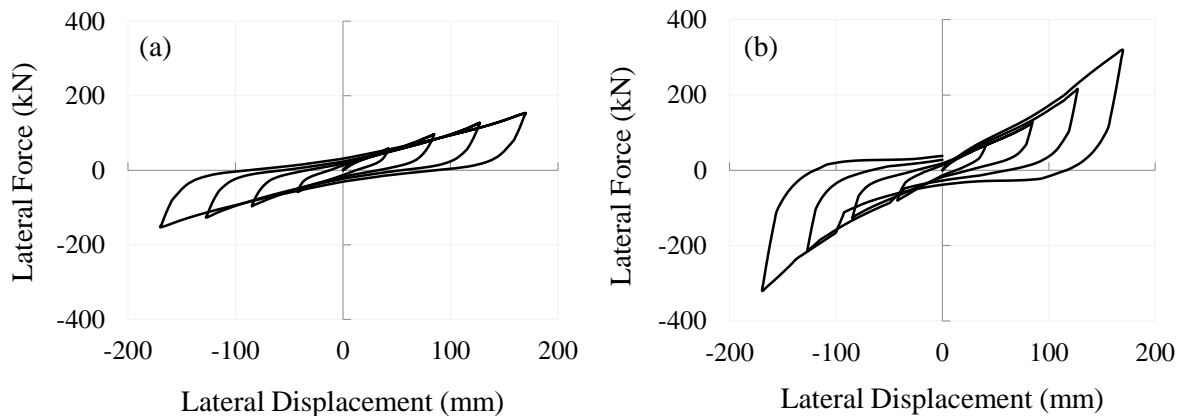
Figure 5.26. Hysteresis curves of (a) SMA-HDRB-C2, (b) SMA-HDRB-S2
($\gamma = 50\%, 100\%, 150\%, 200\%$)

By comparing the hysteresis curves of two high-aspect-ratio SMA-HDRBs (Figure 5.26), it is observed that the effective horizontal stiffness significantly increases when the SMA wires are mounted in the straight arrangement. In order to investigate the effect of SMA wires subjected to strains higher than superelastic strain range, the hysteretic shear behaviour of SMA-HDRB-S2 is re-plotted at shear strain of 150% in Figure 5.27. As

149

can be seen in Figure 5.27, the lateral force does not follow the path indicated by dashed lines. SMA-HDRB-S2 experiences a rapid change in the lateral force at around -35 mm lateral displacement. Considering a complete cycle of lateral displacement, if SMA wires undergo a plastic deformation due to exceeding the superelastic strain, the deformation will remain in the wires when the bearing returns to its initial position in the first half cycle and as a result, the wires get loose at zero lateral displacement. Thus, in the second half cycle, by increasing the lateral displacement, SMA wires will not be effective up to a level of lateral displacement (-35 mm) at which the wires are fitted in their place. In this situation, the strain in SMA wires starts to increase from the plastic strain previously generated and not from zero. When the rubber bearing returns to its initial position in the second half cycle, the stress in SMA wires reaches zero before the lateral displacement reaches zero (at about -50 mm). Therefore, compared to a case in which no plastic deformation happens in SMA wires, the shear force in the base isolator decreases. The shear behaviour of SMA-HDRB-S2 at 200% shear strain can be interpreted similarly.
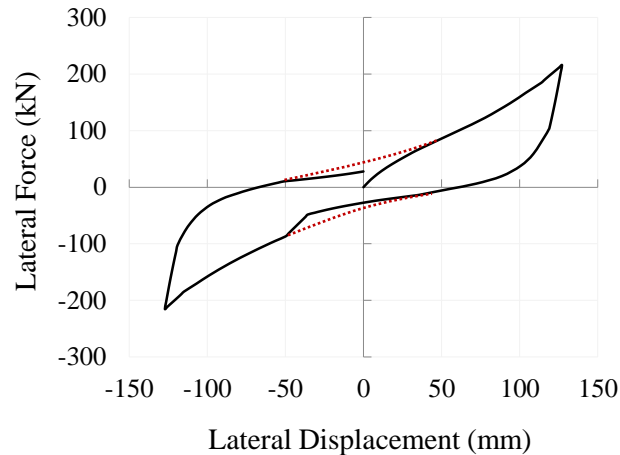
Figure 5.27. Hysteresis curves of SMA-HDRB-S2 ($\gamma = 150\%$)

Knowing the frequency of horizontal cyclic loading, and using Equation (5.3), which provides a relation between the lateral displacement and the strain in SMA wires, the exact time and the lateral displacement level at which the strain in SMA wires exceeds the superelastic strain limit can be specified. Subsequently, the time and the displacement at which the axial stress in wires vanishes while the rubber bearing is returning to its initial position can be determined from the stress-strain curve of SMA (Figure 5.7).

The maximum lateral forces in SMA-HDRB-C2 and SMA-HDRB-S2 at 200% shear strain are 153 kN and 320 kN, respectively. At this shear strain, the straight wires undergo 27.5% strain, which is much higher than the superelastic strain range of FeNCATB. After finishing the forward phase transformation in SMA wires, at strains above 15%, the stress increases rapidly with a rate equal to the martensitic modulus of elasticity. As a result, a significant amount of stress is generated in SMA wires when the strain reaches 27.5%, and consequently, the lateral stiffness of the base isolator considerably increases. Table 5.20 and Table 5.21 compare the performance characteristics of CFR-HDRB, SMA-HDRB-C2, and SMA-HDRB-S2 at different shear strain levels. At 50% shear strain, the effective horizontal stiffness of CFR-HDRB increases by 4% and 46%, respectively, when cross and straight wires are used. At the maximum considered shear strain (200%), the effective horizontal stiffnesses of SMA-HDRB-C2 and SMA-HDRB-S2 are 16% and 142% greater than that of CFR-HDRB, respectively.

Table 5.20. Effective horizontal stiffness of CFR-HDRB and SMA-HDRB ($R = 0.36$)

	CFR-HDRB	SMA-HDRB-C2		SMA-HDRB-S2	
γ (%)	K_H (kN/mm)	K_H (kN/mm)	Δ_{KH} (%)	K_H (kN/mm)	Δ_{KH} (%)
50	1.30	1.36	4	1.89	46
100	0.96	1.14	18	1.52	58
150	0.85	1.00	18	1.70	99
200	0.78	0.90	16	1.89	142

Note: Δ is the relative difference between effective horizontal stiffnesses of SMA-HDRBs and CFR-HDRB

Table 5.21. Residual deformation of CFR-HDRB and SMA-HDRBs ($R = 0.36$)

	CFR-HDRB	SMA-HDRB-C2		SMA-HDRB-S2	
γ (%)	R.D. (mm)	R.D. (mm)	Δ_{RD} (%)	R.D. (mm)	Δ_{RD} (%)
50	14.9	12.4	-17	12.7	-15
100	36.4	33.0	-9	24.7	-32
150	69.2	54.9	-21	60.8	-12
200	109.4	86.6	-22	116.3	6

Note: Δ is the relative difference between residual deformations of SMA-HDRBs and CFR-HDRB

The maximum reduction in the residual deformation of SMA-HDRB-C2 is 32%, which happens in the straight configuration at 100% shear strain (Table 5.21). Under this

condition, the effective horizontal stiffness increases about 58% (Table 5.20). Since SMA wires undergo plastic deformations at 150% and 200% shear strains, they cannot be fully recovered after unloading. As a result, their performance in improving the re-centring capability of rubber bearing is degraded. In the cross configuration, when the residual deformation decreases by 22% at a shear strain of 200%, the effective horizontal stiffness increases by 16%. This fact shows that although the straight configuration of SMA wires can reduce the residual deformation of rubber bearing more than the cross configuration, it has an inferior performance in terms of the lateral flexibility.

5.3.5.4 Thickness of SMA Wires

The dimension of SMA wire can affect the behaviour of smart rubber bearing subjected to a compressive and a cyclic shear loading. When the radius of the wire's cross section increases, the effective force exerted to the base isolator is significantly enhanced. As a case study, the cross FeNCATB wires with two different radii; 2.5 mm and 5.0 mm are chosen to be installed in a CFR-HDRB with an aspect ratio of 0.12. The corresponding cross sectional areas of SMA wires are 19.6 mm^2 and 78.5 mm^2. In reality, for the second case, two 2.5 mm wires can be used rather than a thick wire with a 5 mm radius. In order to investigate the effect of SMA wires' thickness on the performance of the rubber bearing, hysteretic behaviours of smart base isolators are compared (Figure 5.28).
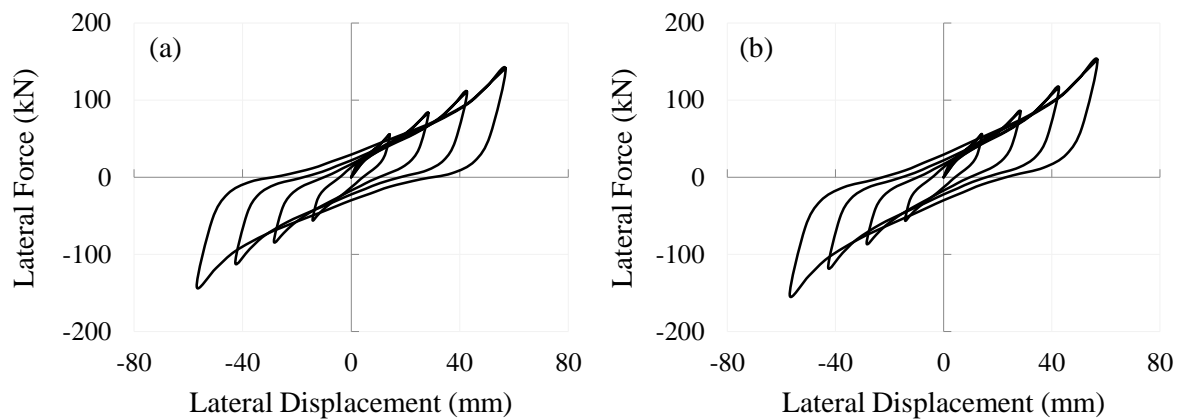
Figure 5.28. Hysteresis curves of Ferrous SMA-HDRB-C1; (a) r_{SMA} = 2.5 mm, (b) r_{SMA} = 5 mm (γ = 50%, 100%, 150%, and 200%)

152

Compared to CFR-HDRB, changes in the effective horizontal stiffness and the residual deformation of SMA-HDRBs are calculated with increasing the radius of SMA wires and shear strain amplitude (Table 5.22). When 2.5 mm SMA wires are used in a HDRB subjected to a 200% shear strain, the effective horizontal stiffness does not change while the residual deformation decreases about 16%. When 5.0 mm SMA wires are incorporated, the effective horizontal stiffness increases by 8% and the residual deformation decreases by 34%. This shows that using an SMA wire with a higher thickness improves the performance of the HDRB in terms of residual deformation reduction. The reason of this behaviour is the increase of the force generated in the SMA wires due to an increase in the cross sectional area of wires.

Table 5.22. The effective horizontal stiffness and the residual deformation of SMA-HDRB-C1 compared to those of the CFR-HDRB for different radii of SMA wire ($R = 0.12$)

r (mm) γ (%)	Effective Horizontal Stiffness (%)		Residual Deformation (%)	
	2.5	5	2.5	5
50	-0.9	-0.3	-11	-12
100	-0.7	2.0	-12	-16
150	-0.2	5.1	-14	-24
200	0.0	8.0	-16	-34

5.3.5.5 Pre-Strain in SMA Wires

In order to investigate the effect of pre-straining on the performance of smart elastomeric bearings, ferrous SMA wires with 2% pre-strain and a cross sectional area of 19.6 mm^2 are mounted on a HDRB with an aspect ratio of 0.36 in cross configuration. When SMA wires are wrapped around the rubber bearing by passing through the steel hooks bolted to the steel end plates, both ends of the wire are attached to a slotted hexagonal head bolt which is mounted in a small box (housing). According to Figure 5.29a, ends of the SMA wire are passed through a hole located in the middle of the bolt (see Figure 5.29b). In order to fix the wire from sliding inside the bolt, before applying a pre-stress, wire is wound around the bolt. To apply a pre-strain to SMA wires, the bolt is rotated and as a result, wires are subjected to a tensile stress. Accordingly, a specific amount of pre-strain is generated in the stretched wires (e.g. 2% pre-strain). The advantage of the proposed mechanism is its high accuracy in adjusting the level of pre-strain by accurately tightening the bolt. In fact, the

level of pre-strain can be controlled by considering the perimeter of the screw and the number of rotation applied to it.
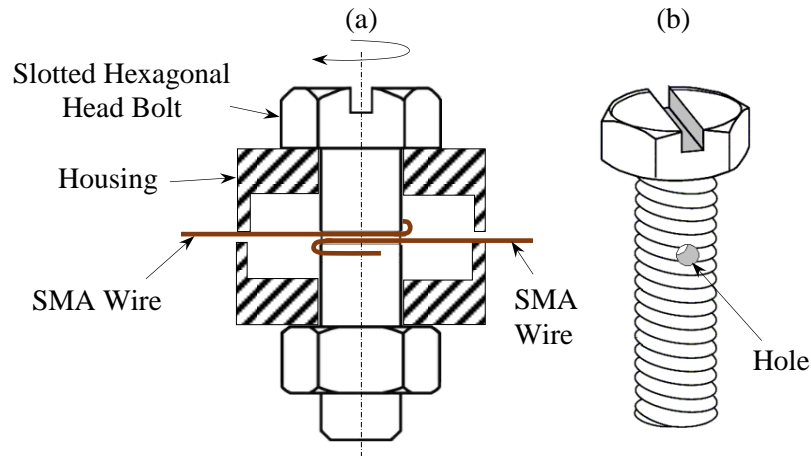
Figure 5.29. Adjustable mechanism for fixing the SMA wire and applying pre-strain; (a) side view of the mechanism, (b) 3D view of slotted hexagonal head bolt with a hole in the middle

Figure 5.30a depicts the hysteresis shear behaviour of a CFR-HDRB, an SMA-HDRB without pre-strain (SMA-HDRB), and an SMA-HDRB with 2% pre-strain. The areas of cross section of SMA wires are the same (19.6 mm^2). All rubber bearings are subjected to 200% shear strain and 6 MPa vertical pressure.
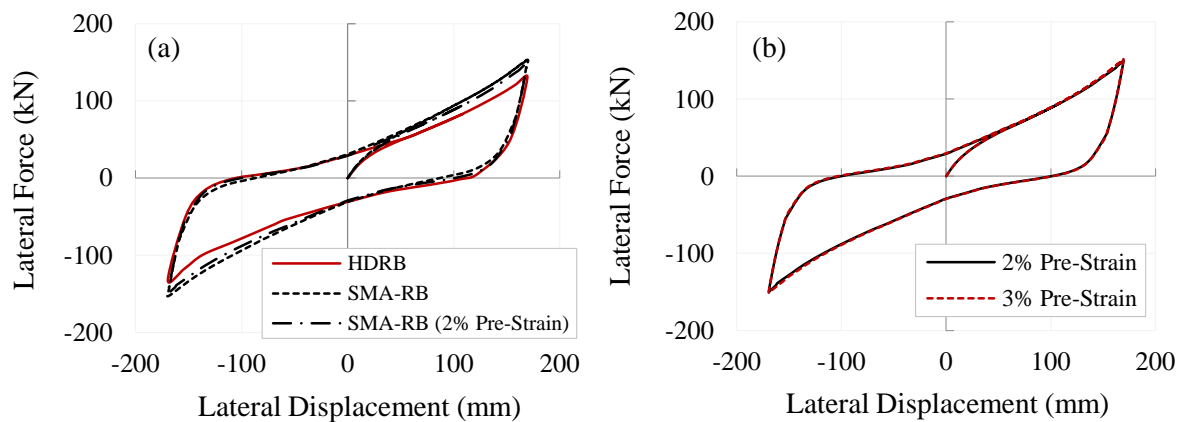
Figure 5.30. Lateral force-displacement curves of (a) CFR-HDRB, SMA-HDRB-C2, and SMA-HDRB-C2 with 2% pre-strain, (b) SMA-HDRB-C2 with 2% and 3% pre-strains ($\gamma = 200\%$)

When 2% pre-strained SMA wires are used, the decrease in the residual deformation is greater and the increase in the effective horizontal stiffness is lower compared to those of

the non-pre-strained SMA-HDRB. These changes show that pre-strained SMA wires can improve the efficiency of the smart rubber bearing more than the regular SMA wires can do.

Changes in the effective horizontal stiffness and the residual deformation are listed in Table 5.23. The effective horizontal stiffness of the SMA-HDRB-C2 is 16% more than that of the HDRB reinforced with CFRP composite plates. When 2% pre-strained SMA wires are used, the effective horizontal stiffness increases to 0.87 kN/mm which is 14% higher than that of CFR-HDRB. This shows that the reduction in the lateral flexibility of SMA-HDRB can be controlled by pre-straining SMA wires. The reason for this behaviour is the lower amount of stress induced in the pre-strained SMA wires after the completion of the forward phase transformation. On the other hand, compared to the CFR-HDRB, the residual deformations of the SMA-HDRB and 2% pre-strained SMA-HDRB are reduced by 22% and 8%, respectively. When the 2% pre-strained SMA wires are elongated due to the horizontal cyclic displacement, the forward phase transformation in the wires starts and finishes at lower stress and strain levels compared to a case in which regular SMA wires are used. Therefore, a smart HDRB with pre-strained SMA wires cannot reduce the residual deformation of CFR-HDRB as much as SMA-HDRB with regular SMA wires.

Table 5.23. Characteristics of CFR-HDRB and SMA-HDRB-C2 for different amounts of pre-strain in SMA wires ($R = 0.36$, $\gamma = 200\%$)

	Horizontal Stiffness		Residual Deformation	
Rubber Bearing	K_H (kN/mm)	Δ_{KH} (%)	$R.D.$ (mm)	Δ_{RD} (%)
CFR-HDRB	0.78		109.4	
SMA-HDRB	0.90	16%	85.8	-22%
SMA-HDRB (2% Pre-Strain)	0.86	14%	100.3	-8%
SMA-HDRB (3% Pre-Strain)	0.89	15%	101.1	-8%

Note: Δ is the relative difference in operational characteristics of SMA-HDRB-C2 and CFR-HDRB

In order to evaluate how the amount of pre-strain in SMA wires affect the performance of the smart rubber bearing, considering same size of cross section, SMA wires with 3% pre-strain are used in the SMA-HDRB. The hysteretic behaviour and performance characteristics of the SMA-HDRB with 3% pre-strained wires are compared to those of the SMA-HDRB with 2% pre-strained SMA wires.

Figure 5.30b demonstrates that changes in the hysteretic response of SMA-HDRBs are negligible when the magnitude of pre-strain increases in the SMA wire. According to Table 5.23, the increase in the effective horizontal stiffness of the SMA-HDRB with 3% pre-strained wires is slightly higher than that of the 2% pre-strained SMA-HDRB. Under the maximum lateral displacement, a higher strain is generated in the 3% pre-strained SMA wires compared to the 2% pre-strained wires. As a result, the maximum stress at which SMA wires are fully martensitic will be larger in the SMA wires with 3% pre-strain. Therefore, a higher lateral force is applied to the rubber bearing from the 3% pre-strained wires and consequently, the horizontal stiffness of the 3% pre-strained SMA-HDRB increases by 15%. Since the stresses of starting and finishing phase transformation in the 2% pre-strained SMA wire are close to those of the 3% pre-strained wire, the performances of SMA-HDRBs with 2% and 3% pre-strains in reducing the residual deformation of the CFR-HDRB are the same (see Table 5.23).

5.4   SMA-based Lead Rubber Bearings (SMA-LRB)

Based on the model proposed for smart NRBs using SMA wires with the cross configuration (Hedayati Dezfuli and Alam, 2013c), similar idea can be applied to LRBs with rectangular cross section. As shown in Figure 5.31, double cross SMA wires are wrapped around the bearing by passing through steel hooks connected to the steel supporting end plates. The difference between this configuration (double cross configuration) and the one proposed in sections 5.2 and 5.3 (cross configuration) is that a symmetric arrangement with a larger amount of wire is used here. As a result, the effective stain in SMA wires generated due to the shear strain in the LRB decreases since wires have a higher initial length.
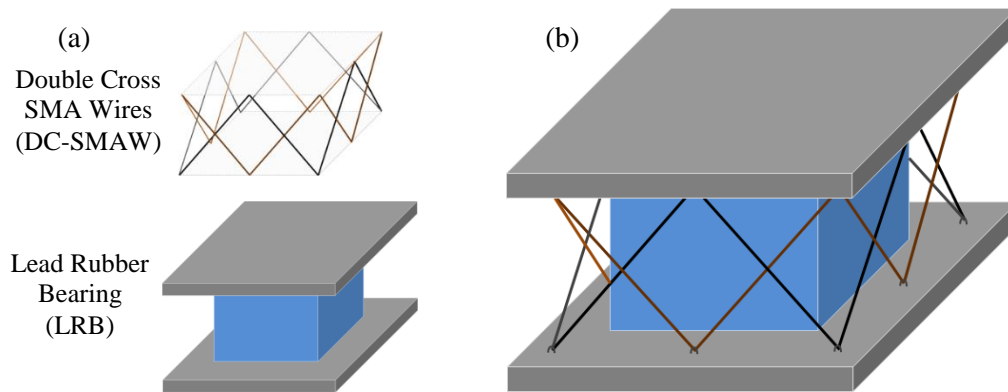
Figure 5.31. SMA-LRB; (a) decoupled systems, (b) integrated SMA-LRB

5.4.1 Finite Element Validation

In order to establish a valid, reliable, and accurate simulation for the response of SMA-LRB using FEM, the LRB should be validated with experimental tests. In this regard, the LRB experimentally tested by Abe et al. (2004) is modelled and then analyzed in ANSYS (ANSYS Mechanical APDL, Release 14.0). Then, the numerical results are compared to the experiment at different shear strain levels, γ, (50% and 150%). Figure 5.32 depicts the side and the top views of LRB adapted from (Abe et al., 2004).
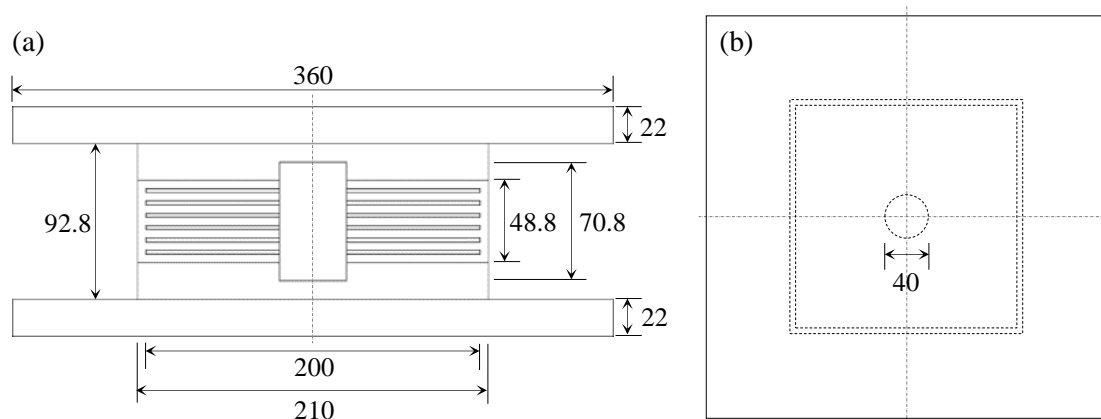
Figure 5.32. LRB used in the experimental tests; (a) side view, (b) top view (dimensions are in mm) (adapted from (Abe et al., 2004))

Defining element types, determining material models and mechanical properties, creating the geometry, meshing the model, defining the boundary and loading conditions as well as contact areas are steps that should be followed before solving and extracting the results in the FEM. The most challenging part is determining the material model since the

157

responses of LRB and SMA-LRB are nonlinear and highly dependent on the materials behaviour. Homogeneous structural element, SOLID185, with eight nodes and three degrees of freedom (translation in x, y, and z directions) at each node and with capability of modelling hyperelasticity, stress stiffening, large deflection, and large strain is chosen for steel shims, supporting plates, and rubber layers. Since elastomeric layers may undergo a large deformation at large shear strain levels, the large-deflection effect is considered in transient analyses. Reinforcement and supporting end plates are made of mild steel which is modelled as an isotropic material with an elastic modulus of 210 GPa, a yield strength of 247 MPa, and a Poisson's ratio of 0.3. Among different types of nonlinear material models available in ANSYS (ANSYS Mechanical APDL, Release 14.0), hyper-viscoelastic model could correctly capture the highly nonlinear behaviour of rubber materials under a combination of normal and shear deformations (Hedayati Dezfuli and Alam, 2012 and 2013a). In this regard, the Mooney-Rivlin hyperelastic model is combined with the Prony viscoelastic model and attributed to the elastomer. The material constants of the hyper-viscoelastic model are given in Table **5.24**.

Table 5.24. Material constants of the hyper-viscoelastic model

Mooney-Rivlin Model	Prony Model
$C_{10} = 0.232$	$\alpha_1 = 1.035$
$C_{01} = 0.107$	$\tau_1 = 0.101$
$C_{11} = -0.0004$	$\alpha_2 = 0.061$
	$\tau_2 = 65.82$

After creating the geometry of LRB according to the sizes indicated in Figure 5.32, mapped meshing is applied in order to discretize the whole model into a finite numbers of SOLID185 elements with a regular pattern. This method of meshing significantly decreases the processing time and accordingly shorten the converging time. Nodes at the bottom of the lower supporting end plate are completely fixed. All the nodes at the top of upper supporting plate move together in the vertical direction (z direction), since it is assumed that supporting steel plates and steel shims are rigid compared to the rubber layers which are flexible in the vertical and horizontal directions. Considering the geometry, loading conditions (combination of a uniform vertical compressive load and cyclic lateral displacements in the x

direction), as well as boundary conditions, the model has one plane of symmetry (plane *xz*) as shown in Figure 5.33.
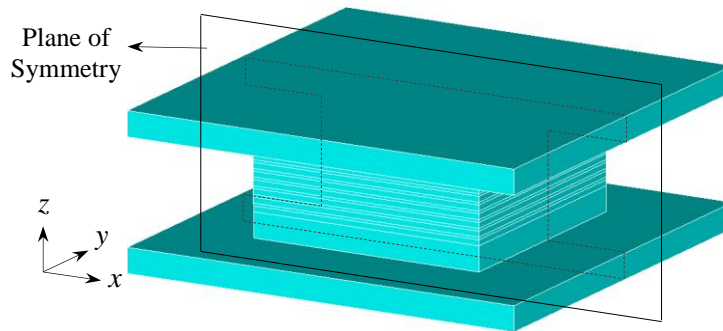
Figure 5.33. LRB modelled in ANSYS software

In order to noticeably decrease the processing time in transient analyses, the model is divided into two halves with respect to the plane of symmetry and just a half of the model is analyzed. In this regard, the symmetry boundary condition is applied to all nodes located on the plane of symmetry according to Figure 5.33.

Here, it is assumed that rubber layers are perfectly bonded to steel shims and steel fixing plates and also there is a perfect bonding between the supporting end plates and fixing plates. Another assumption is that the lead core is glued neither to the elastomer nor to the reinforcement. In this regard, contact areas are defined between the lead and other materials that surround the core. The contact pair consists of two surfaces; target and contact. The contact surface is the one that moves toward and potentially in contact with the target surface. The contact element type is considered to be surface-to-surface. Element CONTA173 with 4 nodes at each corner is used to defined a deformable contact surface which is located on the surface of 3D solid elements, SOLID185. Geometric characteristics of this element is the same as those of SOLID185. Contact occurs when the contact element surface penetrates into one of the target segment elements (TARGE170) on a specified target surface (ANSYS Documentation, Release 14.0). The target surface is discretized by a set of segment elements, TARGE170, and is paired with the associated contact surface.

The hysteresis curves (i.e. shear force versus shear strain) are obtained at 50% and 150% shear strain amplitudes (cyclic loadings in the x direction), a vertical pressure of 7.84 MPa, and a lateral frequency of 0.01 Hz (Abe et al. 2004). Figure 5.34 shows a good match between FE simulations and experimental tests. However, a small difference is observed

159

between numerical and experimental results because of the nonlinear material properties defined for elastomeric layers and the boundary condition (contact area) defined for the lead core. The shear strain is defined as the ratio of the lateral displacement to the total thickness of rubber layers. The maximum difference between the peak shear forces obtained through experiment and FEM is 9% at 50% shear strain and 14% at 150% shear strain. In terms of the energy dissipated per cycle, the maximum variation of two approaches is 3% and 1% for shear strains of 50% and 150%, respectively.
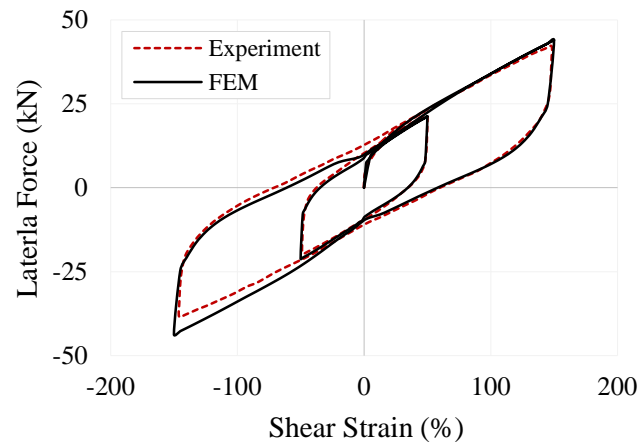
Figure 5.34. Hysteretic shear response of LRB at 50% and 150% shear strains obtained through FEM and experimental tests conducted by Abe et al. (2004)

5.4.2 Performance of SMA-LRB

After validating the FE model through experimental tests, the numerical simulation can be extended to other cases in which shear strain varies while the material properties and the boundary conditions are kept unchanged. In order to model the SMA-LRB in ANSYS, SMA wires are decoupled from the LRB (superposition method) and the FE model of LRB is used. Here, it should be noted that the simplification of symmetry boundary condition considered for LRB does not raise any problem in the FE analysis of SMA-based LRB since the double cross configuration of SMA wires proposed in this study also has the same plane of symmetry (see Figure 5.33). In all simulations, it is assumed that the rubber bearings are subjected to a combination of vertical pressure and uniaxial horizontal cyclic displacements (in the *x* direction). Figure 5.35 demonstrates the half model of SMA-LRB.
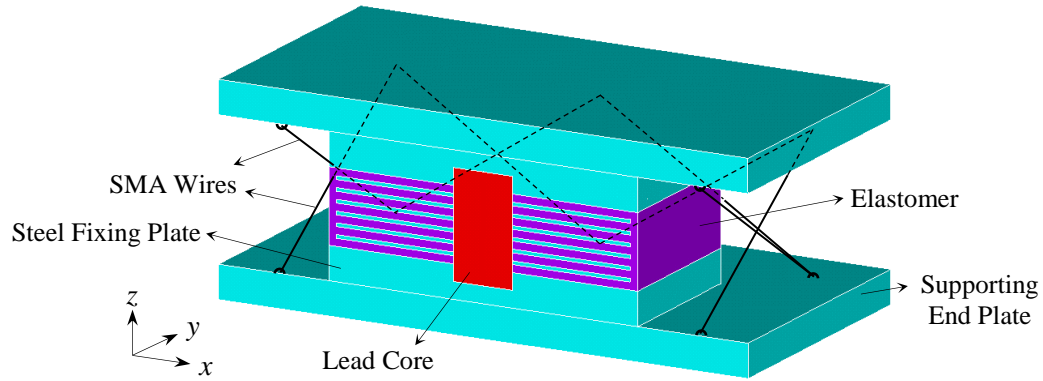
Figure 5.35. Half model of LRB equipped with double cross SMA wires

Same as what was discussed and assumed in section 5.2.4.2 for analyzing the SMA-NRB, the procedure of decoupling SMA wires from the LRB, which is depicted in Figure 5.36, is implemented here. In this approach, after defining the load pattern of cyclic lateral displacements, $x(t)$, the loading frequency, f_H, and the time increment, Δt, the length of SMA wire is calculated as a function of lateral displacement, $X = x(t)$, and size of LRB (Length, L, Width, W, and Height, H) at each time step. Knowing the initial length of wire, L_0, the strain in SMA wires, ε_{SMA} is computed and accordingly, the stress in wires is found based on the SMA constitutive model (stress-strain relation). In the next step, the axial force along the SMA wire having a circular cross section with a radius of r_{SMA} is calculated as a function of time. Then, considering the angles that the SMA wires make with respect to principal directions (x, y, and z) at each node (A, B, C …), components of the force (nodal force) are computed at each time step. Finally, the SMA wire-based LRB can be decoupled to two systems: LRB and nodal forces generated due to SMA wires as shown in the last step of the flowchart in Figure 5.36.

161
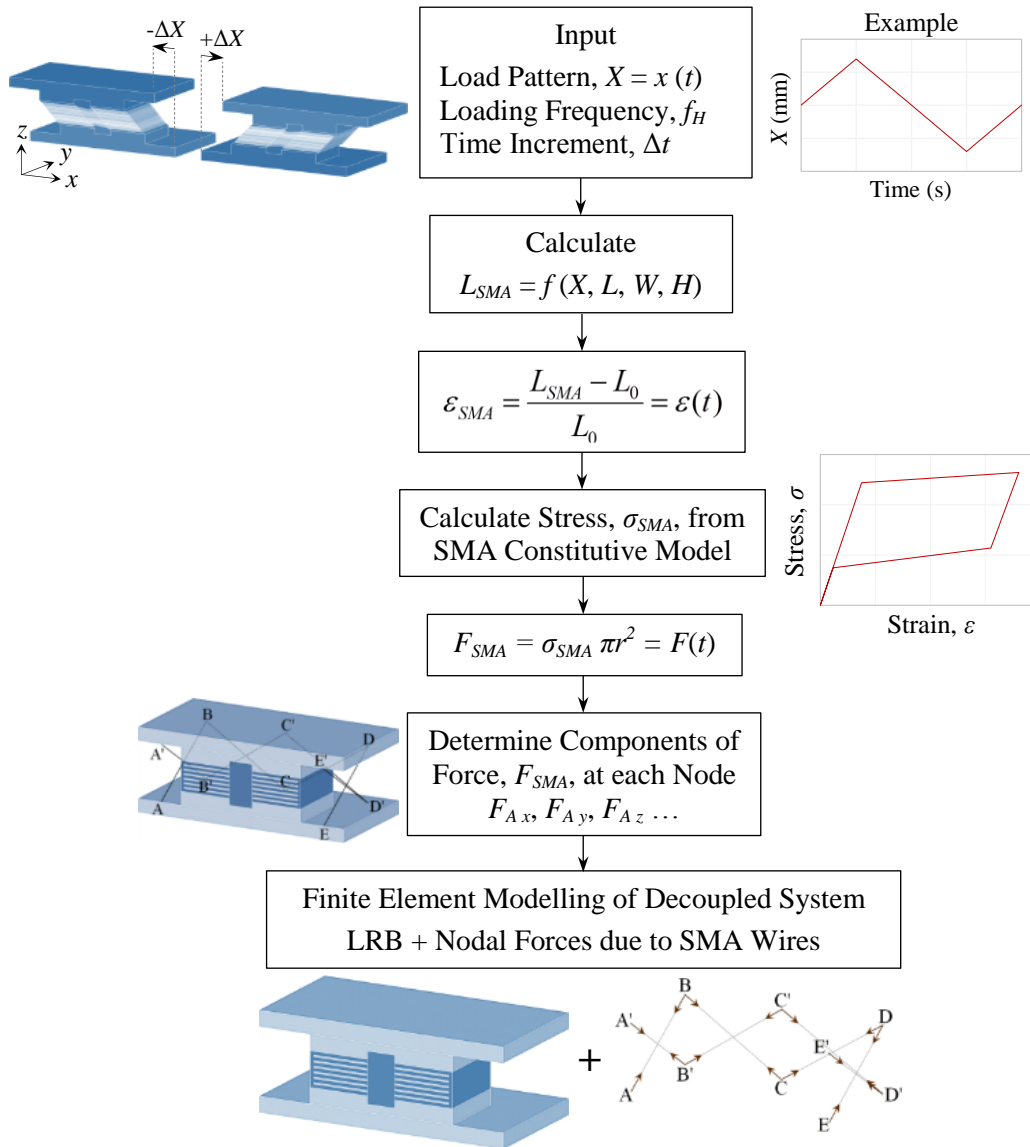
Figure 5.36. Procedure of decoupling SMA wires from LRB

After analyzing the decoupled system through a full transient analysis, the variation of lateral force can be calculated over the time when the shear strain increases from 50% to 200%. Figure 5.37 shows the hysteretic shear responses of LRB and SMA-LRBs with two different SMA wire's radii; 1.5 and 2.5 mm at different shear strain levels. In SMA-LRBs, ferrous SMA (FeNiCoAlTaB) with 13.5% superelastic strain (Tanaka et al., 2010) is used. This ferrous SMA has outstanding characteristics which make it superior to NiTi. It shows a superelastic strain (over 13%) which is almost double that of NiTi. Having the capability of exceptional cold and hot workability, it has a capacity of reaching 800 MPa in the

162

superelastic range. Ferrous SMA can be used along with magnetically activated materials and sensors (e.g. magnetic sensors) due to its ferromagnetic property. As a result, it can be implemented into new applications where such features are necessary such as construction, general manufacturing, and precision machinery (Tanaka et al., 2010; Omori et al., 2011).

At low shear strains (e.g. 50%), the behaviour of SMA-LRB is almost the same as that of the LRB for both wire's thicknesses (r_{SMA} = 1.5 and 2.5 mm). The reason is that at γ = 50%, SMA wires are not activated yet since no transformation happens from austenite to martensite. When the shear strain goes above 100%, the effect of the flag-shaped hysteresis of SMA can be observed on the overall behaviour of SMA-LRBs. The superelastic effect of this material (i.e. capability of returning back to its initial shape after a large deformation (e.g. up to 15%)) causes an improvement in the re-centring capability of smart rubber bearings. As observed in Figure 5.37, the effective lateral stiffness and energy dissipation capacity (i.e. the area inside the hysteresis loop) of the SMA-LRB increases and the residual deformation decreases at shear strains equal to and greater than 100% compared to those of LRB. When SMA wires with a higher radius (r_{SMA} = 2.5 mm) are used, the shear force noticeably increases as a result of an increase in the axial force in SMA wires, F_{SMA}. Therefore, compared to wires with lower radius, the superelastic effect of SMA is augmented on the response of LRB (see Figure 5.37b).
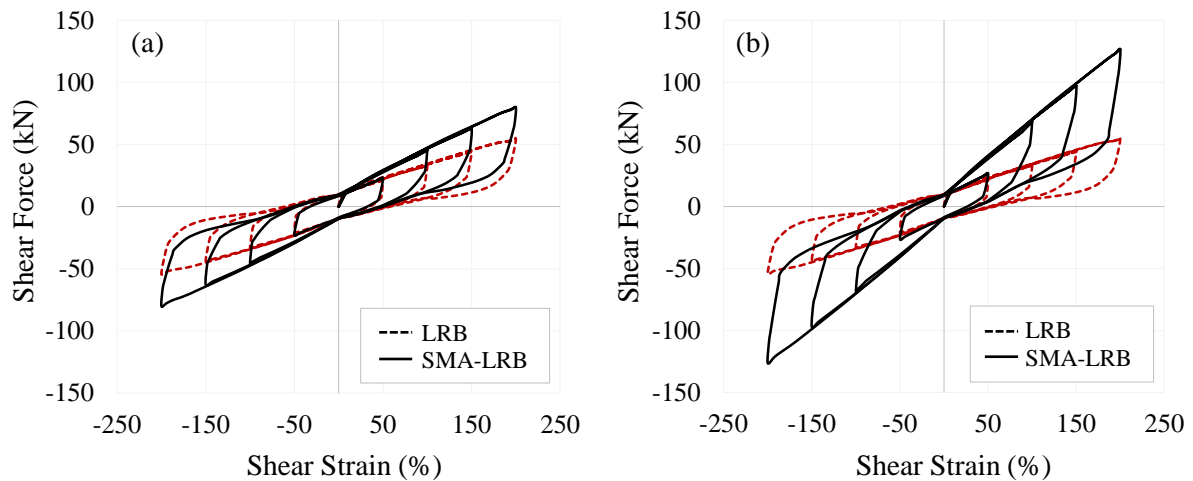
Figure 5.37. Shear force-strain hysteresis curves for LRB and SMA-LRB subjected to different shear strains (50%, 100%, 150%, and 200%); (a) r_{SMA} = 1.5 mm, (b) r_{SMA} = 2.5 mm

SMA wires with 1.5 mm radius increase the effective horizontal stiffness of LRB by 38% and 48% at shear strains of 100% and 200%, repectively. While, using wires with 2.5

mm radius leads to 108% and 133% increase in the effective horizontal stiffness at 100% and 200% shear strains, repectively. Changes of the peak shear force due to implementing SMA wires is same as that of the lateral stiffness. In terms of energy dissipation, SMA wires have significant effect on LRB since at 100% and 200% shear strains they can increase the energy dissipated per cycle of LRB by 12% and 24%, respectively, when the radius of wires is 1.5 mm and by 34% and 74%, respectively, when the radius of wires is 2.5 mm.

5.4.2.1   Pre-Strain in SMA Wires

SMA has a high initial elastic modulus in the austenite phase which increases the effective horizontal stiffness of the LRB before starting forward phase transformation (austenite to martensite). In other words, the lateral flexibility of the bearing significantly decreases before activating SMA wires. Since the unique characteristics of SMAs improve the behaviour of LRB when SMA is activated and generates a large hysteresis upon high-amplitude loadings, it will be highly beneficial if the flag-shaped hysteresis area of SMA enlarges and the effect of high initial elastic modulus is diminished. In order to achieve this goal, SMA wire goes through a process by which a specific amount of pre-strain is generated in the wire. In this process the SMA wire is first loaded up to a strain level greater than the defined pre-strain, ε_0, and then unloaded to ε_0. By generating the pre-strain, a positive initial stress called pre-stress produces in the wire as well.

In Figure 5.38 showing the pre-straining process indicated by dotted lines, the hysteretic behaviours of a regular and a 3% pre-strained SMA wire are compared to each other. In the first case (Figure 5.38a), the wire is elongated up to a strain of 1.84% due to 100% shear strain in the SMA-LRB while in the second case (Figure 5.38b), wire experiences 4.10% strain when the SMA-LRB is subjected to 150% shear strain amplitude. As can be observed, in both cases, the 3% pre-strained wire has a larger hysteresis (indicated by solid lines) compared to non-pre-strained SMA wire (indicated by dashed lines). The reason is that by pre-straining the SMA wire, it partially transforms to the martensite phase and as a result, when the stress increases and the strain goes above the pre-strain level, the forward phase transformation starts and completes sooner compared to a non-pre-strained wire.
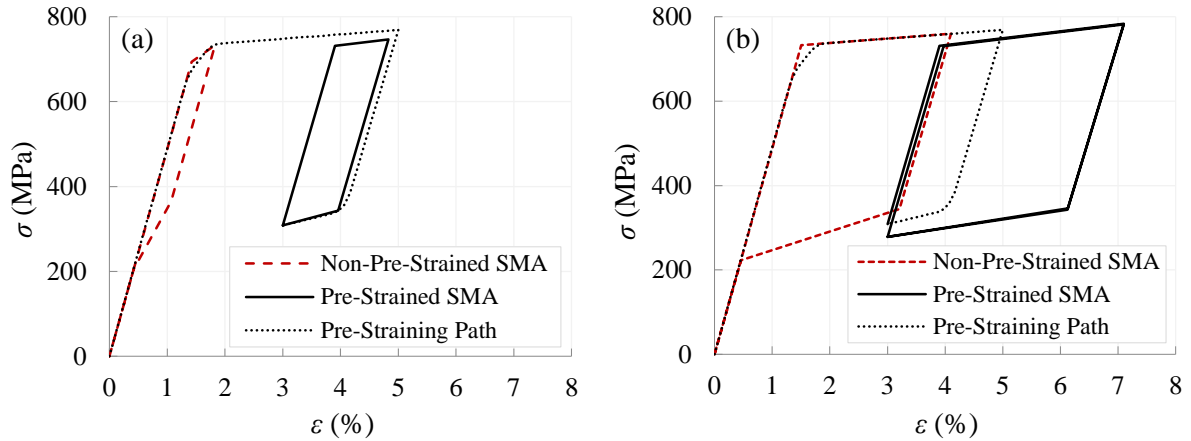
Figure 5.38. Stress-strain behaviours of non-pre-strained and 3% pre-strained SMA wires in SMA-LRB subjected to (a) 100% shear strain and (b) 150% shear strain

In order to explore the effect of pre-strained SMA wires on the behaviour of SMA-LRB and compare the performance of regular and pre-strained wires, hysteretic shear responses of LRB and smart LRB equipped with non-pre-strained wires (SMA-LRB) and pre-strained wires (SMA-LRB (PS)) are obtained. Same as previous part, the radius of SMA wire's cross section in the smart elastomeric isolators is considered to be 2.5 mm. The shear force-strain hysteresis curves of LRB and SMA-based LRBs are plotted in Figure 5.39 at two different strain levels; 100% and 150%.
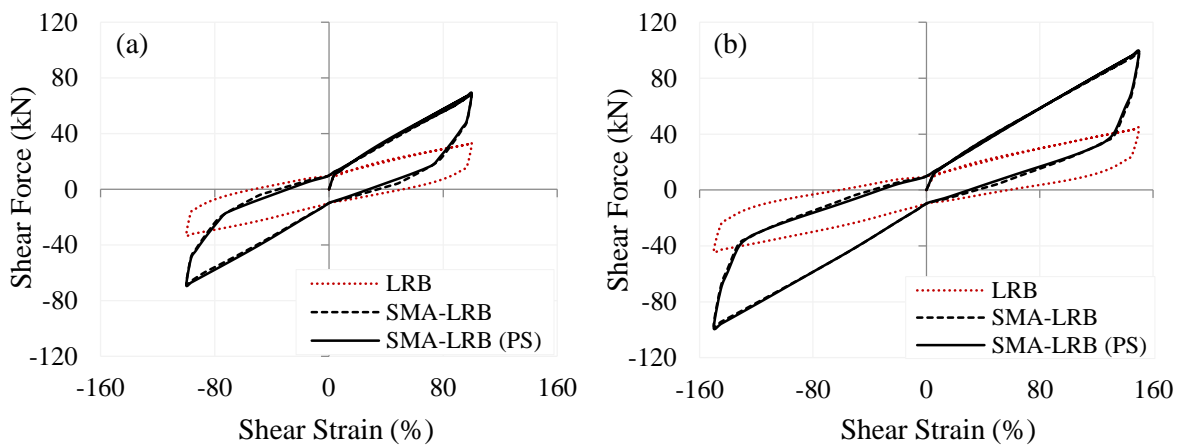
Figure 5.39. Shear force-strain hysteresis curves of LRB, SMA-LRB, and SMA-LRB (PS) ($\varepsilon_0 = 3\%$) under (a) 100% shear strain and (b) 150% shear strain

Shear hysteretic response of SMA-LRB (PS) demonstrates that using pre-strained SMA wires improves the behaviour of SMA-LRB in terms of residual deformation reduction.

in order to quantitatively compare SMA-LRB with and without pre-strain effect, the residual deformations (*R.D.*) of both bearings are compared at 100% and 150% shear strains in Table 5.25. According to the results, when pre-strained wires are used, the residual deformation of SMA-LRB is reduced by around 19% and 15% at shear strain amplitudes of 100% and 150%, respectively.

Table 5.25. Residual deformations of SMA-LRB and SMA-LRB (PS) at different shear strains

| Rubber Bearing | Shear Strain, γ | | | |
| | 100% | | 150% | |
	R.D. (mm)	Δ	*R.D.* (mm)	Δ
SMA-LRB	11.9		12.4	
SMA-LRB (PS)	9.7	-18.6%	10.6	-15.1%

By comparing the energy dissipation capacity of smart rubber bearings, negligible difference is observed between SMA-LRB and SMA-LRB (PS). The reason is that although the energy dissipation (hysteresis area) of the pre-strained SMA is larger than that of the non-pre-strained SMA (see Figure 5.38), the double cross configuration causes the variation of the resultant force of pre-strained wires in the *x* direction (i.e. algebraic summation of *x*-component of nodal forces at A, B, C, … according to Figure 5.36) to be almost same as that of regular wires.

Therefore, it is understood that on one hand, applying pre-strain to SMA wires improves the re-centring capability of SMA-LRB and on the other hand, increasing the energy dissipation capacity of the SMA-LRB by generating pre-strain in wires is highly dependent on the arrangement of wires mounted on the LRB. As discussed in section 5.2.5.4 (SMA-NRB) and section 5.3.5.5 (SMA-HDRB), applying pre-strain to the cross SMA wires could reduce the effective lateral stiffness, however, could not improve the re-centring property of SMA-RBs.

5.5 Design of SMA-based Rubber Bearings

NiTi$_{45}$ wire, in the straight arrangement, undergoes a large strain which is beyond the superelastic strain range (6.8%) at large shear strain amplitudes (Table 5.14). Therefore, to study the effect of SMA type, ferrous (FeNCATB) and NiTi-based (NiTi$_{45}$) wires are

considered to be installed in low-aspect-ratio CFR-HDRBs ($R = 0.12$) with cross arrangement. Ferrous FeNCATB wire, as a more efficient option compared to $NiTi_{45}$, is chosen to be implemented in all four cases (see Table 5.14).

The hysteretic shear behaviour of each SMA-HDRB is compared to that of a CFR-HDRB with the same geometrical and mechanical properties under four different shear strain levels: 50%, 100%, 150%, and 200%.

Increasing the diameter of SMA wires increases the effective horizontal stiffness and the total energy dissipation capacity of the base isolation system. On the other hand, increasing the amount of pre-strain in SMA wires causes the horizontal stiffness to be decreased. Since increasing the lateral flexibility and maximizing the damping capacity of a rubber bearing are both beneficial, it is more advantageous to reach the target horizontal stiffness by changing both the diameter and pre-strain of SMA wires rather than just altering the diameter of wires. In a design procedure, in order to determine the diameter and pre-strain of wires, first, a target value for the effective horizontal stiffness ($K_{H\,d}$) of elastomeric isolator is determined. Then, for a specific size of base isolator, the diameter of SMA wires increases from an initial value. Based on the geometry of rubber bearing and the configuration of SMA wires (cross), a minimum initial diameter (r_{w0}) is obtained from a force ratio (R_F), defined as a ratio of the maximum lateral force generated by SMA wires ($F_{SMA\,max}$) to the maximum shear force of the isolator with no SMA wires ($F_{s\,max}$) at 100% shear strain amplitude. The force ratio is set to a value at which the effect of SMA wires can be observed on the hysteretic shear behaviour of the base isolator (here considered 10%). In fact, knowing the maximum strain in SMA wire at $\gamma = 100\%$ from Equation (5.3), and accordingly the maximum axial stress in wire, σ_{max}, the initial radius of SMA wire, r_w^0, can be obtained from $F_{SMA\,max}$ calculated using the force ratio. The stiffness margin, M_K, is defined in order to determine the relative difference between the calculated effective lateral stiffness of SMA-based rubber bearing, K_H, and the target value of stiffness, $K_{H\,d}$ (initially considered 15%). Under this condition, the radius of wires should increase up to a level at which K_H is 15% higher than the target value. In this step, by fixing the radius, pre-strain in SMA wires goes up and the effective lateral stiffness is calculated. Considering pre-strain values lower than 5%, if the reduction in shear force due to pre-straining the SMA wires causes the lateral stiffness to be reduced and reaches the target point, with a 10% error, the

values of radius and pre-strain are selected and the design procedure is finished. Otherwise, the stiffness ratio decreases by 5%, the radius of wire and the pre-strain are set to their initial values ($r_w{}^0$ and 0, respectively), and then, the effective horizontal stiffness is recalculated again. The flow chart of the design process is shown in Figure 5.40.
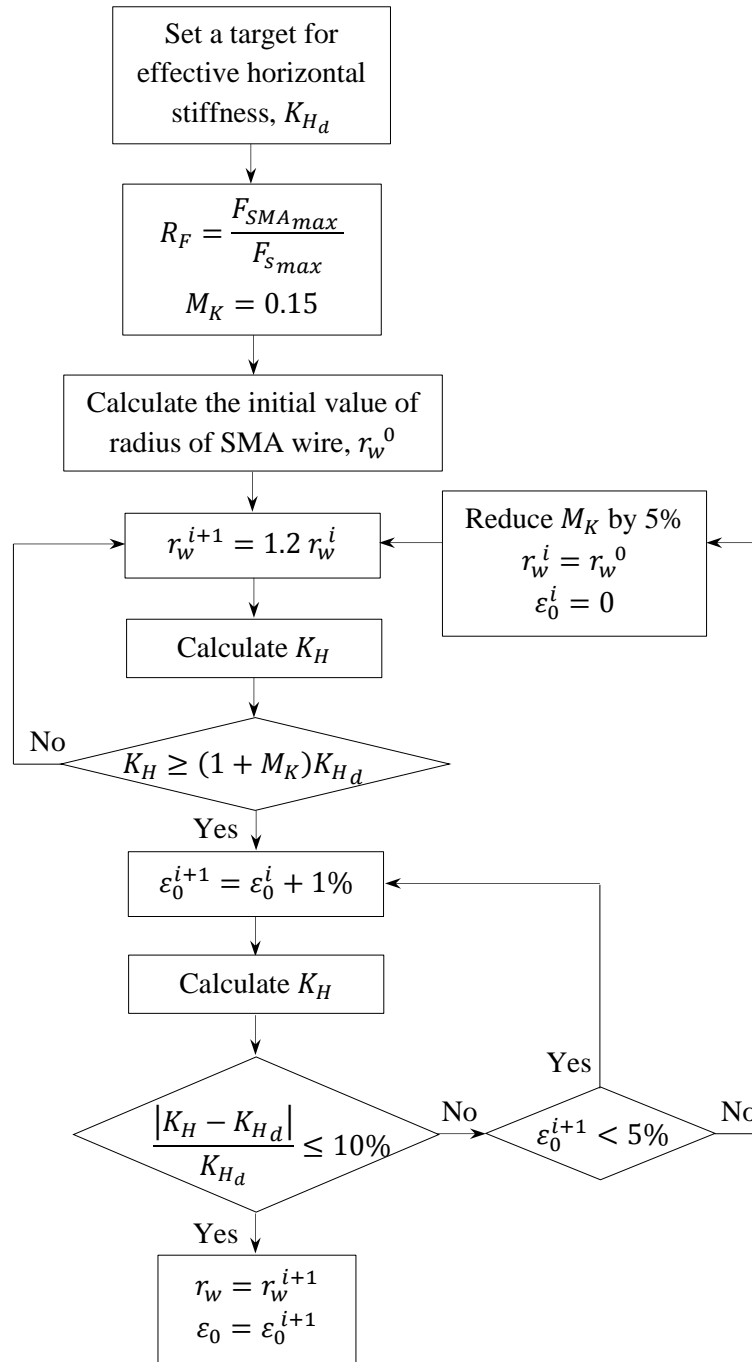
Figure 5.40. Flow chart of design procedure to determine the diameter and pre-strain of SMA wires

Based on the described design procedure, the radius of SMA wires increases from 1 mm, considered as an initial value, to the 2.5 mm. Since the stiffnesses of FeNCATB and NiTi$_{45}$ at the austenite phase are close to each other (Table 5.5), same thicknesses are selected for both types of SMA wires. In order to make the design procedure more clear, an example is given for SMA-HDRB-C2 in Appendix A.

5.6   Summary

This chapter dealt with a new generation smart rubber bearings incorporated with shape memory alloy (SMA) wires. Due to the unique characteristics of SMAs such as the superelastic effect and the re-centring capability, the residual deformation in SMA-based rubber bearing (SMA-RB) decreases and the energy dissipation capacity increases. Therefore, SMA wires can make rubber bearings more reliable by extending service life. SMAs in the form of wire were wrapped around three different rubber bearings (NRB, HDRB, and LRB). Two different configurations of wires (e.g. straight and cross) were considered for SMA-NRB and SMA-HDRB. For SMA-LRB, wires were wrapped around the LRB with a double cross configuration. It was because such an arrangement (double cross) was found to be more efficient for the LRB. The effect of several parameters including the shear strain amplitude, the type of SMA, the aspect ratio of base isolator, the thickness of SMA wire, and the amount of pre-strain in wires was investigated on the performance of the SMA-RBs. Isolators were subjected to a vertical pressure and unidirectional cyclic lateral displacements. Hysteretic shear response of SMA-RBs was determined through FEM.

Results showed that, ferrous SMA wire, FeNiCoAlTaB, with 13.5% superelastic strain and a very low austenite finish temperature (-62°C), is the best candidate to be used in SMA-RBs subjected to high shear strain amplitudes. In terms of the lateral flexibility and wires' strain level, the smart rubber bearing with cross configuration of SMA wires is more efficient. Moreover, the cross configuration can be implemented in high-aspect-ratio elastomeric bearings since the strain induced in wires does not exceed the superelastic range. When cross SMA wires with 2% pre-strain is used in a smart NRB, the dissipated energy is increased by 74% and the residual deformation is decreased by 15%. Using cross SMA wires in HDRBs leads to the highest energy dissipation capacity. However, SMA wires have negligible effect on the residual deformation reduction in HDRBs. Results revealed that

wrapping SMA wires in the double cross arrangement could significantly improve the re-centring capability of LRB by decreasing the maximum shear strain of LRB up to 59%. Findings showed that the pre-straining process advance the re-centring property of SMA-LRB. It was also observed that the maximum shear strain of SMA-LRB could be reduced when 3% pre-strained SMA wires are used. Another point is that enlarging the flag-shaped hysteresis of SMA as a result of pre-straining process does not lead to an increase in the energy dissipation capacity of SMA-LRB because of the configuration of double cross wires.

Finally, a performance-based design flowchart was also provided along with a design example for determining the pre-strain and the radius of cross section of wires in the SMA wire-based rubber bearings.

Chapter 6   Constitutive Model of SMA-based Elastomeric Isolators

6.1   General

In the process of performance evaluation of rubber bearings, experimental-based data is usually obtained by fabricating real size specimens and performing expensive full-scale tests under different loading and environmental conditions. As a reliable alternative, numerical approaches such as finite element method (FEM) can be used in order to significantly reduce the difficulties and costs associated with the experimental procedures. Considering different steps that are followed in the FEM, material behaviour modelling is one of the most challenging parts. In this regard, the constitutive model used in numerical simulations should properly describe the actual behaviour of the system. Therefore, it is of great importance to implement a well-fitted and accurate hysteresis model by either using an existing model or developing a new one.

The hysteretic behaviour of elastomeric isolators is determined based on their components including elastomer, reinforcement (e.g. steel, carbon fibre-reinforced polymers), and supplementary elements (e.g. lead core). In other words, depending on the material model assumed for each component of the isolator, the hysteretic behaviour of the rubber bearing can be identified. By considering different types of elastomer such as low-damping rubber (Takayama and Morita, 2000; Amin et al., 2006a; Gjorgjiev and Garevski, 2013), commercial high quality neoprene (Hedayati Dezfuli and Alam, 2013b and 2014a), and high damping rubber (HDR) (Amin et al., 2006a and b; Hedayati Dezfuli and Alam, 2012), different material models are used. Since HDR is commonly implemented in the base isolation systems and has favourable characteristics (e.g. high damping capacity and resistance to corrosion) but with complex response, it has attracted attentions with experimental (Yoshida et al., 2004; Bhuiyan et al., 2009), analytical (Tsai et al., 2003; Hwang et al., 2002; Bhuiyan and Ahmed, 2007), and numerical (Amin et al., 2006a) perspectives. In FEM, low-damping rubber can be usually simulated using hyperelastic models because it follows the behaviour of a hyperelastic material (Hossa and Marczak, 2010; Ali et al., 2010). Such a model cannot accurately capture the highly nonlinear behaviour of HDR (Hedayati Dezfuli and Alam, 2012 and 2013a). Knowing the fact that HDR shows viscoelastic strain-rate-dependent behaviour under shear deformations, the

hyper-viscoelastic material model (i.e a combination of hyperelastic and viscoelastic models) is an appropriate choice (Bergstrom and Boyce, 1998; Hedayati Dezfuli and Alam, 2012). LRBs can provide a considerable amount of equivalent viscous damping ranging from 15% to 35% (Kelly, 2001). The main advantages of LRB, which makes it the most common type of isolator, is satisfactory amounts of rigidity, flexibility, and damping ratio at different load levels (e.g. service and earthquake) (Kelly, 2001; Chen et al., 2011). In the numerical FE simulations, lead is usually modelled either as an elastic-perfectly plastic material (SAP2000 software) or a bilinear elasto-plastic material with a hardening law (Kelly, 2001; Doudoumis et al., 2005). In both cases, a major amount of energy is dissipated when the lead, with a high initial stiffness, yields and enters the plastic region. However, a significant residual deformation, which is defined as a shear displacement at which the shear force becomes zero, occurs in the material after unloading.

LRBs undergo a large residual deformation under strong excitations. Therefore, it is highly beneficial to implement SMAs, as auxiliary components, in such isolators in order to extend their service life. This improvement is achieved by controlling the displacement and limiting the force transmitted to the superstructure. Attanasi et al. (2008) proposed an innovative SMA-based isolation device and showed that although there is a significant difference in the hysteretic responses of SMA device (flag-shaped hysteresis model) and LRB (elasto-plastic model), both systems have similar displacement and force demands. However, the main advantage of SMA-based device over LRB was zero residual deformation. They concluded that using SMA as a lateral restrainer can improve the re-centring property and energy dissipation capacity of bearing systems. Based on studies performed by Kelly (1997), Choi et al. (2004), and Bhuiyan and Alam (2013), hystereses of LRBs and SMA-RBs were simulated with bilinear models by considering three characteristics: initial stiffness, post-yield stiffness, and yield force for each of them. In a numerical study conducted by Hedayati Dezfuli and Alam (2014b), SMA wires were implemented into a HDRB with a cross configuration (i.e. diagonal). In order to identify the efficiency of the SMA-HDRB, they evaluated the seismic response of a three-span continuous steel-girder RC-pier supported bridge, which was isolated by the proposed SMA-HDRB. They modelled the hysteretic behaviour of both rubber bearings with bilinear kinematic hardening (BKH) models. Although they considered different characteristics (e.g.

initial stiffness and post-yield hardening ratio) for bearings, insignificant differences were observed in the performances. The reason was due to the BKH model which was not able to correctly simulate the actual behaviour of SMA-HDRB.

The objective of this chapter was to develop a hysteresis model for shape memory alloy wire-based rubber bearings (SMA-RBs). In Chapter 5, three types of SMA-RBs were introduced and a thorough discussion was carried out on the advantages of these new smart isolators. However, their real performance on the seismic behaviour of structures, specifically bridges, was yet to be investigated. More importantly, hysteresis models available in structural FE softwares such as SAP2000 (SAP2000 software), Seismostruct (Seismostruct, v6.5), or Opensees (McKenna et al., 2000) cannot accurately capture the actual behaviour of SMA-RBs under seismic loadings. Therefore, the necessity of implementing SMA-RBs into multi-span steel-girder bridges and the lack of an appropriate hysteresis model for such isolators led this study to propose a constitutive model for SMA-RB. For developing the model, it was assumed that the bearing is subjected to a compressive loading and unidirectional lateral displacements. Since the vertical deflection due to the compression was much smaller than the lateral displacements, it was neglected. Due to the complexity of the shear behaviour of SMA-RB, the idea of superposition was used to simplify the model by decoupling the smart isolator into two separate systems; SMA wires and RB. As a result, by considering the bilinear kinematic hardening model for the RB, first, a hysteresis model was developed for SMA wires and then, it was superimposed onto the RB hysteresis model. Before presenting an algorithm for the SMA wires model, the superposition method was verified through the FE model validated by experimental results. In the validation procedure the shear hysteretic response of the SMA-RB, as an integrated system, was compared to that of the superimposed system in which the behaviours of decoupled systems were added together.

6.2   SMA-based Rubber Bearings

In Chapter 5, when performance of NRB, HDRB, and LRB was compared with that of SMA-NRB, SMA-HDRB, and SMA-LRB, it was observed that implementing SMA wires into LRB leads to more significant improvements in terms of re-centring capability and energy dissipation capacity. Therefore, the focus of this chapter is on the behaviour of SMA-

LRB and the hysteresis model is developed for this smart elastomeric isolator (Hedayati Dezfuli and Alam, 2015a). However, it should be mentioned that the same procedure, which will be presented for developing the hysteresis model, can be used for SMA-NRB and SMA-HDRB.

Although bilinear kinematic hardening model can be used for SMA-LRB, it cannot precisely capture the nonlinear behaviour of SMA-LRB, especially at high shear strain levels. Hence, the result will not be accurate enough to be attributed to the real case. Therefore, it is of great interest to develop a constitutive model for the SMA-LRB. The mechanical and geometric properties of the SMA-LRB are the same as what Abe et al. (2004) used in their study for LRB (see Figure 6.1). It should be also mentioned that the FE model of LRB, which is used for analyzing and determining hysteretic shear responses, is the one used in Chapter 5 and validated through the experimental tests conducted by Abe et al. (2004).
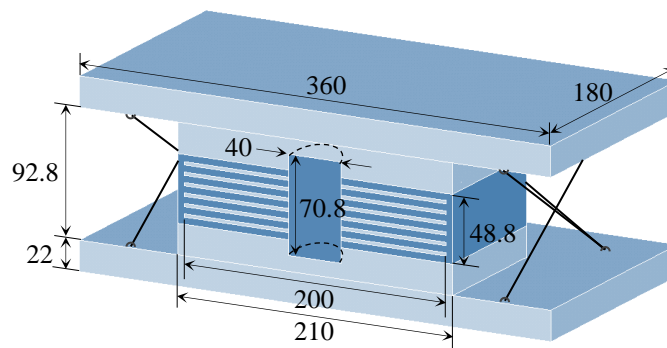
Figure 6.1. Half model of SMA-LRB (dimensions are in mm)

In addition to the dimensions specified in Figure 6.1, other physical and material properties of the LRB and SMA wires are provided in Table 6.1. Ferrous SMA, FeNiCoAlTaB, is chosen for wires with a cross sectional radius of 2.5 mm. In all the FE models, rubber is simulated with hyper-viscoelastic model, and steel and lead are assumed to follow bilinear behaviours with kinematic hardening law.

Table 6.1. Properties of LRB and SMA wire

LRB		SMA Wire	
n_r	7	r_{SMA} (mm)	2.5
n_s	6	E^A (GPa)	46.9
t_r (mm)	5.0	A_f (°C)	-62.0
t_s (mm)	2.3	ε_s (%)	13.5

n_r: number of rubber layers; n_s number of steel shims; t_r: thickness of rubber layers; t_s: thickness of steel shims; r_{SMA}: radius of wires; E^A: elastic modulus of SMA in austenite phase; A_f: austenite finish temperature; ε_s: superelastic strain limit

6.2.1 Superposition Method

The SMA-LRB has a complex hysteretic behaviour. Therefore, in order to determine its shear hysteresis, the whole system is simplified by applying a superposition method. In fact, double cross SMA wires (DC-SMAW) are decoupled from the rubber bearing and then, the effect of SMA wires is superimposed on the LRB (Figure 6.2). To provide a solid proof for this assumption, the hysteresis curves of the integrated system (i.e. LRB equipped with DC-SMAW) are compared to those of the decoupled systems (i.e. LRB and DC-SMAW). In this regard, first, lateral force-deflection curves of the decoupled systems are calculated through FE analysis by using ANSYS (ANSYS Mechanical APDL, Release 14.0) (see Figure 6.3). Then, shear hysteretic responses of superimposed and integrated systems are evaluated (see Figure 6.4). It should be noted that in the superimposed system, the hysteresis of LRB and SMA wires are calculated separately and then their responses are added together. In the integrated system, the SMA-LRB is modelled and analyzed as one system.

LRB   DC-SMAW   SMA-LRB
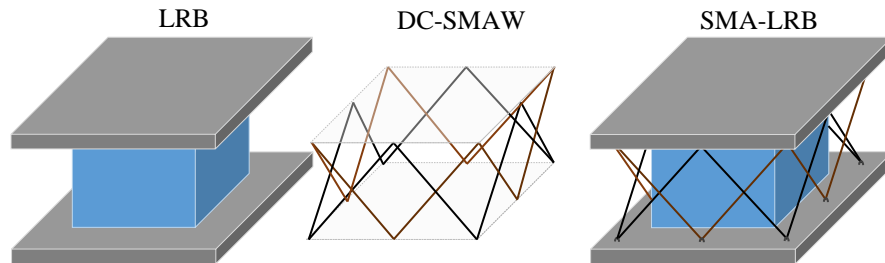
Figure 6.2. Superimposing SMA wires onto LRB

Here it is assumed that wires are in contact with the hooks through a frictionless mechanism similar to what was explained in section 5.3. Hence, instead of modelling the DC-SMAW with details of the connection system in ANSYS, axial forces in SMA wires are

calculated as functions of time and applied to the model. In the FE modelling of DC-SMAW, 16 nodes (8 points on the bottom supporting plate and 8 points on the top plate) are created at locations where steel hooks are attached. Then, nodal forces are applied to these nodes. In order to properly capture the variation of axial force in the SMA wires, the nodal forces are updated at each time step while running the simulation. By fixing the lower supporting steel plate, 8 nodes on this plate are fixed in all directions. Other 8 nodes are free to move laterally and vertically together. It means that the amount of displacement for all of these 8 nodes is the same since it is assumed that they are located on a rigid supporting plate.
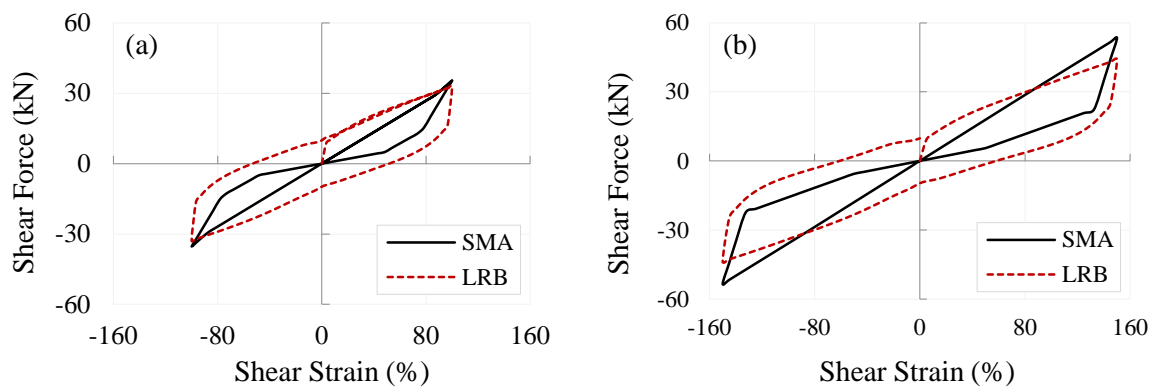
Figure 6.3. Shear hysteresis curves of decoupled systems at shear strains of (a) 100% and (b) 150%
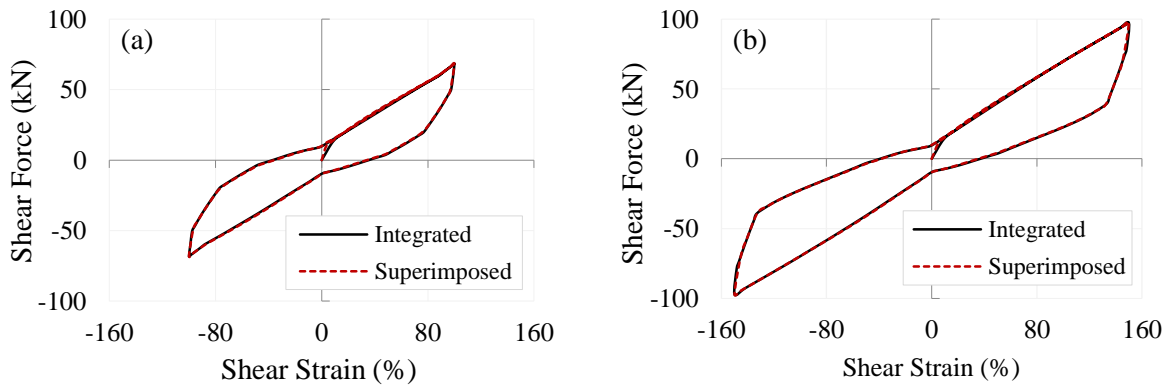
Figure 6.4. Shear hysteretic responses of integrated and superimposed systems at shear strains of (a) 100% and (b) 150%

The comparison shows that the DC-SMA wires can be correctly superimposed onto the LRB as a separate system.

176

6.3 Hysteresis Model

In order to develop a constitutive model for the SMA-LRB, first, a model is proposed for each system (i.e. DC-SMAW and LRB), and then, two models are combined together. Figure 6.5 shows a flow chart by which the basic algorithm of SMA-LRB constitutive model is established by considering characteristics of each model and an input loading.
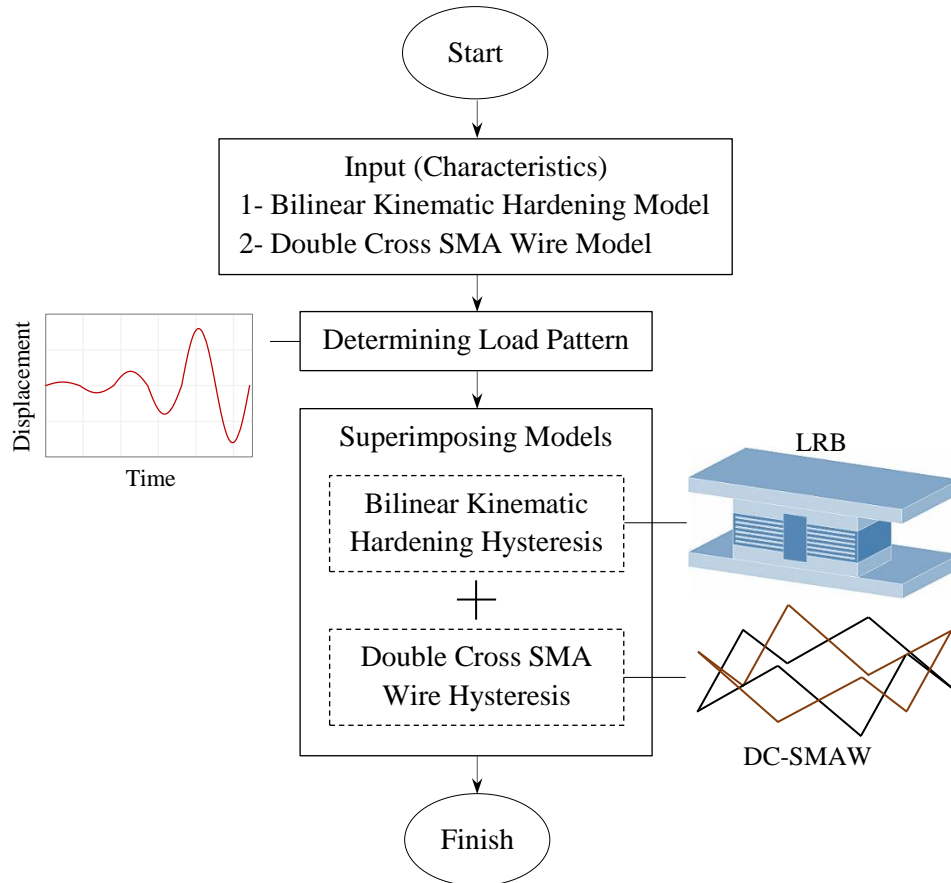
Figure 6.5. Flow chart of SMA-LRB constitutive model

6.3.1 Rubber Bearing Model

A bilinear model can be used for predicting the hysteretic response of LRB in order to simplify the procedure of FE analysis (Attanasi et al., 2008; Kalpakidis, 2010; Zheng and Wang, 2011; Chen et al., 2011). Here, it is assumed that the behaviour of LRB can be simulated using the bilinear kinematic hardening (BKH) model. This model can describe the inelastic rate-independent plasticity behaviour and capture the Bauschinger effect by considering the kinematic hardening law (ANSYS Documentation, Release 14.0). In this

model, three properties; yield force, F_y, initial stiffness (i.e. stiffness in the elastic region), K_0, and post-yield hardening ratio (i.e. ratio of the stiffness in the plastic region to the initial stiffness), r, should be determined in order to characterize the shear force-displacement curve. It should be noted that BKH model is being widely used in structural FE softwares. However, in order to combine this model with the new DC-SMA wires model, which will be developed in the next section, the algorithm of BKH model is re-written here. This algorithm is depicted in Appendix B, Figure B.1.

Assuming the three characteristics of BKH model listed in Table 6.2, the LRB is excited in four different cases and its shear hysteretic responses are evaluated through a MATLAB code written based on the algorithm shown in Figure B.1. It should be noted that the stiffness, the energy dissipated per cycle, and the residual deformation of the real response and the idealized bilinear model with given properties (K_0, F_y, and r) are almost the same. In Figure 6.6, the hysteretic responses in terms of lateral force-displacement curves (R) are plotted along with the corresponding excitations (E) (i.e. shear strain versus time). Number of each curve identifies that for each excitation there is a corresponding response. For example, the response of LRB to excitation number 1 (E1) is R1.

Table 6.2. Properties of bilinear kinematic hardening model used for LRB

Model constant	Symbol	Value	Unit
Initial Stiffness	K_0	5.28	kN/mm
Yield Force	F_y	10.10	kN
Post-Yield Hardening Ratio	r	0.13	-
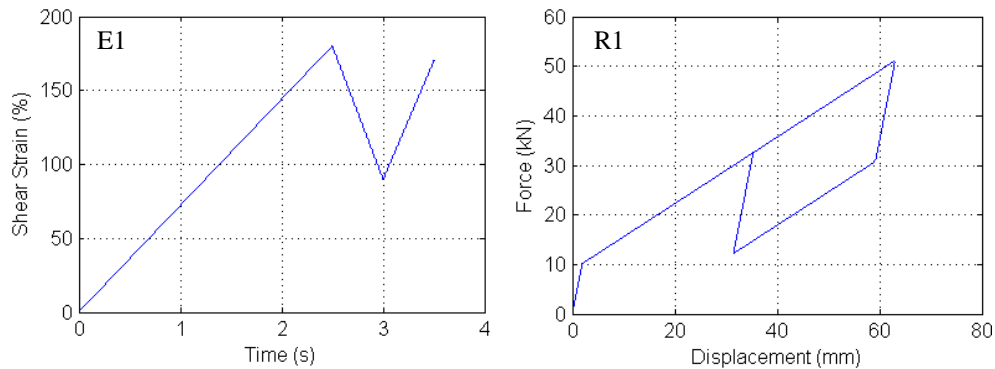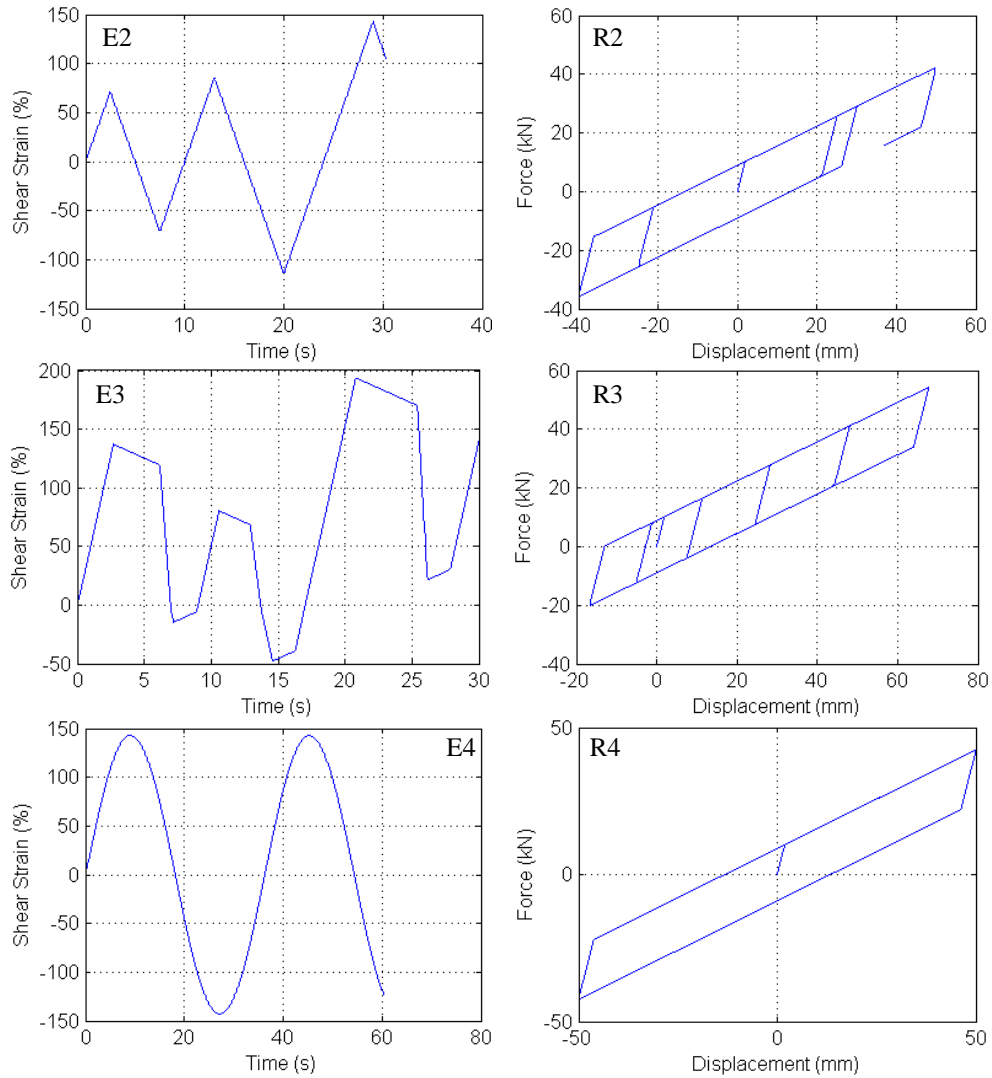
Figure 6.6. Excitations (E) in terms of shear strain over time, and corresponding shear hysteretic responses (R) in terms of force versus displacement of LRB

6.3.2 SMA Wires Model

The input factors for the DC-SMAW model are divided into two groups; five parameters for the geometry and nine parameters for the material properties. For the geometry, h_r and r_{SMA} are the total thickness of rubber layers and the radius of SMA wire's cross section, respectively, and l, w, and h are the horizontal distance between A and C, C and E, and the vertical height of the rubber bearing as shown in Figure 6.7.
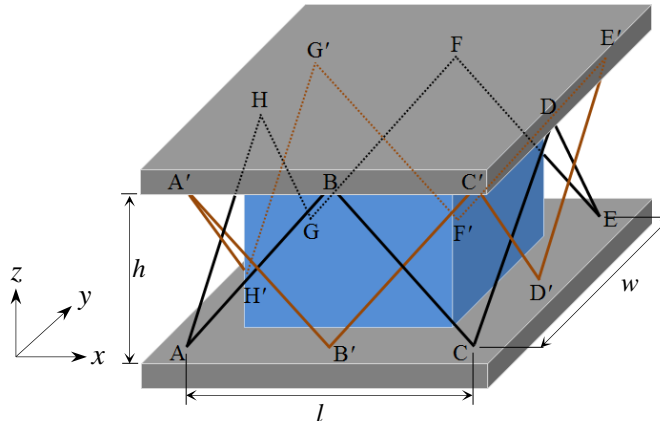
Figure 6.7. SMA-RB with double cross configuration

For material properties, eight parameters (material constants) are defined as characteristic stresses and strains at austenite start, austenite finish, martensite start, and martensite finish levels by assuming the idealized stress-strain diagram of superelastic behaviour of SMA, which is plotted in Figure 6.8.

σ_s^M: Martensite start stress
σ_f^M: Martensite finish stress
σ_s^A: Austenite start stress
σ_f^A: Austenite finish stress

ε_s^M: Martensite start strain
ε_f^M: Martensite finish strain
ε_s^A: Austenite start strain
ε_f^A: Austenite finish strain
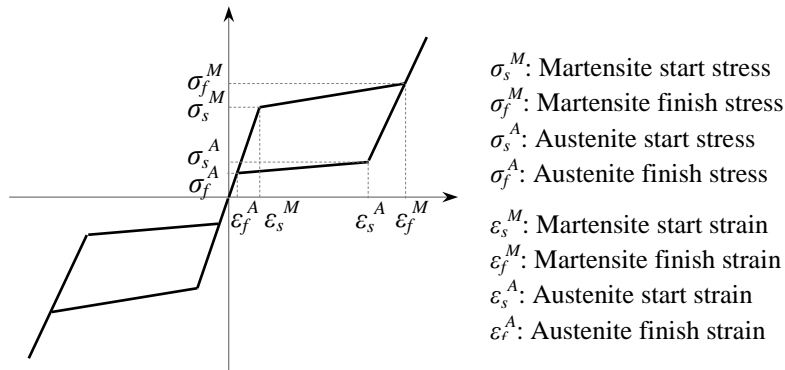
Figure 6.8. Idealized stress-strain diagram of SMA (Auricchio, 2001)

The last material constant, *m*, is a degradation factor defined for the stiffness. In order to have a clear understanding of the hysteretic behaviour of DC-SMAW model and define this parameter, forces in wires generated due to the displacement of the elastomeric isolator should be accurately analyzed. According to the double cross configuration of wires, when the bearing is subjected to a lateral displacement in the *x* direction, as a general case, shown in Figure 6.9a, SMA wires are elongated and the strain in wires varies according to the dashed lines in Figure 6.9a.
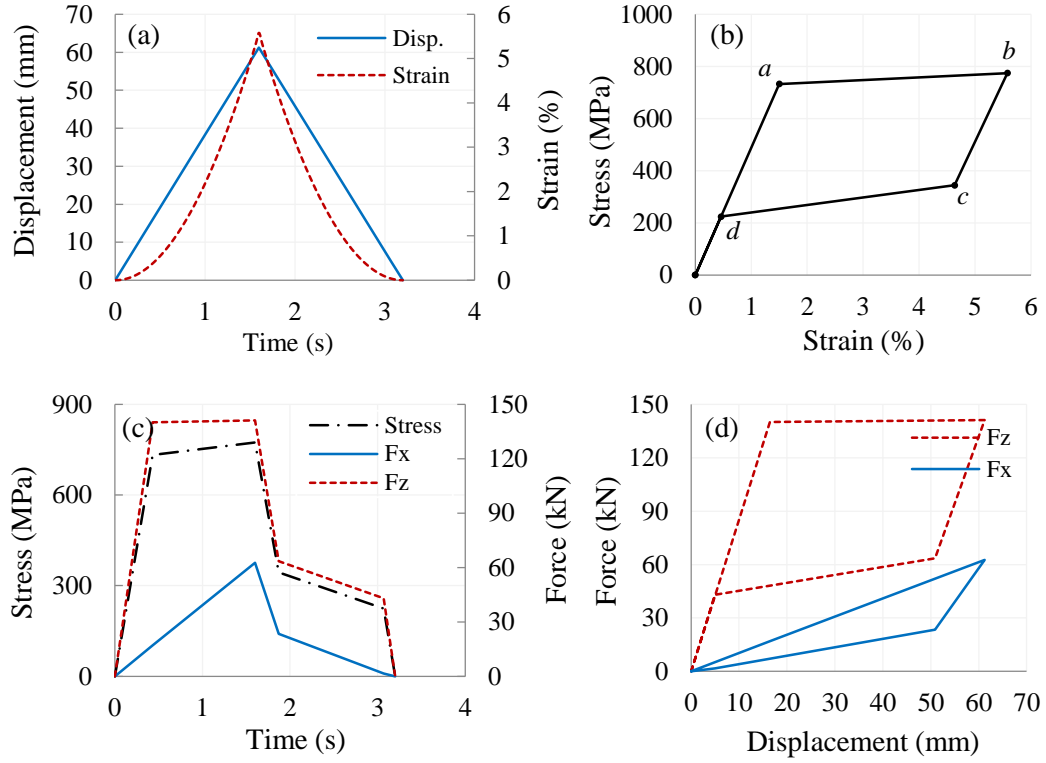
Figure 6.9. Response of DC-SMAW to a general excitation; (a) unidirectional lateral displacement and the corresponding strain generated in wires, (b) idealized stress-strain relation in the wires, (c) variation of axial stress in the wires and corresponding resultant forces in x and z directions over the time, (d) resultant forces generated by the wires in x and z directions versus lateral displacement of bearing

By considering Equations (6.1) to (6.3), the strain in DC-SMA wires is related to the displacement of rubber bearing through a nonlinear relation for a unidirectional lateral displacement (i.e. x direction).

$$\varepsilon_{SMA} = \frac{l_{SMA} - l_{0\,SMA}}{l_{0\,SMA}} \tag{6.1}$$

where $l_{0,SMA}$ is the initial length of the SMA wire and l_{SMA} is the length of SMA wire when the bearing undergoes a deflection of ΔX in the x direction (see Figure 6.10).

$$l_{0\,SMA} = 4\sqrt{\left(\frac{l}{2}\right)^2 + h^2} + 4\sqrt{\left(\frac{w}{2}\right)^2 + h^2} \tag{6.2}$$

181

$$l_{SMA} = 2\sqrt{\left(\frac{l}{2} + \Delta X\right)^2 + h^2} + 2\sqrt{\left(\frac{l}{2} - \Delta X\right)^2 + h^2} + 4\sqrt{\left(\frac{w}{2}\right)^2 + \Delta X^2 + h^2} \tag{6.3}$$

By using the idealized stress-strain relation of superelastic SMA, the stress along the wires is plotted in Figure 6.9b as a function of strain. Knowing the fact that the axial force in the wires, F, can be found from the stress in wires, σ_{SMA}, according to Equation (6.4), the resultant forces in x, y, and z directions are calculated through Equation (6.5).

$$F = \sigma_{SMA}\pi r_{SMA}^{\ 2} \tag{6.4}$$

$$
\begin{aligned}
F_x &= F_{x_B} + F_{x_D} + F_{x_F} + F_{x_H} + F_{x_{A'}} + F_{x_{C'}} + F_{x_{E'}} + F_{x_{G'}} \\
F_y &= F_{y_B} + F_{y_D} + F_{y_F} + F_{y_H} + F_{y_{A'}} + F_{y_{C'}} + F_{y_{E'}} + F_{y_{G'}} \\
F_z &= F_{z_B} + F_{z_D} + F_{z_F} + F_{z_H} + F_{z_{A'}} + F_{z_{C'}} + F_{z_{E'}} + F_{z_{G'}}
\end{aligned}
\tag{6.5}
$$

It is assumed that the lower supporting plate is fixed in all directions and therefore, the resultant forces (F_x, F_y, and F_z) transferred from SMA wires to the laminated pad are a summation of forces at nodes located on the top supporting plate as shown in Figure 6.7. It should be also noted that due to the symmetric configuration of double cross wires, and the boundary and loading conditions, the resultant force in the y direction, F_y, is zero.

Assuming a unidirectional lateral displacement in the x direction, the components of force at each node are determined according to equations provided in Table 6.3.

Table 6.3. Components of nodal forces in x, y, and z directions

Node	Force	Node	Force
A	$F_x = F(\cos\theta_1 + \sin\alpha\sin\phi)$ $F_y = F\cos\alpha$ $F_z = F(\sin\theta_1 + \sin\alpha\cos\phi)$	A'	$F_x = F(\cos\theta_1 - \sin\alpha\sin\phi)$ $F_y = F\cos\alpha$ $F_z = -F(\sin\theta_2 + \sin\alpha\cos\phi)$
B	$F_x = -F(\cos\theta_1 - \cos\theta_2)$ $F_y = 0$ $F_z = -F(\sin\theta_1 + \sin\theta_2)$	B'	$F_x = F(\cos\theta_1 - \cos\theta_2)$ $F_y = 0$ $F_z = F(\sin\theta_1 + \sin\theta_2)$
C	$F_x = F(-\cos\theta_2 + \sin\alpha\sin\phi)$ $F_y = F\cos\alpha$ $F_z = F(\sin\theta_2 + \sin\alpha\cos\phi)$	C'	$F_x = -F(\cos\theta_2 + \sin\alpha\sin\phi)$ $F_y = F\cos\alpha$ $F_z = -F(\sin\theta_2 + \sin\alpha\cos\phi)$
D	$F_x = -2F\sin\alpha\sin\phi$ $F_y = 0$ $F_z = -2F\sin\alpha\cos\phi$	D'	$F_x = 2F\sin\alpha\sin\phi$ $F_y = 0$ $F_z = 2F\sin\alpha\cos\phi$
E	$F_x = F(-\cos\theta_2 + \sin\alpha\sin\phi)$ $F_y = -F\cos\alpha$ $F_z = F(\sin\theta_2 + \sin\alpha\cos\phi)$	E'	$F_x = -F(\cos\theta_2 + \sin\alpha\sin\phi)$ $F_y = -F\cos\alpha$ $F_z = -F(\sin\theta_2 + \sin\alpha\cos\phi)$
F	$F_x = -F(\cos\theta_1 - \cos\theta_2)$ $F_y = 0$ $F_z = -F(\sin\theta_1 + \sin\theta_2)$	F'	$F_x = -F(\cos\theta_1 - \cos\theta_2)$ $F_y = 0$ $F_z = F(\sin\theta_1 + \sin\theta_2)$
G	$F_x = F(\cos\theta_1 + \sin\alpha\sin\phi)$ $F_y = -F\cos\alpha$ $F_z = F(\sin\theta_1 + \sin\alpha\cos\phi)$	G'	$F_x = F(\cos\theta_1 - \sin\alpha\sin\phi)$ $F_y = -F\cos\alpha$ $F_z = -F(\sin\theta_1 + \sin\alpha\cos\phi)$
H	$F_x = -2F\sin\alpha\sin\phi$ $F_y = 0$ $F_z = -2F\sin\alpha\cos\phi$	H'	$F_x = 2F\sin\alpha\sin\phi$ $F_y = 0$ $F_z = 2F\sin\alpha\cos\phi$

In the above equations, angles θ_1, θ_2, α, and ϕ are respectively calculated from Equations (6.6) to (6.9) based on the configuration of DC-SMA wires as illustrated in Figure 6.10.

$$\theta_1 = \tan^{-1}\left(\frac{h}{l/2 + \Delta X}\right) \tag{6.6}$$

$$\theta_2 = \tan^{-1}\left(\frac{h}{l/2 - \Delta X}\right) \tag{6.7}$$

$$\alpha = \tan^{-1}\left(\frac{h}{w/2}\right) \tag{6.8}$$

$$\phi = \tan^{-1}\left(\frac{\Delta X}{h}\right) \tag{6.9}$$
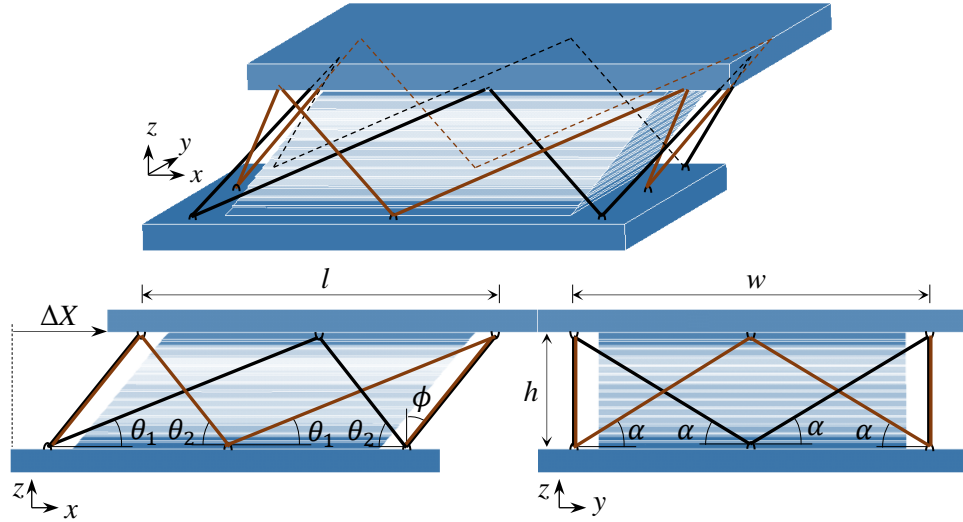
Figure 6.10. SMA-LRB with DC arrangement under a unidirectional displacement of ΔX (in x direction)

Variations of axial stress in DC-SMAW and resultant forces in the x and z directions over the time during which the lateral displacement is applied are demonstrated in Figure 6.9c. Figure 6.9d shows changes of the resultant forces transferred from DC-SMAW to the LRB versus the given lateral unidirectional displacement. It is understood that although the SMA wire has a flag-shaped hysteresis, such behaviour is not observed for the total force in the x direction. On the other hand, when changes of the total force in the z direction (F_z) are plotted versus time and displacement, a different behaviour is detected. These findings show that the configuration of wire is the main factor in determining the hysteretic model of SMA wires.

Since the hysteretic shear response of the SMA-LRB is evaluated under lateral displacements, the variation of total force in the lateral direction is investigated for wire system in order to develop the constitutive model of DC-SMAW. By idealizing the lateral force-deflection curve shown in Figure 6.9d, it is assumed that the hysteresis of DC-SMAW has three different stiffnesses; the initial stiffness, $K_{0,w}$, the intermediate stiffness, K_i, and the re-centring stiffness, K_r. Considering more than twenty loading scenarios with different shapes, amplitudes, and frequencies shows that the initial and the re-centring stiffnesses do not change and the intermediate stiffness vary depending on the local maximum and minimum amplitudes. The idealized flag-shaped hysteresis of SMA used in this study (Figure 6.9b) (Auricchio, 2001) justifies this characteristic of DC-SMAW model. The

184

intermediate stiffness corresponds to a part of SMA hysteresis during which fully martensitic wires are unloaded (line *bc* in Figure 6.9b). Since changing the input loading (maximum applied strain) only affects the slope of this part, the intermediate stiffness undergoes a variation (see Figure 6.11) while, the two other stiffnesses remain constant. Here, it is assumed that the intermediate stiffness decreases linearly by reducing the maximum lateral displacement applied to the isolator. As a result, a degradation factor, *m*, can be defined for this parameter.

In order to calculate the stiffnesses, corresponding displacements, $U_{x,i}$, and corresponding forces, $F_{x,i}$, should be first identified. $U_{x,i}$ are lateral displacements of LRB at which strain in SMA wires reaches its critical values, ε_i, and can be found by solving Equation (6.10).

$$\varepsilon_{SMA} - \varepsilon_i = 0, \quad i = 1, 2, \dots, 6 \tag{6.10}$$

The first four critical strains are characteristic strains (ε_s^A, ε_f^A, ε_s^M, and ε_f^M) and two others (ε_5 and ε_6) are computed from Equations (6.11) and (6.12). Similarly, characteristic stresses (σ_s^A, σ_f^A, σ_s^M, and σ_f^M) are considered as first four critical stresses. Investigating the hysteresis of DC-SMAW model under various excitations as well as theoretical calculations revealed that the initial and the re-centring stiffnesses can be determined from the characteristic strains and stresses; however, for calculating the intermediate stiffness, extra parameters are required. Hence, it is necessary to define additional critical strains (ε_5 and ε_6) and stresses (σ_5 and σ_6). Moreover, it will be shown that these parameters (ε_5, ε_6, σ_5, and σ_6) are used to find out the corresponding values $U_{x,5}$, $U_{x,6}$, $F_{x,5}$, and $F_{x,6}$ in order to estimate the critical values of shear strain and intermediate stiffness. Therefore, in total, six critical values are considered for strain, stress, and accordingly, corresponding displacement and force.

$$\varepsilon_5 = 2\varepsilon_1 \tag{6.11}$$

$$\varepsilon_6 = \frac{\sigma_5 - \sigma_4 + m_3\varepsilon_4 - m_2\varepsilon_5}{m_3 - m_2} \tag{6.12}$$

where

$$\sigma_5 = \sigma_1 + m_1(\varepsilon_5 - \varepsilon_1) \tag{6.13}$$

$$\sigma_6 = \sigma_5 + m_2(\varepsilon_6 - \varepsilon_5) \tag{6.14}$$

185

and

$$m_i = \frac{\sigma_{i+1} - \sigma_i}{\varepsilon_{i+1} - \varepsilon_i}, \quad i = 1, 2, 3 \tag{6.15}$$

Corresponding forces, $F_{x,i}$, are resultant forces in the x direction, transferred to the laminated pad, and calculated from Equation (6.16). This equation shows that $F_{x,1}$ to $F_{x,4}$ are found from characteristic stresses, and $F_{x,5}$ and $F_{x,6}$ correspond to critical stresses σ_5 and σ_6, respectively.

$$F_{x,i} = C_i \sigma_i \pi r_{SMA}^2 \quad i = 1, 2, \dots, 6 \tag{6.16}$$

where coefficients C_i are determined based on the configuration of DC-SMAW shown in Figure 6.10 and the nodal forces provided in Table 6.3.

$$C_i = 4\left(\cos\theta_{1,i} - \cos\theta_{2,i} + 2\sin\alpha_i \sin\phi_i\right) \tag{6.17}$$

in which

$$\begin{aligned}
\theta_{1,i} &= \tan^{-1}\left(\frac{h}{l/2 + U_{x,i}}\right) \\
\theta_{2,i} &= \tan^{-1}\left(\frac{h}{l/2 - U_{x,i}}\right) \\
\alpha_i &= \tan^{-1}\left(\frac{h}{w/2}\right) \\
\phi_i &= \tan^{-1}\left(\frac{U_{x,i}}{h}\right)
\end{aligned} \tag{6.18}$$

Therefore, the initial and the re-centring stiffnesses can be calculated according to Equations (6.19) and (6.20), respectively.

$$K_{0,w} = \frac{F_{x,1}}{U_{x,1}} \tag{6.19}$$

$$K_r = \frac{F_{x,4} - F_{x,3}}{U_{x,4} - U_{x,3}} \tag{6.20}$$

As explained previously, the initial and the re-centring stiffnesses remain constant by changing the amplitude of input loading (lateral displacement). On the other hand, the intermediate stiffness will vary if the maximum or minimum shear strain goes beyond a

starting limit, g_s. This limit is defined as a shear strain level at which the induced strain in SMA wires reaches the martensite start strain, ε_s^M, and is computed from Equation (6.21).

$$g_s = \frac{U_{x,1}}{h_r} \tag{6.21}$$

For peak shear strain amplitudes smaller than or equal to g_s, DC-SMAW has no hysteresis. In other words, the re-centring stiffness is equal to the initial stiffness and the intermediate stiffness is not defined. The reason of such behaviour is that when the shear strain is lower than the starting limit, the induced strain in SMA wires is lower than the martensite start strain and as a result, no phase transformation from austenite to martensite occurs. Consequently, fully austenite SMA wires act like regular wires in the elastic range with an elastic modulus of E^A (i.e. the elastic modulus of SMA at austenite phase) and no flag-shaped hysteresis is observed. On the other hand, when the shear strain exceeds g_s, the forward phase transformation occurs in the SMA wires and accordingly, the effect of flag-shaped hysteresis of SMA appears in the overall response of SMA-LRB. This characteristic of DC-SMAW can be perceived by distinguishing three different stiffnesses ($K_{0,w}$, K_i, and K_r) for a range of shear strain starting from g_s.

As shown in Figure 6.11, the shear hysteretic responses of DC-SMAW are plotted for five different levels of lateral displacement along with corresponding idealized stress-strain behaviours of SMA. At the lowest level, which is indicated by number 1, the peak lateral displacement reaches $g_s h_r$ (i.e. corresponds to shear strain of g_s) and the maximum corresponding strain in SMA wires is equal to ε_s^M. Under this condition, no hysteresis is observed. When the lateral displacement increases above the $g_s h_r$ (cases 2, 3, 4, and 5), wires generate a hysteresis due to the phase transformation in SMA. Here, the important point is that when the peak shear strain increases, the fraction of austenite phase, which transforms into martensite, becomes larger. As a result, the stress-strain curve of SMA forms with a different flag shape depending on the slope of the line in the unloading phase during which the martensite phase transforms into the austenite. This behaviour occurs up to a level of shear strain (i.e. g_m) at which the corresponding strain in SMA wires reaches the maximum allowable superelastic strain and consequently, the forward phase transformation (austenite to martensite) is completed. In other words, if the shear strain amplitude increases above the g_m, the intermediate stiffness of DC-SMAW will no longer change.
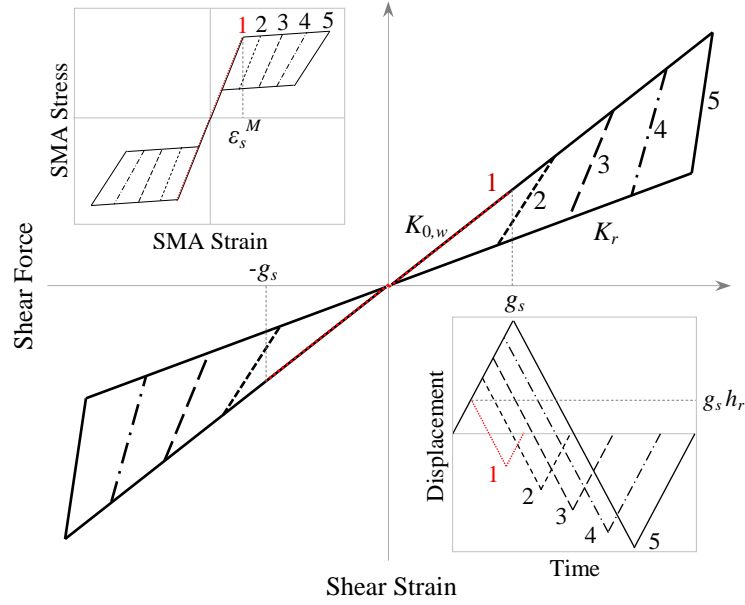
Figure 6.11. Shear hysteretic response of DC-SMAW for different lateral displacements

Evaluating the hysteresis of SMA-LRB subjected to different input displacements indicates that the intermediate stiffness varies approximately linearly by increasing the shear strain between g_s and g_m. Hence, by defining the changing rate of intermediate stiffness (i.e. slope), known as the degradation factor, m, and a starting point including the critical shear strain, g_c, and the critical intermediate stiffness, K_i^c, the intermediate stiffness can be formulated as a linear function of shear strain. After conducting FE simulations and obtaining shear hysteretic responses, it was revealed that the degradation factor is 4.3 for FeNiCoAlTaB and 3.0 for NiTi. Here, FeNiCoAlTaB is used in the SMA-LRB. Critical values of shear strain and intermediate stiffness are defined according to Equations (6.22) and (6.23), respectively.

$$g_c = \frac{U_{x,5}}{h_r} \tag{6.22}$$

$$K_i^{\ c} = \frac{F_{x,6} - F_{x,5}}{U_{x,6} - U_{x,5}} \tag{6.23}$$

Since the hysteresis model of DC-SMAW is developed based on the rate-independent idealized constitutive model of SMA (Auricchio, 2001), and the bilinear kinematic hardening model is also rate-independent, the proposed hysteresis model of SMA-LRB is independent of the strain rate. In Figure 6.12, by knowing the critical strains and stresses, as well as

188

geometrical properties, corresponding values of lateral displacement and force are calculated according to Eqs. (10) and (16), respectively. Then, five characteristics of DC-SMAW model; the initial stiffness ($K_{0,w}$), the critical intermediate stiffness (K_i^c), the re-centring stiffness (K_r), the starting shear strain (g_s), and the critical shear strain (g_c) are determined. In Figure 6.13 (parts 1 and 2), which demonstrate the main sections of the hysteresis algorithm, the lateral force is calculated at each time step by giving the applied shear deformation as an input. In fact, model characteristics determined in the first part of the algorithm (Figure 6.12) are used in two other parts (Figure 6.13) in order to estimate the hysteresis of DC-SMAW. In other words, the first part is linked to the main body of the algorithm via three stiffnesses ($K_{0,w}$, K_i^c, and K_r) and two shear strains (g_s and g_c). Part 1 of Figure 6.13 is used when the rubber bearing moves in the positive direction and the lateral displacement increases ($x_i \geq x_{i-1}$). Accordingly, when the SMA-LRB moves in the negative direction ($x_i < x_{i-1}$), the last part of the algorithm is involved. As shown in Figure 6.13, both parts are divided into two regions; one for non-negative values of input lateral displacement ($x_i \geq 0$) and the other one for negative values of input ($x_i < 0$).

```
                    ┌─────────┐
                    │  Start  │
                    └─────────┘
```

Input Parameters

Material Property: $\varepsilon_s^A, \varepsilon_f^A, \varepsilon_s^M, \varepsilon_f^M, \sigma_s^A, \sigma_f^A, \sigma_s^M, \sigma_f^M, m$

Geometry: l, w, h, h_r, r_{SMA}

Input Displacement

$X = x\,(t); \ [\,X_1, X_2, X_3, \dots X_n\,]$

$$m_i = \frac{\sigma_{i+1} - \sigma_i}{\varepsilon_{i+1} - \varepsilon_i}, \quad i = 1,2,3$$

$$\varepsilon_5 = 2\varepsilon_1, \qquad\qquad \sigma_5 = \sigma_1 + m_1(\varepsilon_5 - \varepsilon_1)$$

$$\varepsilon_6 = \frac{\sigma_5 - \sigma_4 + m_3\varepsilon_4 - m_2\varepsilon_5}{m_3 - m_2}, \ \sigma_6 = \sigma_5 + m_2(\varepsilon_6 - \varepsilon_5)$$

$$\varepsilon_{SMA} = \frac{l_{SMA} - l_{0,SMA}}{l_{0,SMA}}$$

$$l_{0,SMA} = 4\sqrt{(l/2)^2 + h^2} + 4\sqrt{(w/2)^2 + h^2}$$

$$l_{SMA} = 2\sqrt{(l/2 + x)^2 + h^2} + 2\sqrt{(l/2 - x)^2 + h^2} + 4\sqrt{x^2 + (w/2)^2 + h^2}$$

$$U_{x,i} = Solve\,(\varepsilon_{SMA} - \varepsilon_i = 0), \ i = 1,\dots,6$$

$$\theta_{1i} = \tan^{-1}\!\left(\frac{h}{l/2 + U_{x,i}}\right), \quad \theta_{2i} = \tan^{-1}\!\left(\frac{h}{l/2 - U_{x,i}}\right)$$

$$\alpha_i = \tan^{-1}\!\left(\frac{h}{w/2}\right), \qquad \varphi_i = \tan^{-1}\!\left(\frac{U_{x,i}}{h}\right)$$

$$C_i = 4\,(\cos\theta_{1,i} - \cos\theta_{2,i} + 2\,\sin\alpha_i\,\sin\varphi_i)$$

$$F_{x,i} = C_i\,\sigma_i\,\pi\,r^2_{SMA}$$

$$K_{0,w} = F_{x,1}/U_{x,1}$$

$$K_r = \frac{F_{x,4} - F_{x,3}}{U_{x,4} - U_{x,3}}, \quad g_s = \frac{U_{x,1}}{h_r}$$

$$K_i^c = \frac{F_{x,6} - F_{x,5}}{U_{x,6} - U_{x,5}}, \quad g_c = \frac{U_{x,5}}{h_r}$$

Figure 6.12. Flowchart of determining model characteristics for DC-SMAW hysteresis
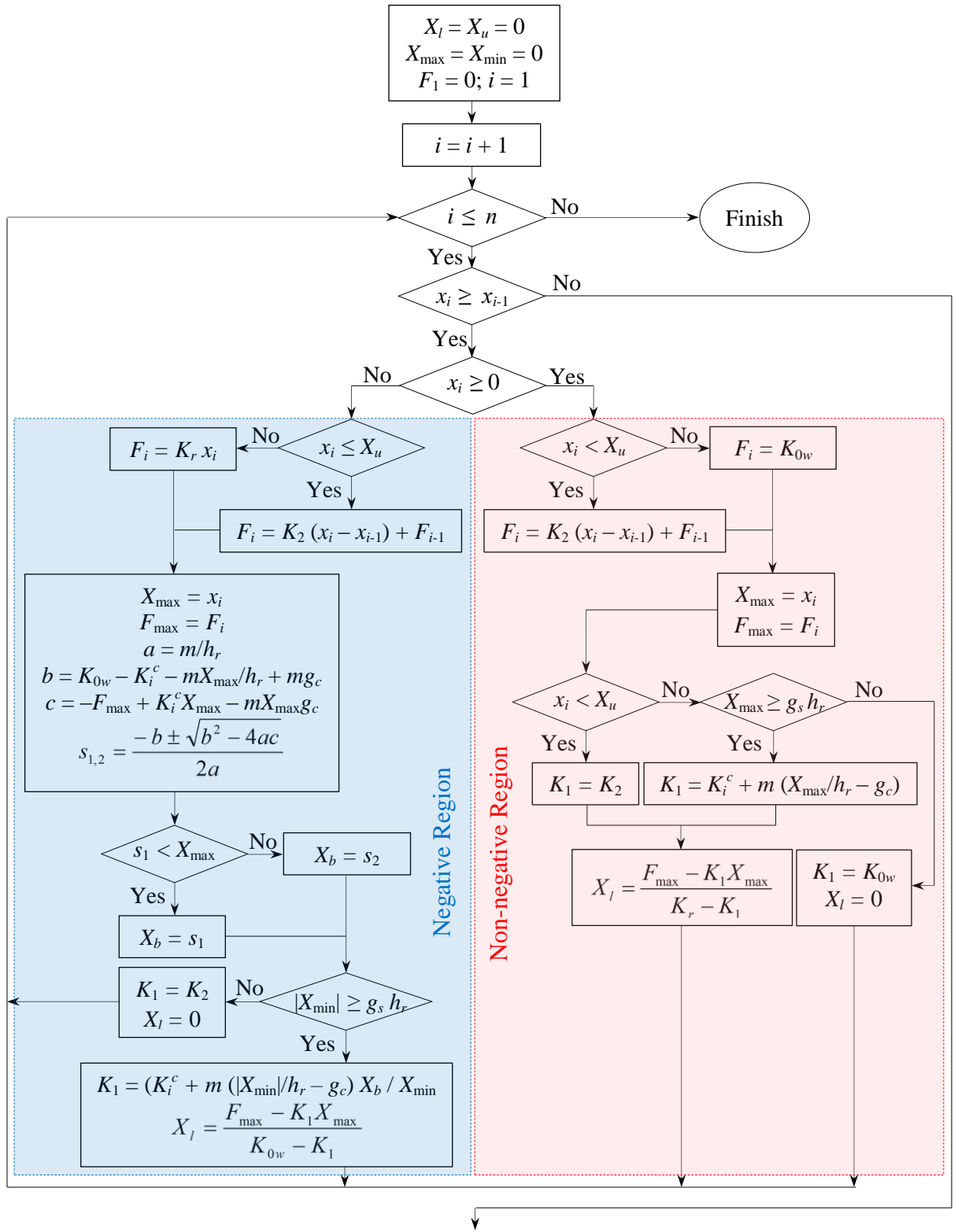
Figure 6.13. Algorithm of DC-SMAW model hysteresis (part 1)
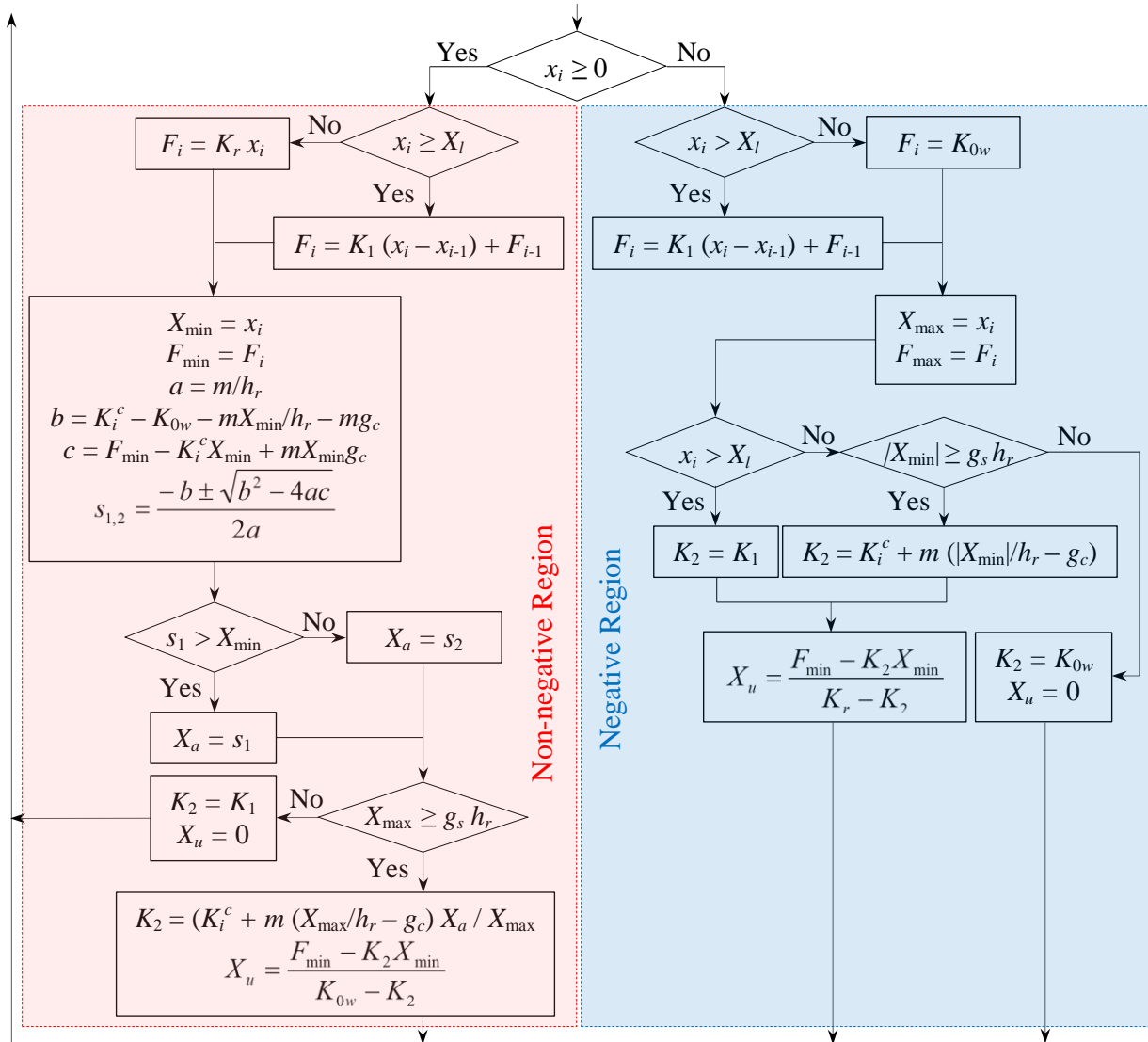
Figure 6.13. Algorithm of DC-SMAW model hysteresis (part 2)

In the algorithm of DC-SMAW hysteresis, lower and upper limits (X_u and X_l) are defined for the horizontal displacement (x_i) and updated in each loop. In fact, these limits indicate locations at which the stiffness (slope) of the hysteresis curve changes if the shear strain goes beyond the starting point (g_s) and the SMA wires are activated. Otherwise, the slope does not change. As illustrated in Figure 6.14, in the positive region and at shear strain amplitudes greater than g_s, when the rubber bearing deflects in the positive direction on path *OAB* (first scenario), if x_i exceeds the upper limit, X_u (at point *A*), the slope will change from the initial stiffness to the intermediate stiffness. Under the same condition, when the rubber bearing moves along path *CDA* (second scenario), if x_i exceeds X_u at point *D*, the slope will

192

change from K_i to the $K_{0,w}$. When the lateral displacement occurs in the negative direction on path *ABO*, the slope changes from the intermediate stiffness to the re-centring stiffness as x_i decreases lower than X_l at point *B* (third scenario). In the fourth scenario, by moving along path *DCO*, the lower limit, X_l, is updated and located at point *C*. The same algorithm is applied in the negative region of hysteresis.
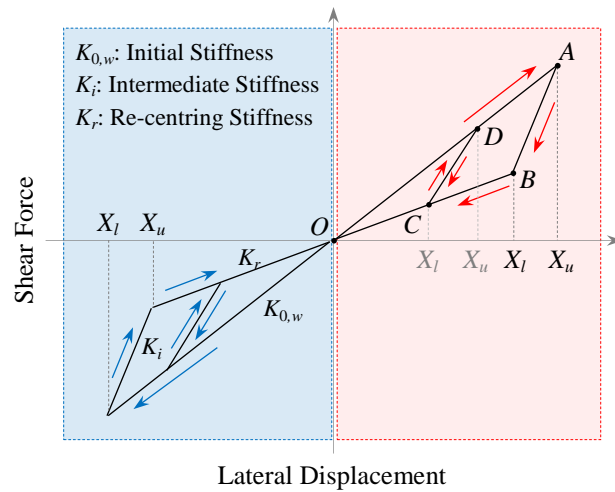
Figure 6.14. Typical shear hysteresis of DC-SMAW

As explained before, the intermediate stiffness, as one characteristic of DC-SMAW hysteresis model, linearly varies in the active range of SMA wires during which the shear strain is greater than g_s. Therefore, a section in the negative region of part 1 and non-negative region of part 2 of the algorithm in Figure 6.13 is dedicated to estimating this stiffness. In this section, the intermediate stiffness is calculated from a linear equation by indicating the rate of change (e.g. degradation factor, m), and critical values of the shear strain amplitude, g_c and the intermediate stiffness, K_i^c.

Based on the material properties of ferrous SMA wire (FeNiCoAlTaB) and geometries of rubber bearing and wire (input parameters), which are given in Table 6.4, five characteristics of the model are calculated through the flowchart depicted in Figure 6.12. These characteristics are listed in Table 6.4.

Table 6.4. Input parameters and characteristics of DC-SMAW model

Input parameters				Characteristics	
Material properties		Geometry			
ε_s^M (%)	1.50	l (mm)	240.0	$K_{0,w}$ (kN/mm)	1.01
ε_f^M (%)	8.44	w (mm)	240.0	K_i^c (kN/mm)	3.54
ε_s^A (%)	7.40	h (mm)	92.8	K_r (kN/mm)	0.49
ε_f^A (%)	0.46	h_r (mm)	35.0	g_s	0.91
σ_s^M (MPa)	732.4	r_{SMA} (mm)	2.5	g_c	1.28
σ_f^M (MPa)	804.7				
σ_s^A (MPa)	343.9				
σ_f^A (MPa)	224.8				
m (kN/mm)	4.3				

6.3.3 Verification of SMA Wires Model

In order to assess the accuracy of prediction, the results, which are attained from the developed computer code written in MATLAB (R2010a), should be validated. In this regard, SMA-LRB is subjected to a number of input displacements and the hysteresis of DC-SMAW system obtained from the computer code (MCODE) is compared to the hysteresis of the same system modelled and analyzed in ANSYS (ANSYS Mechanical APDL, Release 14.0). To make sure that the model is working properly in any condition, input lateral displacements are chosen to follow different functions such as ramp, step, sinusoidal, and combination of them with different peak amplitudes. Here, it should be noted that although the strain-rate is considered to be a variable in input displacements, the response is not a function of it because the proposed model is strain-rate independent. Considering the total thickness of rubber layers in LRB ($h_r = 35$ mm), the lateral displacement is normalized and the variation of shear strain (i.e. ratio of displacement to h_r) over the time is plotted in Figure 6.15 for four cases (E5 to E8).
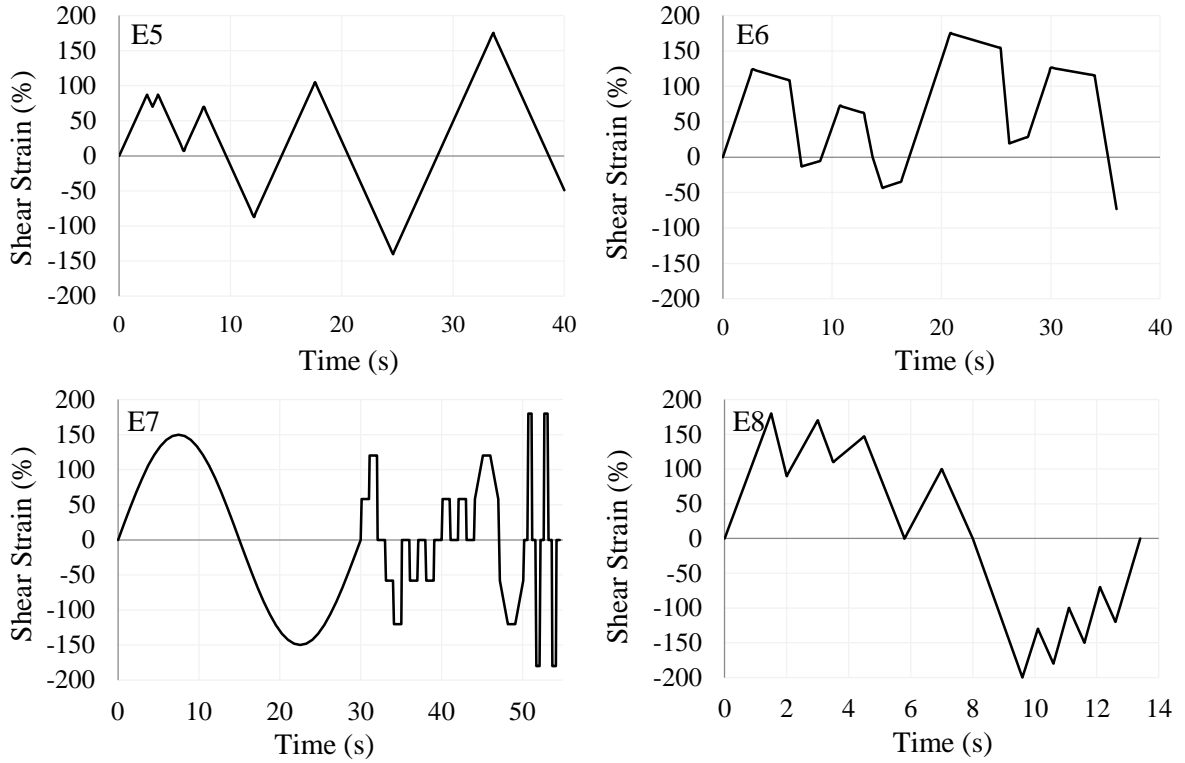
Figure 6.15. Normalized input displacement

In Figure 6.16, which shows responses of the DC-SMAW model, the number of response corresponds to an excitation with the same number. As an instance, curve R5-MCODE and R5-FEM represent the shear hystereses of the model excited by input displacement E5 and obtained using the MATLAB code and ANSYS, respectively.
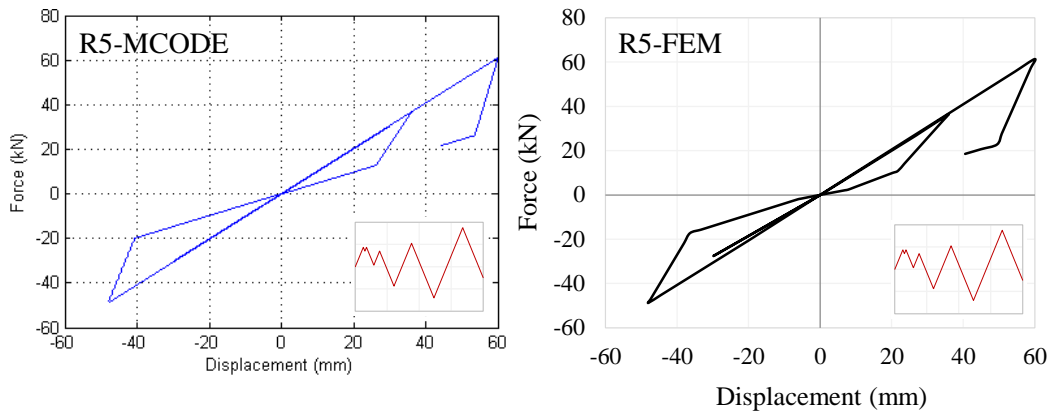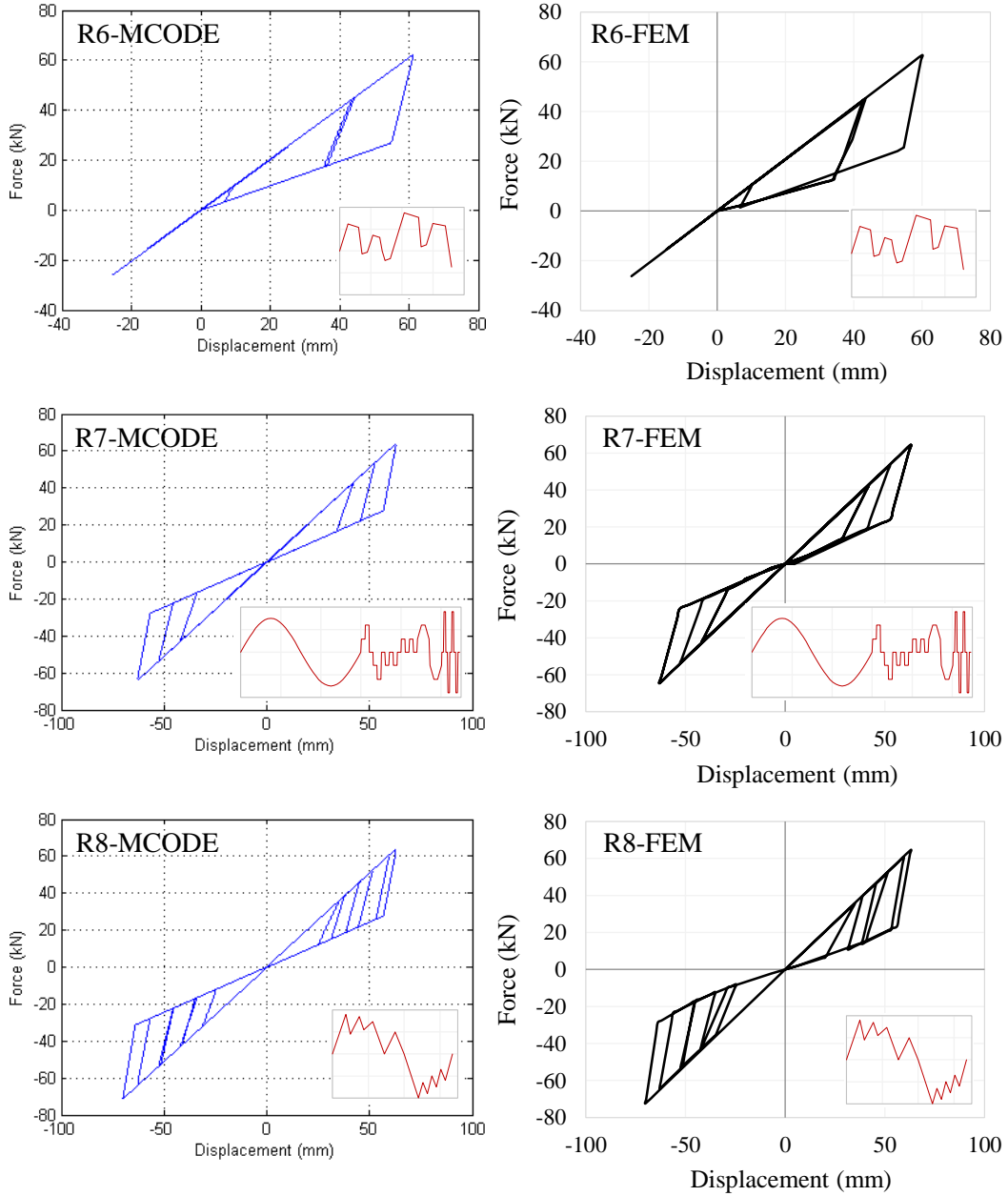
Figure 6.16. Shear hysteretic response of DC-SMAW excited by different input displacements and evaluated through computer code (MCODE) and ANSYS (FEM)

As can be observed in Figure 6.16, a satisfactory agreement between two approaches reveals that the developed algorithm of hysteresis model is capable of accurately predicting the shear response of DC-SMAW model under different excitations.

6.3.4 Hysteresis of SMA-LRB

By evaluating the responses of decoupled models (LRB and DC-SMAW), the hysteresis of SMA-LRB can be determined based on the superposition method. Figure 6.17 depicts the lateral force-deflection curves of the decoupled systems along with the SMA-LRB. As an example, R5-LRB, R5DC-SMAW, and R5-SMA-LRB are hysteretic responses of LRB, DC-SMAW, and SMA-LRB, respectively, which are subjected to the excitation number 5 (E5), shown in Figure 6.15.

The effect of each system can be observed on the overall behaviour of SMA-LRB. Results show that he DC-SMAW model with zero residual deformation could effectively reduce the residual deformation of the LRB when SMA wires are activated. When responses of LRB and SMA-LRB are compared, it is understood that SMA wires increase the maximum shear force due to increasing the lateral stiffness of the system. In fact, when the lead core yields and enters the plastic region, its stiffness dramatically drops from $K_0 = 5.28$ kN/mm (i.e. initial stiffness) to $rK_0 = 0.69$ kN/mm (i.e. post-yield stiffness) which is lower than the initial stiffness of DC-SMAW ($K_{0,w} = 1.01$ kN/mm). Therefore, when the lateral displacement reaches its maximum value, DC-SMAW generates a higher amount of shear force compared to the LRB.
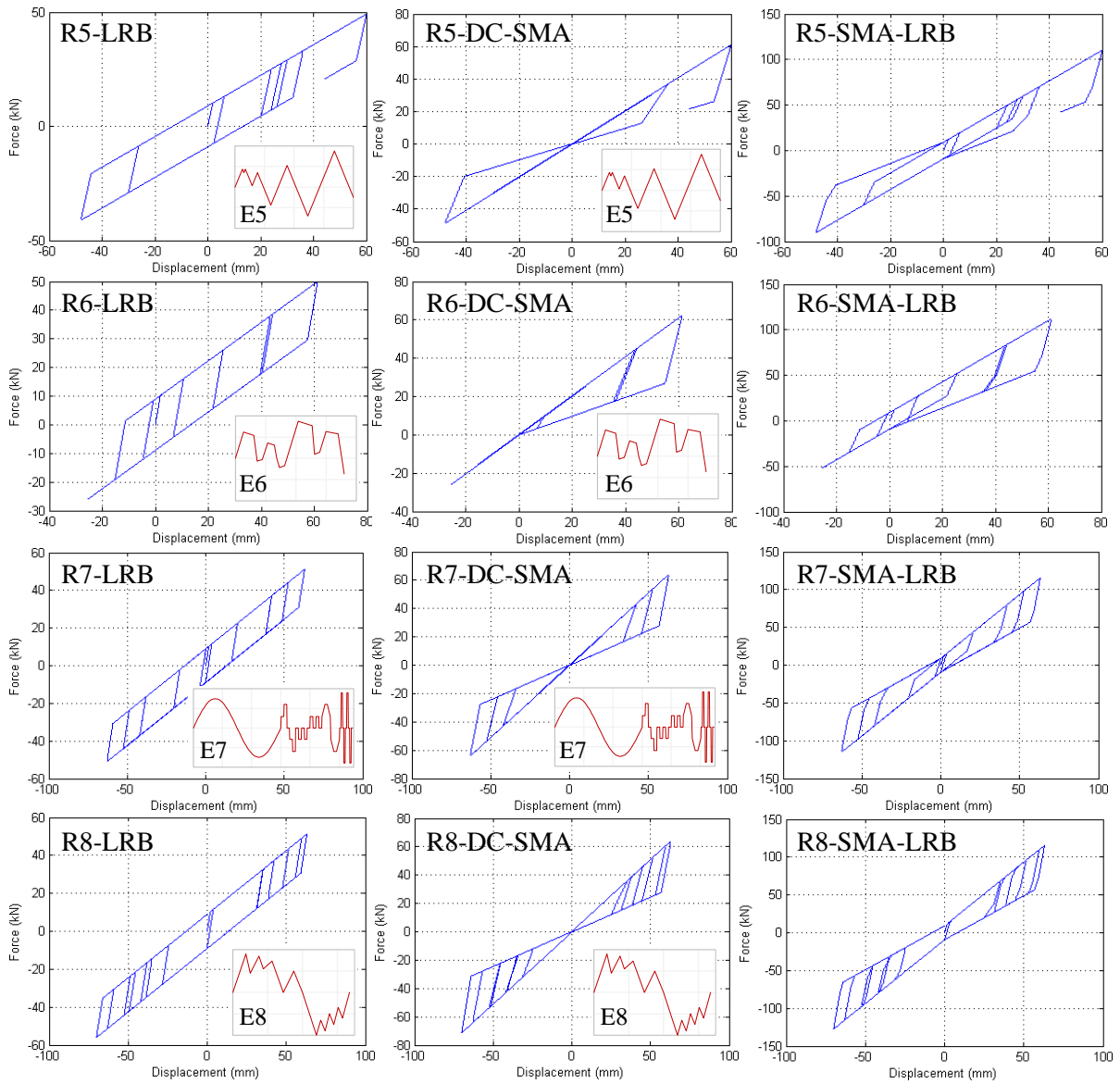
Figure 6.17. Shear hysteretic responses of LRB, DC-SMA, and SMA-LRB excited by input displacements E5, E6, E7, and E8

To more precisely study characteristics of the proposed constitutive model, SMA-LRB is subjected to different excitations by focusing on the magnitude of the shear strain. In the first case (Figure 6.18), a ramp input displacement is applied to the system and the response is measured when the excitation is scaled in three levels (E9-1, E9-2, and E9-3). In the second case (see Figure 6.19), SMA-LRB is subjected to three scaled sinusoidal displacements.
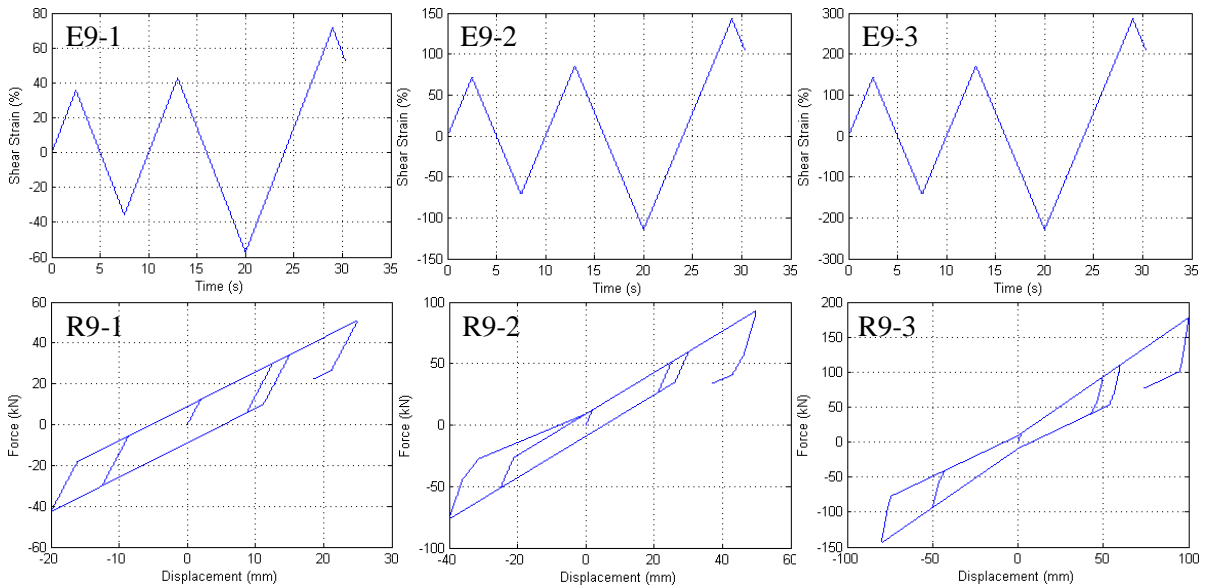
Figure 6.18. Shear hysteretic response of SMA-LRB subjected to a ramp input displacement (E9) scaled with different factors
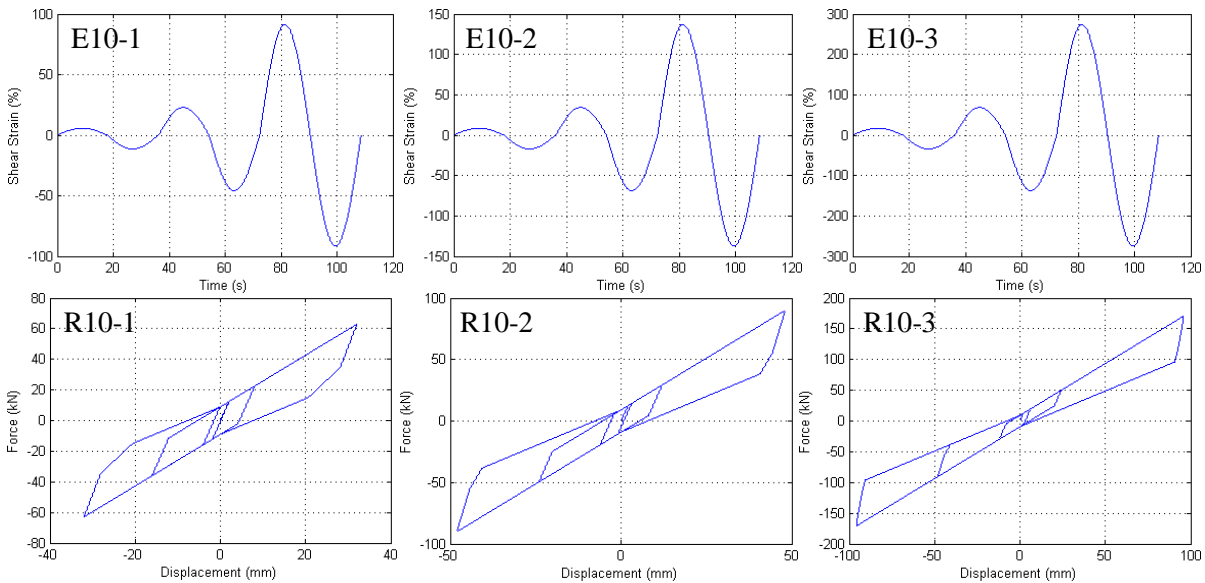
Figure 6.19. Shear hysteretic response of SMA-LRB subjected to a sinusoidal input displacement (E10) scaled with different factors

At low shear strain levels (i.e. strains lower than the starting limit, g_s), the response of SMA-LRB (e.g. R9-1) is analogous to that of the LRB and can be simulated using a bilinear kinematic hardening model. The reason is that the SMA wires are not activated under that level of shear strain and as a result, they do not produce a flag-shaped hysteresis. When the shear strain goes beyond its starting limit, the contribution of DC-SMAW to the response of

199

SMA-LRB (R9-2 and R9-3) can be perceived (see Figure 6.18). Another finding is that by increasing the amplitude of excitation, the superelastic effect of DC-SMAW on the hysteresis of the SMA-LRB increases. Such a behaviour can also be observed in the case of sinusoidal displacements (Figure 6.19).

6.4   Summary

Smart LRBs in which shape memory alloy (SMA) is used in the form of wires are a new generation of elastomeric isolators with improved performance in terms of re-centring capability and energy dissipation capacity. The necessity of implementing SMA-LRB in bridges on one hand, and the lack of an appropriate hysteresis model for accurately simulating the behaviour of such isolators on the other hand, led this chapter to propose a constitutive model for SMA-LRB. LRB was equipped with a double cross configuration of SMA wires (DC-SMAW) and subjected to compression and unidirectional shear loadings. Due to the complexity of the shear behaviour of SMA-LRB, a hysteresis model was developed for DC-SMAW and then combined with the bilinear kinematic hardening model, which was assumed for the LRB. Comparing the hysteretic response of decoupled systems with that of the SMA-LRB showed that the high re-centring capability of the DC-SMAW model with zero residual deformation can noticeably reduce the residual deformation of LRB. The developed constitutive model for DC-SMAW was characterized by three stiffnesses when the shear strain exceeds a starting limit at which the SMA wires are activated due to phase transformation. An important point was that the shear hysteresis of DC-SMAW model looks different from the flag-shaped hysteresis of SMA because of the specific arrangement of wires and its effect on the resultant forces transferred from wires to the rubber bearing.

Chapter 7   Seismic Fragility Assessment of Multi-Span Continuous Steel-Girder Bridges

7.1   General

As a major part of transportation system, highway bridges play a key role in the public safety (e.g. medical services, firefighting, and emergency routes for rescues). Observations from the performance of highway bridges during earthquakes over the last 40 years (e.g. San Fernando 1971, Loma Prieta 1989, Northridge 1994, Great Hanshin 1995, Chi-Chi 1999, Chile 2010, Haiti 2010, and Tohoku 2011) have revealed that these structures are highly vulnerable during seismic events (Basoz et al., 1999; Yamazaki et al., 2000). In such a situation, it is highly important to protect the bridge against earthquakes and systematically investigate its functionality by considering the level of structural damage that might occur in each component (e.g. isolation system, pier, and deck) under different ground excitations.

In order to evaluate the seismic performance of highway bridges, it is critical to assess the level of vulnerability of the bridge when subjected to certain ground motions. In the seismic risk assessment of bridges, fragility curves are developed to determine the probabilities that the structural demand (structural response), which is caused by different levels of seismic excitation, exceeds the structural capacity defined at a damage state. In fact, fragility curves or fragility functions, as common tools for seismic assessment of bridges, represent the probabilities of structural damage due to earthquake as a function of ground motion intensities The intensity measure can be presented through different indices such as peak ground displacement (PGD), peak ground velocity (PGV), peak ground acceleration (PGA), spectral acceleration at the first mode period ($S_a(T_1)$), and spectrum intensity (SI). Among these parameters, the peak ground acceleration, PGA, is known as one of the widely-used intensity measures and suggested as the optimum choice to describe the severity of the ground motion. The reason is due to the efficiency, practicality, sufficiency, and hazard computability of this parameter (Nielson and DesRoches, 2007; Padgett et al., 2008). Several methodologies have been established to generate fragility curves. They are categorized as expert-based, empirical, and analytical methods. The first method is based on the opinions of experts (ATC, 1985). In the second approach, analyses are performed based on the damages

observed after earthquakes (Basoz et al., 1999; Shinozuka et al., 2000; Yamazaki et al., 2000). In the last method, which is mostly used in the vulnerability assessment, fragility curves are developed analytically (Mander and Basoz, 1999; Hwang et al., 2001; Jernigan and Hwang, 2002; Mackie and Stojadinovic, 2006; Nielson and DesRoches, 2007; Alam et al., 2012). The reason is that the analytically generated fragility curves are more readily applicable to bridges and regions where damage data from earthquakes are insufficient or not available. Nonlinear static analysis (Mander and Basoz, 1999; Monti and Nistico, 2002; Moschonas et al., 2009), elastic-spectral analysis (Hwang et al., 2000b; Jernigan and Hwang, 2002), linear/nonlinear time-history analysis (Hwang et al., 2001; Choi et al., 2004; Ramanathan et al., 2010; Billah and Alam, 2012), and Bayesian approach (Gardoni et al., 2002 and 2011) are different analytical methods that are used for developing fragility functions. Billah and Alam (2014) conducted an extensive literature review on the seismic fragility assessment of highway bridges and showed that since 2001, more than 85% of studies are based on the analytical approach and the rest of that used experimental and empirical methods.

Traditionally, bridge piers were considered as the primary component to be an indicative of the overall fragility of the structure (Hwang et al., 2000a; Mackie and Stojadinovic, 2001; Nateghi and Shahsavar, 2004). Since 2001, more than 50% of studies established the fragility of bridge systems based on the fragility of columns (Billah and Alam, 2014). However, Nielson and DesRoches (2004) showed that this is not an appropriate assumption for all types of bridges and could lead to significant errors in estimating the fragility functions of the whole system. With the goal of improving the accuracy, in addition to the piers, Choi et al. (2004) also considered bearings in bridge fragility assessments. Here, an important point is that for bridges with multi-column bents, all major vulnerable bridge components should be considered to maximize the correctness of system fragilities (Nielson and DesRoches, 2004). Alam et al. (2012) analytically assessed the fragility of a three-span continuous highway bridge isolated by laminated rubber bearings (HDRB and LRB) and fitted with SMA restrainers. They found that using SMA restrainers (bars) increases the damage probability of the bridge, especially, when the LRB is implemented as the isolation mechanism. However, SMA bars could significantly reduce the shear displacement demand in rubber bearings. Equipping the isolation system with SMA bars can reduce the bridge deck

displacement and as a result, overcome the unseating problem of the bridge during seismic excitations (Bhuiyan and Alam, 2013).

In Chapter 5, it was shown that SMA-NRB, SMA-HDRB, and SMA-LRB possess higher energy dissipation capacities and superior re-centring properties compared to conventional elastomeric bearings (e.g. NRB, HDRB, and LRB). However, the effect of such smart isolators has not been investigated on the seismic fragility of highway bridges. In order to use SMA-RBs in structural applications, it is critical to make sure that the structure isolated by SMA-RBs responds reliably and efficiently under different seismic excitations and evaluate the effect of such isolation devices on the failure probability of the bridge system. Based on this motivation, the purpose of this chapter was to assess the seismic vulnerability of a multi-span continuous steel-girder (MSCS) highway bridge isolated by SMA-RBs. In the smart isolation systems, SMA wires were wrapped around NRB, HDRB, and LRB in either cross configuration or double cross configuration. Here, a three-span continuous steel-girder irregular bridge with a skew angle of 20 degrees was considered where rubber bearings isolate the bridge. Here, ferrous-based SMA wires were incorporated as supplementary elements in the rubber bearings. 3D FE models were generated and incremental dynamic analyses (IDA) were carried out to determine the seismic fragility functions of the bridge. A total of 30 ground motions with different longitudinal and transverse components were considered in the numerical simulations. In IDAs, each earthquake record was scaled with a number of scaling factors. Two bridge components; bridge pier and isolation bearing were considered for generating the seismic fragility curves of the bridge at four different damage states (i.e. slight, moderate, extensive, and collapse). Finally, in order to provide an estimation of the system vulnerability, the fragility functions of bridge components were combined using the upper bound of the first order reliability theory which results to a conservative assessment.

7.2   Seismic Fragility Methodology

Structural reliability evaluates the vulnerability of a structure affected by a number of input parameters (Nielson and DesRoches, 2007). Seismic fragility defines the probability levels at which the seismic demand of a structure, D, is equal to or greater than the capacity of the structure, C. This statement is subjected to a condition defined as a specified intensity

measure (*IM*), which indicates the level of seismic loading. The conditional probability can be written in the following form:

$$Fragility = P[LS|IM] = P[D \geq C|IM] = P[D - C \geq 0|IM]$$ (7.1)

where *LS* is the limit state or damage level of the bridge or a bridge component. Figure 7.1 shows a schematic view of a fragility curve of a structure at a certain limit state (LS[*]). As an example, when the intensity measure is equal to *x*, the probability that the structure reaches the specified level of damage at the considered limit state is 80%.
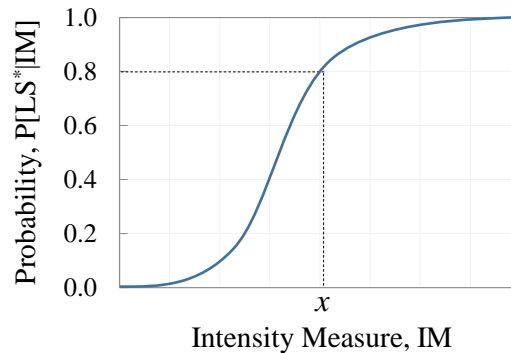
Figure 7.1. Fragility function of a structure at a specified limit state

Considering the conditional situation, a probabilistic seismic demand model (PSDM) is developed to correlate the engineering demand parameters, EDPs, (e.g. bearing deformation, pier ductility) with the intensity measure (e.g. peak ground acceleration, spectral acceleration) and show a probability distribution for the demand. Consequently, a distribution for the capacity is defined to be used along with PSDM in Equation (7.1).

To develop PSDM, two methods are used; the cloud approach and the scaling approach. In the first method, unscaled earthquake records are used in the nonlinear time-history analysis (NTHA) and based on the obtained results, a PSDM is generated (Mackie and Stojadinovic, 2001; Choi et al. 2004; Nielson and DesRoches, 2007; Billah et al., 2013). In the second approach, all records are scaled to selective intensity levels and an incremental dynamic analysis (IDA) is performed at each intensity level (Alam et al., 2012; Bhuiyan and Alam, 2013). In this chapter, the scaling approach is implemented for developing the fragility functions. It should be noted that the purpose of conducting incremental dynamic analysis (IDA) is to generate an adequate number of data for establishing fragility curves.

Often, it is assumed that the distribution of EDP follows a two-parameter lognormal probability distribution about its median (Song and Ellingwood, 1999; Cornell et al., 2002). Here, a power model is used for representing the median demand, S_d, or the engineering demand parameter.

$$EDP = S_d = a \, \mathrm{IM}^b \qquad (7.2)$$

where *a* and *b* are coefficients that can be calculated from a regression analysis of the response obtained from the IDAs.

According to the probability theory, if the variable *EDP* has a lognormal distribution, ln(*EDP*) will have a normal distribution. By applying a logarithmic transformation, Equation (7.2) becomes:

$$\ln(S_d) = \ln(a) + b \ln(\mathrm{IM}) \qquad (7.3)$$

Similar to the demand, lognormal distributions can also be assumed for capacities of bridge components. In this regard, considering same distributions for demand and capacity of the bridge components, the fragility equation (Equation (7.1)) can be written as (Hwang et al., 2001):

$$P[LS|\mathrm{IM}] = P[D > C|\mathrm{IM}] = \Phi\left[\frac{\ln(S_d/S_c)}{\sqrt{\beta_{D|\mathrm{IM}}^2 + \beta_c^2}}\right] \qquad (7.4)$$

in which Φ is the cumulative distribution function (CDF) of the standard normal distribution. S_d and S_c are the median estimates of the demand and the capacity (a certain limit state), respectively, $\beta_{D|\mathrm{IM}}$ is the logarithmic standard deviation of the demand conditioned on the IM, and β_c is the logarithmic standard deviation (dispersion) of the capacity.

Substituting Equation (7.3) into Equation (7.4) and considering the characteristics of natural logarithm function, the fragility function of each bridge component for a selected limit state, *LS*, can be expressed in the following form:

$$P[LS|\text{IM}] = \Phi\left[\frac{b\ln(\text{IM}) - (\ln(S_c) - \ln(a))}{\sqrt{\beta_{D|\text{IM}}^2 + \beta_c^2}}\right]$$ (7.5)

$$= \Phi\left[\frac{\ln(\text{IM}) - \lambda}{\xi}\right]$$

where λ and ξ are the median and the standard deviation (dispersion) of the intensity measure, IM, respectively.

$$\lambda = \frac{\ln(S_c) - \ln(a)}{b}$$ (7.6)

$$\xi = \frac{\sqrt{\beta_{D|\text{IM}}^2 + \beta_c^2}}{b}$$ (7.7)

The conditional dispersion or the standard deviation of the demand, $\beta_{D/IM}$, can be found from Equation (7.8) (Baker and Cornell, 2006):

$$\beta_{D|\text{IM}} = \sqrt{\frac{\sum_{i=1}^{N}\left[\ln(EDP_i) - \ln\left(a\,\text{IM}_i^{\,b}\right)\right]^2}{N-2}}$$ (7.8)

in which *N* is the total number of simulations. It should be noted that the statistical degrees of freedom is equal to the number of data points (*N*) minus the number of estimated parameters.

7.2.1   Limit/Damage States

The limit/damage states (structural capacities) for each bridge component, should be quantitatively defined in terms of *EDPs* and have a qualitative representation for that component. The limit states used in this chapter (e.g. slight, moderate, extensive and collapse) are the same limit states defined and used in the FEMA loss assessment package HAZUS-MH (FEMA, 2003). The qualitative description of these damage states are provided in Table 7.1.

Table 7.1. Qualitative limit states (FEMA, 2003)

Limit State	Description
Slight	Minor cracking and spalling to the abutment, cracks in shear keys at abutments, minor spalling and cracks at hinges, minor spalling at the column (damage requires no more than cosmetic repair) or minor cracking to the deck.
Moderate	Any column experiencing moderate (shear cracks) cracking and spalling (column structurally still sound), moderate movement of the abutment (<2"), extensive cracking and spalling of shear keys, any connection having cracked shear keys or bent bolts, keeper bar failure without unseating, rocker bearing failure or moderate settlement of the approach.
Extensive	Any column degrading without collapse – shear failure – (column structurally unsafe), significant residual movement at connections, or major settlement approach, vertical offset of the abutment, differential settlement at connections, shear key failure at abutments.
Collapse (Complete)	Any column collapsing and connection losing all bearing support, which may lead to imminent deck collapse, tilting of substructure due to foundation failure.

To determine the capacity levels (limit states) of bridge components, there are two approaches; descriptive and prescriptive. The descriptive approach, which is based on the judgment of experts, describes the functionality levels that would be assigned to the structure by bridge inspectors for various levels of observed damage (Hwang et al., 2000a). On the other hand, the perspective approach deals with the physics of the problem and prescribes levels of operation to be allocated to the structure for different levels of damage (Mackie and Stojadinovic, 2006). Since the prescriptive method involves an engineering analysis, it is preferred over the descriptive method especially in the absence of expert decision makers (Nielson and DesRoches, 2007). In addition, using the Bayesian approach, which is a combination of subjective and physics-based assessments, the distribution parameters of limit states (S_c, β_c) can also be determined for each structural component.

In this chapter, bridge piers and isolation bearings are assumed the main vulnerable components of the highway bridge because they often show nonlinear behaviour under strong ground motions. The quantitative measure of the limit/damage state considered for the pier is displacement ductility, μ_d. For the isolation bearing, the limit/damage state is quantified with the horizontal displacement or in the normalized form, the shear strain. Based on the available literature, the range of *EDPs* considered for each component is specified at each limit state according to Table 7.2. The limit states of isolation system are determined based

on the design considerations (i.e. pounding and unseating effects) as well as experimental investigations.

Table 7.2. Limit/damage states of bridge components

Bridge Component	Assigned EDP	Limit States				Reference
		Slight	Moderate	Extensive	Collapse	
Pier	Displacement Ductility	$\mu_d > 1.00$	$\mu_d > 1.20$	$\mu_d > 1.76$	$\mu_d > 4.76$	Hwang et al. 2001
Isolation Bearing	Shear Strain	$\gamma > 100\%$	$\gamma > 150\%$	$\gamma > 200\%$	$\gamma > 250\%$	Zhang and Huo 2009

Here, an important point is that modern isolation bearings can experience high shear strains (e.g. 400%) with no failure; however, this large amount of lateral displacement can cause unseating or pounding problems in the bridge. Hence, it is assumed that when the shear strain reaches 250%, bearings collapse (JRA, 2002).

In order to describe capacity models of the bridge pier and the isolation bearing, the distribution parameters of limit states; median (S_c) and lognormal standard deviation (β_c) are required for each component. In fact, the median values are defined with some levels of uncertainty which are defined in the form of lognormal standard deviations. The distribution parameters of capacities are listed in Table 7.3 based on the recommendations in the literature (Hwang et al., 2001; Nielson and DesRoches, 2007; Ramanathan et al., 2010). The median values for capacities of piers and elastomeric isolators are unitless. It is important to mention that the values listed in Table 7.3 for isolation systems are capacities of regular elastomeric bearings. For SMA-RBs, the median and the standard deviation values should be updated in a future study.

Table 7.3. Capacity of RC piers and elastomeric isolation bearings

Limit/Damage State	Displacement Ductility		Shear Strain	
	S_c	β_c	S_c	β_c
Slight	1.00	0.73	100	0.79
Moderate	1.20	0.61	150	0.68
Extensive	1.76	0.74	200	0.73
Collapse	4.76	0.77	250	0.66

7.2.2 Ground Motion Suite

A data set of inputs (earthquake records) and outputs (damage) is necessary to establish a relationship between the ground motions and the structural damage. This is achieved by either collecting actual seismic records and damage data or conducting earthquake response analysis for specified models and inputs, and then acquiring resultant damages. The first approach is more accurate since the analysis is performed based on the real data and actual seismic damages. However, sometimes it is not possible to acquire adequate earthquake records near the structural damage. On the other hand, in the second approach, it is easy to generate well-distributed data. Since the time history analysis carried out in the second method should appropriately capture the nonlinear behaviour of structural members, it is highly important to precisely model the structure (bridge) in order to get reliable and correct results. Another point is that the bridge response depends on the characteristics of earthquake components (e.g. intensity, frequency content, and soil type) having uncertainties which can significantly affect the nonlinear structural response. Therefore, it is critical to properly select the ground motion parameters and correlate them with the structural damage.

Based on PEER strong motion database (PEER), 30 far-field earthquake records having different longitudinal and transverse components are collected to develop the fragility curves of bridge piers and elastomeric isolation bearings. Considering PGA as the intensity measure, the selected ground motion records have PGA values ranging from 0.04g to 1.16g with epicentral distances higher than 10 km. Since the MSCS bridge considered in this chapter is located in the province of British Columbia (western Canada), it is assumed that the ratio of PGA to PGV is between 0.8 and 1.2 (Naumoski et al., 1988). Table 7.4 presents the characteristics of the selected earthquake records.

Assuming a damping ratio of 5%, the acceleration response spectra of 30 far-field earthquake records are plotted along with their mean amplitude in Figure 7.2.
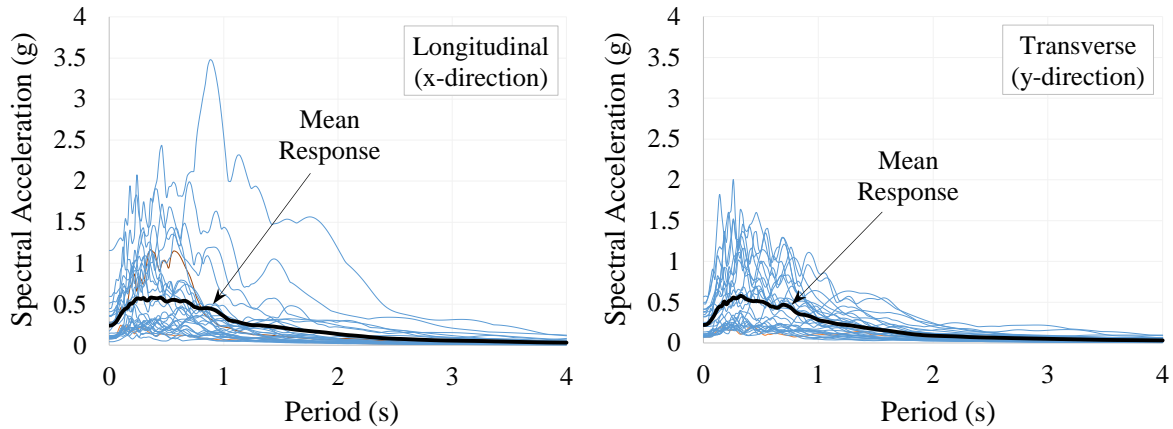
Figure 7.2. Spectral acceleration versus time period for 30 fear-field earthquake records

Table 7.4. Characteristics of the earthquake records

No	Earthquake	Location	Year	Magnitude (Richter)	Epicentral Distance (km)	PGA (g)		PGV (cm/s)	
						x	y	x	y
1	Chalfant Valley	USA	1986	6.2	33.4	0.08	0.07	7.0	7.9
2	Chi-Chi	Taiwan	1999	7.6	35.4	0.12	0.20	14.2	17.8
3	Chi-Chi	Taiwan	1999	7.6	44.0	0.09	0.08	9.2	7.3
4	Chi-Chi	Taiwan	1999	7.6	48.5	0.09	0.11	10.2	12.0
5	Chi-Chi	Taiwan	1999	7.6	13.7	0.60	0.35	73.3	40.9
6	Chi-Chi	Taiwan	1999	7.6	10.4	1.16	0.42	114.7	45.6
7	Coalinga	USA	1983	6.4	25.5	0.28	0.23	25.8	23.6
8	Coalinga	USA	1983	6.4	29.2	0.09	0.07	11.0	6.4
9	Coalinga	USA	1983	6.4	32.3	0.10	0.14	11.8	13.5
10	Friuli	Italy	1976	6.5	10.8	0.11	0.09	10.2	10.6
11	Hollister	USA	1986	5.4	14.9	0.04	0.09	5.3	9.3
12	Imperial Valley	USA	1979	6.5	28.7	0.27	0.25	24.9	30.1
13	Imperial Valley	USA	1979	6.5	43.6	0.35	0.24	33.0	26.0
14	Imperial Valley	USA	1979	6.5	12.6	0.36	0.38	34.5	42.1
15	Landers	USA	1992	7.3	90.6	0.12	0.09	12.9	9.6
16	Landers	USA	1992	7.3	21.2	0.28	0.42	25.6	42.3
17	Loma Prieta	USA	1989	6.9	12.7	0.37	0.32	32.9	39.1
18	Loma Prieta	USA	1989	6.9	64.4	0.24	0.33	25.5	27.9
19	Loma Prieta	USA	1989	6.9	10.3	0.45	0.50	51.3	44.6
20	Loma Prieta	USA	1989	6.9	77.0	0.10	0.11	10.0	13.1
21	Loma Prieta	USA	1989	6.9	79.7	0.08	0.09	6.7	10.4
22	Morgan Hill	USA	1984	6.2	28.3	0.08	0.08	7.2	10.0
23	Morgan Hill	USA	1984	6.2	28.3	0.10	0.10	10.3	11.6
24	Northridge	USA	1994	6.7	22.6	0.51	0.57	52.2	52.1
25	Northridge	USA	1994	6.7	13.0	0.41	0.48	43.0	45.1
26	Northridge	USA	1994	6.7	38.3	0.15	0.09	14.9	10.5
27	Northridge	USA	1994	6.7	37.7	0.09	0.07	7.8	7.1
28	Northridge	USA	1994	6.7	22.2	0.25	0.39	28.0	38.0
29	San Fernando	USA	1971	6.6	21.2	0.17	0.21	14.9	18.9
30	San Fernando	USA	1971	6.6	45.1	0.10	0.11	9.3	9.7

In the incremental dynamic analysis, a number of scaling factors ranging from 0.5 to 10.0 are selected in order to cover a wide range of possibilities (damage levels) and also increase the accuracy of the results for developing fragility curves.

7.2.3   System Fragility Curves

As discussed in section 7.1, for all types of bridges, the overall damage state of the structure cannot be expressed by the damage state of only one component (Nielson and DesRoches, 2004). Another point is that different bridge components such as isolation bearings, piers, and abutments experience different levels of damage during a seismic event. Therefore, in order to correctly assess the seismic fragility of the bridge system, the effects of major vulnerable components must be taken into account. Estimating the system fragility from the fragilities of bridge components can be performed through different methods such as the first order reliability theory, probabilities union theory, and joint probability seismic demand model (JPSDM).

The first order reliability theory is used to find the lower and upper bounds of the system fragility function. The application of this approach is in systems where the failure of one component causes failure of the entire system. In this method, the limit/damage state of the system, DS_{System}, is equal to the maximum limit/damage state of components, $DS_{comp\,i}$.

$$DS_{System} = \max_{i=1:n}\left(DS_{comp_i}\right) \tag{7.9}$$

where *n* is the total number of bridge components considered in the fragility assessment. Using the lower bound of the system fragility leads to an un-conservative evaluation and underestimate the failure probability of the system. Considering the upper bound tends to conservatively assess the failure probability of the system.

$$\max_{i=1:n}\left(P\left[F_{comp_i}\right]\right) \leq P\left[F_{System}\right] \leq 1 - \prod_{i=1}^{n}\left(1 - P\left[F_{comp_i}\right]\right) \tag{7.10}$$

in which P[F_S] and P[$F_{comp\,i}$] are probabilities of failure of the system and *i*th bridge component, respectively, and Π is the product operator.

In the second approach, the probability that the bridge fails (system failure, F_S), defined as a condition that the structure is at or beyond a specific limit state, is considered as the union of the probabilities of components being in that same limit state ($F_{comp\,i}$).

211

Therefore, the probability of system failure for a bridge with n components can be found from the following equation.

$$P[F_S] = \bigcup_{i=1}^{n} P\left[F_{comp_i}\right]$$

(7.11)

By recognizing some level of correlation between the demands of bridge components, the overall seismic demand of the system can be the joint demand on the components. In this regard, a joint probability seismic demand model (JPSDM) is developed in order to evaluate the fragility of bridge as a system. By estimating the correlation coefficients between the transformed demands (i.e. the logarithmic form of the demand model), defined according to Equation (7.3), the covariance matrix is formed and the JPSDM is generated in the transformed state. Then, having the JPSDM and the capacity models, Monte Carlo simulation is used for different levels of the IM to evaluate the probability of the failure of the system. Finally, the parameters of system fragility function are calculated through a regression analysis. Since conducting Monte Carlo simulation is computationally more expensive than the first approach, in this research, the upper bound of the first order reliability theory is used to conservatively estimate the fragility of the bridge system. Based on the assumptions and simplifications, a chart is provided for the methodology of seismic fragility assessment in Figure 7.3. Seven steps are followed to establish fragility functions of the bridge system.

1 Selecting a set of N_{EQ} earthquake

Intensity Measure ($IM = PGA$)	Location (*Western Canada*)
0 < PGA < 1.16	*0.8 < PGA/PGV < 1.2*

2 Generating N models for the MSCS

Isolation Systems ($N_{RB} = 6$)	Earthquake records ($N_{EQ} = 30$)

$N = N_{RB} \times N_{EQ} = 180$

3 Conducting Incremental Dynamic Analysis

Scaling Factors: 0.5, 1.0, 2.0, 3.0, ..., 10.0

4 Extracting results
Peak responses vs. Peak values of

Shear Strain of Rubber Bearing, γ	Displacement Ductility of Pier, μ_d

5 Performing regression analysis to develop Probabilistic Seismic Demand Models

Coefficients: a, b, and $\beta_{D|IM}$

EDP	PSDM	Dispersion
μ_d	$ln\,(a_\mu) + b_\mu\,ln$ (PGA)	$\beta_{\mu\,|\,PGA}$
γ	$ln\,(a_\gamma) + b_\gamma\,ln$ (PGA)	$\beta_{\gamma\,|\,PGA}$

Damage States (Capacity models)

Coefficients: S_c and β_c

Slight	Moderate
Extensive	Collapse

6 Obtaining fragility curves of

$$P[D > C | IM] = \Phi\left[\frac{\ln(\mathrm{IM}) - \lambda}{\xi}\right]; \quad \lambda = \frac{\ln(S_c) - \ln(a)}{b}, \xi^2 = \frac{\beta_{D|IM}^2 + \beta_c^2}{b^2}$$

Rubber Bearing	*Bridge Pier*

7 Estimating fragility curves of the

Upper bound in the 1st order reliability theory

$$P[F_{System}] = 1 - (1 - P[F_{Pier}])(1 - P[F_{Rubber\ Bearing}])$$

Figure 7.3. Methodology of seismic fragility assessment for the MSCS bridge

For generating a PSDM, steps 1 to 5 should be followed.

1. Choosing a set of N_{EQ} earthquake records which are well-suited to the geographical area of interest and include an acceptable range of values for the selected *IM* (PGA).

2. Generating *N* models of the MSCS bridge by considering the number of ground motions (N_{EQ}) and the number of isolation systems (N_{RB}), ($N = N_{EQ} \times N_{RB}$).

3. Conducting an incremental dynamic analysis (IDA) for each bridge model. In each IDA, a number of nonlinear time history analyses, which is equal to the number of scaling factors (N_{SF}), are performed for each model.

4. Extracting and plotting peak responses versus the peak value of the *IM* for each IDA. (This step is repeated for major vulnerable components of the bridge)

5. Performing a regression analysis of the obtained results to estimate regression coefficients *a*, *b*, and $\beta_{D|IM}$.

In steps 6 and 7, fragility functions of the bridge components and the bridge system are determined respectively, with considering the median and the standard deviation of capacity models at each limit state.

7.3   Fragility Assessment of a Highway Bridge

7.3.1   Finite Element Modelling

The bridge considered in this study is a multi-span continuous steel-girder (MSCS) highway bridge located in the province of British Columbia (western Canada), as shown in Figure 7.4. The bridge is irregular (i.e. piers with different heights) and consists of three spans supported on two reinforced concrete multi-column bents having a skew angle of 20 degrees. By considering six different isolation systems; three conventional rubber bearings (NRB, HDRB, and LRB) and three smart SMA-based rubber bearings (SMA-NRB, SMA-HDRB, and SMA-LRB), six models are generated. In each case, the MSCS highway bridge is isolated with one type of elastomeric isolator.
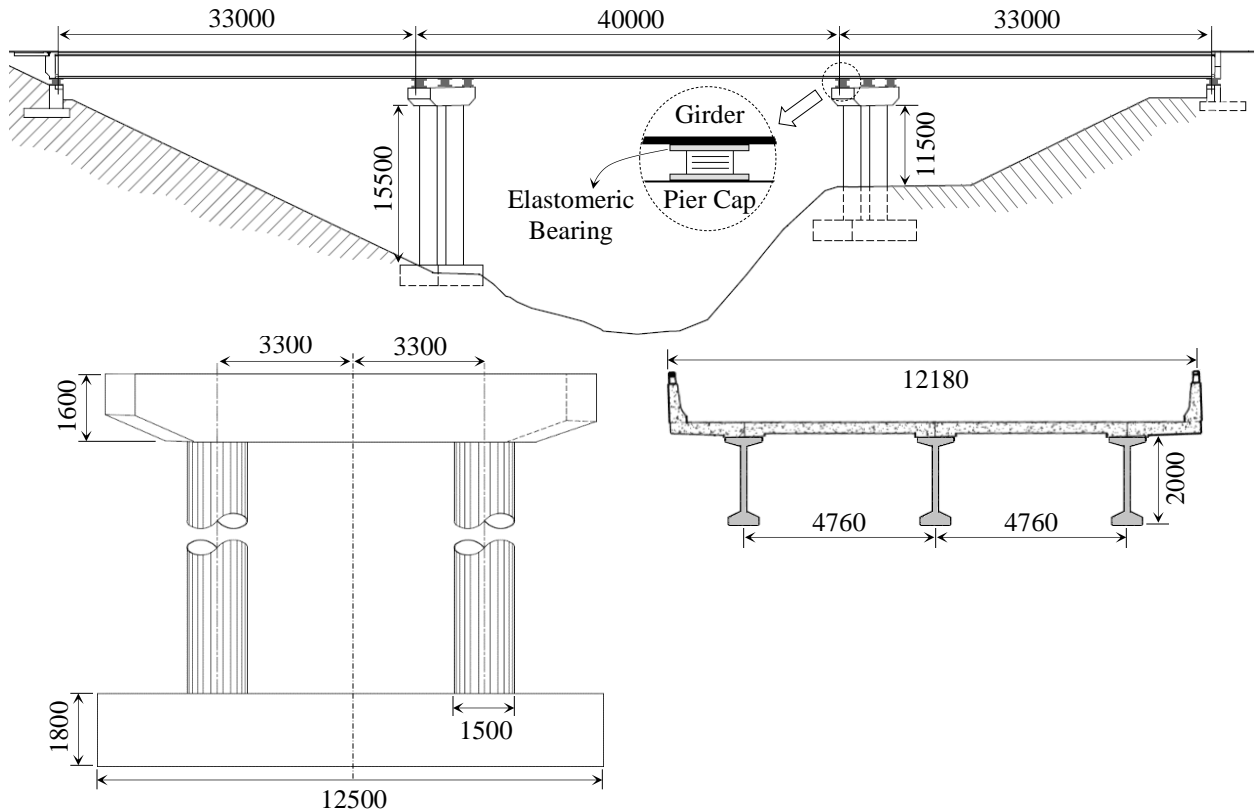
Figure 7.4. Multi-span continuous steel-girder (MSCS) bridge; (a) elevation view, (b) side view of footing, piers, and pier cap, (c) superstructure consisting of deck and steel girders

To numerically simulate the bridge, a 3D FE model is generated in SeismoStruct (SeismoStruct, v6.5).

In order to evaluate the seismic performance of the bridge, incremental dynamic analyses (IDAs) are performed. SeismoStruct has the capability of accurately capturing the large deformation and the collapse load of framed structures under static and dynamic loadings when material inelasticity and geometry nonlinearities are considered (Pinho et al., 2007). In the analytical model, the Menegotto-Pinto steel model (Menegotto and Pinto, 1973) with the isotropic strain-hardening property is used for steel material. For the concrete, the nonlinear variable confinement model of Madas and Elnashai (1992) is implemented. The material properties of concrete and steel (reinforcement) used in the bridge are listed in Table 7.5. It should be noted that although uncertainty in the material properties can affect the system fragility, this factor is not considered in this study in order to simplify the problem and reduce the amount of calculations.

Table 7.5. Material properties of concrete and steel reinforcement

Material	Property	Value	Unit
Concrete	Compressive Strength	30	MPa
	Tensile Strength	0	MPa
	Strain at Peak Stress	0.2	%
	Specific Weight	24000	N/m^3
Steel	Elastic Modulus	200	GPa
	Yield Stress	525	MPa
	Strain Hardening Parameter	0.5	%
	Specific Weight	78000	N/m^3

The steel girders are modelled using elastic frame elements so that they remain elastic under the seismic loadings. Girders are divided into a number of small discrete segments. The mass of each segment is assumed to be equally distributed between each two adjacent nodes in the form of point mass. Knowing the fact that the response of the bridge is typically governed by the foundation, piers, and isolation bearings (Choi et al., 2004), it is assumed that the stiffness of the superstructure has a minor effect on the seismic response of the bridge (Ghobarah and Ali, 1988). For modelling the columns (piers) and pier caps, nonlinear inelastic beam-column (frame) elements are used. To represent the distribution of the material nonlinearity along the length and cross-section of the piers and beams, the fibre-modelling approach is implemented. Each fibre has a constitutive (stress-strain) relationship through which the unconfined concrete, the confined concrete, and the longitudinal steel reinforcement can be specified. The confinement effect of the concrete section is considered on the basis of reinforcement detailing showed in Figure 7.5.
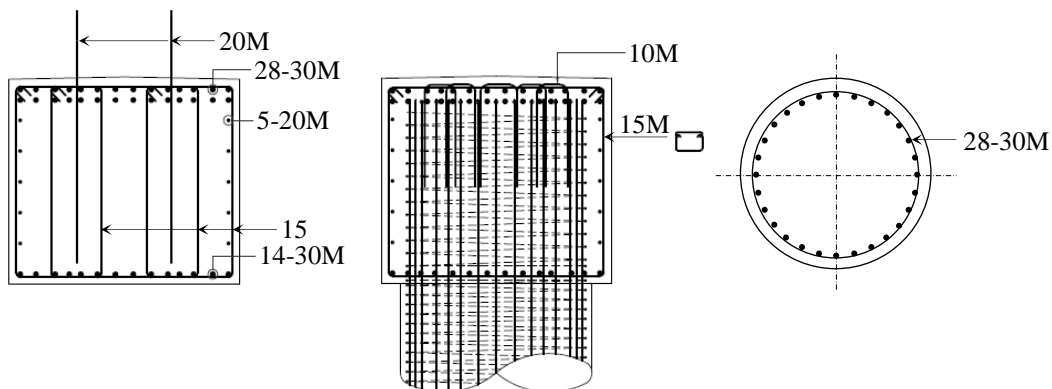
Figure 7.5. Reinforcement details of the bent and the column

216

In order to simplify the analysis, the effect of abutment on the seismic vulnerability of the MSCS bridge is not considered. Moreover, it is assumed that the bridge bent is supported on a rigid foundation (i.e. the pier supports are assumed to be fixed).

In order to investigate the performance of each type of rubber bearing on the seismic fragility of the bridge and determine the most efficient isolation system, six different cases are modelled, analyzed, and then compared to each other. Based on the cross and double cross arrangements of wires, discussed in Chapter 5, SMA wire-based elastomeric isolators are presented here. For SMA-NRB and SMA-HDRB, two wires are wrapped around the bearing in a cross configuration and for SMA-LRB, double cross (DC) wires are employed. The reason that the wires are implemented in different arrangements is that DC wires led to a better performance in the LRB compared to the cross wires. SMA-based elastomeric isolators equipped with the cross and double cross configurations are schematically illustrated in Chapter 5 in Figure 5.2 and Figure 5.31, respectively.

All six rubber bearings have the same plan area of 350 mm by 350 mm with identical total thicknesses of rubber layers (70 mm). In order to simulate the behaviour of rubber bearings, the bilinear kinematic model is used. The reason of choosing such a model for capturing the behaviour of isolation systems is that bilinear model with kinematic hardening is the most suitable and well-fitted model available in Seismostruct (Seismostruct, v6.5). The actual shear force-deflection hysteresis along with the idealized bilinear behaviour are plotted in Figure 7.6 for each elastomeric isolator.
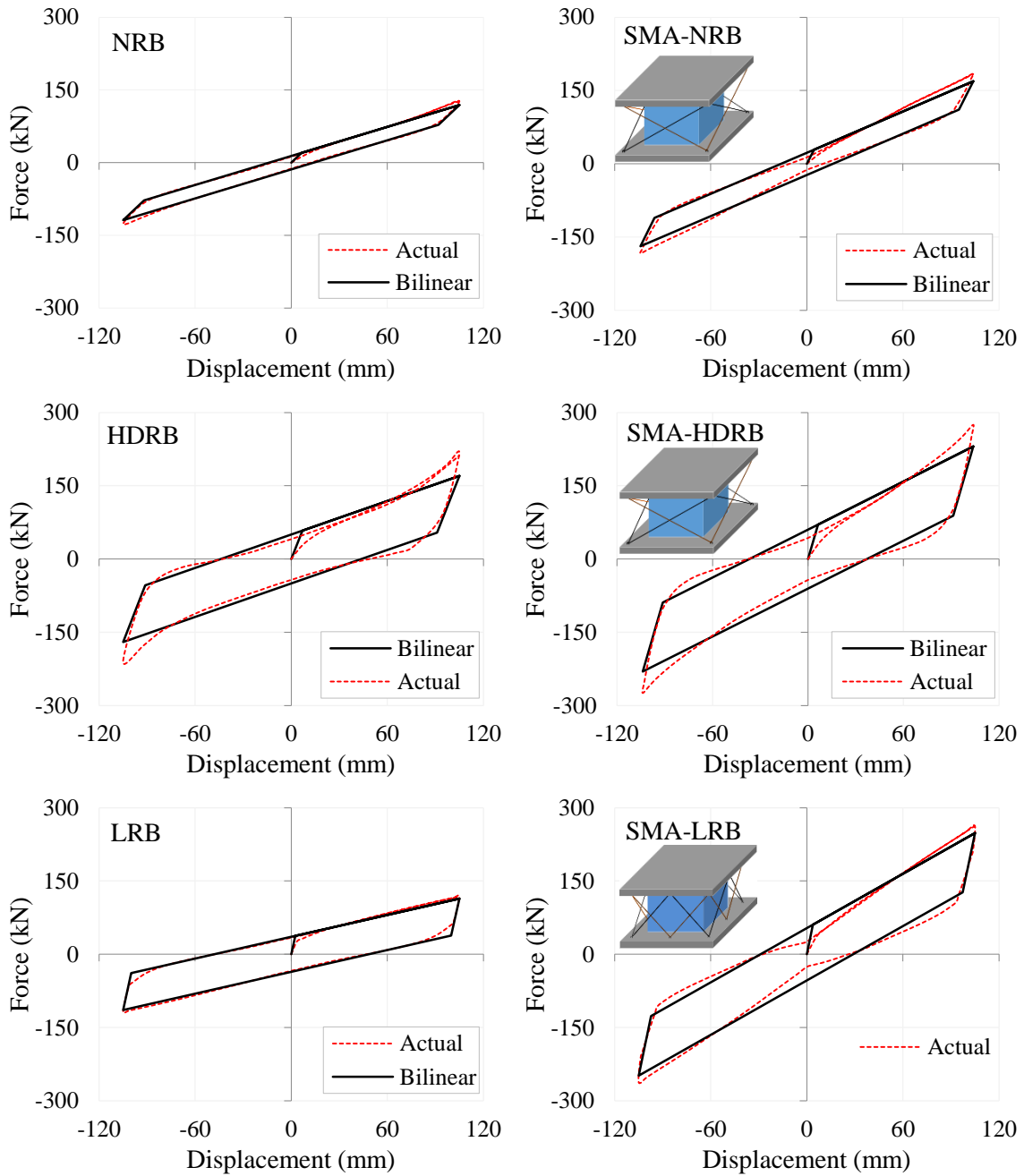
Figure 7.6. Actual and idealized shear hysteretic responses of rubber bearings

In the process of idealizing the hysteretic responses and determining the model properties (i.e. K_0, F_y, and r), the stiffness, the energy dissipated per cycle, and the residual deformation are taken into account. This consideration can be observed in Figure 7.6 when the actual hysteresis is compared with the ideal one. The model properties are listed in Table 7.6 for each bilinear model.

Table 7.6. Properties of bilinear model with kinematic hardening

Isolation System	K_0 (kN/mm)	F_y (kN)	r
NRB	3.13	20.36	0.319
HDRB	8.37	57.99	0.136
LRB	14.78	37.77	0.050
SMA-NRB	6.55	29.01	0.215
SMA-HDRB	11.11	70.71	0.147
SMA-LRB	15.87	60.79	0.117

7.3.2 Probabilistic Seismic Demand Models (PSDM)

By considering two components of the bridge, pier and rubber bearing, which have major contributions to the fragility of the system, two engineering demand parameters are evaluated; displacement ductility of the bridge pier and the shear strain of the elastomeric isolator.

7.3.2.1 Displacement ductility

When a structure is subjected to large amplitude deformations it undergoes a stiffness reduction. If this stiffness loss exceeds a certain level, the structure can collapse (Park, 1988). Displacement ductility, μ_d, is defined as a ratio of the ultimate displacement, Δ_u, to the yield displacement, Δ_y, (see Equation (7.12)). This parameter shows the capability of the structure to undergo a large deformation without excessive strength degradation. Based on this definition, when a ductile structure experiences large inelastic deformations it can dissipate a considerable amount of energy.

$$\mu_d = \frac{\Delta_u}{\Delta_y} \tag{7.12}$$

To determine the yield displacement of the reinforced-concrete (RC) piers, the behaviour of steel reinforcements should be monitored. In fact, the time at which the first yield occurs in a steel rebar is captured as t_y and the corresponding displacement of the pier consisting of the yielded reinforcement is recorded as the yield displacement. The yielding of longitudinal rebar is monitored by defining the yield strain of steel as a performance criteria. Δ_u is the maximum displacement experienced by the structure during an earthquake. Since the considered earthquake records have different longitudinal and transverse components, as

it is in the real case, the yield and ultimate displacements should be calculated by taking into account the displacements in both x and y directions.

$$\Delta_y = \sqrt{\Delta_x^{*\,2} + \Delta_y^{*\,2}} \tag{7.13}$$

where Δ_x^{*} and Δ_y^{*} are displacements of the pier in which the first steel rebar yields in longitudinal and transverse directions, respectively.

After conducting IDAs and extracting the results in terms of the ultimate and yield displacements, displacement ductility ratios are obtained for a range of PGAs. By assuming a two-parameter lognormal probability distribution for EDPs (see Equation (7.2)), if the logarithm of the displacement ductility, $ln(\mu_d)$, is plotted versus the logarithm of the intensity measure, $ln(\text{PGA})$, points will follow a linear trend. Figure 7.7 depicts this pattern for pier when the bridge is isolated with six different rubber bearings (e.g. conventional and smart isolators).
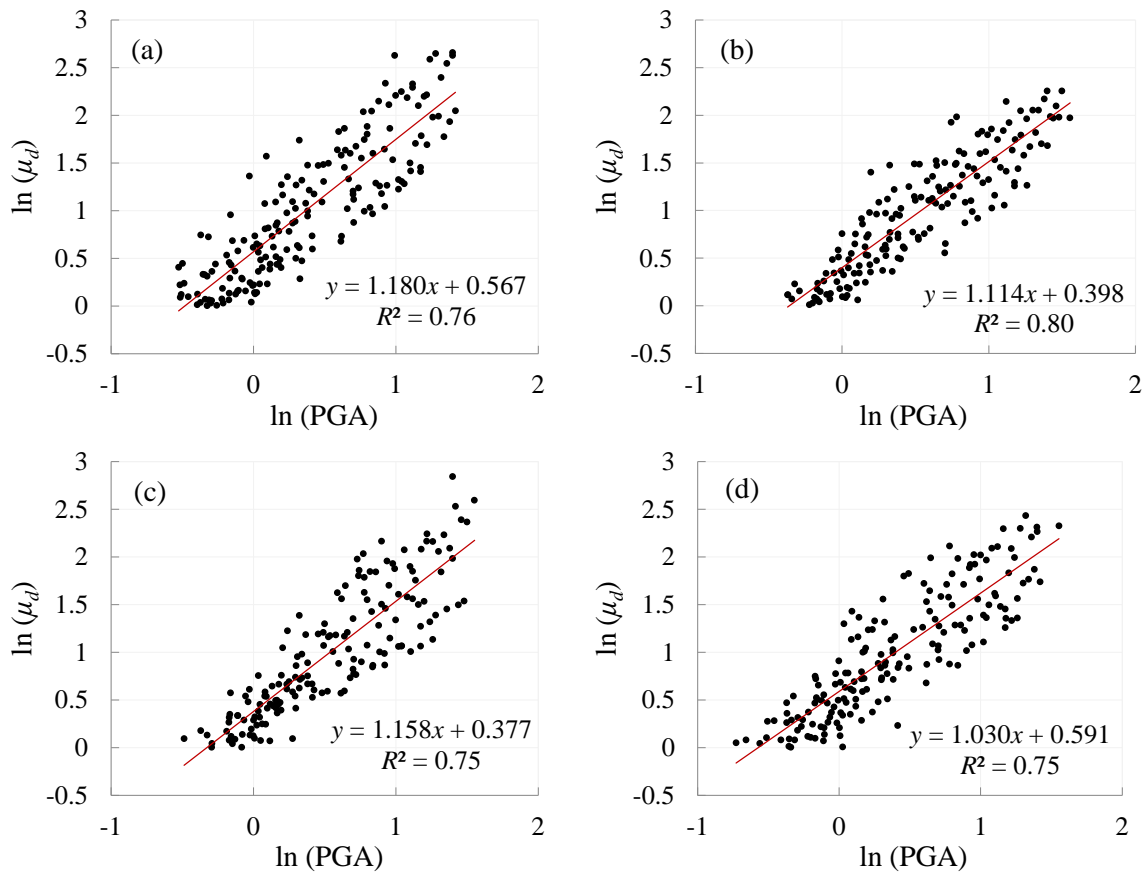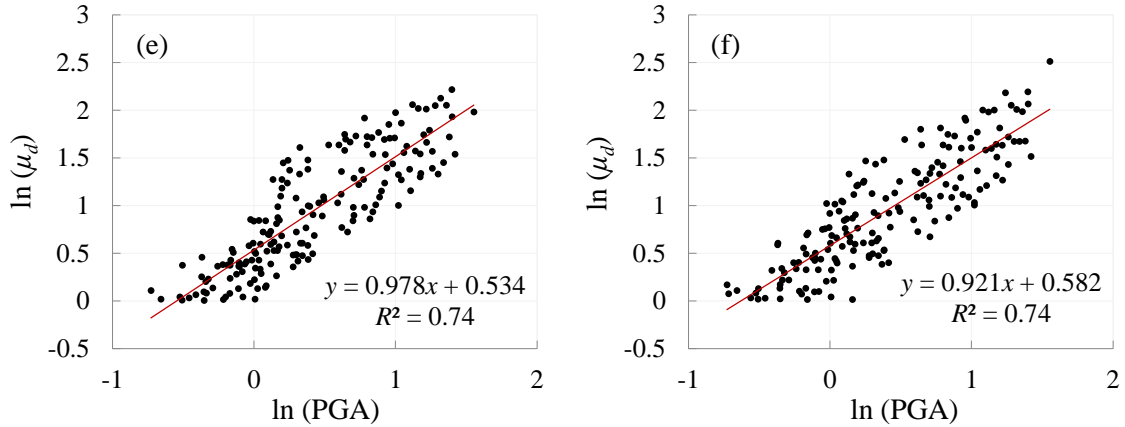
Figure 7.7. PSDMs for displacement ductility of pier equipped with different isolation systems; (a) NRB, (b) HDRB, (c) LRB, (d) SMA-NRB, (e) SMA-HDRB, (f) SMA-LRB

In order to determine the coefficients of the PSDMs, a regression analysis is performed. As can be seen in each plot of Figure 7.7, R^2 values higher than 0.70 reveal that the relations between $\ln(\mu_d)$ and $\ln(\text{PGA})$ are almost linear. By comparing the linear regression equations with Equation (7.3), coefficients a and b can be calculated (see Table 7.7). $\ln(a)$ and b respectively denote the intercept and the slope of regression models.

Table 7.7. Regression coefficients of displacement ductility of pier

Isolation System	Displacement Ductility, μ_d		
	a	b	$\beta_{D/PGA}$
NRB	1.763	1.180	0.353
HDRB	1.489	1.114	0.273
LRB	1.457	1.158	0.335
SMA-NRB	1.805	1.030	0.319
SMA-HDRB	1.705	0.978	0.305
SMA-LRB	1.789	0.921	0.298

The standard deviation of the demand, $\beta_{D/PGA}$, is calculated using Equation (7.8). The impact of using different isolation systems on the demand models is investigated in Table 7.7 for displacement ductility. Comparing intercept values shows that implementing SMA wires in rubber bearings increases the ductility demand in piers. In fact, the increased lateral stiffness of the isolation systems due to the addition of SMA wires increases the ductility demand. However, the rate of change (slope) in the displacement ductility decreases by using SMA-based rubber bearings. Another point is that when SMA-NRB or SMA-LRB is used,

the variation (dispersion) of data values decreases compared to the cases where NRB or LRB is placed in the bridge. It indicates that by using SMA-NRB or SMA-LRB, the values obtained from the corresponding regression models are closer to the mean (the expected value) of the set, which means that the regression models can more accurately predict the response (displacement ductility) of the pier. In the case of SMA-HDRB, the dispersion of the demand is higher than that of the case where HDRB is use. After conducting IDAs and extracting the results, the number of data ($\underline{N}$) in the case SMA-HDRB was lower than that in the case of HDRB. Therefore, according to Equation (7.8), the dispersion of the demand for the pier equipped with SMA-HDRB was higher.

7.3.2.2 Shear Strain

In elastomeric isolators, shear strain is defined as a ratio of the lateral displacement, Δ, to the total thickness of rubber layers, t_r. Although each rubber bearing has identical mechanical properties in the longitudinal and transverse directions, they show different hysteretic behaviours in x and y directions because they are excited by ground motions having different longitudinal and transverse components. As a result, the maximum shear strain in x direction is different from that in y direction. Under such a situation, the peak shear strain, γ_p, as an indication of the capacity of rubber bearing, is the maximum of peak shear strains in x and y directions.

$$\gamma_p = \max\left(\gamma_{x_{max}}, \gamma_{y_{max}}\right) \tag{7.14}$$

Therefore, the peak shear strain may happen in either the longitudinal direction or the transverse direction depending on the earthquake components.

In Figure 7.8, peak shear strain is plotted versus peak ground acceleration in the logarithmic form for six isolation systems. As shown in each plot, similar to the displacement ductility, points are distributed almost linearly.
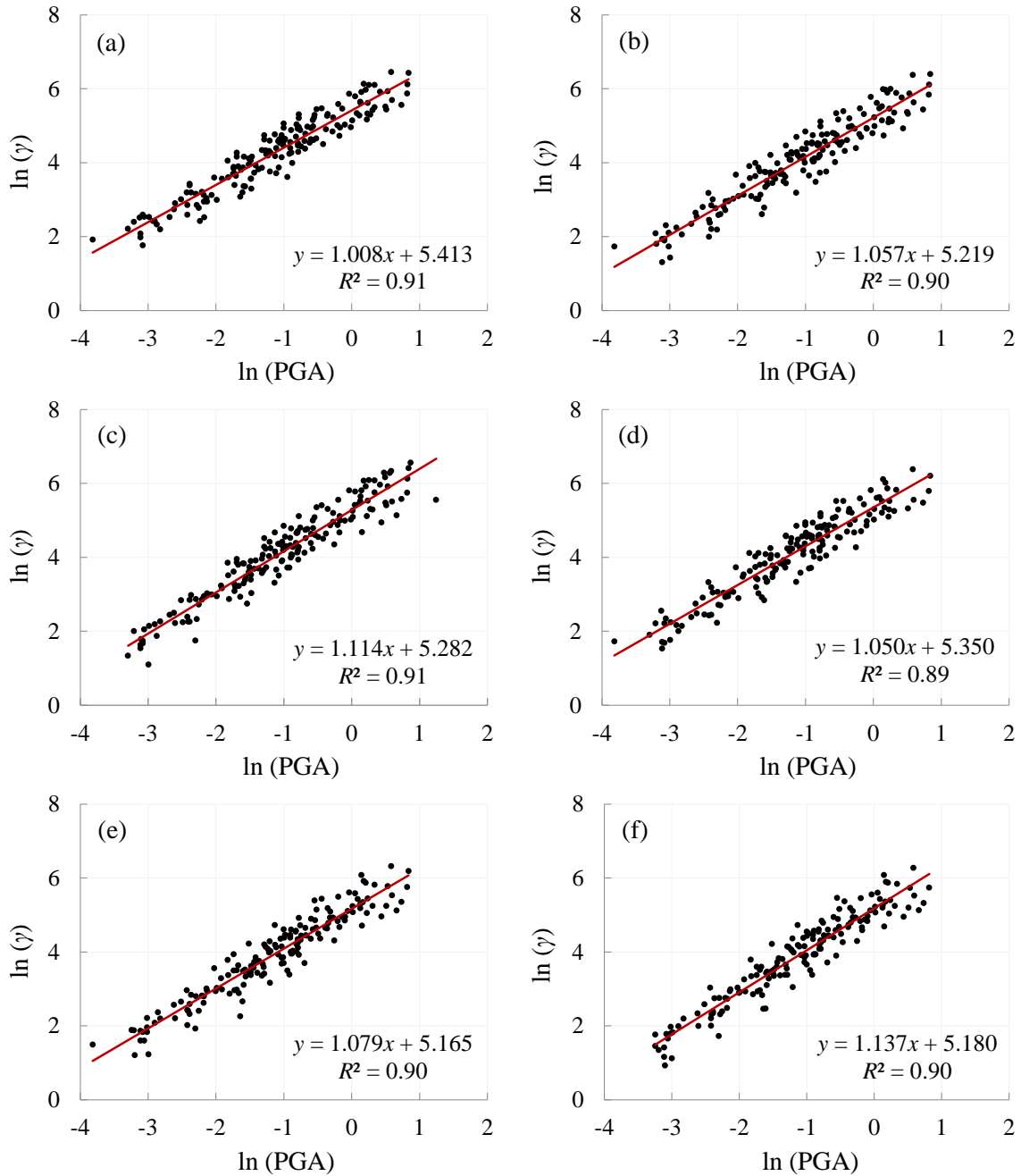
Figure 7.8. PSDMs for shear strain of elastomeric bearings; (a) NRB, (b) HDRB, (c) LRB, (d) SMA-NRB, (e) SMA-HDRB, (f) SMA-LRB

Regression coefficients of PSDMs for shear strain of rubber bearing are given in Table 7.8 when six different isolation systems are used.

Table 7.8. Regression coefficients of shear strain of elastomeric bearings

Isolation System	Shear Strain, γ		
	a	b	$\beta_{D|PGA}$
NRB	224.4	1.008	0.420
HDRB	184.7	1.057	0.361
LRB	196.8	1.114	0.367
SMA-NRB	210.7	1.050	0.390
SMA-HDRB	175.0	1.079	0.366
SMA-LRB	177.7	1.137	0.397

The effect of using different isolation systems on the demand models is investigated in Table 7.8 for the shear strain. Comparing intercept values reveals that using SMA wires decreases the lateral displacement demand in rubber bearings due to increasing the horizontal stiffness of isolation systems. However, the rate of change (slope) in the shear strain increases by using SMA-based rubber bearings. When SMA-HDRB or SMA-LRB is used, the dispersion of data values increases compared to the cases where HDRB or LRB is implemented in the bridge. It shows that by using SMA-HDRB or SMA-LRB, the variation of demand values predicted by the regression models increases. When NRB is compared to SMA-NRB, it is observed that the model demand has a lower dispersion for SMA-NRB.

7.3.3 Component Fragility Curves

In order to establish the fragility curves for each bridge component (e.g. pier and elastomeric bearing), the normal distribution of logarithmic intensity measure should be quantified according to Equation (7.5). In this regard, the mean, λ, and the standard deviation, ξ, of the logarithmic intensity measure, ln(PGA), are calculated at each limit state using Equations (7.6) and (7.7), respectively. Then, the cumulative distribution functions (CDF), Φ, is computed for each component at each damage level.

7.3.3.1 Bridge Pier

The mean and the standard deviation of fragility functions are presented in Table 7.9 for the bridge pier at four limit/damage states when the MSCS bridge is equipped with six different isolation systems.

Table 7.9. Mean and standard deviation of fragility functions for the bridge pier

Isolation System	Slight		Moderate		Extensive		Collapse	
	λ	ξ	λ	ξ	λ	ξ	λ	ξ
NRB	-0.44	0.69	-0.23	0.60	0.01	0.70	0.65	0.72
HDRB	-0.31	0.70	-0.09	0.60	0.17	0.71	0.84	0.73
LRB	-0.28	0.69	-0.07	0.60	0.18	0.70	0.83	0.73
SMA-NRB	-0.53	0.77	-0.28	0.67	-0.01	0.78	0.72	0.81
SMA-HDRB	-0.50	0.81	-0.24	0.70	0.05	0.82	0.82	0.85
SMA-LRB	-0.58	0.86	-0.31	0.74	0.00	0.87	0.82	0.90

Figure 7.9 to Figure 7.11 demonstrate the fragility curves of bridge pier. In order to compare the performance of conventional SREIs with that of the smart SMA-based elastomeric isolators, two sets of fragility functions are plotted in each figure.
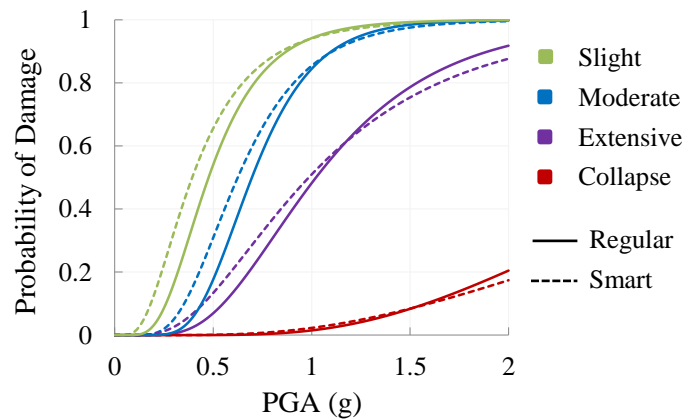
Figure 7.9. Fragility curves of the bridge pier isolated with NRB (regular) and SMA-NRB (smart)

As can be observed in Figure 7.9, when the SMA-NRB is used as the isolation system, compared to the NRB, the probability of damage of the bridge pier increases at slight, moderate, and extensive limit states for PGA values lower than 1.0g. For instance, at a PGA of 0.5g, the probabilities of slight, moderate, and extensive damages in the pier equipped with NRB are 54%, 18%, and 7%, respectively, while in the case of SMA-NRB, the corresponding probabilities are 66%, 31%, and 13%, respectively. It means that by using SMA-NRB, the pier becomes more vulnerable to the seismic records with PGA values ranging from 0 to 1.0g. The reason is that implementing SMA wires in the NRB, increases the stiffness of the isolation system, as shown in Chapters 5 and 6, which causes a higher seismic force demand in the bridge pier (Wilde et al., 2000; Hedayati Dezfuli, 2015b). When the intensity measure increases above 1.0g, NRB becomes more fragile with a higher failure

probability at the slight, moderate, and extensive damage states. Similar behaviour is observed at collapse damage state when PGA goes beyond 1.5g. It can be attributed to the fact that at high PGA values, which corresponds to high values of peak ground displacement (PGD), the isolation system undergoes large amplitude deformations and SMA-NRB, with a higher damping capacity compared to NRB, dissipate a higher seismic energy.
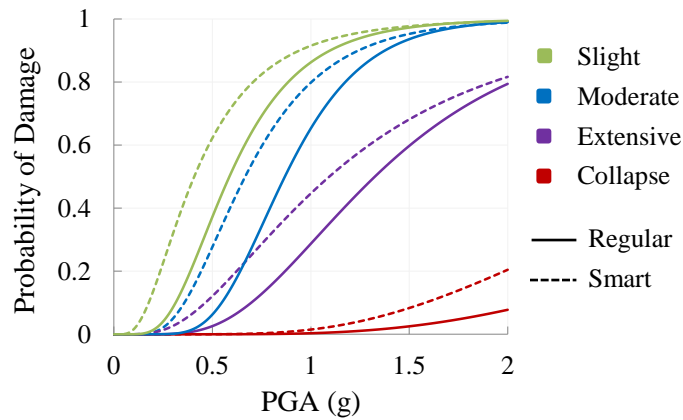
Figure 7.10. Fragility curves of the bridge pier isolated with HDRB and SMA-HDRB
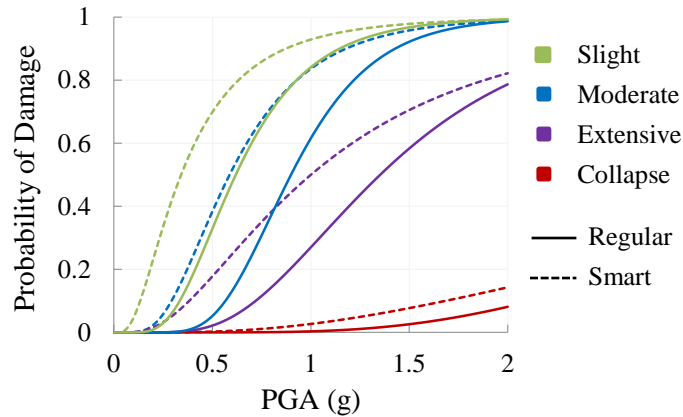
Figure 7.11. Fragility curves of the bridge pier isolated with LRB and SMA-LRB

Comparing fragility curves of the bridge pier isolated by HDRB, LRB, SMA-HDRB, and SMA-LRB (Figure 7.10 and Figure 7.11) depicts that using SMA wires in HDRB and LRB increases the probability of damage of the pier as a result of stiffening the system. For example, if the bridge is excited by an earthquake with a PGA of 1.0g, the probabilities of occurring a moderate damage are 65%, 62%, 80%, and 84% in the pier isolated by HDRB, LRB, SMA-HDRB, and SMA-LRB, respectively. Here, an important finding is that the difference between the fragilities of pier equipped with LRB and SMA-LRB (see

Figure 7.11) is more than the difference between the fragility functions in which HDRB and SMA-HDRB are used (see Figure 7.10). The reason, which refers to the mechanical responses of rubber bearings (Figure 7.6), is that the SMA-LRB has a higher initial and effective stiffnesses than the SMA-HDRB and as a result, it makes the system stiffer. Such a behaviour is observed at all damage states for PGA values ranging from 0 to 2.0g.

At high values of PGA (between 1.0g and 2.0g), SMA-HDRB and SMA-LRB cannot have the effect that SMA-NRB has on the damage probability reduction of pier (Figure 7.9). It is because the effective stiffnesses of SMA-HDRB and SMA-LRB are considerably higher than those of HDRB and LRB (see Figure 7.6). In fact, both stiffness and energy dissipation capacity have contributions to the vulnerability of the pier. The fragility of pier increases by increasing the stiffness of rubber bearings and decreases by increasing the energy dissipation of isolation systems. In the cases of using SMA-HDRB and SMA-LRB, the influence of effective stiffness of elastomeric isolators is more than that of the energy dissipation capacity and as a result, the fragility of pier increases (see Figure 7.10 and Figure 7.11).

In Figure 7.12, the fragility functions of the bridge pier isolated by SMA-NRB, SMA-HDRB, and SMA-LRB are separately depicted at four limit states in order to more clearly compare the performances of these three smart isolation systems.
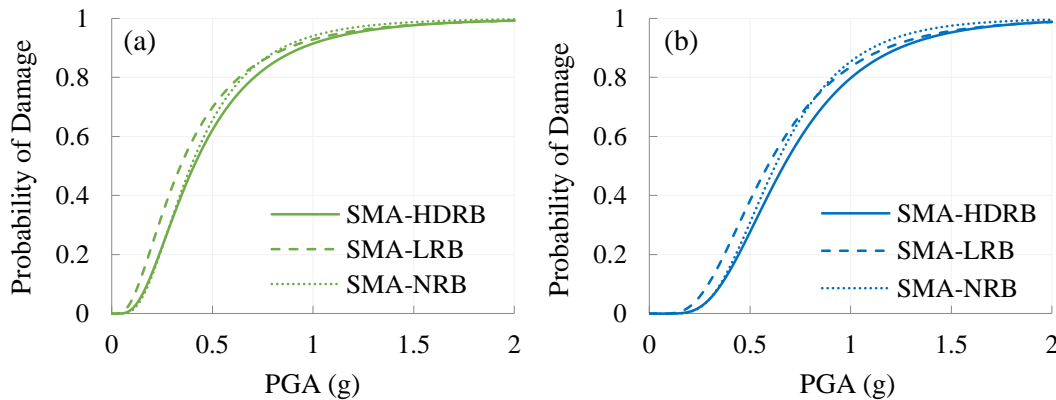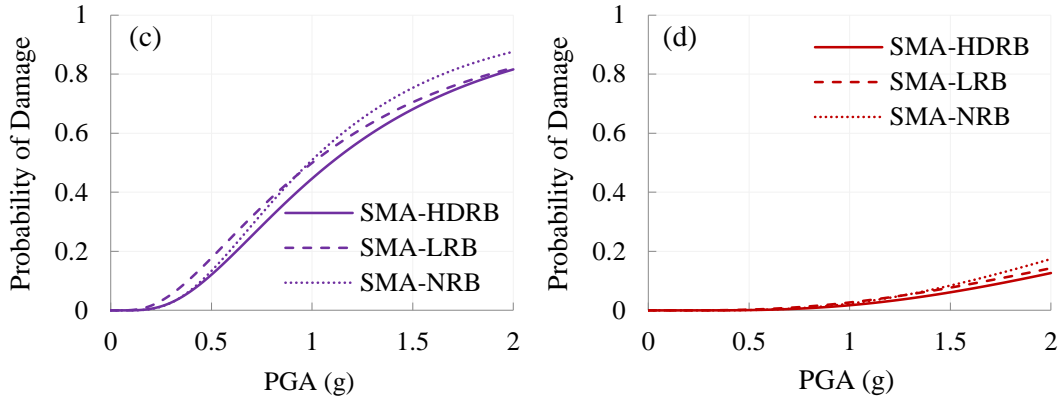
Figure 7.12. Fragility curves of the bridge pier isolated with SMA-NRB, SMA-HDRB, and SMA-LRB at (a) slight, (b) moderate, (c) extensive, and (d) collapse limit states

Results reveal that implementing SMA-HDRB in the bridge makes the pier less vulnerable and safer at all damage levels. It is because, compared to SMA-NRB and SMA-LRB, the SMA-HDRB has a higher energy dissipation capacity due to the improved material properties of the HDR. It means that in the pier fitted with the SMA-HDRB, more seismic energy can be dissipated through the isolation system and as a result, the fragility of the pier decreases. As an example, by considering a ground motion with a PGA of 1.0g, the probabilities of occurring different damage levels in the pier equipped with three smart SMA-based rubber bearings are provided in Table 7.10.

Table 7.10. Damage probabilities of bridge pier fitted with smart rubber bearings at 1.0g PGA

Rubber Bearing	Slight		Moderate		Extensive		Collapse	
	P^*	Δ^*	P^*	Δ^*	P^*	Δ^*	P^*	Δ^*
SMA-HDRB	0.915	-	0.798	-	0.446	-	0.017	-
SMA-NRB	0.941	2.8%	0.854	7.0%	0.509	14.1%	0.023	31.5%
SMA-LRB	0.929	1.5%	0.836	4.8%	0.499	11.9%	0.027	54.2%

P: probability of damage
Δ: relative difference between damage probabilities of SMA-HDRB and two other types of bearing in the table

According to Table 7.10, at the moderate damage state, the possibilities of failure in piers fitted with SMA-NRB and SMA-LRB will be reduced by 7.0% and 4.8%, respectively, if the isolation systems are replaced with SMA-HDRB. At the extensive limit state, the damage probabilities in piers equipped with SMA-NRB and SMA-LRB decrease by 14.1% and 11.9%, respectively, when SMA-HDRB are implemented rather than two other types of

bearings. Under the same situation, in the collapse state, the failure probabilities decrease by 31.5% and 54.2%, respectively.

7.3.3.2 Rubber Bearing

Similar to the bridge pier, the fragility curves are derived for rubber bearing as one of the major vulnerable components of the bridge. It should be noted that for each bridge model the most vulnerable rubber bearing, which undergoes the maximum lateral displacement, is used in the fragility assessment. The mean and standard deviation of fragility functions are calculated at four damage states when the MSCS bridge is isolated with six isolation systems. Results are provided in Table 7.11.

Table 7.11. Mean and standard deviation of fragility functions for the elastomeric bearing

Isolation System	Slight		Moderate		Extensive		Collapse	
	λ	ξ	λ	ξ	λ	ξ	λ	ξ
NRB	-0.80	0.89	-0.40	0.79	-0.11	0.84	0.11	0.78
HDRB	-0.58	0.82	-0.20	0.73	0.08	0.77	0.29	0.71
LRB	-0.61	0.78	-0.24	0.69	0.01	0.73	0.21	0.68
SMA-NRB	-0.71	0.84	-0.32	0.75	-0.05	0.79	0.16	0.73
SMA-HDRB	-0.52	0.81	-0.14	0.72	0.12	0.76	0.33	0.70
SMA-LRB	-0.51	0.78	-0.15	0.69	0.10	0.73	0.30	0.68

Figure 7.13 to Figure 7.15 depict the fragility curves of conventional and SMA-based rubber bearings at slight, moderate, extensive, and collapse damage states. Results show that when SMA wires are incorporated into rubber bearings, the vulnerability of elastomeric isolation system decreases. In fact, SMA wires with a high re-centring capability and a flag-shaped hysteresis stiffen the rubber bearing and improve the dynamic stability of the device by restricting it from over displacement. Another important finding is that compared to the first (NRB and SMA-NRB) and second (HDRB and SMA-HDRB) cases, which are respectively demonstrated in Figure 7.13 and Figure 7.14, using SMA wires in LRB leads to a superior performance in terms of the damage probability reduction. The reason is that when SMA wires are used, not only the residual deformation of LRB is reduced more than that of NRB and HDRB, but the amount of increase in the horizontal effective stiffness and energy dissipation capacity of LRB is higher. This fact can be seen in Figure 7.6 where shear hysteretic responses of conventional and SMA-based rubber bearings are plotted.
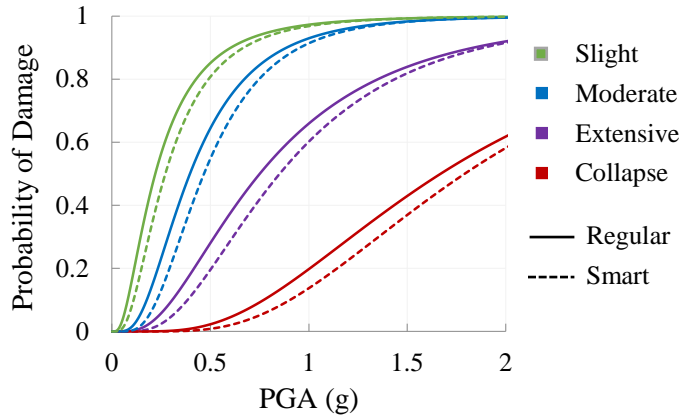
Figure 7.13. Fragility curves of NRB with and without SMA wires
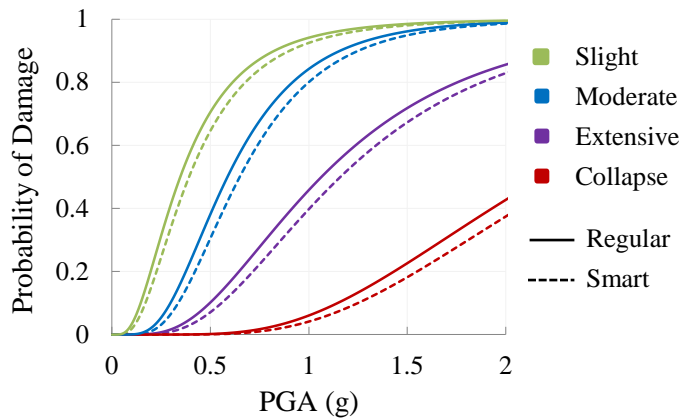
Figure 7.14. Fragility curves of HDRB with and without SMA wires
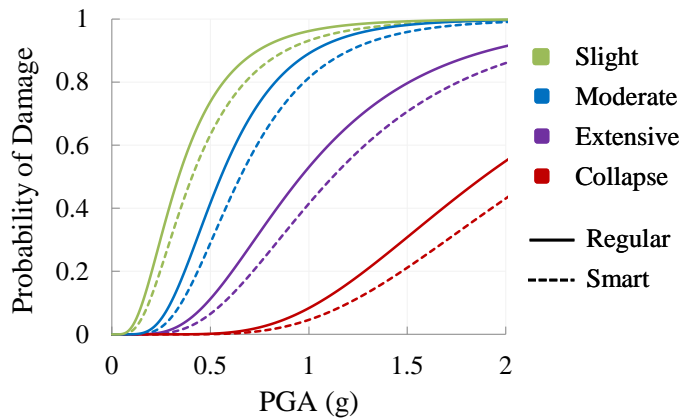
Figure 7.15. Fragility curves of LRB with and without SMA wires

To be more specific, four PGA values (e.g. 0.5g, 1.0g, 1.5g, and 2.0g) are selected and probabilities of damage at different limit states are listed in Table 7.12 for six rubber bearings.

Table 7.12. Damage probabilities of rubber bearings at PGAs of 0.5g, 1.0g, 1.5g, and 2.0g

X	PGA (g)	Slight			Moderate			Extensive			Collapse		
		XRB	SMA-XRB	Δ^*	XRB	SMA-XRB	Δ^*	XRB	SMA-XRB	Δ^*	XRB	SMA-XRB	Δ^*
N	0.5	0.85	0.81	5%	0.64	0.55	15%	0.28	0.20	30%	0.02	0.01	63%
	1.0	0.97	0.97	0%	0.93	0.91	2%	0.66	0.60	9%	0.20	0.14	31%
	1.5	0.99	0.99	0%	0.98	0.98	0%	0.84	0.82	2%	0.43	0.37	14%
	2.0	1.00	1.00	0%	0.99	1.00	0%	0.92	0.92	0%	0.62	0.58	6%
HD	0.5	0.71	0.65	8%	0.38	0.31	20%	0.10	0.07	30%	2e-3	8e-4	54%
	1.0	0.94	0.92	2%	0.84	0.80	5%	0.46	0.40	13%	0.06	0.04	32%
	1.5	0.98	0.98	0%	0.96	0.95	1%	0.72	0.67	6%	0.23	0.18	20%
	2.0	1.00	0.99	0%	0.99	0.99	0%	0.86	0.83	3%	0.43	0.37	12%
L	0.5	0.74	0.63	14%	0.42	0.29	30%	0.11	0.06	42%	2e-3	7e-4	64%
	1.0	0.96	0.93	3%	0.89	0.81	9%	0.53	0.41	22%	0.08	0.05	45%
	1.5	0.99	0.98	1%	0.98	0.96	2%	0.80	0.71	11%	0.31	0.21	31%
	2.0	1.00	1.00	0%	1.00	0.99	1%	0.91	0.86	6%	0.55	0.43	22%

Δ^*: relative difference between damage probabilities of XRB and SMA-XRB

In Table 7.12, XRB and SMA-XRB denote the conventional and smart elastomeric isolators, respectively. In this case, by replacing X with N, HD, or L, as presented in the first column, it can be recognized that the probability of reaching a certain level of damage belongs to which type of rubber bearing. According to Table 7.12, at collapse limit state, for a PGA of 1.5g, SMA wires can reduce the damage probabilities of NRB, HDRB, and LRB by 14%, 20%, and 31%, respectively. At moderate limit state, for 0.5g PGA, SMA wires can reduce the damage possibilities of NRB, HDRB, and LRB by 15%, 20%, and 30%, respectively.

In Figure 7.16, the fragility curves of SMA-NRB, SMA-HDRB, and SMA-LRB are compared at different damage levels. It is found that probabilities of reaching the slight and moderate damage levels in the SMA-HDRB and SMA-LRB are almost the same and lower than that in the SMA-NRB. For example, at the slight damage level, for a PGA of 0.5g, the probability of damage is around 65% in SMA-HDRB and SMA-LRB and 80% in SMA-NRB. On the other hand, for a PGA value of 1.0g, there is a chance of 80% for SMA-HDRB and SMA-LRB to reach their moderate damage level while, the SMA-NRB reaches the same level of damage with a 90% probability.

When the fragility functions of rubber bearings are compared at extensive and collapse damage states, it is observed that for PGA values greater than 1.0g, the SMA-HDRB is less fragile than the SMA-LRB and SMA-NRB. It is because at high PGA values and

accordingly, high peak ground displacements, SMA-HDRB shows a higher effective stiffness which makes it safer against the seismic ground motions. As a quantitative comparison, the possibilities of observing an extensive damage in SMA-HDRB, SMA-LRB, and SMA-NRB at a PGA of 1.5g are 67%, 71%, and 82%, respectively. At a PGA value of 2g, the probabilities of collapsing SMA-HDRB, SMA-LRB, and SMA-NRB are 38%, 44%, and 58% respectively.
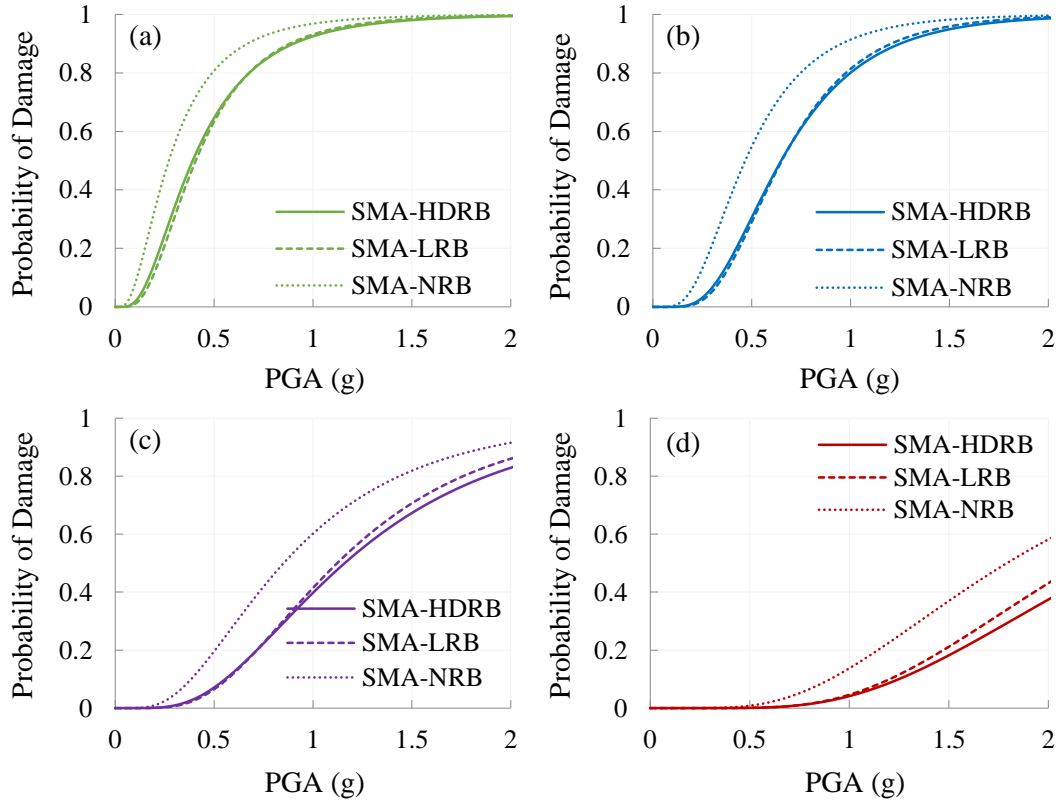
Figure 7.16. Fragility curves of SMA-NRB, SMA-HDRB, and SMA-LRB at
(a) slight, (b) moderate, (c) extensive, and (d) collapse limit states

As an example, at three PGA values (e.g. 0.5g, 1.0g and 2.0g), the likelihood of slight, moderate, extensive, and collapse damages in rubber bearings are listed in Table 7.13. In order to quantitatively compare the SMA-HDRB with the SMA-NRB and SMA-LRB, relative differences, Δ, are measured between damage probabilities of SMA-HDRB and two other types of SMA-based elastomeric isolators. According to Table 7.13, at 0.5g, the probability of occurring slight, moderate, extensive, and collapse damages respectively increases by 25%, 79.5%, 175.9%, and 931.7% when SMA-NRB is used instead of SMA-HDRB. It indicates that at a low PGA value (0.5g), the SMA-HDRB is more efficient than

232

SMA-NRB in reducing the possibility of damage occurrence. However, comparing SMA-HDRB with SMA-LRB reveals that the SMA-LRB has a superior performance because the damage probability at slight, moderate, extensive, and collapse levels reduces by 2.0%, 5.1%, 8.4%, and 13.8%, respectively. At 1.0g and 2.0g PGAs, the maximum differences occur between SMA-HDRB and SMA-NRB at the collapse level, which are 232.5% and 55.4%, respectively. It means that if the SMA-HDRB is used instead of SMA-NRB, the probability of collapse of isolation system significantly decreases. In the case of replacing SMA-LRB with SMA-HDRB, the probability reductions at the same damage state are 11.5% and 15.1% for 1.0g and 2.0g PGAs, respectively.

Table 7.13. Damage probabilities of smart rubber bearings at PGAs of 0.5g, 1.0g, and 2.0g

PGA (g)	Rubber Bearing	Slight		Moderate		Extensive		Collapse	
		P^*	Δ^*	P^*	Δ^*	P^*	Δ^*	P^*	Δ^*
	SMA-HDRB	0.646	-	0.305	-	0.071	-	0.0008	-
0.5	SMA-NRB	0.807	25.0%	0.548	79.5%	0.196	175.9%	0.0083	931.7%
	SMA-LRB	0.633	-2.0%	0.289	-5.1%	0.065	-8.4%	0.0007	-13.8%
	SMA-HDRB	0.925	-	0.800	-	0.397	-	0.041	-
1.0	SMA-NRB	0.968	4.7%	0.914	14.2%	0.602	51.4%	0.137	232.5%
	SMA-LRB	0.931	0.7%	0.813	1.6%	0.414	4.2%	0.046	11.5%
	SMA-HDRB	0.994	-	0.986	-	0.829	-	0.374	-
2.0	SMA-NRB	0.998	0.4%	0.995	1.0%	0.915	10.4%	0.582	55.4%
	SMA-LRB	0.996	0.2%	0.990	0.4%	0.860	3.8%	0.431	15.1%

P: probability of damage
Δ: relative difference between damage probabilities of SMA-HDRB and two other types of bearing in the table

7.3.4 System Fragility Curves

Knowing the fact that major vulnerable components significantly affect the seismic fragility of the whole bridge, as a system, fragility curves of bridge pier and elastomeric isolator are combined to obtain the fragility functions of the system. In this regard, the upper bound in the first order reliability theory (Equation (7.10)) is used to estimate the fragility of the bridge system. It should be pointed out that the upper bound provides a conservative evaluation of the failure probability of the system.

Figure 7.17 to Figure 7.20 show the fragility curves of pier, elastomeric bearing, and bridge at four limit states when different isolation systems are used in the MSCS bridge. As can be seen, the seismic vulnerability of the bridge is greater than that of each component. It

means that the whole system is more fragile than any of the bridge components. It is understood that considering only one component in the seismic fragility assessment leads to an underestimation of the bridge fragility functions.
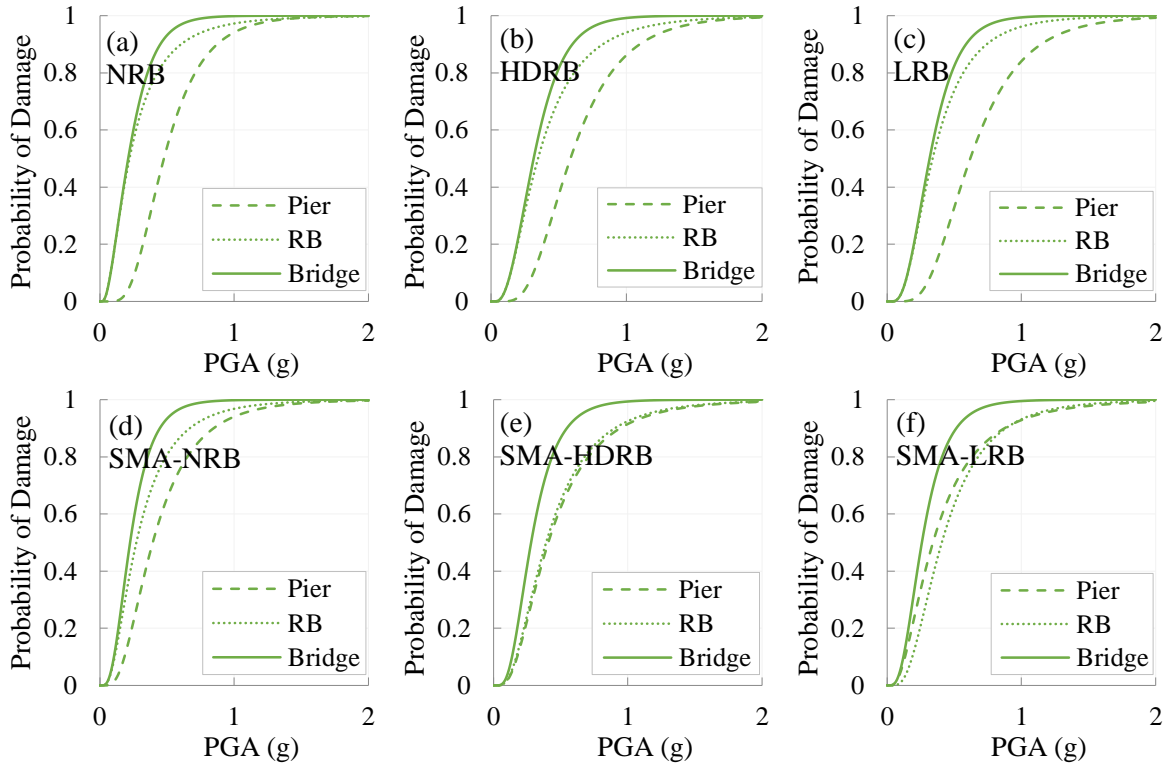
Figure 7.17. Fragility curves of the bridge isolated with six different isolation systems at slight damage state

Comparing the fragilities of two bridge components reveals that conventional rubber bearings (NRB, HDRB, and LRB) are more fragile than pier at four limit states and PGA values ranging from 0 to 2.0g. When SMA wires are wrapped around the bearings, such behaviour (higher vulnerability) is not observed for all levels of damage and PGA values. Although SMA-NRB is more fragile than the bridge pier, probabilities of damage in SMA-HDRB and SMA-LRB are lower than those of pier at some limit states and peak ground accelerations. At slight, moderate, and extensive damage states, when SMA-LRB is used as the isolation system, the rubber bearing becomes less fragile at PGA values between 0 and 1.0g (Figure 7.17f, Figure 7.18f, and Figure 7.19f). When SMA-HDRB is used, this situation occurs only at extensive level of damage (Figure 7.19e).
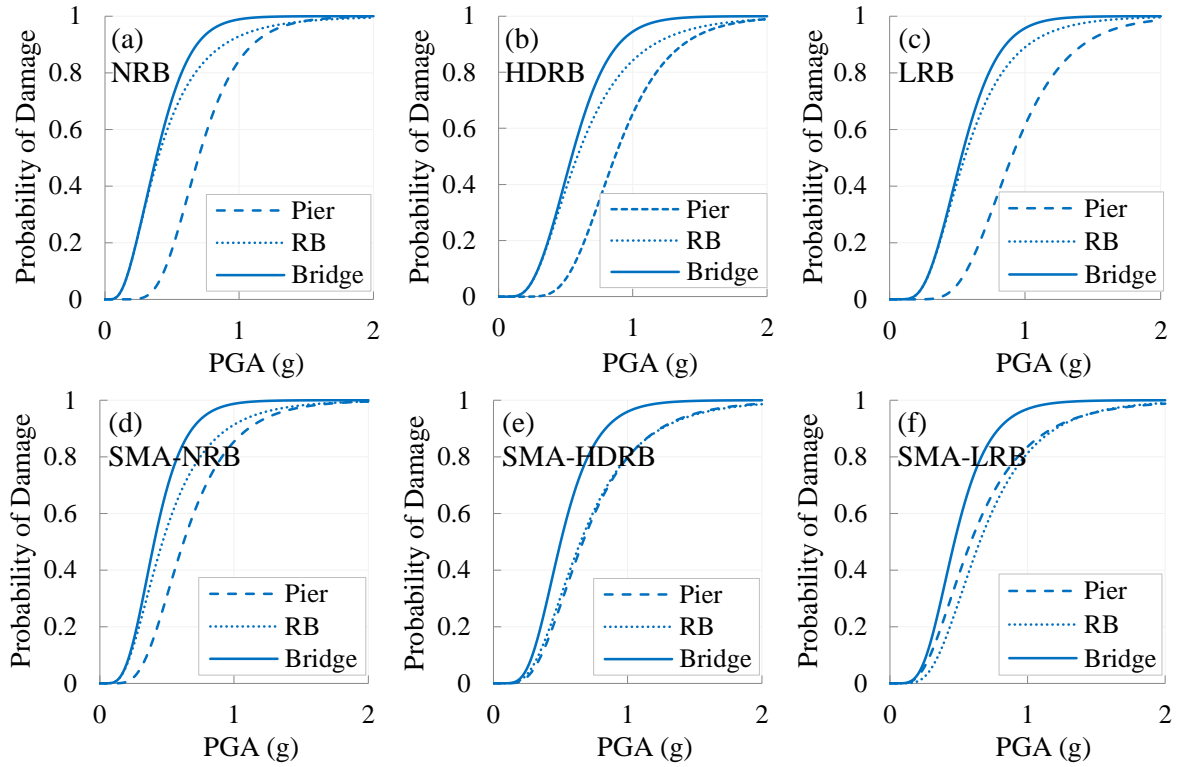
Figure 7.18. Fragility curves of the bridge isolated with six different isolation systems at moderate damage state
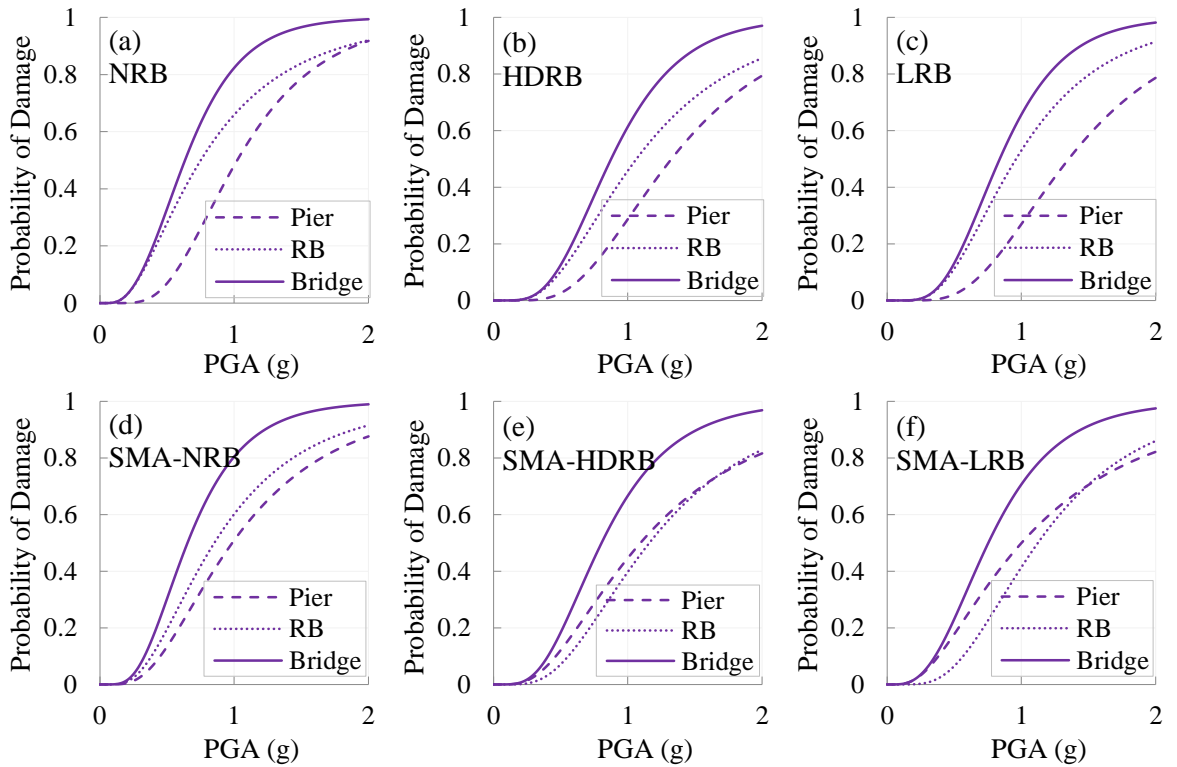
Figure 7.19. Fragility curves of the bridge isolated with six different isolation systems at extensive damage state

235
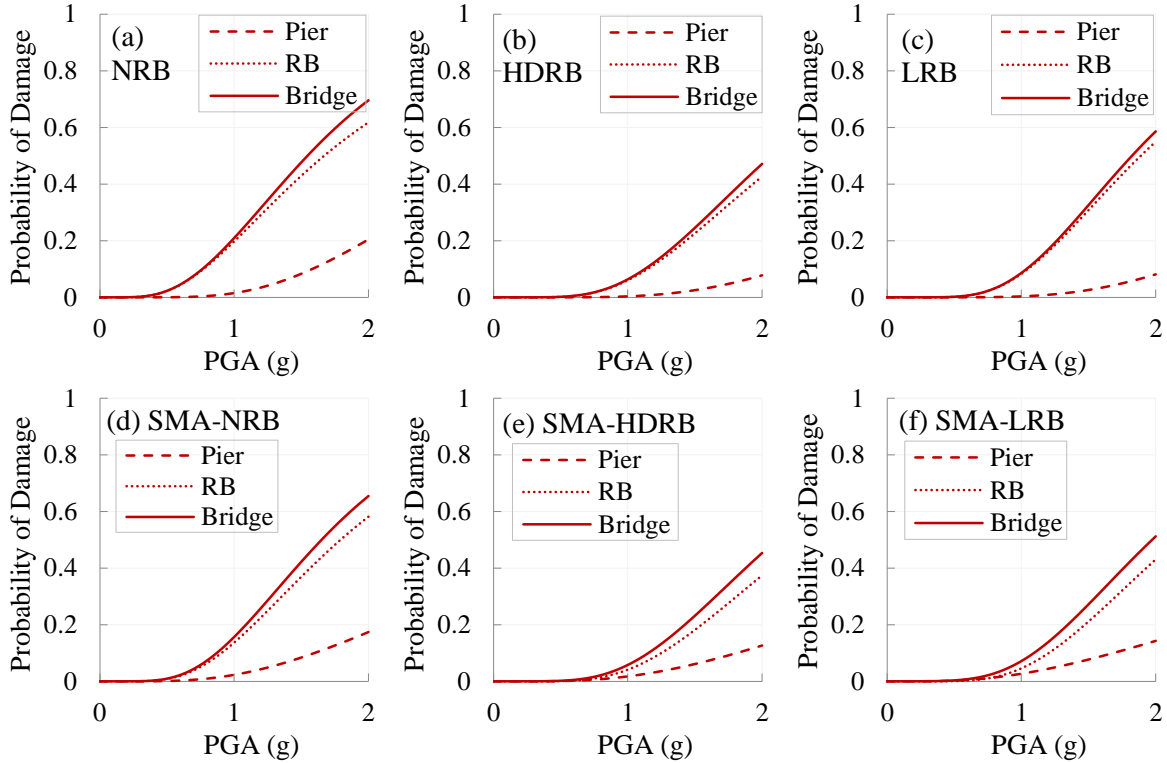
Figure 7.20. Fragility curves of the bridge isolated with six different isolation systems at collapse damage state

Another finding is that at slight and moderate limit states, in the case of using SMA-HDRB (Figure 7.17e and Figure 7.18e), pier and elastomeric isolator are almost at the same level of vulnerability, and have nearly equal contributions to the fragility of the bridge. The SMA-LRB experiences such a situation at slight and moderate damage levels and PGAs greater than 1.0g (Figure 7.17f, Figure 7.18f). The reason is attributed to the capacities of bridge components. It fact, by changing the capacity of a component at a certain limit state, the fragility of that component can be significantly affected.

7.3.4.1 Conventional Elastomeric Isolators

Figure 7.21 demonstrates the fragility curves of the bridge isolated by NRB, HDRB, and LRB at slight, moderate, extensive, and collapse limit states. At a PGA of 0.5g, probabilities of the slight damage in bridges isolated by NRB, HDRB, and LRB are 93%, 81%, and 82%, respectively. At the same level of PGA, there is 71%, 42%, and 45% possibility of observing a moderate damage in bridges fitted by NRB, HDRB, and LRB, respectively.
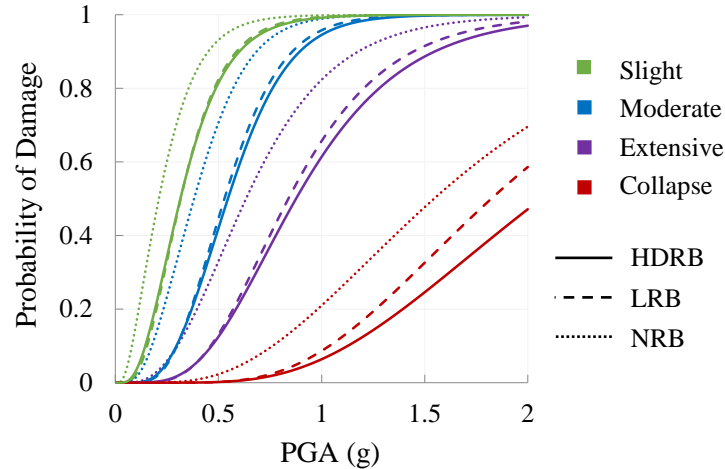
Figure 7.21. Fragility curves of the bridge isolated with NRB, HDRB, and LRB

Results show that when NRB is used as the isolation system, the damage probability of the bridge reaches the highest level. In other words, the bridge isolated by NRB is the most vulnerable system in the case of using conventional rubber bearings. This fact is due to the lower lateral stiffness of NRB compared to the HDRB and LRB. On the other hand, the least fragile bridge is the one isolated by HDRB, which has the highest effective stiffness and energy dissipation capacity. Another finding is that at low and medium damage levels (e.g. slight and moderate), the performances of HDRB and LRB are almost the same while, at high levels of damage (e.g. extensive and collapse), HDRB becomes more effective in reducing the possibility of damage in the bridge. It is because at large displacement capacities and accordingly, at large amplitude deformations, the HDRB shows a higher horizontal stiffness.

Failure probability of bridges isolated by NRB, HDRB, and LRB are presented in Table 7.14 for four values of PGA (0.5g, 1.0g, 1.5g, and 2.0g). Since HDRB shows the best isolation performance among conventional bearings (see Figure 7.21), the likelihood of damages of bridges isolated by NRB and LRB are compared with those of the bridge fitted with HDRB.

Table 7.14. Damage probabilities of the bridge isolated by conventional rubber bearings

at four PGA values

PGA (g)	Isolation System	Slight P^*	Δ^*	Moderate P^*	Δ^*	Extensive P^*	Δ^*	Collapse P^*	Δ^*
0.5	HDRB	0.815	-	0.420	-	0.125	-	0.002	-
	NRB	0.931	14.3%	0.707	68.3%	0.330	164.1%	0.023	1180%
	LRB	0.824	1.1%	0.446	6.3%	0.132	5.2%	0.002	8.1%
1.0	HDRB	0.992	-	0.945	-	0.614	-	0.064	-
	NRB	0.998	0.7%	0.989	4.6%	0.823	34.2%	0.210	229.6%
	LRB	0.994	0.2%	0.958	1.3%	0.657	7.0%	0.086	35.5%
1.5	HDRB	1.000	-	0.998	-	0.886	-	0.246	-
	NRB	1.000	0.0%	1.000	0.2%	0.966	8.9%	0.477	94.1%
	LRB	1.000	0.0%	0.998	0.1%	0.915	3.2%	0.326	32.6%
2.0	HDRB	1.000	-	1.000	-	0.970	-	0.471	-
	NRB	1.000	0.0%	1.000	0.0%	0.993	2.4%	0.696	47.6%
	LRB	1.000	0.0%	1.000	0.0%	0.982	1.2%	0.586	24.3%

P: probability of damage

Δ: relative difference between damage probabilities of HDRB and two other types of bearing in the table

At the slight, moderate, extensive, and collapse damage levels, the maximum differences, which are 14.3%, 68.3%, 164.1%, and 1180%, respectively, occur between HDRB and NRB cases when PGA is 0.5g. When LRB is replaced with HDRB, the probabilities of extensive and collapse damages in the bridge respectively reduce to 3.2% and 32.6% for 1.5g, and 1.2% and 24.3% for 2.0g.

7.3.4.2 Smart SMA-based elastomeric isolators

Three sets of fragility functions for the isolated bridge are depicted in Figure 7.22. Elastomeric isolation systems in these cases are fitted with SMA wires. As can be seen in this figure, the bridge isolated by SMA-HDRB is the least vulnerable system and the bridge isolated by SMA-NRB is the most fragile system, which tends to undergo a damage sooner than other systems. It is expected to observe such a behaviour among bridges isolated by SMA-based rubber bearings, because the SMA-NRB provides the lowest amount of stiffness increase to the system and on the other hand, SMA-HDRB provides the highest amount of increase.
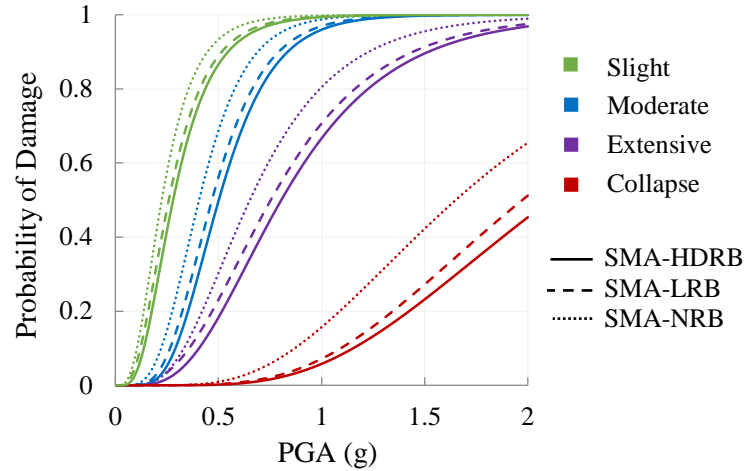
Figure 7.22. Fragility curves of the bridge isolated with SMA-NRB, SMA-HDRB, and SMA-LRB

Similar to the previous case, probabilities of damage in isolated bridges at four levels of PGA and four limit states along with the relative differences are given in Table 7.15 for SMA-based isolation systems. Same as bridges isolated by conventional rubber bearings, the maximum probability differences are achieved when SMA-NRB is replaced with SMA-HDRB. However, the amounts of changes are lower than those in the previous case (conventional rubber bearings). For example, at a PGA of 0.5g, the probabilities that an MSCS bridge isolated by SMA-NRB undergoes slight, moderate, extensive, and collapse damages respectively are 7.8%, 38.2%, 65.4%, and 410.8% higher than cases where SMA-HDRB is used. At collapse level, the fragilities of an MSCS bridge equipped with LRB are 79.4%, 23.6%, 17.3%, and 12.9% higher than bridges fitted with SMA-HDRB for PGA values of 0.5g, 1.0g, 1.5g, and 2.0g, respectively.

Table 7.15. Damage probabilities of the bridge isolated by SMA-based rubber bearings

at four PGA values

PGA (g)	Isolation System	Slight P^*	Slight Δ^*	Moderate P^*	Moderate Δ^*	Extensive P^*	Extensive Δ^*	Collapse P^*	Collapse Δ^*
	SMA-HDRB	0.866	-	0.497	-	0.183	-	0.002	-
0.5	SMA-NRB	0.934	7.8%	0.687	38.2%	0.303	65.4%	0.009	410.8%
	SMA-LRB	0.889	2.7%	0.562	12.9%	0.231	26.1%	0.003	79.4%
	SMA-HDRB	0.994	-	0.960	-	0.666	-	0.058	-
1.0	SMA-NRB	0.998	0.5%	0.987	2.9%	0.805	20.7%	0.157	170.8%
	SMA-LRB	0.995	0.2%	0.969	1.0%	0.707	6.0%	0.072	23.6%
	SMA-HDRB	1.000	-	0.998	-	0.896	-	0.232	-
1.5	SMA-NRB	1.000	0.0%	1.000	0.2%	0.955	6.7%	0.422	82.2%
	SMA-LRB	1.000	0.0%	0.998	0.1%	0.913	2.0%	0.272	17.3%
	SMA-HDRB	1.000	-	1.000	-	0.969	-	0.453	-
2.0	SMA-NRB	1.000	0.0%	1.000	0.0%	0.989	2.2%	0.654	44.4%
	SMA-LRB	1.000	0.0%	1.000	0.0%	0.975	0.7%	0.512	12.9%

P: probability of damage

Δ: relative difference between damage probabilities of HDRB and two other types of bearing in the table

7.3.4.3 Conventional versus smart elastomeric isolators

In order to compare the performances of conventional and smart rubber bearings, fragility curves of the system isolated by NRB, HDR, and LRB are plotted along with the ones isolated by SMA-NRB, SMA-HDRB, and SMA-LRB in Figure 7.23 to Figure 7.25 in three cases. As can be seen in Figure 7.23, using SMA-NRB instead of NRB leads to a less vulnerable bridge system. The difference between fragilities becomes noticeable at collapse damage state. It shows that SMA-NRB performs more efficiently when the bridge system is at the collapse level.
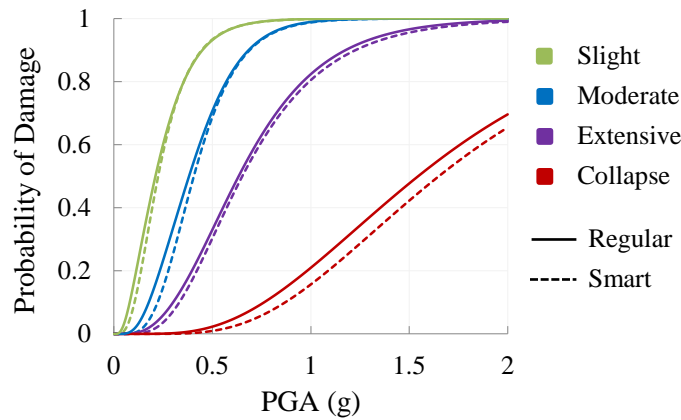
Figure 7.23. Fragility curves of the bridge isolated with NRB and SMA-NRB

In contrast to the first case, when HDRB is replaced with SMA-HDRB, the bridge system becomes more fragile at slight, moderate and extensive limit states. The reason is that although using SMA wires in HDRB can reduce the possibility of damage in rubber bearing (Figure 7.24), it increases the fragility of the bridge pier in a way that the damage probability of the whole system increases. At the collapse level, using SMA-HDRB instead of HDRB is in support of the seismic response of system. It is because the fragility reduction in the rubber bearing outweighs the fragility increase in the pier and as a result, the seismic vulnerability of the whole system decreases.
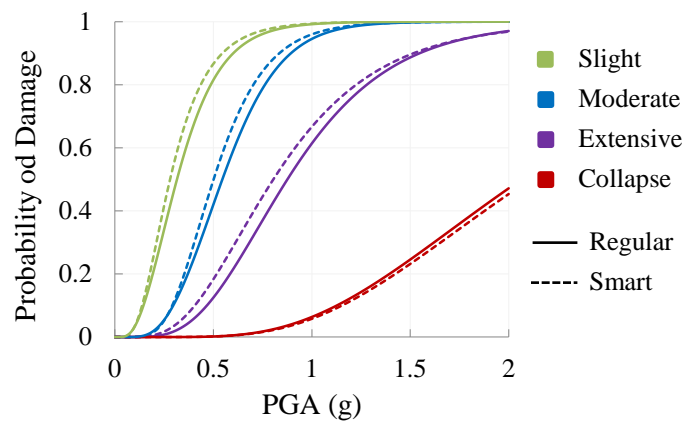
Figure 7.24. Fragility curves of the bridge isolated with HDRB and SMA-HDRB

When Figure 7.24 is compared to Figure 7.25, it is understood that using SMA-LRB instead of LRB (third case) leads to similar results obtained in the second case where SMA-HDRB is implemented rather than HDRB. However, it is observed that differences between the fragility curves in the third case are greater than those in the second case, especially at the collapse level. The reason is that more significant improvements (e.g. effective lateral stiffness increase, energy dissipation capacity increase, and residual deformation decrease) are achieved by incorporating SMA wires into LRB compared to the SMA-HDRB.
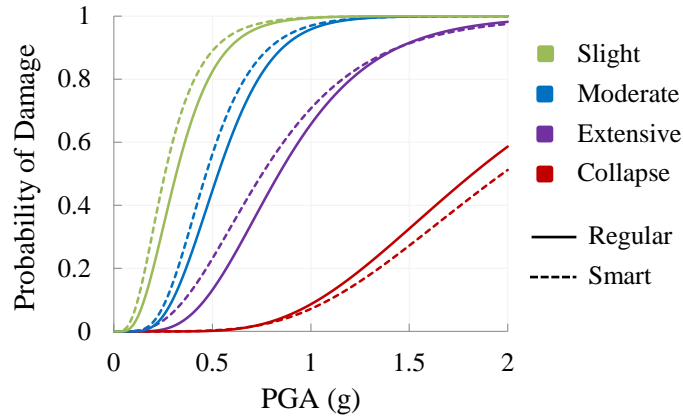
Figure 7.25. Fragility curves of the bridge isolated with LRB and SMA-LRB

Finally, by comparing the fragility functions of bridges isolated with six considered rubber bearings (see Figure 7.23 to Figure 7.25), the most suitable elastomeric isolator for the seismic vulnerability of the MSCS bridge can be identified. At slight, moderate and extensive damage states, HDRB is the most efficient isolation system and at the collapse level, SMA-HDRB is considered as the most effective one. In order to quantitatively compare the performance of the two most efficient isolation systems (e.g. HDRB and SMA-HDRB), the damage probabilities of isolated bridges are given in Table 7.16 for four PGA values and four limit states. For low PGA values (0.5g), damage probabilities of the bridge increases at all limit states when HDRB is replaced with the SMA-HDRB. At 1.0g, this increase occurs at slight, moderate, and extensive limit states, while the probability of collapse decreases by 9%. For PGA values higher than 1.5g, implementing SMA-HDRB in place of HDRB makes negligible changes (e.g. 1% or lower) in the fragility of the system at slight, moderate, and extensive damage levels. At the collapse state, replacing HDRB with SMA-HDRB causes about 6% and 4% reduction in the vulnerability of the isolated MSCS bridge when earthquakes with PGAs of 1.5g and 2.0g take place, respectively.

Table 7.16. Damage probabilities of the bridge isolated by HDRB and SMA-HDRB

at four PGA values and four damage states

PGA (g)	Isolation System	Slight		Moderate		Extensive		Collapse	
		P^*	Δ^*	P^*	Δ^*	P^*	Δ^*	P^*	Δ^*
0.5	HDRB	0.815	-	0.420	-	0.125	-	0.002	-
	SMA-HDRB	0.866	6.3%	0.497	18.4%	0.183	46.6%	0.002	3.2%
1.0	HDRB	0.992	-	0.945	-	0.614	-	0.064	-
	SMA-HDRB	0.994	0.2%	0.960	1.5%	0.666	8.6%	0.058	-9.0%
1.5	HDRB	1.000	-	0.998	-	0.886	-	0.246	-
	SMA-HDRB	1.000	0.0%	0.998	0.0%	0.896	1.0%	0.232	-5.6%
2.0	HDRB	1.000	-	1.000	-	0.970	-	0.471	-
	SMA-HDRB	1.000	0.0%	1.000	0.0%	0.969	-0.2%	0.453	-3.8%

P: probability of damage

Δ: relative difference between damage probabilities of HDRB and SMA-HDRB

The damage probability differences, Δ, for fragilities of MSCS bridges isolated by HDRB and SMA-HDRB are demonstrated in a bar chart in Figure 7.26.
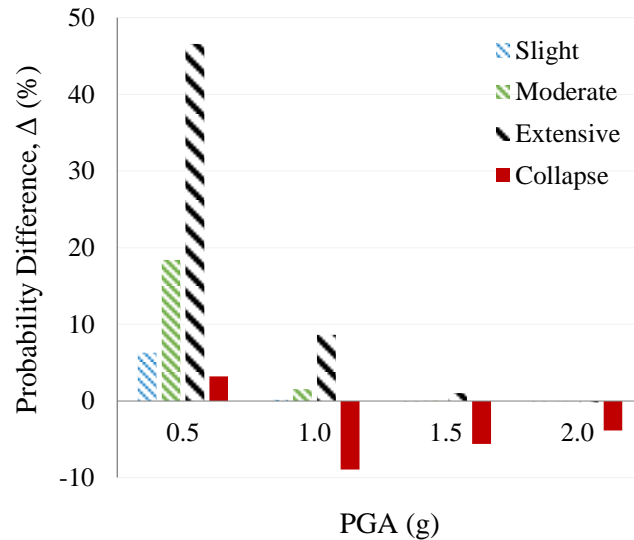
Figure 7.26. Differences between damage probability of HDRB and SMA-HDRB

7.3.4.4 Median Peak Ground Accelerations

The median values of the intensity measure, PGA, for the MSCS bridge are given in Table 7.17 and the corresponding bar chart is plotted in Figure 7.27. The median value of PGA is estimated as a level of peak ground acceleration at which the probability of damage at each limit state reaches 50%. For the same level of damage, lower values of median correspond to higher damage probabilities and as a result, indicate that the bridge system is

more fragile. For instance, at slight, moderate, extensive, and collapse limit states, the bridge isolated by NRB has the lowest values of median, respectively, 0.21g, 0.38g, 0.63g, and 1.55g. It means that NRB has the most inferior isolation performance in the seismic vulnerability of the MSCS bridge.

Table 7.17. Median values of PGA for the bridge system equipped with different isolation systems

Isolation System	Slight	Moderate	Extensive	Collapse
HDRB	0.32g	0.55g	0.88g	2.07g
LRB	0.32g	0.53g	0.84g	1.82g
NRB	0.21g	0.38g	0.63g	1.55g
SMA-HDRB	0.28g	0.50g	0.80g	2.11g
SMA-LRB	0.26g	0.47g	0.75g	1.97g
SMA-NRB	0.22g	0.41g	0.65g	1.65g
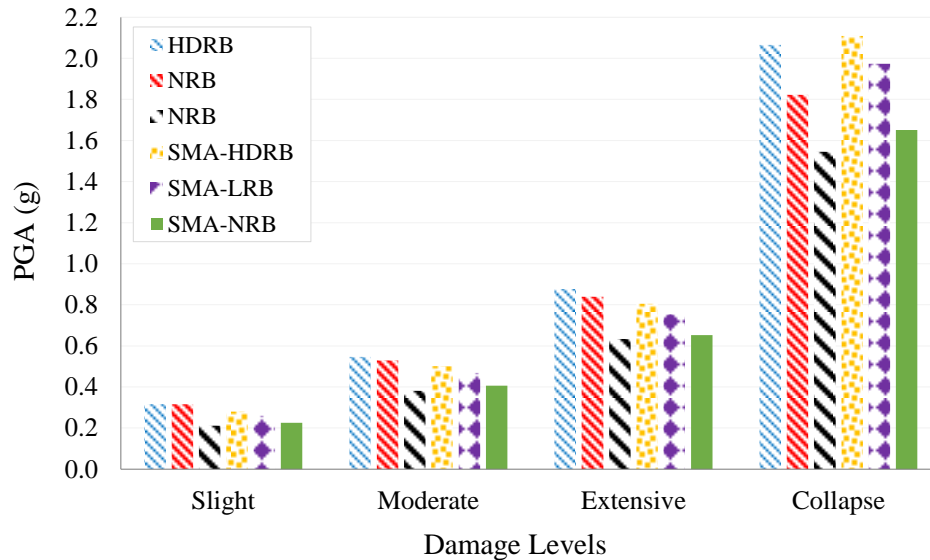
Figure 7.27. Bar chart of median values of PGA for the MSCS bridge equipped with six different isolation systems

7.4 Summary

Seismic fragility assessment of highway bridges is a technique to predict the probability of the structure reaching a certain level of damage under a given ground motion. Vulnerable structural components such as base isolators and columns have significant contributions to the failure probability of the bridge system. Smart shape memory alloy (SMA) wire-based rubber bearings (SMA-RB), which are known as new generations of

elastomeric base isolators, possess improved properties in terms of energy dissipation capacity and self-centering. The performance of different types of SMA-RBs with different wire configurations had been numerically studied in Chapter 5. However, the seismic response of structures, which are isolated by such smart elastomeric bearings, had not been thoroughly investigated. The goal of this chapter was to analytically explore the effect of SMA-RBs on the seismic fragility of a multi-span continuous steel-girder (MSCS) bridge. Effects of bridge pier and isolation system, as major vulnerable components, were taken into account for evaluating the damage probability of the bridge system. Three conventional SREIs including NRB, HDRB, and LRB with identical plan areas and same rubber thicknesses were equipped with SMA wires and used to isolate the MSCS bridge. 30 far-field earthquake records having different longitudinal and transverse components with PGA values ranging from 0 to 1.16g were chosen and incremental dynamic analyses were performed on each model. It was observed that SMA wires with a good superelastic behaviour and re-centring capability stiffen the isolation system and as a result, improve the dynamic stability of the device. Results showed that the MSCS bridge isolated by NRB is the most vulnerable system. On the other hand, at the slight, moderate, and extensive limit states, using HDRB caused the bridge to be the least fragile system with the lowest failure probability. At the collapse level of damage, the bridge isolated by SMA-HDRB had the lowest fragility. Another finding was that equipping NRB with SMA wires decreases the probability of the damage of the bridge while, replacing HDRB with SMA-HDRB or LRB with SMA-LRB increases the possibility of slightly, moderately, and extensively failing the system.

Chapter 8 Summary, Conclusions, and Future Works

8.1 Summary

This thesis presented a new generation smart elastomeric isolator in which shape memory alloy wires were implemented. Different types of base isolators (e.g. rubber bearings), as passive earthquake protective systems; steel-reinforced elastomeric isolators (SREIs), fibre-reinforced elastomeric isolators (FREIs), and smart SMA-based rubber bearings (SMA-RB) were introduced in the review of literature. In this thesis, numerical finite element method (FEM) was used along with an experimental approach.

In the first part, a performance analysis and a multi-objective optimization of carbon fibre-reinforced high damping rubber bearings (CFR-HDRBs) were performed using FEM. By proposing a material model for high damping rubber (HDR), the effect of different parameters was investigated on the performance of CFR-HDRB. The performance of rubber bearings was optimized through a multi-criteria decision making process.

In the experimental section, nine 1/4-scale rectangular carbon fibre-reinforced elastomeric isolators (C-FREIs) were manufactured through a simple and fast process (i.e. cold-vulcanization process) to be used in bonded applications. All specimens consisted of laminated pads with identical length and width (70 mm by 70 mm), but different numbers and thicknesses of rubber and fibre-reinforced layers. The specimens were made of commercial high quality neoprene layers bonded to bi-directional carbon fibre fabrics using an adhesive called rubber compound (rubber cement). C-FREIs were tested under different loading conditions including the vertical pressure and the cyclic lateral displacements. Based on the experimental tests, finite element models were developed. In order to comprehensively study and analyze the behaviour of full-size C-FREIs produced through a cold-vulcanization process, numerical simulations were carried out using ANSYS. The effects of various parameters was explored on the vertical and horizontal stiffnesses, and the equivalent viscous damping of the C-FREIs.

In Chapter 5, novel SMA wire-based rubber bearings (SMA-RBs) were proposed. SMA wires were wrapped around three different rubber bearings; NRB, HDRB, and LRB, with different configurations. NRB and HDRB were equipped with straight and cross configurations of wires and, LRB was fitted with double cross SMA wires. The effect of

246

several parameters; the aspect ratio of rubber bearings, the material type and thickness of SMA wires, and the amount of pre-strain in wires were investigated on the performance of SMA-RBs using FEM. In the process of modelling and analyzing the SMA-RBs, a superposition method was developed through a flowchart showing the procedure of decoupling SMA wires from RBs. The hysteretic shear response of SMA-LRB was determined through FE simulations, which were verified with experimental results. Moreover, in order to determine appropriate amounts of diameter and pre-strain of SMA wires, a design procedure was established.

Due to the lack of a suitable constitutive model for SMA-RBs, it is not possible to accurately evaluate the performance of such smart RBs. Consequently, it is not reliable enough to assess the seismic behaviour of structures, which are isolated by SMA-RBs. Therefore, in the next step, a hysteresis model was developed for SMA-RBs with a capability of implementing in structural finite element softwares. It was assumed that the isolator is subjected to lateral displacements in just one direction. As a result, the proposed constitutive model was capable of predicting the response of SMA-RB for unidirectional cases. The superposition method was used to decouple the effect of SMA wires from the RB and simplify the system. In this regard, a new algorithm was developed for SMA wires model and then combined with RB by writing a computer code in MATLAB. It should be noted that a bilinear kinematic hardening model was considered for RB.

Finally, with the purpose of evaluating the performance of SMA-RBs in structural applications, the seismic response of a highway bridge isolated with such rubber bearings was studied using FEM. In this regard, the seismic fragility of a three-span continuous steel-girder bridge was assessed in six different cases where NRB, HDRB, LRB, SMA-NRB, SMA-HDRB, and SMA-LRB were implemented throuhg an anylitical approach. Two major vulnerable components including the bridge pier and the rubber bearing were taken into account in developing fragility functions of the bridge system. The upper bound in the first order reliability theory, which provides a conservative evaluation of the failure probability of the system, was used to estimate the fragility of the bridge. 30 earthquake ground motions having different longitudinal and transverse components, with PGA values ranging from 0 to 1.16g, were considered in this study. Incremental dynamic analyses were carried out in order to obtain acceptable amount of data for establishing fragility functions.

8.2   Conclusions

8.2.1   Carbon Fibre-Reinforced Elastomeric Isolator (C-FREI)

Among different material models including bilinear, hyperelastic, viscoelastic and viscoplastic models, a combined hyperelastic-viscoelastic model can simulate the highly nonlinear and complex response of high damping rubber (HDR). In fact, a combination of the Mooney-Rivlin model with nine or five material constants (depending on the desired accuracy of the model) and the Prony model with four material constants presents the most well-fitted and accurate result. The Mooney-Rivlin option, as a hyperelastic model, simulates the nonlinear, rate-independent, and hyperelastic behaviour of elastomer. The Prony viscoelastic model, which captures the variation of shear modulus over time, could describe the rate-dependency of HDR under pure shear loading.

According to the t-statistic values of main, interaction and 2nd order effects, the most significant factors for predicting the vertical stiffness, the effective horizontal stiffness and the equivalent viscous damping were respectively, the number of rubber layers, shear modulus of elastomer and thickness of FRP composite plates. Using thicker carbon fibre-reinforced layers increased the vertical and horizontal stiffnesses and slightly decreased the equivalent viscous damping of CFR-HDRBs. When the shear modulus of elastomer increases, the CFR-HDRB was stiffened in both vertical and horizontal directions and the equivalent viscous damping increased around 2%. In the multi-criteria decision making (MCDM) problem, the energy dissipation capacity and the lateral flexibility were two important performance characteristics of seismic base isolators. It was found that the most important factor in optimization of CFR-HDRs is the number of rubber layers.

Experimental tests showed that carbon fibre-reinforced (CFR) layers deformed under large lateral displacements (i.e. rollover deformation) because they have a very low flexural rigidity. As a result, the stress (a combination of tensile and shear stresses) in the exterior elastomeric layers exceeded the bonding strength between rubber layer and supporting steel plate and consequently, debonding occurred. This partial debonding mainly affected the effective horizontal stiffness of C-FREIs.

By increasing the shear strain in all C-FREIs, the effective shear modulus decreased due to Mullins effect (the stress softening phenomenon). This behaviour happens when the

load, here shear force, increases beyond its prior maximum value. The reduction in the effective horizontal stiffness with increasing the shear strain was mainly because of the decrease in the shear modulus of elastomer and the rollover deformation.

CFR layers could be considered as a source of the frictional damping due to the interfacial slip between carbon fibres. As a result, these layers can increase the damping ratio of C-FREIs. However, in order to confirm this finding and before widespread application of CFREIs in real structures, full scale bearings with realistic loadings must be tested. Another finding was that, compared to rubber layers, CFR layers have almost no flexibility and therefore have no contribution to the horizontal stiffness and energy dissipation capacity. However, increasing the thickness of CFR layers from 0.5 mm to 1.25 mm could increase the vertical stiffness of rubber bearing up to 7.2%.

Delamination in the composite laminated pad or debonding of rubber layer and steel supporting plate can lead to local or global failures in C-FREIs depending on the loading condition and the bonding strength of adhesive. Under pure vertical pressure (up to 3 MPa), no detachment was observed. Although at shear strains greater than 50%, partial debonding occurred due to the rollover deformation, all C-FREIs could properly operate up to 100% shear strain with no deficiency or global failure. However, in order to correctly determine the failure limits, the effects of lateral excitation in longitudinal and transverse directions should be considered.

By increasing the number and thickness of rubber layers, the efficiency of C-FREIs degrades in terms of vertical stiffness and damping capacity but, improves in terms of lateral flexibility. This behaviour is due to an increase in the overall thickness of rubber layers used in C-FREIs because the elastomer mostly provides the horizontal flexibility and energy dissipation capability. Among three considered factors; number and thickness of rubber layers, and thickness of CFR layers, the thickness of elastomeric layers had the most influence, first, on the vertical stiffness, and then, on the effective horizontal stiffness. Increasing the vertical pressure from 1 MPa to 3 MPa showed that, within this range, the manufactured C-FREIs are almost insensitive to the compressive pressure regardless of the level of shear strain (25% to 100%). By increasing the lateral cyclic rate, the elastomeric layers were stiffened, and as a result, the rubber bearings showed a lower flexibility in the horizontal direction. On the other hand, when the stiffness of the rubber layers increased at

high lateral cyclic rate, the elastomeric isolator could restore more energy and the capability of the device in dissipating the earthquakes' energy degraded. Another point was that, compared to the high damping rubber, which has a highly nonlinear and sensitive behaviour, the neoprene used in the C-FREIs has a low sensitivity to the rate of the cyclic lateral displacements.

8.2.2 SMA Wire-based Rubber Bearing (SMA-RB)

8.2.2.1 Performance of SMA-RBs

The main objectives of using SMA wires are to improve the re-centring capability and the energy dissipation capacity of RBs. These goals are achieved when SMA wires are activated and show a good superelastic effect with a flag-shaped hysteresis. Results revealed that SMA wires could effectively improve the self-centering and energy damping of NRBs. However, implementing SMA wires in HDRBs was not satisfactory because SMA wires could not considerably reduce the residual deformation of HDRBs. Nevertheless, the influence of SMA wires on the energy dissipation capacity of HDRBs is noticeable. For LRBs, which experience high residual deformations due to the plastic deformation of lead core under strong excitations, using pre-strained SMA wires could significantly increase the re-centring property and energy dissipation capacity of SMA-LRBs.

Among several types of SMAs, FeNiCoAlTaB, a ferrous polycrystalline SMA, was the best candidate to be used in seismic applications due to its high superelastic strain range (13.5%) and a very low austenite finish temperature (-62°C). The superelastic strain range determines the maximum amount of shear strain amplitude at which the SMA wire can efficiently operate in the superelastic range without any plastic deformation. The austenite finish temperature of SMA wires indicates whether or not the SMA-NRB can effectively work within the superelastic range at different thermal conditions. It was observed that the flag-shaped hysteresis of a SMA wire could enlarge the shear hysteresis of rubber bearing (RB) and as a result, improved the energy dissipation capacity of the device.

The rate of increasing the length of wires arranged in cross and double cross (DC) configurations was much lower than that in the straight (S) configuration. As a result, the cross or double cross SMA wire reaches its superelastic strain limit at larger shear strain amplitudes. Therefore, a rubber bearing equipped with cross or double cross SMA wires

(SMA-RB-C or SMA-RB-DC) can undergo a higher horizontal displacement. This characteristic is be very advantageous for high-aspect-ratio rubber bearings. On the other hand, the straight configuration can be implemented in a limited number of applications where the aspect ratio and the shear strain amplitude are quite low. The hysteretic shear behaviour of SMA-RBs indicated that the effective horizontal stiffness and the energy dissipation capacity increase for all configurations of wire.

By increasing the radius of SMA wire, a higher reduction in the residual deformation was achieved and a larger amount of energy was dissipated while, the lateral flexibility of SMA-RBs decreased due to increasing the force in SMA wires. The latter characteristic is not desirable since a more flexible isolation system can shift the fundamental period of the isolated structure more efficiently. In order to overcome this problem, pre-strained SMA wires were used. The yield stress in the pre-strained wires significantly decreases and as a result, a smaller force is transferred to the rubber bearing. An important finding was that if the amount of pre-strain in SMA wires is higher than the strain at which the forward phase transformation is started (1.6%), an increase in the pre-strain level will have negligible effect on the performance of the SMA-RB. Moreover, the pre-straining process, by which an initial strain (and accordingly an initial stress) generates in the wires, enlarged the flag-shaped hysteresis of SMA. However, this behaviour did not lead to an increase in the energy dissipation capacity of SMA-RBs equipped with double cross wires. This fact implies that in addition to the thickness of wires and the amount of pre-strain, the arrangement of wires could play an important role in the performance improvement of RBs.

According to the proposed performance-based design approach, an SMA wire with 2% pre-strain and 2.5 mm radius was chosen for RBs with a plan size of 250 mm by 250 mm. For low-aspect-ratio RBs ($R \leq 0.22$), pre-strained SMA wires in the straight configuration lead to a better performance and for high-aspect-ratio RBs ($R \geq 0.36$), pre-strained cross or double cross SMA wires were more efficient.

8.2.2.2 Constitutive Model of SMA-RBs

Analyzing the axial stress in SMA wires and decomposing the nodal forces at each point where the force is transferred from the wires to the RB revealed that the variation of force versus deflection in the direction of applied displacement (x direction) was totally different from the flag-shaped hysteresis of SMA. However, similar pattern was observed

between the hysteresis of SMA and that of SMA wire in the vertical direction (z). The reason was attributed to the configuration of wires (double cross) and the idealized stress-strain relation of SMA.

The proposed hysteresis model of SMA wire was characterized by initial, intermediate, and re-centring stiffnesses when SMA wires are activated. The activation occurred when the shear strain exceeded a starting limit (g_s). This limit was defined as a shear strain level at which the strain induced in SMA wires reaches the martensite start strain. If the shear strain is lower than g_s, no phase transformation will happen and the SMA wire model will behave linearly with a constant elastic stiffness equal to the modulus of elasticity in the austenite phase. The initial and re-centring stiffnesses were constant while the intermediate stiffness changed linearly by changing the peak shear strain. By decreasing the peak shear strain within the effective range (i.e. a range of strain during which SMA wires are activated), the intermediate stiffness reduced with a degradation factor, which was defined as a material property. Therefore, in order to take advantage of SMA wires in the performance improvement of SMA-RBs, the induced strain in SMA wires should exceed the martensite start strain. This goal is achieved by choosing proper values for geometrical parameters (l, w, and h) during the design procedure of RB and SMA wires.

Since an idealized rate-independent constitutive model was considered for SMA, the developed hysteresis model was independent of strain-rate effect. However, the influence of the strain rate associated with the thermo-mechanical coupling is important as it could modify the SMA hysteresis loop and as a result, it could change the intermediate stiffness. Future investigations will be performed considering strain rate effect on the hysteresis of SMA-wire based rubber bearing. The zero residual deformation of SMA wires could significantly improve the re-centring property of RB. The proposed constitutive model could accurately capture this behaviour. In addition, compared to bilinear models available in FE-based computer softwares, this model can provide a precise simulation of SMA-LRB for a wide range of shear strains.

In contrast to the bilinear kinematic hardening model, which requires performance properties (e.g. stiffness and yield force) to be fully defined, inputs of the proposed SMA wires model consist of material and geometrical properties of SMA and RB. This

characteristic helps users more easily define the hysteresis model of SMA wires with a clear understanding.

8.2.2.3 Seismic Fragility of Isolated Highway Bridge

SMA wire increased the stiffness of the isolation system and as a result, caused a higher seismic force demand in the bridge pier. Therefore, implementing SMA-RBs instead of conventional RBs made the pier more fragile. However, such a behaviour was not observed in piers fitted with SMA-NRB when PGA exceeded 1.0g. It could be attributed to the fact that in addition to the stiffness, the energy dissipation capacity of isolation system affects the vulnerability of the pier. At high PGA values, which correspond to high peak ground displacements (PGD) and accordingly, large amplitude deformations, the SMA-NRB could dissipate a higher amount of earthquake's energy. In such a situation, since the contribution of damping capacity was more than that of stiffness, the ductility demand in bridge piers increased. In SMA-HDRB and SMA-LRB, the effect of lateral stiffness was more than the effect of damping capacity. Among three considered SMA-RBs, SMA-HDRB made the pier less fragile and as a result, safer. The reason was that compared to SMA-NRB and SMA-LRB, SMA-HDRB had a higher energy dissipation capacity owing to the material properties of the HDR.

SMA wires stiffened the RBs and improved the dynamic stability of the devices by restricting them from over displacement. As a result, SMA wires could reduce the vulnerability of elastomeric isolation systems. Another point was that not only SMA wires could reduce the residual deformation of LRB more than that of NRB and HDRB, but the amount of increase in the energy dissipation capacity was higher in SMA-LRB. Hence, incorporating SMA wires into LRB caused more reduction in the seismic fragility of the isolation system. Compared to SMA-NRB and SMA-LRB, SMA-HDRB shows higher lateral effective stiffness and damping capacity, especially, at large amplitude lateral displacements. Therefore, at extensive and collapse limit states, which correspond to high shear strain capacities (e.g. higher than 200%), SMA-HDRB is less vulnerable and safer against the seismic excitations. However, probabilities of reaching the slight and moderate damage levels in the SMA-HDRB and SMA-LRB are almost the same and lower than that in the SMA-NRB.

NRB had the lowest lateral stiffness among six elastomeric isolators. Therefore, when the bridge was isolated by NRB, the system reached the maximum level of vulnerability. On the other hand, the least fragile bridge at first three limit states (slight, moderate, and extensive) was the one fitted with HDRB. Although using SMA wires in HDRB could reduce the possibility of damage in RBs, it increased the fragility of the bridge pier in a way that the damage probabilities of the whole system increased. At the collapse damage level, the least vulnerable bridge was the one isolated by SMA-HDRB. It was because the contribution of SMA-HDRB to the system fragility was more than that of the pier and as a result, the failure probability of bridge reduced up to 9%. When LRB was replaced with SMA-LRB, changes in the fragility functions of the bridge became more significant compared to other cases. The reason was that more improvements were achieved in terms of the effective lateral stiffness, the energy dissipation capacity, and the residual deformation.

8.3 Future Works

8.3.1 Experimental Study

8.3.1.1 Full-Size C-FREIs

Based on the failure tests performed on the scaled manufactured C-FREIs, the load and the displacement capacities of rubber bearings in the vertical and horizontal directions were limited to 3 MPa vertical pressure and 100% shear strain amplitude. It should be noted that for low-rise residential buildings, the elastomeric bearings are subjected to a vertical pressure of around 2 MPa (Toopchi-Nezhad et al., 2008b). However, in the bridge applications, the maximum allowable pressure reaches 10 MPa. In order to thoroughly assess the effect of the vertical load and also the lateral driving velocity on the response of C-FREIs, real size rubber bearings should be designed, manufactured and tested in a future study.

By controlling the delamination within a limited range, the safety and the reliability of C-FREIs will enhance. In order to reduce or even eliminate the local delamination, the bonding strength of the adhesive used for attaching rubber layers to CFR layers and steel plates should be increased. The improvement can also be done by modifying the whole manufacturing process such as applying temperature or using supplementary elements.

Another important factor which was not considered in this thesis is temperature. Since rubber bearings are installed and operate in different regions with different climate conditions in terms of temperature and humidity, it is very crucial to have an evaluation of the behaviour of C-FREIs. The temperature can affect the behaviour of elastomer by changing its shear modulus. In addition, the effect of thickness of adhesive on the response of C-FREIs can be considered in future works. Another point is that determining the curing level of adhesive using a DSC (Differential Scanning Calorimeter) test can be also done in a future study.

Further experimental works including 3D-excitation tests with simulation of real earthquake records need to be conducted in order to reach a solid, reliable, and valid conclusion about FREIs manufactured through the cold-vulcanization process. The other point is that, because of the large nonlinearities involved in materials behaviour, full scale rubber bearings should be fabricated and tested in order to achieve accurate results which will be valid for design, manufacturing, and construction. In this regard, based on the experimental results, further study will be conducted where FE simulations will be performed to model FREIs with full scale. This study will evaluate the performance of real-size C-FREIs and provide a generalized specification guideline.

In order to predict the response of the C-FREI, mathematical regression models can be established with certain key parameters. Experimental data can be used to calibrate the parameters of the model. By considering a specific number of factors (key parameters) and a minimum number of two levels for each factor, the total number of runs (specimens and experiments) increases beyond what we considered in this thesis. Therefore, more specimens need to be fabricated and further experimental and numerical investigations should be conducted in order to develop such mathematical models.

The reinforcement, carbon fibre-reinforced layers (CFR), provides a vertical stiffness several hundred times the horizontal stiffness (Hedayati Dezfuli and Alam, 2014a) and as a result, the manufactured C-FREIs appear to be stable within the considered range of vertical pressure. However, an instability, known as the buckling phenomenon, can occur due to a low lateral stiffness (Kelly and Marsico, 2004). In fact, when the horizontal stiffness is small, the rubber bearing can easily undergo a large lateral deflection. As a result, the effective plan area (i.e. an area which is effective in carrying the vertical load) noticeably reduces and the

possibility of instability (buckling) increases. This instability can be recognized when the shear force encounters a significant reduction by increasing the shear strain. Another important point is that, although using thinner reinforcement layers reduces the weight of rubber bearings as an advantage, it can have an undesirable effect on the buckling load. The reason is that by decreasing the thickness of reinforcement, both vertical and horizontal stiffnesses decrease. Therefore, in analyzing the buckling of elastomeric isolators, the effect of reinforcement's flexibility and thickness should be taken into account in addition to the shear deformation and warping of cross section (Tsai and Kelly, 2004). By replacing rigid steel shims with carbon fibre-reinforced layers, the thickness and flexibility of reinforcement change. In this situation, the stability of elastomeric isolators might be noticeably affected. Therefore, further investigation is required to understand the buckling behaviour of C-FREIs.

In analyzing the buckling of elastomeric isolators, the effect of the reinforcement's flexibility should be taken into account in addition to the shear deformation and the warping of cross section (Tsai and Kelly, 2004). By replacing rigid steel shims with fibre-reinforced layers, the thickness and the flexibility of the reinforcement changes. In this situation, the stability of elastomeric isolators might be noticeably affected. Therefore, it is highly important to investigate the buckling of C-FREIs.

8.3.1.2 SMA wire-based Rubber Bearings

With the purpose of validating the numerical results discussed in Chapter 5, and validating the constitutive model of SMA wires proposed in Chapter 6, SMA wires-based rubber bearings with different configurations of wires should be designed and manufactured, and different experimental tests will be conducted.

Considering the cross and double cross configurations of SMA wires, in reality, a frictional force is generated between the wire and the hook in the contact area. In such a situation, the relative displacement between the wire and the hook will be limited or fixed in the worst case. In future works, more realistic comparisons can be performed by considering two types of contact including smooth (current case) and friction (real case). This further study can indicate how much the smooth contact assumption is close to the real case.

8.3.2   Numerical Study

8.3.2.1   Constitutive Model of SMA-RBs

Since idealized bilinear models were used for simulating the hysteretic response of SMA-RB, the actual effect of such smart bearings was not captured on the seismic fragility of the isolated bridge in this thesis. Therefore, in a future study, the constitutive model developed in Chapter 6, should be implemented in a FE-based computer software such as OpenSEES, and the seismic performance and fragility of isolated structures should be assessed.

8.3.2.2   Seismic Fragility of Highway Bridges

Seismic fragility assessment is based on the theory of probability. It means that for establishing a comprehensive vulnerability assessment, a wide range of parameters such as type and geometry of the bridge, material properties, structural components, intensity measures, location, and interaction of the soil and structure should be considered in order to capture uncertainties, minimize errors, and prevent solutions from underestimating the seismic performance of the structure. In addition, the method by which the fragility curves are obtained plays an important role in the accuracy of results. In this study, some assumptions were made in order to simplify the problem and develop the fragility functions of a MSCS bridge by focusing on the type of elastomeric isolation systems. Therefore, in order to make the fragility responses more accurate and improve the level of prediction, several factors should be taken into account in future works; more appropriate models for hysteretic shear response of SMA-based rubber bearings, the effect of abutments and foundations, uncertainties in the geometry and material properties, different types of bridge, and earthquake records with high PGA values. Since far-field ground motions were considered in this study, fragility of bridges should also be estimated under near-field earthquakes.

Another point is that the probabilistic seismic demand models (PSDMs) of shear strain in isolation systems were developed based on the capacities of rubber bearings, which were specified in the literature. Since new smart isolation devices have been developed in this thesis, it is necessary to determine the capacities of SMA-RBs and then establish fragility functions of the system in a future work.

References

Abe, M., Yoshida, J., Fujino, Y. 2004. Multiaxial behaviours of laminated rubber bearings and their modeling. I: experimental study. *Journal of Structural Engineering-ASCE*, 130, 1119-1132.

ACP Composites, Inc. 2012. Product Specification Sheet, CA, USA.

Alam, M.S., Youssef, M.A., and Nehdi, M. 2007. Utilizing shape memory alloys to enhance the performance and safety of civil infrastructure: A review. *Canadian Journal of Civil Engineers*, 34(9):1075-1086.

Alam, M.S., Youssef, M.A., and Nehdi, M. 2008. Analytical prediction of the seismic behaviour of superelastic shape memory alloy reinforced concrete elements. *Engineering Structures*, 30(12): 3399-3411.

Alam, M.S., Bhuiyan, A.R., and Billah, A.H.M.M. 2012. Seismic fragility assessment of SMA-bar restrained multi-span continuous highway bridge isolated with laminated rubber bearing in medium to strong seismic risk zones. *Bulletin of Earthquake Engineering*, 10(6), 1885-1909.

Ali, A., Hosseini, M., Sahari, B.B. 2010. A Review of constitutive models for rubber-like materials. *American Journal of Engineering and Applied Sciences,* 3(1): 232-239.

Amin, A.F.M.S., Wiraguna, S.I., Bhuiyan, A.R., and Okui, Y. 2006a. Hyperelasticity model for finite element analysis of natural and high damping rubbers in compression and shear. *Journal of Engineering Mechanics-ASCE*, 132(1): 54-64.

Amin, A.F.M.S., Lion, A., Sekita, S., and Okui, Y. 2006b. Nonlinear dependence of viscosity in modeling the rate-dependent response of natural and high damping rubbers in compression and shear: Experimental identification and numerical verification. *International Journal of Plasticity*, 22(9): 1610-1657.

Andrawes, B., and DesRoches, R. 2007. Comparison between Shape Memory Alloy seismic restrainers and other bridge retrofit devices. *Journal of Bridge Engineering-ASCE*, 12(6), 700-709.

ANSYS Software, Documentation, ANSYS Inc., Canonsburg, PA, USA (www.ansys.com).

ANSYS Software, Mechanical APDL, Release 14.0, 2012, ANSYS Inc., Canonsburg, PA, USA (www.ansys.com).

ATC. 1985. Earthquake damage evaluation data for California. ATC-13. Applied Technology Council.

Attanasi, G., Auricchio, F., Crosti, C., and Fenves, G.L. 2008. An innovative isolation bearing with shape memory alloys. *In Proceedings of the 14ᵗʰ World Conference on Earthquake Engineering*, Beijing, China, 12-17 October 2008.

Attanasi, G., and Auricchio, F. 2011. Innovative superelastic isolation device. *Journal of Earthquake Engineering*, 15(S1): 72-89.

Auricchio F. 2001. A robust integration-algorithm for a finite-strain shape memory alloy. *International Journal of Plasticity*, 17(7): 971-90.

Baker, J.W., and Cornell, C.A. 2006. Vector-valued ground motion intensity measures for probabilistic seismic demand analysis. Pacific Earthquake Engineering Research Rep. 2006/08, Pacific Earthquake Engineering Research Center, Univ. of California, Berkeley, CA.

Basoz, N., Kiremidjian, A.S., King, S.A., and Law, K.H. 1999. Statistical analysis of bridge damage data from the 1994 Northridge, CA, earthquake. *Earthquake Spectra*, 15, 25-53.

Bauschinger, J. 1881. Changes of the elastic limit and the modulus of elasticity on various metals. Zivilingenieur, 27: 289-348.

Bergstrom, J.S., and Boyce, M.C. 1998. Constitutive modeling of the large strain time-dependent behaviour of elastomers. *Journal of the Mechanics and Physics of Solids*, 46(5): 931-954.

Bhuiyan, M.A.R., and Ahmed, E. 2007. Analytical expression for evaluating stress-deformation response of rubber layers under combined action of compression and shear. *Construction and Building Materials*, 21(9): 1860-1868.

Bhuiyan, M.A.R., Okui, Y., Mitamura, H., and Imai, T. 2009. A rheology model of high damping rubber bearings for seismic analysis: Identification of nonlinear viscosity. *International Journal of Solids and Structures*, 46(7-8): 1778-1792

Bhuiyan, M.A.R., and Alam, M.S. 2013. Seismic performance assessment of highway bridges equipped with superelastic shape memory alloy-based laminated rubber isolation bearing. *Engineering Structures*, 49: 396-407.

Billah, A.H.M.M., and Alam, M.S. 2012. Seismic fragility assessment of concrete bridge pier reinforced with shape memory alloy considering residual displacement. *In Proceedings of SPIE Conference on Active and Passive Smart Structures and Integrated Systems*, VI, Vol. 8341, 83411F, 1–13.

Billah, A.H.M.M., Alam, M.S., and Bhuiyan, M.A.R. 2013. Fragility analysis of retrofitted multicolumn bridge bent subjected to near-fault and far-field ground motion. *Journal of Bridge Engineering-ASCE*, 18:992-1004.

Billah, M.A.H.M., and Alam, M.S. 2014. Seismic fragility assessment of highway bridges: a state-of-the-art review. *Structure and Infrastructure Engineering*, doi: 10.1080/15732479.2014.912243.

Boyd, J.G., and Lagoudas, D.C. 1996. A thermodynamical constitutive model for the shape memory materials. Part I. The monolithic shape memory alloy. *International Journal of Plasticity*, 12(6): 805-842.

Buckle, J.G., and Mayes, R.L. 1990. Seismic isolation: history, application and performance – a world overview. *Earthquake Spectra*, 6(2): 161-202.

Burtscher, S., Dorfmann, A., and Bergmeister, K. 1998. Mechanical aspects of high damping rubber. *2nd International Ph.D. Symposium in Civil Engineering*, Budapest.

Canadian Standard Association (CSA). 2006. Canadian highway bridge design code (CHBDC) CAN/CSA-S6-06. Rexdale, Ontario, Canada.

Chaudhary, M.T.A., Abe, M., Fujino, Y., and Yoshida, J. 2000. System identification of two base-isolated bridges using seismic records, *Journal of Structural Engineering-ASCE*, 126, 1187-1195.

Chen, L., Jiang, L., and Liu, P. 2011. Dynamic properties of lead rubber bearings and its seismic isolation applications in high-speed railway bridge. *Advanced Materials Research*, 150-151: 164-167.

Choi, E., DesRoches, R., and Nielson, B.G. 2004. Seismic fragility of typical bridges in moderate seismic zones, *Engineering Structures*, 26: 187-199.

Choi, E., Nam, T.H., and Cho, B.S. 2005. A new concept of isolation bearings for highway steel bridges using shape memory alloys. *Canadian Journal of Civil Engineering*, 32(5): 957-967.

Christensen, R.M. 1982. Theory of Viscoelasticity – An Introduction. 2nd ed. Academic Press, New York.

Cornell, A.C., Jalayer, F., and Hamburger, R.O. 2002. Probabilistic basis for 2000 SAC federal emergency management agency steel moment frame guidelines. *Journal of Structural Engineering-ASCE*, 128: 526-532.

Dall'Asta, A., and Ragni, L. 2006. Experimental tests and analytical model of high damping rubber dissipating devices. *Engineering Structures*, 28(13): 1874-1884.

Dehghani Ashkezaria, G., Aghakouchaka, A.A., and Kokabib, M. 2008. Design, manufacturing and evaluation of the performance of steel like fiber reinforced elastomeric seismic isolators. *Journal of Materials Processing Technology*, 197(1-3): 140-150.

DesRoches, R., and Delemont, M. 2002, Seismic retrofit of simply supported bridges using shape memory alloys. *Engineering Structures*, 24(3): 325-332.

Dolce, M., Cardone, D., and Marnetto, R. 2000. Implementation and testing of passive control devices based on shape memory alloys. *Earthquake Engineering & Structural Dynamics*, 29(7): 945-968.

Doudoumis, I.N., Gravalas, F., and Doudoumis, N.I. 2005. Analytical modeling of elastomeric lead rubber bearings with the use of finite element micromodels. *5ᵗʰ GRACM International Congress on Computational Mechanics*, Limassol, Cyprus, 29 June-1 July 2005.

FEMA. 2003. HAZUS-MH MR1: Technical Manual, Vol. Earthquake Model. Federal Emergency Management Agency, Washington DC.

Gardoni, P., Der Kiureghian, A., and Mosalam, K.M. 2002. Probabilistic capacity models and fragility estimates for reinforced concrete columns based on experimental observations. *Journal of Engineering Mechanics-ASCE*, 128: 1024-1038.

Gardoni, P., and Rosowsky, D. 2011. Seismic fragility increment functions for deteriorating reinforced concrete bridges. *Structure and Infrastructure Engineering*, 7: 869-879.

Ghobarah, A. and Ali, H.M., 1988. Seismic performance of highway bridges, *Engineering Structures*, 10: 157-166.

Ghobarah, A., and Ali, H.M. 1990. Seismic design of base-isolated highway bridges utilizing lead-rubber bearings. *Canadian Journal of Civil Engineers*, 17(3): 413-422.

Gjorgjiev, I., Garevski, M. 2013. A polynomial analytical model of rubber bearings based on series of tests. *Engineering Structures*, 56: 600-609.

GoodCo Z-Tech. 2010. Elastomeric bearings catalogue, Laval, QC.

Graesser, E.J., and Cozzarelli, F.A. 1991. Shape-memory alloys as new materials for aseismic isolation. *Journal of Engineering Mechanics-ASCE*, 117(11): 2590-2608.

Hedayati Dezfuli F., and Alam, M.S. 2012. Material modeling of high damping rubber in finite element method. *In Proceedings of the 3ʳᵈ International Structural Specialty Conference*, June 6-9, 2012, Edmonton, Alberta, Canada.

Hedayati Dezfuli F., and Alam, M.S. 2013a. Multi-criteria optimization and seismic performance assessment of carbon FRP-based elastomeric isolator. *Engineering Structures,* 49: 525-540. Doi:10.1016/j.engstruct.2012.10.028.

Hedayati Dezfuli F., and Alam, M.S. 2013b. Sensitivity analysis of carbon fiber-reinforced elastomeric isolators based on experimental tests and finite element simulation. *Bulletin of Earthquake Engineering*, 12(2): 1025-1043.

Hedayati Dezfuli F., and Alam, M.S. 2013c. Shape memory alloy wire-based smart natural rubber bearing. *Smart Materials and Structures*, 22(4) 045013.

Hedayati Dezfuli, F., and Alam, M.S. 2014a. Performance of carbon fiber-reinforced elastomeric isolators manufactured in a simplified process: experimental investigations. *Structural Control and Health Monitoring*, 21(11): 1347–1359.

Hedayati Dezfuli F., and Alam, M.S. 2014b. Performance-based assessment and design of FRP-based high damping rubber bearing incorporated with shape memory alloy wires. *Engineering Structures*, 61: 166-183.

Hedayati Dezfuli, F., and Alam, M.S. 2014c. Finite element simulation of carbon fiber-reinforced elastomeric isolators manufactured through a cold-vulcanization process. *In Proceedings of 9th International Conference on Short and Medium Span Bridges, SMSB,* July 15-18, 2014, Calgary, Alberta, Canada.

Hedayati Dezfuli, F., and Alam, M.S. 2015a. Hysteresis model of shape memory alloy (SMA) wire-based laminated rubber bearing under compression and unidirectional shear loadings. *Smart Materials and Structures,* In Press.

Hedayati Dezfuli, F., and Alam, M.S. 2015b. Vulnerability assessment of multi-span continuous steel-girder bridges isolated by SMA wire-based natural rubber bearing (SMA-NRB), In Proceedings of *Structures Congress 2015 Conference*, April 23-25, 2015, Portland, Oregon, USA.

Hoss, L., and Marczak, R.J. 2010. A new constitutive model for rubber-like materials. *In Proceedings of Conference on Computational Mechanics*, 29: 2759-2773. Buenos Aires, Argentina, 15-18 November 2010.

Howie, I., and Karbhari, V.M. 1994. Effect of materials architecture on strengthening efficiency of composite wraps for deteriorating columns in north-east. *In Proceedings of 3rd Materials Engineering Conference, Infrastructure: New Materials and Methods of Repair*, pp. 199-206.

Hwang, C.L., and Yoon, K. 1981. Multiple attribute decision making: methods and applications: a state-of-the-art survey. Springer-Verlag, Berlin and New York.

Hwang, H., Jernigan, J.B., Billings, S., and Werner, S.D. 2000a. Expert opinion survey on bridge repair strategy and traffic impact. *Post-Earthquake Highway Response and Recovery Seminar.* CERI: St. Louis, MO.

Hwang, H., Jernigan, J.B., and Lin, Y.W., 2000b. Evaluation of seismic damage to Memphis bridges and highway systems, *Journal of Bridge Engineering-ASCE*, 5: 322-30.

Hwang, H., Liu, J.B., and Chiu, Y.H. 2001. Seismic fragility analysis of highway bridges, MAEC report: project MAEC RR-4. Urbana: Mid-America Earthquake Center.

Hwang, J.S., and Chiou, J.M. 1996. An equivalent linear model of lead-rubber seismic isolation bearings. Engineering Structures, 18(7): 528-536.

Hwang, J.S., Wu, J.D., Pan, T.C., and Yang, G., 2002. A mathematical hysteretic model for elastomeric isolation bearings, *Earthquake Engineering and Structural Dynamics.* 31(4), 771-789.

Ibrahim, Y.E. 2005. A new visco-plastic device for seismic protection of structures. Ph.D. thesis, Virginia Polytechnic Institute and State University, Virginia.

Jernigan, J.B., and Hwang, H. 2002. Development of bridge fragility curves. *7th US National Conference on Earthquake Engineering*, EERI: Boston, MA.

Japan Road Association (JRA). 2002. Specifications for highway bridges, Part V: Seismic design, Tokyo, Japan.

Kalpakidis, I.V., Constantinou, M.C., and Whittaker, A.S. 2010. Modeling strength degradation in lead-rubber bearings under earthquake shaking. *Earthquake Engineering and Structural Dynamics*, 39:1533-1549.

Kang, B.S., Kang, G.J., and Moon, B.Y. 2003. Hole and lead plug effect on fiber reinforced elastomeric isolator for seismic isolation. *Journal of Materials Processing Technology*, 140: 592-597.

Kelly, J.M. 1986. Aseismic base isolation: review and bibliography, *Soil Dynamics and Earthquake Engineering*, 5(4): 202-216.

Kelly, J.M. 1997. Earthquake-resistant design with rubber. 2nd ed. *Springer*, London. U.K.

Kelly, J.M. 1999. Analysis of fiber-reinforced elastomeric isolator. *Journal of Seismology and Earthquake Engineering (JSEE),* 2(1): 19-34.

Kelly, J.M. 2002. Seismic isolation systems for developing countries. *Earthquake Spectra*, 18(3): 385-406.

Kelly, J.M., and Marsico, M.R. 2004. Tension buckling in rubber bearings affected by cavitation, *Engineering Structures*, 56: 656-663.

Kelly, T.E. 2001. Base isolation of structures - design guidelines. Holmes Consulting Group Ltd, Wellington, New Zealand.

Kikuchi, M., and Aiken, I.D. 1997. An analytical hysteresis model for elastomeric seismic isolation bearings, *Earthquake Engineering and Structural Dynamics*, 26, 215-231.

Kunde, M. C., and Jangid, R.S. 2003. Seismic behaviour of isolated bridges: A-state-of-the-art review. *Electronic Journal of Structural Engineering-EJSE*, 3, 140-170.

Lagoudas, D.C. 2008. Shape memory alloys. Springer Science and Business Media, LLC.

Liu, Y. 2003. Mechanical and thermomechanical properties of a $Ti_{50}Ni_{25}Cu_{25}$ melt spun ribbon. *Materials Science and Engineering: A*; 354(1):286-291.

Liu, H., Wang, X., and Liu, J. 2008. The shaking table test of an SMA strands-composite bearing. *Earthquake Engineering and Engineering Vibration*, 28(3): 152-156.

Mackie, K.R., and Stojadinovic, B. 2001. Probabilistic seismic demand model for California bridges. *Journal of Bridge Engineering-ASCE*, 6(6), 468–480.

Mackie, K.R., and Stojadinovic, B. 2006. Post-earthquake functionality of highway overpass bridges. *Earthquake Engineering and Structural Dynamics*; 35:77–93.

Madas, P., and Elnashai, A.S. 1992. A new passive confinement model for transient analysis of reinforced concrete structures. *Earthquake Engineering and Structural Dynamics*, 21(5), 409-431.

Mander, J.B., and Basoz, N. 1999. Seismic fragility curve theory for highway bridges. *5th US Conference on Lifeline Earthquake Engineering. ASCE*, Seattle, WA, USA.

Marioni, A. 1998. The use of high damping rubber bearings for the protection of the structures from seismic risk. *Jornadas Portuguesas de Engenharia de Estruturas*, Lisbon, 25-28 November 1998.

McKenna, F., Fenves, G.L., and Scott, M.H. 2000. Open system for earthquake engineering simulation (OpenSees). Berkeley, CA: University of California. Available from http://opensees.berkeley.edu.

Menegotto, M., and Pinto, P.E. 1973. Method of analysis for cyclically loaded R.C. plane frames including changes in geometry and non-elastic behaviour of elements under combined normal force and bending. *In Proceedings of Symposium on the Resistance and Ultimate Deformability of Structures Acted on by Well Defined Repeated Loads, International Association for Bridge and Structural Engineering*, Zurich, Switzerland, 15-22.

Monti G., and Nistico, N. 2002. Simple probability-based assessment of bridges under scenario earthquakes. *Journal of Bridge Engineering-ASCE*, 7: 104-114.

Moon, B.Y., Kang, G.J., Kang, B.S., and Kelly, J.M. 2002. Design and manufacturing of fiber reinforced elastomeric isolator for seismic isolation. *Journal of Materials Processing Technology*, 130-131: 145-150.

Mordini, A., and Strauss, A. 2008. An innovative earthquake isolation system using fiber reinforced rubber bearings. *Engineering Structures*, 30: 2739-2751.

Moschonas, I.F., Kappos, A.J., Panetsos, P., Papadopoulos, V., Makarios, T., and Thanopoulos, P. 2009. Seismic fragility curves for Greek bridges: Methodology and case studies. *Bulletin of Earthquake Engineering*, 7(2): 439-468.

Mottahedi, M., Dadalau, A., Hafla, A., and Verl, A. 2010. Numerical analysis of relaxation test based on prony series material model. *Stuttgart Research Centre for Simulation Technology (SRC SimTech)*, Stuttgart. Germany.

Nateghi, F., and Shahsavar, V.L. 2004. Development of fragility and reliability curves for seismic evaluation of a major prestressed concrete bridge. *13th World Conference on Earthquake Engineering*, Vancouver, B.C. Canada.

Naumoski, N., Tso, W.K., and Heidebrecht, A.C. 1988. A selection of representative strong motion earthquake records having different A/V ratios, EERG Report 88-01, *Earthquake Engineering Research Group*, Department of Civil Engineering, McMaster University, Hamilton, ON, Canada.

Naeim, F., and Kelly, J.M. 1999. Design of seismic isolated structures: from theory to practice. John Wiley & Sons, Inc., New York.

Nielson, B.G. and DesRoches, R. 2004. Improved methodology for generation of analytical fragility curves for highway bridges. *9th ASCE Specialty Conference on Probabilistic Mechanics and Structural Reliability*, Albuquerque, NM, USA.

Nielson, B.G., and DesRoches, R., 2007. Seismic fragility methodology for highway bridges using a component level approach, *Earthquake Engineering and Structural Dynamics*, 36: 823-839.

Ogden, R.W. 1972. Large deformation isotropic elasticity - on the correlation of theory and experiment for incompressible rubberlike solids. In Proceedings of the Royal Society of London. Series A, *Mathematical and Physical Sciences*, 326(1567): 565-584.

Omori, T., Ando, K., Okano, M., Xu, X., Tanaka, Y., Ohnuma, I., Kainuma, R., and Ishida, K. 2011. Superelastic effect in polycrystalline ferrous alloys. *Science*, 333(6038): 68-71.

Ozbulut, O.E., Mir, C., Moroni, M.O., Sarrazin, M., and Roschke, P.N. 2007. A fuzzy model of superelastic shape memory alloys for vibration control in civil engineering applications. *Smart Materials and Structures*, 16(3), 818-829.

Ozbulut, O.E., and Hurlebaus, S. 2010. Performance evaluation of shape memory alloy/rubber-based isolation systems for seismic response mitigation of bridges. *Sensors and Smart Structures Technologies for Civil, Mechanical, and Aerospace Systems*, 76473.

Ozbulut, O.E., and Hurlebaus, S. 2011. Seismic assessment of bridge structures isolated by a shape memory alloy/rubber-based isolation system, *Smart Materials and Structures,* 20(1): 015003.

Ozdemir, G. Avsar, O., and Bahyan, B. 2011. Change in response of bridges isolated with LRBs due to lead core heating. *Soil Dynamics and Earthquake Engineering*, 31: 921-929.

Ozkaya, C., Akyuz, U., Caner, A., Dicleli, M., and Pınarbası, S. 2011. Development of a new rubber seismic isolator: 'Ball Rubber Bearing (BRB)'. *Earthquake Engineering and Structural Dynamics*, 40(12): 1337-1352.

Padgett, J.E., Nielson, B.G., and DesRoches, R. 2008. Selection of optimal intensity measures in probabilistic seismic demand models of highway bridge portfolios. *Earthquake Engineering and Structural Dynamics*, 37: 711-725.

Park, R. 1988. Ductility evaluation from laboratory and analytical testing. *In Proceedings of 9th World Conference on Earthquake Engineering - 9WCEE*, Tokyo, Japan, 8:605-616.

PEER Strong Motion Database, http://peer.berkeley.edu/smcat/search.html

Perzyna, P. 1966. Fundamental problems in viscoplasticity. *Advances in Applied Mechanics*, 9(2): 244-368.

Pinho, R., Casarotti, C., and Antoniou, S. 2007. A comparison of singlerun pushover analysis techniques for seismic assessment of bridges. *Earthquake Engineering and Structural Dynamics*, 36(10), 1347-1362.

Ramanathan, K., DesRoches, R., and Padgett, J.E. 2010. Analytical fragility curves for multi-span continuous steel girder bridges in moderate seismic zones. Transportation Research Record 2202, Transportation Research Board, Washington, DC, 173–182.

Russo, G., Pauletta, M., and Cortesia, A. 2013. A study on experimental shear behaviour of fiber-reinforced elastomericisolators with various fiber layouts, elastomers and aging conditions. *Engineering Structures*, 52, 422-433.

SAP2000 Software, Computers and Structures, Integrated Software for Structural Analysis and Design CSI, Berkeley, California, USA (www.csiamerica.com)

Sarrazinn, M., Moroni, O., Neira, C., and Venegas, B. 2013. Performance of bridges with seismic isolation bearings during the Maule earthquake, Chile, *Soil Dynamics and Earthquake Engineering*. 47: 117-131.

SeismoStruct software, SeismoSoft Inc., v6.5, 2014, Pavia, Italy (www.seismosoft.com)

Shinozuka, M., Feng, M.Q., Lee, J., and Naganuma, T. 2000. Statistical analysis of fragility curves. *Journal of Engineering Mechanics-ASCE*, 126:1224–1231.

Siqueiraa, G.H., Sanda, A.S., Paultre, P., and Padgett, J.E. 2014. Fragility curves for isolated bridges in eastern Canada using experimental results, *Engineering Structures*, 74: 311-324.

Skinner, R.I., Robinson, W.H., and McVerry, G.H. 1993. An introduction to seismic isolation, John Wiley & Sons Ltd., U.K.

Song, J., and Ellingwood, B.R. 1999. Seismic reliability of special moment steel frames with welded connections: II. *Journal of Structural Engineering-ASCE*, 125:372–384.

Soong, T.T., and Dargush, G.F. 1997. Passive energy dissipation systems in structural engineering. John Wiley and Sons, Inc., Chichester, England.

Strnadel, B., Ohashi, S., Ohtsuka, H., Ishihara, T., and Miyazaki, S. 1995. Cyclic stress-strain characteristics of Ti-Ni and Ti-Ni-Cu shape memory alloys. *Materials Science and Engineering: A*, 202(1-2): 148 156.

Suduo, X., and Xiongyan, L. 2007. Control devices incorporated wit shape memory alloy. *Earthquake Engineering and Engineering Vibration*, 6(2): 159-169.

Takayama, M., and Morita, K. 2000. Finite element analysis focused on the flange plates and connecting bolts of rubber bearings. *12th World Conference on Earthquake Engineering*, Auckland, New Zealand, 30 January - 4 February, 2000.

Tanaka, Y., Himuro, Y., Kainuma, R., Sutou, Y., Omori, T., and Ishida, K. 2010. Ferrous polycrystalline shape-memory alloy showing huge superelasticity. *Science*, 327(5972): 1488-1490.

The MathWorks, Inc. MATLAB R2010a, 2011.

Toopchi-Nezhad, H., Tait M.J., and Drysdale, R.G. 2008a. Lateral response evaluation of fiber-reinforced neoprene seismic isolators utilized in an unbonded application. *Journal of Structural Engineering-ASCE*, 134(10): 1627-1637.

Toopchi-Nezhad, H., Tait M.J., and Drysdale, R.G. 2008b. Testing and modeling of square carbon fiber-reinforced elastomeric seismic isolators. *Structural Control and Health Monitoring*, 15(6): 876-900.

Tsai, C.S., Chiang, T.C., Chen, B.J., and Lin, S.B. 2003. An advanced analytical model for high damping rubber bearings. *Earthquake Engineering and Structural Dynamics*, 32(9):1373-1387.

Tsai, H.C., and Kelly, J.M. 2002. Stiffness analysis of fiber-reinforced rectangular seismic isolators. *Journal of Engineering Mechanics-ASCE*, 128(4), 462-470.

Tsai, H.S., and Kelly, J.M. 2004. Buckling load of seismic isolators affected by flexibility of reinforcement. *International Journal of Solids and Structures*, 42(1), 255-269.

Turkington, D.H., Cooke, N., Moss, P.J., and Carr, A.J. 1989. Development of a design procedure for bridges on lead-rubber bearings. *Engineering Structures*, 11: 2-8.

Van Engelen, N.C., Osgooei, P.M., Tait, M.J., and Konstantinidis, D. 2014. Experimental and finite element study on the compression properties of Modified Rectangular Fiber-Reinforced Elastomeric Isolators (MR-FREIs). *Engineering Structures*, 74: 52-64.

Wadham-Gagnon, M., Hubert, P., Semler, C., Paidoussis, M.P., Vezina, M., and Lavoie, D. 2006. Hyperelastic modeling of rubber in commercial finite element software (ANSYS). *In Proceedings of Conference on SAMPE 2006*, Long Beach, CA, April 30 - May 4, 2006.

Warn, G.P., and Whittaker, A.S. 2004. Performance estimates in seismically isolated bridge structures. *Engineering Structures*, 26(9): 1261-1278.

Wen, Y.K. 1976. Method for random vibration of hysteretic systems. *Journal of the Engineering Mechanics-ASCE*, 102(2), 249-263.

Wilde, K., Gardoni, P., and Fujino, Y. 2000. Base isolation system with shape memory alloy device for elevated highway bridges. *Engineering Structures*, 22(3): 222-229.

Yamazaki, F., Motomura, H., and Hamada, T. 2000. Damage assessment of expressway networks in Japan based on seismic monitoring, *In Proceedings of 12th World Conference on Earthquake Engineering*, CD-ROM, 2000; Paper No. 0551.

Yoon, K.P., and Hwang, C.L. 1995. Multiple Attribute decision making an introduction. SAGE Publications, Inc., Thousand Oaks, London, New Delhi.

Yoshida, J., Abe, M., and Fujino, Y. 2004. Constitutive model of high-damping rubber materials. *Journal of Engineering Mechanics-ASCE*, 130(2): 129-141.

Zhang, Y., Hu, H., and Zhu, S. 2009. Seismic performance of benchmark base-isolated bridges with superelastic Cu-Al-Be restraining damping device. *Structural Control and Health Monitoring*, 16(6): 668-685.

Zhang, H., Peng, T., Li, J., and Li, W. 2011. Experimental study of FRP rubber bearing. *Advanced Materials research*, 169-170: 1621-1624.

Zheng L., and Wang, T. 2011. Application of lead rubber bearing in curved continuous bridge. *Advanced Materials research*. 250-253: 1533-1536.

Appendices

Appendix A: Design procedure of determining the radius and pre-strain of SMA wires

1. Set a target value for the effective horizontal stiffness, K_{Hd}:

$$K_{Hd} = 1.00 \ kN/mm$$

   This value corresponds to the maximum shear force $F_{s\ max} = 81.5$ kN at $\gamma = 100\%$

2. Considering a force ratio of 10%, the maximum lateral force generated by SMA wire, $F_{SMA\ max}$ can be calculated.

$$F_{SMA_{max}} = R_F \cdot F_{S_{max}} = 8.2 \ kN$$

3. Knowing the maximum strain in SMA wires at $\gamma = 100\%$ (from Equations (5.3), (5.4), and (5.6)), and accordingly, the maximum axial stress in wires, σ_{max}, the initial radius of SMA wires, $r_w{}^0$, can be obtained from $F_{SMA\ max}$.

$$r_w^0 = \left(\frac{F_{SMA_{max}}}{\pi \sigma_{max}}\right)^{0.5} \approx 1.75 \ mm$$

4. Choosing a radius for SMA wire, calculating the effective horizontal stiffness, K_H, and comparing it with K_{Hd}.

   K_H should be greater than K_{Hd}, with a minimum relative difference of 15% (M_K)

$$r_w^1 = 1.2 \ r_w^0 \approx 2.10 \ mm$$
$$K_H = 1.11 \ kN/mm$$
$$K_H < 1.15 \ K_{Hd}$$

   Since K_H is lower than the desired value, radius of wire increases and step 4 is repeated.

$$r_w^2 = 1.2 \ r_w^1 \approx 2.50 \ mm$$
$$K_H = 1.14 \ kN/mm$$
$$K_H > 1.15 \ K_{Hd}$$

5. Considering a zero initial pre-strain, for the first try, the pre-strain in SMA wire, $\varepsilon_0{}^1$, is 1%.

$$\varepsilon_0^1 = 0 + 0.01 = 0.01$$
$$K_H = 1.12 \ kN/mm$$

$$\frac{\left|K_H - K_{H_d}\right|}{K_{H_d}} > 10\%$$

6. Considering the pre-strain value lower than 5%, since the relative difference between the new and the target values of the effective horizontal stiffness is higher than 10%, step 5 should be repeated.

$$\varepsilon_0^2 = \varepsilon_0^1 + 0.01 = 0.02$$

$$K_H = 1.07 \ kN/mm$$

$$\frac{\left|K_H - K_{H_d}\right|}{K_{H_d}} < 10\%$$

7. Final result: $r_w = 2.5$ mm and $\varepsilon_0 = 2\%$

Appendix B: Bilinear kinematic hardening model flowchart
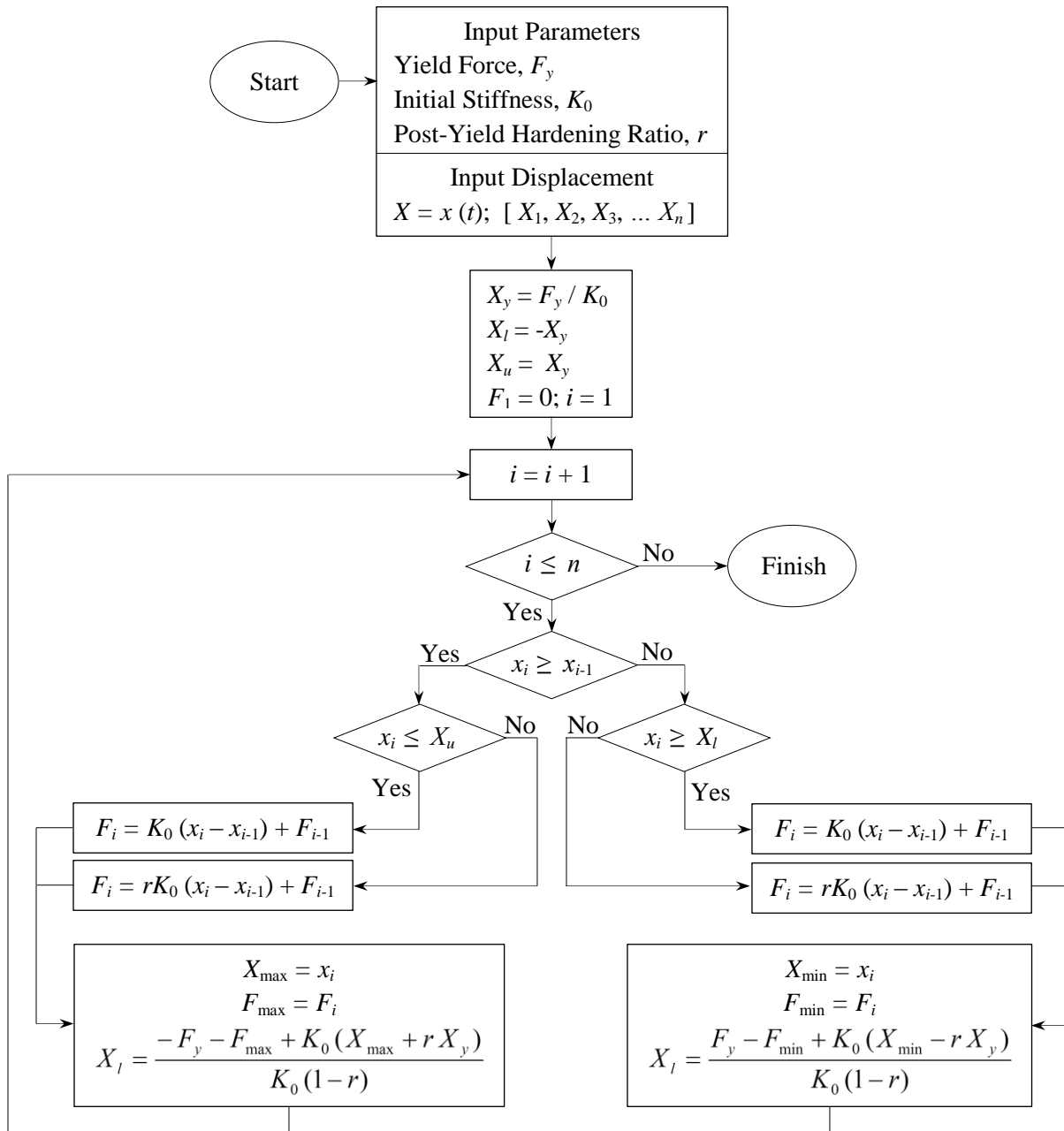
Figure B.1. Flow chart of bilinear kinematic hardening model

The flowchart contains the following elements:

Start

Input Parameters
Yield Force, F_y
Initial Stiffness, K_0
Post-Yield Hardening Ratio, r

Input Displacement
$X = x(t);\ [\ X_1, X_2, X_3, \ldots X_n\ ]$

$X_y = F_y / K_0$
$X_l = -X_y$
$X_u = X_y$
$F_1 = 0;\ i = 1$

$i = i + 1$

$i \leq n$ — No → **Finish**

Yes ↓

$x_i \geq x_{i-1}$ — Yes (left) / No (right)

Left branch (Yes):
$x_i \leq X_u$ — Yes / No

$F_i = K_0\,(x_i - x_{i-1}) + F_{i-1}$

$F_i = rK_0\,(x_i - x_{i-1}) + F_{i-1}$

$X_{max} = x_i$
$F_{max} = F_i$
$$X_l = \frac{-F_y - F_{max} + K_0\,(X_{max} + r\,X_y)}{K_0\,(1-r)}$$

Right branch (No):
$x_i \geq X_l$ — No / Yes

$F_i = K_0\,(x_i - x_{i-1}) + F_{i-1}$

$F_i = rK_0\,(x_i - x_{i-1}) + F_{i-1}$

$X_{min} = x_i$
$F_{min} = F_i$
$$X_l = \frac{F_y - F_{min} + K_0\,(X_{min} - r\,X_y)}{K_0\,(1-r)}$$

271